UNIVERSIDAD COMPLUTENSE DE MADRID
FACULTAD DE CIENCIAS FÍSICAS

TESIS DOCTORAL

Materiales vitrocerámicos funcionales basados en feldespatos jerárquicamente micro-nanoestructurados

MEMORIA PARA OPTAR AL GRADO DE DOCTOR

PRESENTADA POR

Víctor Fuertes de la Llave

Directores

Esther Enríquez Pérez
José Francisco Fernández Lozano

Madrid

UNIVERSIDAD COMPLUTENSE DE MADRID

FACULTAD DE CIENCIAS FÍSICAS

Departamento de Física de Materiales

TESIS DOCTORAL

Materiales vitrocerámicos funcionales basados en feldespatos jerárquicamente micro-nanoestructurados

MEMORIA PARA OPTAR AL GRADO DE DOCTOR EN FÍSICA

PRESENTADA POR

Víctor Fuertes de la Llave

Directores

Dra. Esther Enríquez Pérez

Prof. José Francisco Fernández Lozano

Madrid, 2019

UNIVERSIDAD COMPLUTENSE DE MADRID

FACULTAD DE CIENCIAS FÍSICAS

Departamento de Física de Materiales

Tesis doctoral

Materiales vitrocerámicos funcionales basados en feldespatos jerárquicamente micro-nanoestructurados

Memoria para Optar al Grado de Doctor en Física

Víctor Fuertes de la Llave

Dirigida por:

Dra. Esther Enríquez Pérez

Prof. José Francisco Fernández Lozano

Madrid, 2019

Instituto de Cerámica y Vidrio

Consejo Superior de Investigaciones Científicas

UNIVERSIDAD COMPLUTENSE MADRID

DECLARACIÓN DE AUTORÍA Y ORIGINALIDAD DE LA TESIS PRESENTADA PARA OBTENER EL TÍTULO DE DOCTOR

D./Dña. Víctor Fuertes de la Llave,
estudiante en el Programa de Doctorado en Física,
de la Facultad de Ciencias Físicas de la Universidad Complutense de Madrid, como autor/a de la tesis presentada para la obtención del título de Doctor y titulada:

Materiales vitrocerámicos funcionales basados en feldespatos jerárquicamente micro-nanoestructurados

y dirigida por: la Dra. Esther Enríquez Pérez y el Prof. José Francisco Fernández Lozano

DECLARO QUE:

La tesis es una obra original que no infringe los derechos de propiedad intelectual ni los derechos de propiedad industrial u otros, de acuerdo con el ordenamiento jurídico vigente, en particular, la Ley de Propiedad Intelectual (R.D. legislativo 1/1996, de 12 de abril, por el que se aprueba el texto refundido de la Ley de Propiedad Intelectual, modificado por la Ley 2/2019, de 1 de marzo, regularizando, aclarando y armonizando las disposiciones legales vigentes sobre la materia), en particular, las disposiciones referidas al derecho de cita.

Del mismo modo, asumo frente a la Universidad cualquier responsabilidad que pudiera derivarse de la autoría o falta de originalidad del contenido de la tesis presentada de conformidad con el ordenamiento jurídico vigente.

En Madrid, a 21 de mayo de 2019

Fdo.: Víctor Fuertes de la Llave

A mi madre y mi abuela.

A mi hermano.

"Cuando creíamos que teníamos todas las respuestas, de pronto, cambiaron todas las preguntas".

Mario Benedetti

"La suerte favorece sólo a la mente preparada".

Louis Pasteur

Agradecimientos

Cuando uno empieza una Tesis Doctoral, probablemente esta es uno de las partes que más veces se imagina escribiendo. Durante estos casi tres años y medio han sido muchos los momentos vividos, con innumerables alegrías y emociones, los cuales siempre recordaré con el paso del tiempo. En numerosas ocasiones a lo largo de estos años he pensado que no podía olvidarme de mencionar en los agradecimientos a una determinada persona, sin embargo, llegado a este punto, son muchas las personas que han contribuido a que llegue hasta aquí, por lo que si me dejo alguna en el tintero espero que no me lo tome en cuenta.

En primer lugar me gustaría agradecer a mis directores de tesis, la Dra. Esther Enríquez Pérez y el Prof. José Francisco Fernández Lozano. Sin vuestra dedicación y continua predisposición en la dirección de esta tesis, alcanzar esta meta no hubiera sido posible. He aprendido muchas cosas de vosotros, entre ellas, a ir siempre un paso más allá, despertando mi curiosidad científica en todo momento. Gracias por la confianza depositada en mí y por haber logrado introducirme en el mundo de "***La Ciencia***", convirtiéndola en mi vocación.

En segundo lugar me gustaría agradecer a la empresa Centro Tecnológico Vidres, S.L por el apoyo económico, así como, por la posibilidad de conocer un poco más de cerca el trabajo a nivel industrial, complementándolo y enriqueciéndolo con un trabajo a nivel científico, lo cual no es siempre una tarea sencilla.

También me gustaría agradecer a todo el personal del Instituto de Cerámica y Vidrio (ICV) por su colaboración y disposición a la hora de emplear las diferentes técnicas y servicios que han permitido el desarrollo de este trabajo.

Como no, a mis compañeros del ICV, por todos los momentos buenos vividos a lo largo de este tiempo. Cuando entré hace cinco años y vi el buen rollo que había en el ICV no podía creerlo, pero definitivamente, se ha ido reafirmando con el paso de los años. Sois muchos los que habéis presenciado esta etapa de mi vida y aunque algunos ya no estéis aquí, que sepáis que ha sido un placer coincidir con vosotros. Quiero hacer un agradecimiento especial a Esther (mi "creti favorita"), por hacer constantemente de jefa, compañera y sobre todo amiga. Te estaré eternamente agradecida por tu paciencia y dedicación, así como por tu apoyo y consejos, a veces tan necesarios, en los momentos buenos y sobre todo en los malos. A todos mis "Caraculos", por las bromas y risas vividas tanto dentro como fuera del ICV, con Esther y Carmen, casi siempre, como protagonistas. A Juli, por estar siempre dispuesto a ayudarte y sacarte una sonrisa sin recibir nada a cambio. Sin tus bromas y jugarretas el ICV no sería lo mismo. A Manu, por tus consejos y nuestros piques futbolísticos ("pequeño", siempre sabrás que Getafe es mejor que Leganés…). A Carmen, por todos esos momentos de cachondeo (y tu rica comida), que han hecho este camino sea mucho más sencillo. A Jesús ("el Titi"), quien nos iba a decir que después de coincidir en un congreso íbamos a acabar en el mismo equipo. Tus bromas (siempre en "tono jocoso"), han conseguido hacerme el día a día mucho más llevadero. A Eva, por tu simpatía y tus habilidades informáticas, que me han sacado de algún que otro aprieto. Gracias al resto de compañeros de mi grupo, "Ceramic for Smart Systems": Adrián, Patri, Ceci, Alberto, Aida, Fer, Adolfo, Carlitos y Rocío, por vuestra ayuda y dedicación en diferentes momentos de esta bonita etapa. También quiero agradecer de forma especial a "los Muñecos" (Trivi, Zapata, JJ, Titi, Juli, Manu y Luis). La mayoría llegasteis a mitad de mi Tesis, pero desde ese momento han sido muchos y buenos los momentos que hemos pasado haciendo "piña", ¡habiendo incluso una boda de por medio! Gracias también a funceramics: Marco, David, Teresa, Carlos, Isa, Mónica, Pablo y Raquel por todas esas conversaciones y anécdotas que hemos

compartido durante las comidas, desayunos o incluso en el propio laboratorio. No quisiera olvidarme tampoco de: Joaquín, Sara, Ana, Laura, Giulio y Maca.

A mis amigos de toda la vida: Isma, Jorge, Alex, Marcos e Iván, así como, a mis amigos del pueblo, especialmente a: David, Raúl, Sergio y Pichu. También a Miguel Ángel, nuestras eternas conversaciones han hecho todo esto más fácil. Gracias a todos por los momentos de desconexión vividos juntos.

Por último y de manera muy especial, me gustaría agradecer a mi familia por haberme inculcado unos buenos principios y haberme permitido estudiar lo que quería. Gracias a ti mamá, por impulsarme desde pequeñito a esforzarme para cumplir mis sueños, puedo decir que soy un "**Doctor en Física**". A ti abuela, por tu cariño y apoyo incondicional, sé que siempre estarás enormemente orgulloso de "tu hijo". Finalmente a mi hermano, Alejandro, que en estos diez años has conseguido transmitirme una alegría y felicidad infinita en tu día a día. Tu "brother" siempre estará a tu lado para verte crecer.

A todos y cada uno de vosotros, **¡GRACIAS DE CORAZÓN!**

La realización de este trabajo de Tesis doctoral ha sido posible gracias a la financiación del Ministerio de Economía y Competitividad (MINECO), por los proyectos de investigación MAT2017-86450-C4-1-R y CDTI (IDI-20130894 y IDI-20161120)

Índice de contenido

Índice de figuras

Índice de tablas

Abstract

The Spanish ceramic industry is one of the main world powers, positioning itself as a leader in terms of technological development, design and product quality. Traditionally, the main objective of the sector was to reduce costs, as well as the environmental impact. However, due to the great competition existing in this sector, the need arises to achieve a differentiation in the products. This can be achieved by the introduction of new functionalities, compared to the traditional demands of resistance and durability. [1,2]

The great boom of nanoscience in recent years has allowed the creation of new materials with improved properties. Traditionally, nanoparticles have been introduced into ceramic glazes for decorative purposes. However, this research line has hardly been followed, mainly due to its high price, the difficulty of handling, the toxicity associated with its small size and the tendency to form agglomerates due to the high reactivity, limiting its use at an industrial level. In situ formation of nanostructured materials could be a good alternative, since it would avoid the aforementioned difficulties, simultaneously providing the ceramic material with improvements in its properties, as well as exclusive functionalities. However, this work methodology has hardly been implemented in the ceramic sector, despite being an innovative and promising alternative.[3–8]

On the other hand, glass-ceramic materials are widely used in the ceramic sector, in part, due to the possibility of obtaining different functionalities depending on the application, which is intimately conditioned by the chemical composition and the developed microstructure. So far, it has been demonstrated that glass-ceramic materials based on feldspar crystallisations have very remarkable mechanical properties, [9,10] which makes them suitable for their use in industrial construction applications. However, little attention has been paid to the characterization of the rest of its properties, as well as its development in a nanostructured form, despite the versatility and advantages that it could offer.

Therefore, the main objective of this thesis work has been the development of micro-nanostructured glass-ceramic materials, based on crystallizations of plagioclase-type feldspars, that are industrially scalable and that present new and improved functionalities thanks to a thorough engineering of their structure and microstructure.

To obtain these materials, a conventional ceramic process and a fast sintering route have been followed, easily reproducible, in order to obtain highly sustainable materials and economically viable, in order to scale them at an industrial level. The glass-ceramic materials obtained (sodium and calcium-rich plagioclase) are characterized by having a hierarchical micro-nanostructuration, high crystallinity, > 90%, high densification and low porosity.

For the study of these materials, firstly, the crystallization mechanism of this new family of micro-nanostructured glass-ceramic materials was established and an exhaustive study of the structure and the developed micro-nanostructure was carried out, especially for the glass-ceramic material based on crystallizations of sodium-rich plagioclase. For this purpose, quenching experiments, different techniques of chemical analysis (DTA/TG and hot-stage microscopy), structural characterization (XRD, XPS, NMR and Raman) and microstructural characterization by means of different types of microscopy (FE-SEM, TEM and HRTEM, confocal Raman microscopy and Rayleigh light- scattering microscopy) were carried out. This study reveals that the nucleation of microcrystals and nanocrystals begins on heating. However, it is during the cooling when the unique micro-nanostructure is developed, in which the microcrystals are isolated from each other by nanostructured regions. In addition, the analysis of the atomic environments of Si, by means of NMR, allows to establish the presence of a slightly disordered Si,Al distribution in the tetrahedral sites of the feldspar network, which is corroborated by Raman spectroscopy. This explains some remarkable properties of this material, such as good luminescent behavior. Rayleigh light-scattering microscopy and TEM measurements allowed the identification of unmixing domains by spinodal decomposition, of ~ 2-3 μm.

The structural and microstructural study of these materials opens the way to a systematic characterization of their properties, corroborating their improvement thanks to the developed micro-nanostructured. Therefore, the next step was the study of their dielectric, mechanical, heat-reflective and luminescent properties, and their correlation with structural and microstructural characteristics.

The combination of micro and nanometric-size crystals results in a greater number of grain boundaries regarding ceramic standard materials, which favour that a larger number of electron, phonon and photon scattering processes occur. These good microstructural characteristics are, likewise, enhanced by the combination of high crystallinity and low porosity, with an average pore size < 5μm. Regarding the heat-reflective properties, these materials are characterized by having a high albedo and a low thermal diffusivity ($0{,}17 \cdot 10^{-6} m^2/s$). The mechanical response is

characterized by having a high fracture toughness (up to 2.1 $MPa \cdot m^{1/2}$) and flexural strength (in the range 83-111 MPa), as well as reaching the best hardness values (9.5 GPa) obtained for a ceramic glaze. With regard to the dielectric properties, these materials have a dielectric insulating behavior far higher than other conventional ceramic materials, highlighting by having the largest dielectric strength values reported for ceramic insulators, > 59 kV/mm at room temperature and 30-44 kV/mm up to 200 ºC. Finally, the slight disorder distribution of Si, Al in the tetrahedral sites of the feldspar network, favours the presence of structural defects, mainly Al-O$^-$-Al and [AlO_4/alkali$^+$] complexes These defects act as active luminescent centers allowing an improvement of one order of magnitude and six times in the UV/blue and red emissions, respectively, regarding a natural feldspar. Furthermore, such photoluminescent emission can be modulated, both in intensity and in wavelength, by modifying the Si,Al disorder in the structure, by means of slight chemical variations of the structural elements.

Based on these results, a wide range of possibilities is opened for their use in high voltage applications, such as electrical insulators, in high pedestrian traffic pavements or linings for buildings, for their excellent mechanical properties. They can also be used in reflective pavements or linings and in cool roofs, as well as safety markers or light emitting glasses.

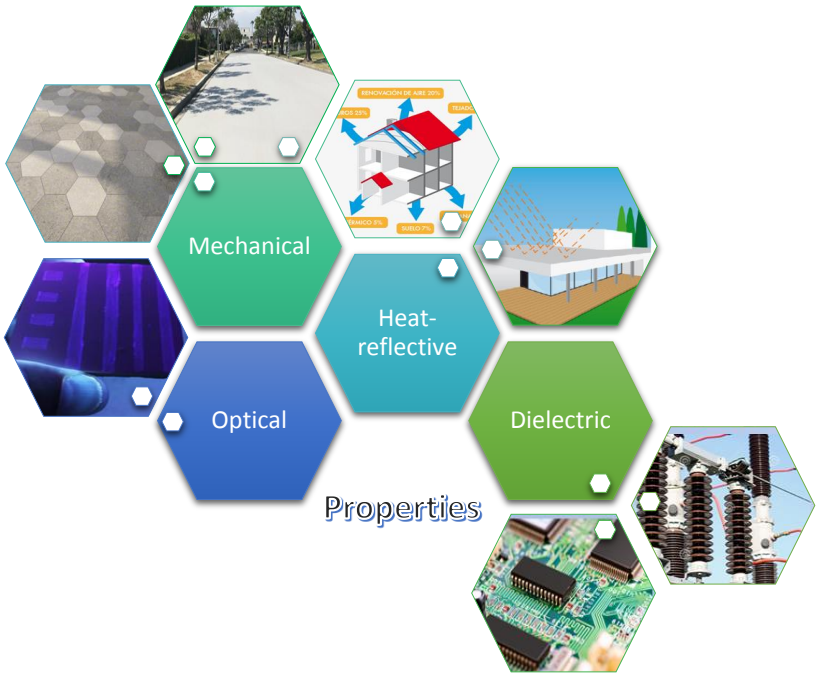

Figure 1. Summary outline of the possible applications of the micro-nanostructured glass-ceramic materials developed, thanks to their good dielectric, optical, mechanical and heat-reflective properties

.

Resumen

La industria cerámica española es una de las principales potencias a nivel mundial, posicionándose como líder en cuanto a desarrollo tecnológico, diseño y calidad de los productos. Tradicionalmente, el principal objetivo del sector era tanto reducir costes, como el impacto medioambiental. Sin embargo, debido a la gran competencia existente en dicho sector, surge la necesidad de conseguir una diferenciación en los productos. Esto se puede lograr gracias a la introducción de nuevas funcionalidades, frente a las tradicionales exigencias de resistencia y durabilidad.[1,2]

El gran auge de la nanociencia en los últimos años ha permitido la creación de nuevos materiales con propiedades mejoradas. Tradicionalmente, las nanopartículas han sido introducidas en esmaltes cerámicos con fines decorativos. Sin embargo, apenas se ha seguido esta línea de investigación debido, fundamentalmente, a su elevado precio, la dificultad de manipulación, la toxicidad asociada a su pequeño tamaño y la tendencia a formar aglomerados debido a la alta reactividad, limitando su uso a nivel industrial. La formación in situ de materiales nanoestructurados podría ser una buena alternativa, ya que evitaría las dificultades anteriormente mencionadas, dotando simultáneamente al material cerámico de mejoras en sus propiedades, así como de funcionalidades exclusivas. Sin embargo, esta metodología de trabajo apenas ha sido implementada en el sector cerámico, a pesar de ser una alternativa innovadora y prometedora. [3–8]

Por otra parte, los materiales vitrocerámicos son muy empleados en el sector cerámico, en parte, debido a la posibilidad de obtener diferentes funcionalidades en función de la aplicación, lo cual está íntimamente condicionado por la composición química y la microestructura desarrollada. Hasta la fecha, se ha demostrado que los materiales vitrocerámicos basados en cristalizaciones de feldespatos presentan propiedades mecánicas muy destacables, [9,10] las cuales los hace aptos para ser empleados en aplicaciones industriales de construcción. Sin embargo, apenas se ha prestado interés en la caracterización del resto de sus propiedades, así como en su desarrollo en forma nanoestructurada, a pesar de la versatilidad y las ventajas que podría ofrecer.

Por todo ello, el objetivo principal de este trabajo de tesis ha consistido en el desarrollo de materiales vitrocerámicos micro-nanoestructurados, basados en cristalizaciones de feldespatos

de tipo plagioclasa, que sean escalables industrialmente y que presenten nuevas y mejoradas funcionalidades gracias a una minuciosa ingeniería de su estructura y microestructura.

Para la obtención de estos materiales, se ha empleado un método cerámico convencional de sinterización rápida fácilmente reproducible, con el fin de conseguir materiales de alta sostenibilidad y viabilidad económica, de cara a su escalado a nivel industrial. Los materiales vitrocerámicos obtenidos (plagioclasas ricas en sodio o en calcio) se caracterizan por presentar una micro-nanoestructuración jerárquica, elevada cristalinidad, > 90 %, elevada densificación y una baja porosidad.

Para el estudio de estos materiales, en primer lugar, se estableció el mecanismo de cristalización de esta nueva familia de materiales vitrocerámicos micro-nanoestructurados y se realizó un estudio exhaustivo de la estructura y la micro-nanoestructura desarrollada, especialmente para el material vitrocerámico basado en cristalizaciones de plagioclasa rica en sodio. Para ello, se emplearon experimentos de quenching, diferentes técnicas de análisis químico (ATD/TG y microscopía de calefacción), de caracterización estructural (XRD, XPS, RMN y Raman) y microestructural por medio de diferentes tipos de microscopías (FE-SEM, TEM y HRTEM, microscopía confocal Raman y microscopía de dispersión Rayleigh). Dicho estudio revela que la nucleación de los microcristales y nanocristales comienza durante el calentamiento. Sin embargo, es durante el enfriamiento cuando se desarrolla la micro-nanoestructuración singular que presentan dichos materiales, en la que los microcristales están aislados entre sí por regiones nanoestructuradas. Además, el análisis de los entornos atómicos del Si, mediante RMN, permite establecer la presencia de una distribución de Si,Al ligeramente desordenada en las posiciones tetraédricas de la red del feldespato, lo cual es corroborado mediante espectroscopia Raman. Esto explica algunas propiedades destacables de este material, como, por ejemplo, el buen comportamiento luminiscente. Las microscopías Rayleigh y TEM, permitieron identificar por primera vez para un feldespato vitrocerámico, la presencia de zonas de desmezcla por descomposición espinodal, de ~2-3 μm.

El estudio estructural y microestructural abre paso a una caracterización sistemática de las propiedades de estos materiales, corroborando la mejora de las mismas, gracias a la micro-nanoestructuración desarrollada. Por tanto, a continuación, se procedió al estudio de sus propiedades dieléctricas, mecánicas, termorreflectantes y luminiscentes, y su correlación con las características estructurales y microestructurales.

La combinación de cristales de tamaño micro y nanométrico resulta en un mayor número de fronteras de grano con respecto a los materiales convencionales del sector cerámico, lo cual va a favorecer que se produzcan una mayor cantidad de fenómenos de dispersión de electrones, fonones y fotones. Estas buenas características microestructurales, están, a su vez, potenciadas por la combinación de una elevada cristalinidad y una baja porosidad, con un tamaño medio de poro < 5μm. En relación a las propiedades termorreflectantes, estos materiales se caracterizan por poseer un elevado albedo y una baja difusividad térmica ($0{,}17 \cdot 10^{-6} m^2/s$). La respuesta mecánica se caracteriza por poseer una elevada resistencia a la fractura (hasta 2,1 $MPa \cdot m^{1/2}$) y a la flexión (en el rango 83-111 MPa), así como por alcanzar los mejores valores de dureza (9,5 GPa) obtenidos para un esmalte cerámico. En lo que respecta a las propiedades dieléctricas, estos materiales poseen un comportamiento aislante dieléctrico muy superior a otros materiales cerámicos convencionales, destacando por tener los valores más altos de resistencia dieléctrica en un material cerámico, > 59 kV/mm a temperatura ambiente y 30-44 kV/mm hasta 200 ºC. Por último, el ligero desorden en la distribución de Si,Al en las posiciones tetraédricas de la red del feldespato favorecen la aparición de defectos estructurales de tipo Al-O^--Al o complejos [AlO_4/$alkali^+$]. Estos defectos actúan como centros activos luminiscentes permitiendo una mejora de un orden de magnitud y de seis veces en las emisiones del UV/azul y rojo, respectivamente, con respecto a un feldespato natural. Además, dicha emisión fotoluminiscente puede ser modulada, tanto en intensidad como en longitud de onda, mediante la modificación de dicho desorden Si,Al en la estructura, por medio de ligeras variaciones químicas de los elementos estructurales.

En base a estos resultados, se abre un amplio abanico de posibilidades de cara a su uso en aplicaciones de alto voltaje como aislador eléctrico, en pavimentos de alto tránsito y revestimientos de edificios, gracias a sus excelentes propiedades mecánicas. También pueden ser empleados en pavimentos o revestimientos reflectantes y en “cool roofs”, así como en marcadores de seguridad o vidrios emisores de luz.

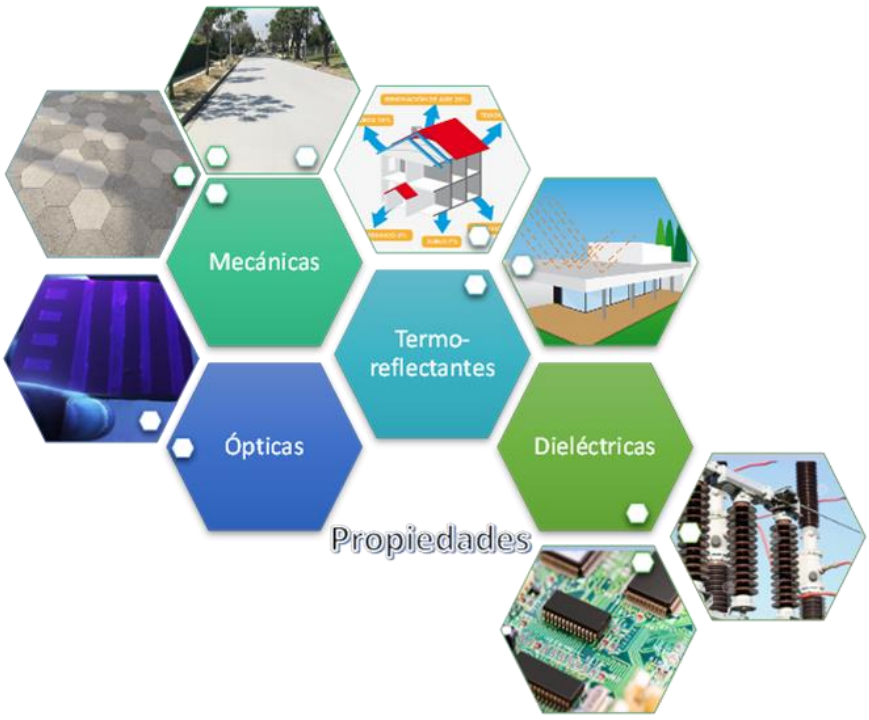

Figura 2. Esquema resumen de las posibles aplicaciones de los materiales vitrocerámicos micro-nanoestructurados desarrollados, gracias a las buenas propiedades dieléctricas, ópticas, mecánicas y termorreflectantes que poseen.

Capítulo 1. Introducción:

Aplicaciones funcionales de los feldespatos

1.1. La evolución del sector cerámico: uso de feldespatos en la industria

Los feldespatos son minerales de la familia de los tectosilicatos formados principalmente por silicatos dobles de aluminio, con distintas proporciones de potasio, sodio y calcio. Los principales usos del feldespato se dan como fuente de alúmina y sílice en la industria de fabricación del vidrio y la cerámica: sanitarios, baldosas, esmaltes, fritas, vajillas, encimeras, refractarios, porcelanas, etc.[11]. Su aplicación principal se centra en la fabricación de cerámica, en torno a un 35 %, y vidrio, en torno a un 60 %.[11] Su empleo permite una mejora en las prestaciones del producto final, tales como la durabilidad, la blancura, la resistencia a la decoloración, resistencia mecánica, química o a la abrasión, entre otros. El empleo anual de feldespatos en España muestra una tendencia ascendente en los últimos años, situándose, en 2016, en 650.000 toneladas métricas.[12]

La industria cerámica española es una de las más competitivas a nivel mundial, posicionándose como líder en cuanto a desarrollo tecnológico, diseño y calidad de los productos. España es el primer exportador europeo de azulejos cerámicos con un volumen de facturación de 3.510 millones de euros en el año 2017.[13]

Hasta hace unos años, el principal objetivo del sector se orientaba en reducir costes y el impacto medioambiental para mejorar la competitividad. Sin embargo, debido al auge de dicho sector y la gran competencia existente, surge la necesidad de introducir nuevas funcionalidades en los productos, con el fin de conseguir una cierta diferenciación con respecto a las tradicionales exigencias de resistencia y durabilidad.[1,2]

Sin embargo, la búsqueda de nuevas funcionalidades en el sector de baldosas cerámicas ha quedado completamente eclipsada en la última década por el desarrollo de tintas ink-jet de colores cerámicos obtenidos por molturación en molinos de microbolas.[14] El predominio de los efectos cromáticos y estéticos ha predominado gracias a la revolución que ha supuesto la decoración digital de baldosas cerámicas.

El desarrollo de la nanociencia y la nanotecnología en los últimos años ha permitido la mejora y creación de materiales con nuevas propiedades, por lo que, en este contexto, el empleo de nanomateriales en esmaltes cerámicos aporta soluciones para satisfacer las nuevas demandas del mercado.[15] Tradicionalmente, las nanopartículas han sido introducidas en esmaltes cerámicos con fines decorativos. Principalmente, nanopartículas metálicas (cobre,

plata…) con el fin de tener propiedades de *lustre* o brillo. [6–8] En 2009 Jaquotot et al. [16] fueron los primeros en optar por esta vía y desarrollaron un esmalte nanoestructurado multifuncional a partir de nanopartículas metálicas soportadas en fibras de sepiolita. La multifuncionalidad está basada en la presencia de patrones fractales en la superficie de nanopartículas que aportan un efecto hidrófobo, propiedades biocidas y una amplia variedad cromática, aprovechando efectos de plasmón superficial.[17] Rambaldi et al. [18] mejoraron las características mecánicas superficiales del gres porcelánico gracias a la incorporación de óxidos de partículas nanométricas, circona y alúmina. Ambrosi et al.[19] desarrollaron un recubrimiento basado en compuestos de circonio para baldosas de gres porcelánico con propiedades anti-manchado. Falk et al. [5] diseñaron un recubrimiento de sílice nanoestructurada con propiedades antimicrobianas. Zeng et al. [20] desarrollaron un esmalte cerámico fotocatalítico, basado en nanopartículas de TiO_2. Sin embargo, esta línea de investigación no prosperó, en parte debido a que el uso de los nanomateriales está, en cierto modo, limitado en la práctica, sobre todo en aplicaciones industriales. El elevado precio de los nanomateriales que incrementa el precio del producto final, junto con la dificultad de manipular una gran cantidad de nanopartículas, la toxicidad potencial asociada a su tamaño "*nanométrico*", la alta reactividad durante el proceso de sinterización y la tendencia a formar aglomerados, [15] dificultan la implementación de las nanopartículas cerámicas a gran escala. Sin embargo, la formación in situ de materiales nanoestructurados podría ser una buena alternativa, ya que evitaría las dificultades arriba mencionadas, a la vez que dotaría al material cerámico de ciertas mejoras en sus propiedades, así como de funcionalidades exclusivas, derivadas de su tamaño nanométrico.

Una alternativa funcional consiste en los materiales vitrocerámicos procesados a partir de polvos cerámicos, ya que, además de poseer mejores propiedades que los materiales cerámicos tradicionales, se pueden obtener con el mismo equipamiento presente en una planta cerámica tradicional. [21] Bernardo et al. [9,10] observaron que los materiales vitrocerámicos basados en cristalizaciones de feldespatos presentaban propiedades mecánicas muy destacables, siendo aptos para su empleo como materiales de construcción. Reinosa et al. [3] y Man et al. [22] obtuvieron esmaltes vitrocerámicos nanoestructurados basados, principalmente, en cristalizaciones de piroxenos y anortita, respectivamente, mediante una ruta de sinterización rápida por medio de hornos que simulan los empleados industrialmente. Sin embargo, apenas se ha prestado interés en la caracterización de sus propiedades.

Por tanto, hasta la fecha, tanto los materiales vitrocerámicos basados en cristalizaciones de feldespatos como los materiales vitrocerámicos nanoestructurados, apenas han sido

explorados a pesar de su elevada versatilidad y la gran cantidad de aplicaciones en las que podrían ser empleados. Con el objetivo de lograr una correcta comprensión del trabajo realizado, se consideran a continuación algunos de los aspectos relevantes relacionados con la estructura de los feldespatos y las aplicaciones funcionales a partir de los mismos en las que se centrará el estudio.

1.1. Feldespatos minerales

1.1.1. Consideraciones generales

Los silicatos son el grupo de minerales más abundante en la corteza terrestre, constituyendo en torno a un 95 % de su composición. La unidad de construcción fundamental de los silicatos es el tetraedro de silicio, $(SiO_4)^{4-}$. Dicho anión posee cuatro cargas negativas que son compensadas por la presencia de iones de metales alcalinos o alcalinotérreos. En función de cómo estén unidos estos tetraedros, se van a diferenciar distintos subgrupos. Entre ellos cabe destacar el grupo de los tectosilicatos, el cual está caracterizado por tener una estructura con anillos de tetraedros unidos por sus cuatro vértices, formándose un entramado tridimensional. Dentro de los tectosilicatos encontramos diferentes grupos, como el del cuarzo, las zeolitas, las escapolitas, los feldespatoides y los feldespatos. Los feldespatos son aluminosilicatos que constituyen el grupo mineralógico más abundante de la corteza terrestre, formando más del 50 % de la composición de muchas rocas, [23] siendo un componente esencial en rocas ígneas, metamórficas y sedimentarias. Su formación ocurre cuando en algunos tetraedros se produce una sustitución de Si^{4+} por Al^{3+}, lo cual origina un defecto de carga positiva que va a ser compensado por diferentes cationes, principalmente Na^+, K^+ y Ca^{2+}. Estos cationes se sitúan en los intersticios entre dichos tetraedros y en función de la proporción de los cationes presentes en la estructura, se van a dar diferentes composiciones en un sistema ternario formado principalmente por tres grandes grupos: los feldespatos potásicos ($KAlSi_3O_8$), la albita ($NaAlSi_3O_8$) y la anortita ($CaAl_2Si_2O_8$).

1.1.2. Soluciones sólidas de feldespatos

Los feldespatos se encuentran a menudo mezclados, en lugar de darse como una fase pura, formando soluciones sólidas. El rango de composiciones existentes da lugar, generalmente, a dos grupos: feldespatos alcalinos y plagioclasas, tal y como se puede observar en la Figura 1.1. La composición en el grupo de los feldespatos alcalinos varía en el sistema "*K*-

end member" (o miembro final de K) ($KAlSi_3O_8$) - "*Na-end member*" ($NaAlSi_3O_8$), mientras que el de las plagioclasas tiene composición en el sistema "*Ca-end member*" ($CaAl_2Si_2O_8$) - "*Na-end member*" ($NaAlSi_3O_8$).

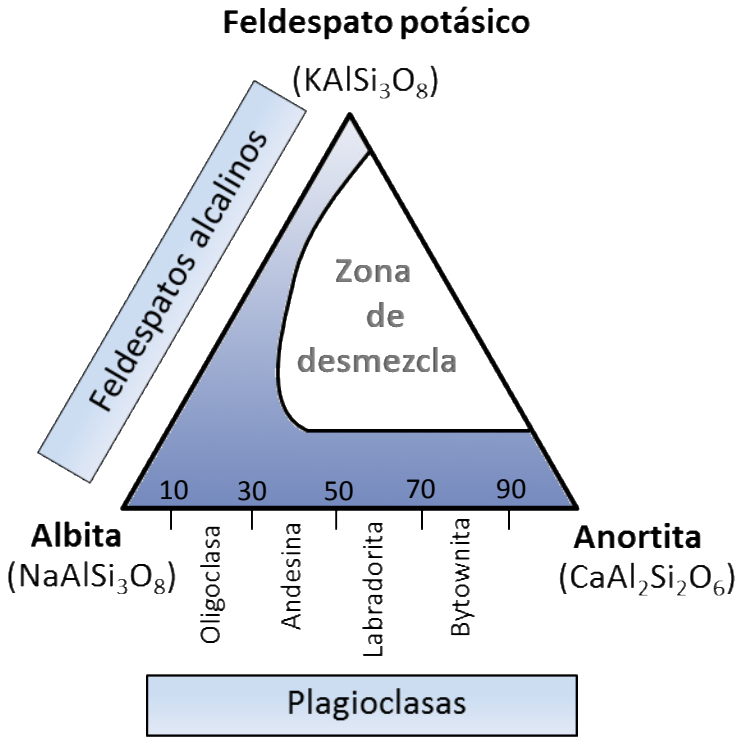

Figura 1.1. Esquema del diagrama ternario de los feldespatos, distinguiéndose dos grupos: los feldespatos alcalinos (albita-feldespato potásico) y las plagioclasas (albita-anortita).

Sin embargo, estos tres componentes no tienen la capacidad de mezclarse totalmente. Tal y como se observa en la Figura 1.1, existe una zona de desmezcla que aparece para las composiciones comprendidas entre anortita y los feldespatos potásicos. En este rango de composiciones no existirá una solución sólida, sino cristales con una composición rica en potasio por un lado y rica en calcio por otro. Dicha zona de desmezcla, o "gap de miscibilidad", va a depender drásticamente de las condiciones físicas y químicas de los feldespatos involucrados, siendo muy sensible a cambios en temperatura, composición y presión. [24]

Cuando una solución sólida se enfría por debajo de la temperatura de "solvus", la cual define el límite de solubilidad sólida de la misma, se produce la separación de dichas fases. Este proceso se suele denominar también como exsolución o proceso de desmezcla, y se produce por ser un proceso más favorable desde un punto de vista energético, de acuerdo con el diagrama de energía libre de dicha solución sólida. [25] Este proceso de exsolución puede ocurrir

por un fenómeno denominado descomposición espinodal o uno de nucleación y crecimiento . [25–27] La descomposición espinodal es un mecanismo a nivel atómico que conduce al crecimiento coherente de las fases involucradas. La descomposición espinodal no es exclusiva de los feldespatos y es un fenómeno de gran interés estructural desde el punto de vista práctico, ya que se trata de un mecanismo por medio del cual se pueden generar microestructuras que mejoran notablemente las propiedades físicas de los materiales en cuestión. Se ha utilizado en una amplia gama de materiales, tales como: materiales termoeléctricos, polímeros, materiales magnéticos y vidrios, así como en feldespatos. [28–33] Por otro lado, si los "end-members" de la solución sólida tienen estructuras notablemente diferentes, la exsolución se produce por nucleación y crecimiento. [26]

1.1.3. Estructura y distribución de Al-Si (orden/desorden) en posiciones tetraédricas de las plagioclasas

Para realizar una caracterización completa de los feldespatos, se requiere analizar su composición química, la simetría de la estructura y la caracterización del orden/desorden en la distribución de Al-Si. El orden/desorden en los feldespatos está definido a partir de la posición que ocupan los átomos de Al y Si en los sitios tetraédricos de la propia red del feldespato. Esta distribución puede variar considerablemente de un tipo de feldespato a otro, e incluso dentro de un mismo tipo se pueden producir cambios en dicho ordenamiento por efecto de la presión, la temperatura o la composición.

El grupo de las plagioclasas es muy abundante en la corteza terrestre (y el mineral más abundante en la Luna) y de gran importancia. [34] La solución sólida formada entre sus "end-members", albita ($NaAlSi_3O_8$) y anortita ($CaAl_2Si_2O_8$), es completa por encima de 700 ºC y va a presentar una proporción variable de Si/Al. Las plagioclasas son comúnmente definidas en función del contenido de anortita presente (An_x). Típicamente, según los rangos, las plagioclasas se clasifican en: albita (An_0-An_{10}), oligoclasa (An_{10}-An_{30}), andesina (An_{30}-An_{50}), labradorita (An_{50}-An_{70}), bytownita (An_{70}-An_{90}) y anortita (An_{90}-An_{100}), tal y como se observa en la Figura 1.1.

Con respecto a la albita, la estructura consiste en anillos de cuatro tetraedros, donde cada tetraedro consiste en un átomo de silicio o de aluminio coordinado tetraédricamente a cuatro átomos de oxígeno$^+$, siendo la relación Si^{4+}:Al^{3+} de 3:1. Cada átomo de oxígeno se encuentra situado en los vértices de cada tetraedro y uniendo dos de ellos, tal y como se puede

observar en la Figura 1.2. La albita puede tener una estructura triclínica (grupo espacial $C\bar{1}$) o monoclínica (grupo espacial C2/m), en la cual varía el grado de orden/desorden Al/Si. En la estructura triclínica existen cuatro sitios simétricamente no equivalentes, designados como $T_1(0)$, $T_1(m)$, $T_2(0)$ y $T_2(m)$ (Figura 1.2), mientras que la estructura monoclínica sólo tiene dos (T_1 y T_2). En la estructura más ordenada, conocida como albita baja ("low albite") y perteneciente al sistema cristalino triclínico pinacoidal (Figura 1.2), el catión de Al^{3+} se sitúa en las posiciones $T_1(0)$. Sin embargo, la albita también tiene tres polimorfos diferentes de alta temperatura, donde los cationes Al^{3+} y el Si^{4+} ven afectada su distribución entre los sitios tetraédricos. Cuando aumenta la temperatura, comienza el proceso de desorden en la red del feldespato, y el catión Al^{3+} comienza a migrar desde las posiciones $T_1(0)$ a las $T_1(m)$, $T_2(0)$ y $T_2(m)$. En un estado de desorden perfecto, el 25% de los átomos de Al están colocados en las posiciones $T_1(0)$, mientras que el 75% restante se distribuye por igual entre los sitios T_1 (m), T_2 (0) y T_2 (m). La albita triclínica completamente desordenada se conoce como albita alta o "high albite" y conserva su estructura triclínica a pesar de ser calentada. La analbita, en cambio, es topoquímicamente monoclínica ($T_1(0) = T_1(m)$ y $T_2(0) = T_2(m)$), pero topológicamente triclínica y sufre una transformación de fase reversible a monoalbita a 980 ºC (a una presión de 0.1 MPa). Finalmente, la monoalbita es un polimorfo monoclínico y está completamente desordenado. [24,35–39] Las plagioclasas ricas en albita van a poseer una simetría de tipo $C\bar{1}$, con cierto desordenamiento Al/Si. Dicho desorden va a dar lugar a la generación de enlaces Al-O^--Al. [28]

En cambio, la anortita tiene una relación Si:Al de 1:1 y una estructura esencialmente ordenada, desde un punto de vista de distribución de Al/Si. [28] Dicha anortita ordenada es triclínica y pertenece al grupo espacial $I\bar{1}$. En dicha simetría está permitido un cierto grado de desorden, sin embargo, va a ser por encima de 2000 ºC cuando se alcance un estado de desorden total (simetría $C\bar{1}$, al igual que en la "high albite"). [28] Las plagioclasas ricas en anortita (An_{50}-An_{90}) van a tener una simetría media de tipo $I\bar{1}$. [39]

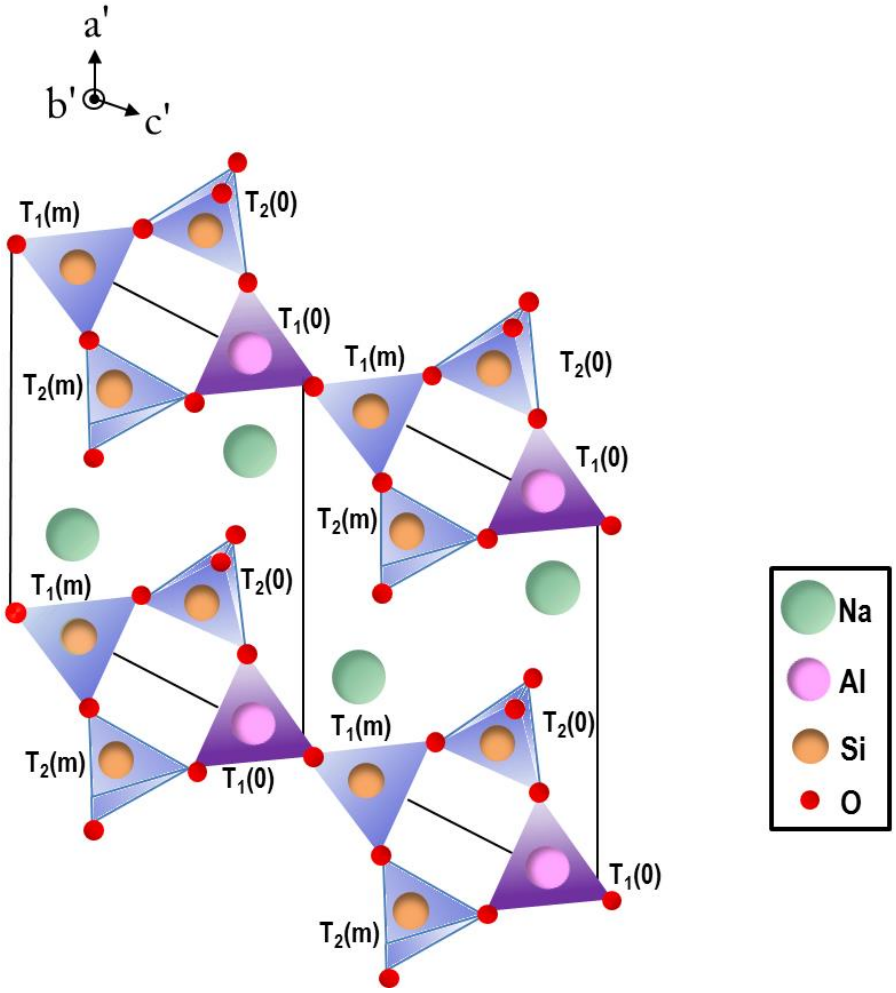

Figura 1.2. Estructura de una albita baja ("low albite"), formada por anillos de cuatro tetraedros, donde los átomos de silicio (representados en color naranja) o aluminio (representados en color rosa), están coordinados con cuatro átomos de oxígeno (representados en color rojo). El defecto de carga generado por la presencia de cationes Al^{3+} se compensa con cationes Na^{1+} (representados en verde). En la estructura triclínica existen cuatro sitios simétricamente no equivalentes, etiquetados como $T_1(0)$, $T_1(m)$, $T_2(0)$ y $T_2(m)$. En la estructura más ordenada, los átomos de aluminio están situados en las posiciones $T_1(0)$. Con respecto al sistema cartesiano XYZ, el eje X forma un ángulo de aproximadamente 2 ° con el eje cristalográfico *a*, el eje Y coincide aproximadamente con el eje cristalográfico *b*, y el eje Z es casi perpendicular al plano *ab*, a aproximadamente 26 ° desde el eje *c*. (Adaptado de [37,39]).

1.2. Feldespatos sintéticos

El impacto industrial mencionado anteriormente hace interesante el estudio de los feldespatos, tanto desde un punto de vista de ciencia fundamental, como para la posible exploración de sus propiedades de cara a su uso en nuevas aplicaciones. Por todo ello, se han realizado investigaciones dirigidas al estudio de su producción de forma artificial, para lo que se han seguido diferentes métodos de síntesis. La ruta hidrotermal ha sido empleada en numerosas ocasiones, [40–42] así como la síntesis a partir de geles de hidróxidos precursores [43] o mediante intercambio catiónico [44]. Métodos como el sol-gel también han sido implementados en la literatura para la síntesis de partículas de varios aluminosilicatos y minerales. [45–47] Uno de los métodos más comunes para la síntesis de feldespatos es la cristalización a partir del correspondiente fundido de un vidrio precursor. Sin embargo, esta ruta no es sencilla debido a la complejidad que presentan los feldespatos, especialmente cuando se pretende conseguir la cristalización de feldespatos alcalinos desde un fundido anhidro [48]. Liu et al. [44] sintetizan albita vitrocerámica a partir de un fundido de un vidrio de albita, gracias al uso de semillas nucleantes ("*seeds*") de albita cristalina [49] y de anortita. [50] Krzmanc et al. [51] optaron por una reacción de estado sólido bajo condiciones subsólidas para sintetizar cerámicas de albita y anortita. [51] La ruta de procesamiento es aún más complicada cuando se intenta sintetizar un material vitrocerámico con una alta cristalinidad y, por tanto, una pequeña cantidad de fase vítrea residual, lo cual suele requerir el empleo de tratamientos térmicos de larga duración [52] y en algunos casos el empleo de sistemas de vacío. [53] Sin embargo, Bernardo et al. [9], consiguieron sintetizar un material vitrocerámico basado en cristalizaciones de nefelina ($NaAlSiO_4$), con un tratamiento térmico a 930 ºC de, aproximadamente, 6 horas de duración. Posteriormente, se reporta la síntesis de materiales vitrocerámicos basados en cristalizaciones de feldespatos potásicos (microclina y ortoclasa) [10] a una temperatura de 750 ºC con un tiempo aproximado de duración de 4 horas y media.

En resumen, los procesos de obtención de síntesis de feldespatos están limitados, ya que implican tiempos muy largos de síntesis, que comprenden semanas o incluso meses. [40–43]

1.3. Materiales vitrocerámicos

Los materiales vitrocerámicos son materiales policristalinos obtenidos por medio de la cristalización controlada de un vidrio de partida. El tratamiento térmico llevado a cabo, a temperaturas inferiores al punto de fusión de dicho vidrio, juega un papel fundamental, ya que va a condicionar la cantidad de cristales que se obtendrán, la velocidad de crecimiento de éstos, así como su tamaño. [54,55] Finalmente, se consigue la precipitación de una o varias fases cristalinas cerámicas dentro de la matriz vítrea.

Una de las principales ventajas de los materiales vitrocerámicos es la posibilidad de obtener diferentes funcionalidades en base a la aplicación que se le vaya a dar. En todo ello, juega un papel fundamental la microestructura, la cual puede ser adaptada gracias al control de la composición química y la desvitrificación del vidrio de partida, que va a condicionar la elección del tratamiento térmico que se lleve a cabo, de acuerdo con su comportamiento cinético y termodinámico. [1] Dicho proceso de desvitrificación controlado puede llevarse a cabo por medio de un único ciclo de fusión-enfriamiento, obteniendo el vidrio en primer lugar y llevando a cabo la posterior desvitrificación de éste. [54] En el segundo caso, se habla de una vía vitrocerámica y es el proceso llevado a cabo para la producción de la gran mayoría de los materiales vitrocerámicos que se comercializan, tanto a partir de materias primas de síntesis, como de materias primas naturales.

De cara a la producción industrial, el método de procesado llevado a cabo debe cumplir ciertos requisitos de sostenibilidad y viabilidad económica. Una buena alternativa es la producción de materiales vitrocerámicos procesados a partir de polvos, los cuales son obtenidos por sinterización y cristalización controlada de polvos del vidrio precursor. El interés de estos materiales en el sector cerámico tradicional radica en que, además de poseer mejores propiedades que los materiales cerámicos tradicionales, se pueden obtener económicamente con el mismo equipamiento presente en una planta cerámica tradicional. [21] Dicho proceso está constituido por las siguientes etapas: i) fusión y enfriamiento del vidrio, ii) atomización, iii) conformado (prensado, moldeo por inyección, extrusión etc.) y d) sinterización. El método de producción debe tener en cuenta factores relevantes, como son la duración del ciclo de sinterización o el tipo de materias primas empleadas.

Desde que se produjo el desarrollo del primer material vitrocerámico industrial a cargo de la empresa Corning Glass en 1957, se han incentivado los estudios de I+D destinados a la búsqueda de materiales vitrocerámicos con nuevas funcionalidades y propiedades mejoradas.

Los materiales vitrocerámicos han suscitado un gran interés científico y tecnológico en los últimos años, debido a las excelentes propiedades (eléctricas, térmicas, mecánicas, ópticas, luminiscentes o biocompatibles, entre otras) y las posibilidades que ofrecen con respecto a los correspondientes vidrios precursores. Su aplicación destaca en múltiples campos, desde la óptica, la medicina o la electrónica, hasta los materiales de construcción, revestimientos o pavimentos. [54,56] Teniendo en cuenta el amplio rango de posibilidades que ofrecen los materiales vitrocerámicos, se van a analizar diferentes propiedades que podrían ser de interés para feldespatos de síntesis o de ingeniería.

1.3.1. Luminiscencia en materiales vitrocerámicos y en feldespatos

En el campo de la fotónica, los materiales vítreos y los vitrocerámicos son considerados buenas matrices para aplicaciones luminiscentes o de emisión de luz. A menudo, estos materiales son denominados fósforos. Los primeros destacan por su bajo coste, el gran volumen de producción y la facilidad que presentan para ser moldeados. [57,58] Sin embargo, uno de los principales inconvenientes de los vidrios con respecto a su comportamiento luminiscente es la presencia de gran cantidad de defectos puntuales, que generan sitios de atrapamiento responsables de recombinaciones no radiativas, disminuyendo su rendimiento con respecto a los cristales. [59] En contraste, los vitrocerámicos pueden ser sintetizados con una mayor cristalinidad, reduciendo dicho problema. Además, los materiales vitrocerámicos son fáciles de procesar, se pueden elaborar muestras grandes y de formas complejas, es posible su dopado efectivo y son más económicos que los correspondientes monocristales. Todo ello les hace idóneos para aplicaciones ópticas. [60] Por tanto, las emisiones luminiscentes en los materiales vitrocerámicos se ven afectadas fuertemente por la cristalinidad, además de la microestructura, la cantidad de centros activos presentes, la composición de la matriz y el campo cristalino, entre otros. La mayoría de las matrices inorgánicas son dopadas con elementos activadores, principalmente iones de tierras raras y en menor medida, metales de transición. [61] Las propiedades únicas que presentan los iones de tierras raras y la amplia variedad de colores que se pueden obtener en las emisiones, justifican su elevado uso [62], siendo los principales centros emisores considerados hasta la fecha los cationes de $Eu^{2+/3+}$, Tb^{3+}, Y^{3+}, $Ce^{3+/4+}$, La^{3+}, $Gd^{3+,}$ etc. Sin embargo, China produce más del 95 % de todos los elementos de tierras raras y ha reducido las exportaciones en, aproximadamente, un 40 % en los últimos diez años, [63] debido a los problemas ambientales derivados de su extracción y el procesamiento de los elementos de tierras raras. Por tanto, dicho

suministro limitado junto con el aumento de los precios de los mismos conduce a la búsqueda de nuevos fósforos libres de tierras raras. [61,63–65] Una buena alternativa, con el fin de preservar los recursos naturales, son los fósforos basados en materiales vitrocerámicos, debido a las buenas características que presentan. Por tanto, una de las principales tendencias en el sector es el desarrollo de tecnologías de emisión de luz que sean mucho más sostenibles y de menor coste, manteniendo una alta eficiencia. [66]

En la naturaleza hay materiales que pueden presentar una notable luminiscencia sin ser atribuida a la presencia de tierras raras, como ocurre en minerales de feldespatos. La luminiscencia en feldespatos es un fenómeno ampliamente conocido y utilizado en mineralogía para diferentes propósitos, tales como separación cuantitativa de especies minerales, la zonación o la datación, entre otros. [67] Los feldespatos, generalmente, presentan tres bandas de emisión anchas: una en el rango UV/azul (380-500 nm), otra en el azul/verde (500-570 nm) y en el rango rojo/NIR (690-760 nm). [67] Las emisiones en el rango UV/azul pueden ser causadas por diferentes centros emisores, como son los enlaces (''linkages'') [AlO_4/alcalino$^+$], [AlO_4]^0 , Al-O$^-$ -Al, Al-O$^-$-Ti . [68,69] Los dos primeros tipos de defectos se producen cuando el catión Al^{3+} sustituye a Si^{4+}, lo que provoca un desequilibrio local de la carga. Para mantener dicho equilibrio de carga local, un catión alcalino puede situarse en posiciones adyacentes a los cationes Al^{3+}, dando lugar a la formación de un centro [AlO_4/alcalino$^+$]. En cambio, si se atrapa un hueco, el centro resultante será del tipo [AlO_4]^0. [68] En el caso de los centros Al-O$^-$-Al, también conocidos como puentes de Löwenstein, surgen cuando una vacante de oxígeno se comparte con dos cationes de Al^{3+}, uno de ellos estructural. [67,69] Estos defectos estructurales son los más comunes en feldespatos y ocurren, típicamente, en el rango de 400-480 nm. Por último, caben destacar los centros de Ti o puentes Al-O-Ti, [67,69] cuya emisión correspondiente se produce cuando cationes Ti^{4+} se reducen a cationes Ti^{3+} en sitios tetraédricos en los que debería estar situado el Al^{3+}. Ambos centros de emisión se han propuesto en la bibliografía para explicar la luminiscencia azul en los feldespatos. Las emisiones correspondientes al rango azul/verde son causadas normalmente por defectos de tipo Si-O-... M^{2+} (iones metálicos de Mg^{2+}, Zn^{2+} o Be^{2+} situadas en posiciones adyacentes a una vacante de oxígeno), Mn^{2+} en posiciones de Ca^{2+} o transiciones de Fe^{2+}. [67] En cuanto a la luminiscencia roja en los feldespatos alcalinos, tiene lugar cuando un ion Fe^{3+} ocupa alguna posición tetraédrica de Al^{3+} en la estructura del feldespato, dando lugar a una transición $^4T1 \rightarrow {}^6Al$ por parte de los iones Fe^{3+}. [67] Aunque las principales emisiones en feldespatos minerales son atribuidas a defectos estructurales, también se observan bandas de emisión asociadas a elementos activadores incorporados en la propia estructura del feldespato,

como iones metálicos Tl^{+}, Pb^{2+}, Cr^{3+}, Cu^{2+} o Ga^{3+}, así como trazas de iones de tierras raras, principalmente Eu^{2+}, Eu^{3+}, Ce^{3+}, Sm^{3+}, Tb^{3+} y Nd^{3+}. La luminiscencia en feldespatos también es un fenómeno fuertemente afectado por la composición, lo cual provoca modificaciones en el campo cristalino del material y desplazamientos de la correspondiente banda de emisión, tal y como se observa en la emisión roja debida a iones de Fe^{3+}. [70]

A pesar de la notable luminiscencia que presentan los feldespatos naturales, la diversidad de emisiones que se observan en función del tipo de defecto involucrado y el gran conocimiento sobre ellas, es un fenómeno apenas explorado en feldespatos sintéticos. En la bibliografía tan solo hay dos trabajos en los cuales se evalúa la luminiscencia de feldespatos potásicos sintéticos. García-Guinea et al. [71] comprobaron que un gel amorfo de $KAlSi_3O_8$ no presentaba termoluminiscencia, mientras que Slaats et al. [72] sintetizaron cristales de "high sanidine" con un flujo de K_2WO_4 y dopados para obtener las correspondientes emisiones luminiscentes de cationes de Ti^{3+} (λ_{em}=460 nm), Fe^{3+} (λ_{em}=710-720 nm) y W^{6+} (λ_{em}=530 nm).

Por lo tanto, la estructura de feldespato resulta interesante para generar un material luminiscente potencialmente utilizable aplicaciones de emisión de luz.

1.3.2. Propiedades dieléctricas en aisladores eléctricos cerámicos y feldespatos

Los materiales cerámicos son ampliamente utilizados como aisladores dieléctricos, es decir, son materiales que bloquean el paso de la corriente eléctrica además de poseer un adecuado comportamiento térmico. Los aisladores cerámicos son utilizados en gran variedad de dispositivos microelectrónicos, que forman parte del sector de la industria del automóvil, aeroespacial o de electrodomésticos. Los aisladores cerámicos son fundamentales en electrotecnia, tanto en aplicaciones de alto voltaje como de alta potencia. [73] Las propiedades requeridas por un aislador en el campo de la electrotecnia son: alta resistividad, baja constante dieléctrica, bajo factor de pérdidas (tgδ), alta rigidez dieléctrica o ruptura dieléctrica, elevada resistencia mecánica, químicamente inerte y elevado punto de fusión. Una de las principales limitaciones de estos materiales es su ruptura dieléctrica, que una vez superada provoca la pérdida de propiedades aislantes y la degradación mecánica del material. Desde el punto de vista de seguridad eléctrica, los dispositivos están sobredimensionados para garantizar el empleo de los aisladores dieléctricos en condiciones de uso. La ruptura dieléctrica está

fuertemente afectada por los procesos de dispersión o "scattering" y de atrapamiento de carga eléctrica en zonas específicas del material aislador en cuestión. En los defectos, la polarizabilidad se ve modificada y se favorece la localización de la carga. En las cerámicas, dichos defectos pueden deberse a la porosidad, defectos cristalográficos, distorsiones de la red, impurezas, fronteras de grano, así como intercaras con otras fases secundarias. [74] La ruptura dieléctrica se ve fuertemente determinada por la microestructura, ya que las intercaras pueden actuar como lugares favorables para el atrapamiento de carga eléctrica. Es bien sabido que valores bajos de porosidad y de tamaño de grano mejoran la resistencia a dicha ruptura dieléctrica. [75] La cantidad de fase vítrea presente en el material cerámico también afecta al comportamiento dieléctrico del material, principalmente a las pérdidas dieléctricas, registrándose valores generalmente altos en la mayoría de los aisladores de vidrio. [76] La rigidez dieléctrica en aplicaciones de aislamiento eléctrico de alta tensión debe ser superior a 30 kV/mm. [77] Tan solo los aisladores de mica natural proporcionan valores de resistencia dieléctrica superiores a dicho valor, en el rango 39,5- 79,1 kV/mm. [78] En la

Tabla **1.1** se recogen valores típicos de rigidez dieléctrica, constante dieléctrica (ε') y pérdidas dieléctricas (tgδ) para materiales cerámicos empleados como aisladores dieléctricos.

Material	ε' (a 1 MHz)	tgδ (a 1 MHz)	Rigidez dieléctrica (kV/mm)
Al_2O_3 al 99.9%	9.9	0.0002	17
BeO al 99%	6	0.001	13
Porcelanas de aluminosilicatos alcalinos	5-7	0.012	20
Porcelanas de aluminosilicatos alcalinotérreos y circonio	5-12	0.005-0.007	10-20
Forsterita	7.9-11.9	0.003-0.007	7.9 - 11.9
Cordierita	4.1-5.3	0.003-0.005	10
Esteatita	6	0.001-0.007	15
Circón	8.0-9.6	0.001	6.3 - 11.5
Circonia	12	0.01	~ 5
Cuarzo	3.8-5.4	0.0003	15 - 25
Mica	5.4-8.7	0.0002	39.5 - 79.1

Tabla 1.1. Valores habituales de constante dieléctrica (ε') y pérdidas dieléctricas (tgδ) a 1 MHz, así como la rigidez dieléctrica en aisladores cerámicos convencionales (*adaptado de* [78]).

El mecanismo de ruptura dieléctrica en sólidos es principalmente intrínseco (electrónico o por avalancha) o térmico. [79–81] Si se aplica una tensión durante un breve periodo de tiempo, aproximadamente 10^{-8} s, la resistencia dieléctrica aumenta rápidamente hasta un límite, conocida como la resistencia dieléctrica intrínseca. La ruptura dieléctrica intrínseca es sencilla de identificar y puede clasificarse en electrónica y de avalancha. La primera tiene lugar cuando al aplicar un campo eléctrico, se promueven electrones desde la banda de conducción a la banda de valencia repetidamente, lo que termina desencadenando la ruptura. En cambio, cuando los electrones en el dieléctrico son suficientemente acelerados por el campo eléctrico aplicado y son capaces de liberar los electrones ligados a los átomos, se produce una ruptura de tipo avalancha. [79,82,83] Además, el campo eléctrico aplicado va a generar una corriente de conducción por efecto Joule que calienta el material. Cuando este calor generado es mayor que el calor disipado por el material, ocurre lo que se conoce como ruptura térmica.

Uno de los principales problemas que pueden sufrir los aisladores incorporados en dispositivos electrónicos es la pérdida de sus propiedades aislantes como consecuencia del aumento de temperatura producido durante el tiempo de operación. En los materiales cerámicos empleados como aisladores, los procesos de conducción eléctrica se activan térmicamente, [75] al igual que ocurre en los feldespatos minerales. De acuerdo con la literatura, la conductividad eléctrica en los feldespatos alcalinos (ricos en Na^+ o K^+) está basada en un mecanismo de conducción iónica en el que los cationes alcalinos son los portadores de carga dominante y migran por los sitios intersticiales dentro de la red del propio feldespato [84,85]. El comportamiento dieléctrico de feldespatos también ha sido analizado en la bibliografía. La albita y la anortita mineral poseen valores de ε' de 6,02 y 6,98 [86] respectivamente, medidos a una temperatura de 20 ºC y una frecuencia de 60 Hz. En el caso de cerámicas con cristalizaciones de feldespatos de tipo albita el valor de ε' está comprendido entre 5 y 6, mientras que para tipo anortita es de 7,4, en un rango de frecuencias 1kHz-1MHz [51]. Además, a alta frecuencia se ha demostrado que los materiales vitrocerámicos basados en anortita son adecuados para aplicaciones de tipo LTCC (de las siglas en inglés "low temperature cofired ceramic"), registrando valores de constante dieléctrica de ~8 a una frecuencia de 10 GHZ. Sin embargo, otras propiedades importantes como la rigidez dieléctrica no han sido evaluadas hasta la fecha en materiales basados en cristalizaciones de feldespatos.

1.3.3. Propiedades mecánicas en materiales y esmaltes vitrocerámicos

Uno de los usos más extendidos de las composiciones basadas en feldespatos en la industria son los esmaltes para baldosas cerámicas. Actualmente, se busca mejorar ciertas propiedades específicas, así como otorgar nuevas funcionalidades, de manera que puedan diferenciarse de los materiales tradicionales del sector. Por ejemplo, con respecto a aplicaciones en suelos en zonas de elevado tránsito, uno de los principales desafíos en este sector es el aumento considerable de la resistencia al desgaste, junto con el ahorro en tiempo de reparación y en costes de reemplazo. Los esmaltes estándar tienen una baja resistencia a la abrasión y pierden fácilmente sus características superficiales, como el brillo, el color y la textura superficial [87]. Para superar estos inconvenientes en la industria de las baldosas cerámicas, se requieren nuevos productos que, principalmente, muestren una mejor resistencia al desgaste por abrasión y una mayor dureza de la superficie que las vitrocerámicas tradicionales. [87,88]

Las propiedades mecánicas de estos esmaltes, tales como la dureza (H_V) o el módulo de Young (E) pueden ser obtenidos a partir de un ensayo de indentación Vickers. A pesar de que ambos son comúnmente considerados como propiedades inherentes al material, dependen fuertemente de la carga aplicada, lo cual es comúnmente conocido como el efecto de tamaño de la indentación ("indentation size effect"). Los valores típicos de dureza para un esmalte tradicional en baldosas para suelos ("floor tile glazes") están situados en torno a 5,9 N (para 1N de carga aplicada). [89] Estos valores de dureza se han ido mejorado considerablemente en algunos esmaltes reportados en la literatura, especialmente en esmaltes vitrocerámicos, como se puede observar en la Tabla 1.2.

Factores como la proporción de fases cristalinas y el tamaño de las mismas o la porosidad, están íntimamente relacionados con la dureza del material. A partir de las curvas de carga-descarga y de las características de las huellas de indentación de un ensayo Vickers, se puede estimar la tenacidad del material a la fractura (K_{IC}), es decir, la resistencia que opone dicho material al avance la grieta. En esmaltes cerámicos se obtienen valores de K_{IC} en el rango 0,74-1,41 $MPa \cdot m^{1/2}$ en azulejos, en el rango 0,66-1,3 $MPa \cdot m^{1/2}$ en baldosas vitrificadas para suelos y entre 1,1-1,3 $MPa \cdot m^{1/2}$ en baldosas de gres porcelánico, todos ellos a una carga de 9,8 N. [90] Bernardo et al. obtuvieron que los materiales vitrocerámicos basados en cristalizaciones de nefelina y feldespatos potásicos presentan valores de K_{IC} de 1,5 $MPa \cdot m^{1/2}$. [9,10] Carbajal et al. [91] reportaron valores más elevados de K_{IC} para materiales porcelánicos cuya fase vítrea se ha reforzado composicionalmente, obteniendo valores de K_{IC} 2,0 $MPa \cdot m^{1/2}$.

Esmalte	Carga (N)	H_V (GPa)	Referencias
Esmalte tradicional en baldosas para suelos	1	5,9	[89]
Esmalte con partículas de zircón dispersas	2	6,3	[92]
Esmalte vitrocerámico basado en el sistema $CaO\text{-}MgO\text{-}SiO_2\text{-}Al_2O_3$	1	6,4	[93]
Baldosa vitrocerámica con cristalizaciones de β-wollanstonita y hardystonita	5	6,5	[94]
Esmalte vitrocerámico basado en el sistema $CaO\text{-}MgO\text{-}SiO_2\text{-}Al_2O_3\text{-}ZrO_2$	1	7,2	[89]
Esmalte vitrocerámico basado en mullita	3	7,1	[88]
Esmalte vitrocerámico basado en cordierita	3	8,4	[88]
Vitrocerámico con cristalizaciones de nefelina	5	6,6	[9]
Vitrocerámico con cristalizaciones de feldespatos potásico	5	7,2	[10]

Tabla 1.2. Valores de microdureza Vickers (H_V) para un esmalte tradicional empleado en baldosas para suelos, así como los mejores valores reportados en varios esmaltes vitrocerámicos para diferentes valores de carga empleados.

Además de la dureza o la tenacidad a la fractura del material, las propiedades tribológicas, tales como el coeficiente de fricción o la resistencia al desgaste (típicamente evaluado por medio de la tasa de desgaste o "wear rate", W_R), requieren especial atención cuando un esmalte es considerado para aplicaciones de pavimentos en zonas de alto tránsito. La resistencia al desgaste es un mecanismo complejo que puede verse afectado por muchos factores, como las propiedades físicas (dureza, tenacidad a la fractura, módulo de Young, resistencia a la flexión, etc.), [95] las características de las fases presentes y la microestructura (tamaño del cristal, porosidad, fases secundarias o cristalinidad, entre otras). [96,97] Se ha comprobado en diversos trabajos que el refuerzo de una matriz cerámica con nanopartículas logra aumentar su resistencia mecánica y su resistencia al desgaste. Esto es debido a que, al aumentar su superficie específica, se favorece la transferencia de carga de la matriz a las nanopartículas dispersas en la matriz. [98] Algunas nanopartículas empleadas comúnmente como aditivos en la literatura han sido SiC, SiO_2, Al_2O_3, ZrO_2, $ZrSiO_4$, ZrO_2, TiO_2 o ZnO. [15,92,98,99] Sin

embargo, el uso de nanopartículas tiene ciertos inconvenientes, anteriormente mencionados, como su elevado precio, la dificultad para ser manipuladas a gran escala y la toxicidad. Todo ello, lleva a la búsqueda de alternativas, como pueden ser los materiales nanoestructurados, en los cuales se podría obtener una cierta funcionalidad a la vez que se superan las dificultades anteriormente mencionadas para las nanopartículas. A pesar de ser una alternativa innovadora y prometedora con respecto al uso de nanopartículas, ésta ha sido una metodología de trabajo apenas seguida en el sector cerámico. [3,22]

Heo et al. [100] publican valores de W_R de $9{\cdot}10^{-3}$ $mm^3/ N{\cdot}m$ para una porcelana tradicional ("whiteware") y valores de $4{\cdot}10^{-2}$ $mm^3/N{\cdot}m$ para esmaltes transparentes con ~70% en peso de SiO_2, ~20 wt.% de Al_2O_3 y un contenido variable de óxidos de calcio, sodio y potasio. Pina-Zapardiel et al. [92] reportaron valores de W_R de $4{,}90{\cdot}10^{-5}$ $mm^3/N{\cdot}m$ para un esmalte comercial vítreo y de $4{,}32{\cdot}10^{-5}$ $mm^3/N{\cdot}m$ para un esmalte con nanopartículas de zircón dispersas, mientras que este valor se reduce hasta cuatro veces mediante la generación de cristales de wollastonita además de las nanopartículas de zircón, obteniendo un esmalte de alta resistencia con valores de W_R en torno a $1{\cdot}10^{-5}$ $mm^3/N{\cdot}m$.

Previamente, Bernardo et al. [9,10] comprobaron que los materiales vitrocerámicos basados en cristalizaciones de feldespatos presentan propiedades mecánicas muy reseñables y, por tanto, eran aptos para aplicaciones industriales como materiales de construcción. Todo esto indica que podría resultar interesante el estudio de las propiedades mecánicas (como la dureza, el módulo de Young, la tenacidad o las propiedades tribológicas) en nuevos materiales vitrocerámicos nanoestructurados, basados en cristalizaciones de feldespatos, con el fin de comprobar si es posible mejorar la respuesta mecánica de los esmaltes para baldosas cerámicas modificando bien la composición, bien la micro-nanoestructura.

1.3.4. Aplicación de materiales cerámicos en el sector de la construcción: ahorro energético y mitigación del efecto isla de calor

i. Propiedades termorreflectantes

La conductividad térmica (K) de un material es la propiedad física que mide la capacidad de conducir el calor a través del mismo. Los materiales que ofrecen una alta resistencia (R) a dicha conducción térmica tienen una elevada resistividad térmica y son conocidos como aislantes térmicos. La conductividad térmica y su magnitud inversa, la resistividad, son magnitudes inherentes al material, mientras que la resistencia va a depender del cociente entre el espesor (e) y K del material en cuestión, siendo mayor cuanto mayor sea el espesor de dicho material. En el ámbito de la construcción, el aislamiento térmico tiene como objetivo dificultar la trasmisión de calor del interior al exterior de un edificio y viceversa, para evitar las pérdidas de calor en períodos fríos e impedir su propagación al interior en épocas cálidas, respectivamente. Este aislamiento, correspondiente a una conductividad térmica baja, va a contribuir al incremento del confort térmico en el interior de las viviendas, así como a limitar el consumo energético de los equipos de refrigeración y calefacción.

En el caso de los materiales cerámicos no magnéticos, el calor es transportado por medio de las vibraciones de la red o fonones. [101] A una temperatura dada, la conductividad térmica de los materiales puede estar afectada por muchos factores como son la naturaleza cristalina del material, la presencia de impurezas, la densidad en bulk, imperfecciones en la red, porosidad, fronteras de grano, etc. [102] Cualquier factor que favorezca la dispersión de los fonones va a reducir la conductividad térmica del material, típicamente: una estructura desordenada, la presencia de defectos, la presencia de fases secundarias, una elevada porosidad o un gran número de fronteras de grano. [102] Sin embargo, puede haber otros factores que afecten a la conductividad del material, particulares del sistema, como la exsolución lamelar o procesos de descomposición espinodal presentes en algunos feldespatos. [24] Esto afecta en gran medida a la conducción del calor, ya que se favorece la dispersión de fonones en las intercaras de dichas estructuras lamelares, reduciendo, por tanto, su recorrido libre medio. [103] La conductividad térmica de las rocas y minerales puede variar enormemente. Minerales como la dolomita, la sal gema o los piroxenos tienen conductividades relativamente altas, mientras que rocas como la granita tienen conductividades térmicas intermedias. En cambio, los feldespatos son uno de los peores conductores del calor, pudiendo llegar a tener valores tan bajos como el vidrio. [103] En el caso de los feldespatos minerales, se ha comprobado que los procesos de dispersión de fonones

no se ven fuertemente afectados por la composición. En concreto, para las plagioclasas, los valores de conductividad térmica se encuentran en un rango aproximado de 1,7 a 2,4 W/mK [103] según su composición, siendo K de 1,7 W/mK para un mineral puro de anortita y de 2,4 W/mK en uno de albita.

Otro parámetro clave a la hora de evaluar el comportamiento térmico de un material es la difusividad térmica (α), que mide la velocidad a la que la temperatura de un material cambia al ser puesto en contacto con una fuente de calor, hasta alcanzar el equilibrio térmico. La difusividad térmica, cuya dimensión en el S.I. es m^2/s, depende de la conductividad térmica, la densidad del material (ρ) y el calor específico (c) siguiendo la relación expresada en la ecuación 1.1: [104]

$$\alpha = \frac{K}{\rho\, c} \qquad \text{(ec.1.1)}$$

Donde el calor específico o capacidad calorífica específica de un material es la magnitud física que se define como la cantidad de calor necesaria para elevar la temperatura de una unidad de masa en un grado, siendo sus unidades en el S.I. *J/Kg·K*. Por tanto, un buen aislante tendrá valores de calor específico elevados.

Por otro lado, a la hora de evaluar un material termorreflectante, hay que tener en cuenta una serie de conceptos relacionados con las propiedades ópticas del material, como son: la reflectancia y la reflectancia solar.

La reflectancia (R) de un material mide la relación entre la potencia electromagnética reflejada en una intercara del material con respecto a la potencia electromagnética incidente para una λ dada.

La radiación solar presenta diferentes intensidades a lo largo del espectro electromagnético, como se puede ver en la Figura **1.3**, por lo tanto, para poder evaluar correctamente el comportamiento de un material en aplicaciones termorreflectantes, será necesario calcular la reflectancia solar (SR) del material analizado en cuestión. La reflectancia solar es la habilidad que tiene un material para reflejar la energía solar desde su superficie y es expresada en tanto por uno, tomando un valor de 0 cuando el material absorbe toda la energía solar y un valor de 1 cuando la refleja en su totalidad, en cuyo caso, su espectro de reflectancia coincide con el espectro solar. Esta magnitud puede ser calculada por medio de la ecuación 1.2:[105]

$$SR=\frac{\int_{\lambda_1}^{\lambda_2} R_\lambda I_\lambda d\lambda}{\int_{\lambda_1}^{\lambda_2} I_\lambda d\lambda} \qquad \text{(ec. 1.2)}$$

Donde R es la reflectancia espectral del material en cuestión e I_λ la irradiancia espectral solar en la superficie de la tierra ($W \cdot m^{-2} \cdot nm^{-1}$).

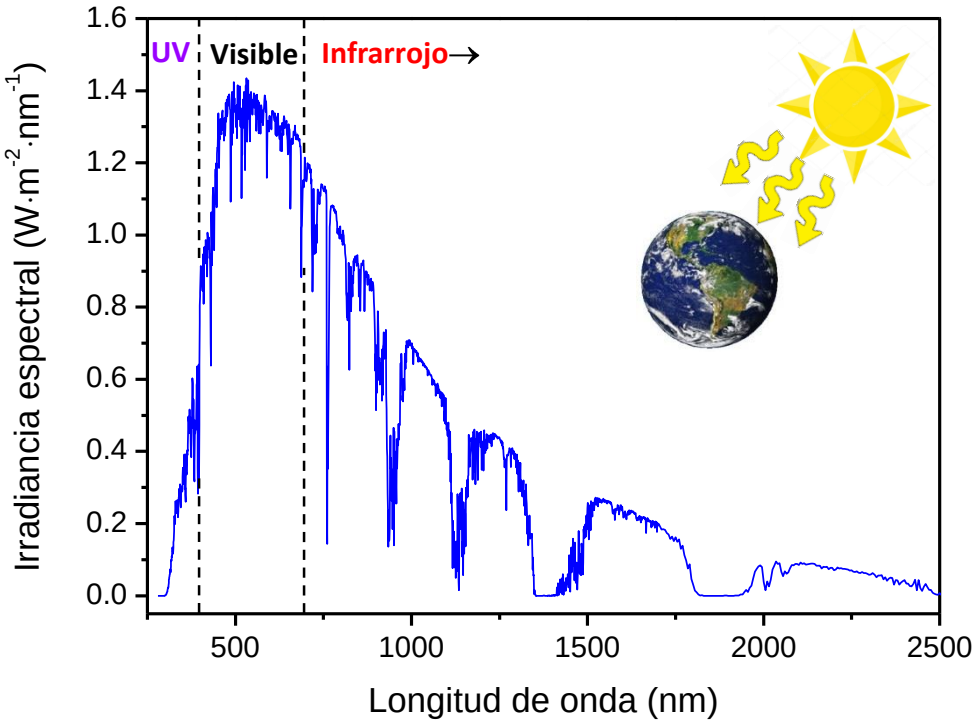

Figura 1.3. Irradiancia espectral solar vs longitud de onda en el rango 250-2500 nm.

ii. Cool roofs y efecto isla de calor

Actualmente, el calentamiento global es uno de los problemas medioambientales que más atención recibe a nivel mundial. Numerosas investigaciones se han emprendido en los últimos años con el fin de intentar reducir su impacto sobre el planeta. En las grandes ciudades, uno de los factores que afecta en mayor medida a este efecto es la creación del efecto isla de calor [106]. Se trata de un fenómeno que tiene lugar en las zonas urbanas, debido a una edificación masiva, y se traduce en un aumento de la temperatura en el centro de las ciudades (que puede llegar hasta 8 ºC), con respecto a las áreas de alrededor, como el extrarradio o zonas rurales (ver Figura 1.4). La acumulación de calor por parte de los materiales que absorben radiación solar a lo largo del día es liberada durante la noche, lo cual intensifica este fenómeno,

especialmente durante la noche. Dicho efecto de isla de calor contribuye al incremento de la pérdida de confort humano, así como al aumento de problemas en la salud [107]. Además, también hay consecuencias medioambientales inmediatas derivadas del aumento del consumo de energía destinada a aclimatar los espacios cerrados para lograr un mayor confort [108]. Con el fin de refrigerar el interior de los edificios, se favorece el aumento de la generación y propagación de los llamados gases de efecto invernadero, principalmente CO_2, aumentando a su vez los niveles de contaminación de la atmosfera [109].

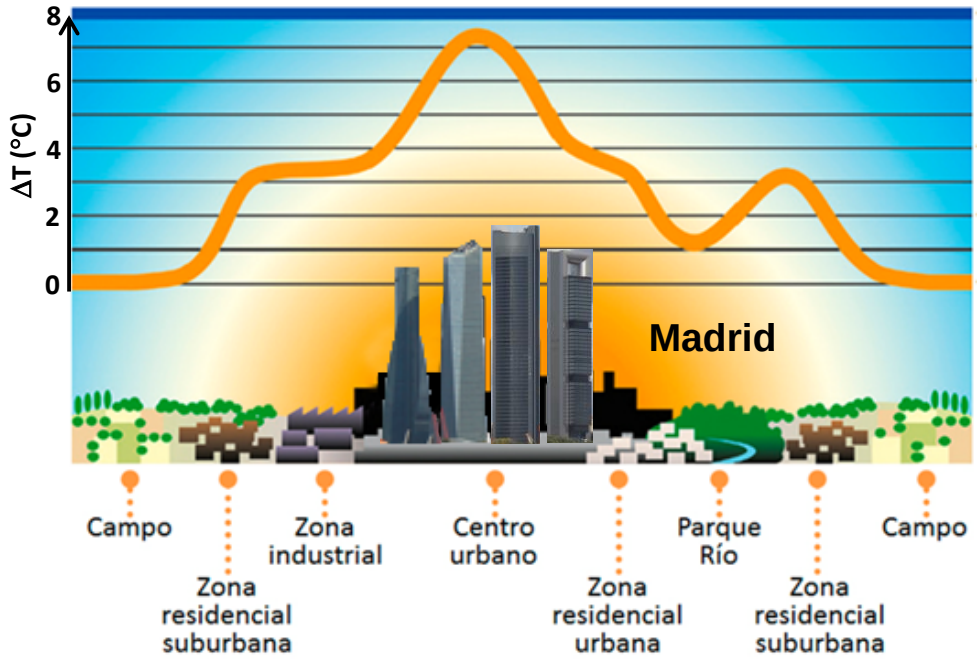

Figura 1.4. Perfil de temperaturas urbanas en comparación con zonas del extrarradio y el área rural. El efecto isla de calor es el responsable de dichas diferencias observadas (Adaptado de[110])

Algunas estrategias que se han llevado a cabo para intentar mitigar este efecto han sido: el incremento de zonas verdes, el uso de "cool pavements" en las ciudades (pavimentos que emplean ciertos aditivos para reflejar la radiación solar, frente al pavimento negro convencional, el cual absorbe ~80-95 % de la luz solar) o el incremento del albedo en los edificios, entre otros [106]. Con respecto al incremento del albedo, una solución que se ha llevado a cabo ha sido el uso de los llamados "green roofs", que son azoteas o tejados que están cubiertos de vegetación parcialmente o en su totalidad. [111] Sin embargo, las dificultades en su mantenimiento han llevado a adoptar otras vías como son los "cool roofs", los cuales, además, favorecen la mitigación del

efecto isla de calor de manera más efectiva. Los materiales empleados en dichas aplicaciones se caracterizan por tener una elevada emisividad térmica, así como una alta reflectancia solar. Los "cool roofs" están típicamente compuestos de cubiertas reflectantes, basados en pinturas blancas con compuestos como TiO_2, Alúmina trihidratada (ATH) o compuestos orgánicos. [105,112–114] El principal inconveniente que presentan es la degradación que sufren por parte de la suciedad [115] y la fotodegradación que sufren los componentes orgánicos por la incidencia de radiación UV, lo que lleva a la decoloración de la pintura hacia tonalidades amarillentas. El elevado albedo que se consigue en estas superficies es principalmente debido a la gran blancura de estas, [94] lo cual va a suponer que casi todo el rango visible del espectro solar sea reflejado. No obstante, el uso de pigmentos opacificantes basados en TiO_2 o $ZrSiO_4$ incrementa considerablemente el precio del producto final. Además, estas pinturas no suelen reflejar la radiación del Infrarrojo cercano ("NIR") y, por tanto, la temperatura se va a transmitir fácilmente a través de él, lo cual no va a ser favorable desde un punto de vista energético y se va a agravar el efecto isla de calor.

A raíz de ello, surgen investigaciones en las que se trata de solucionar este problema, dotando además al "cool roof" de diferentes tonalidades, lo cual puede ser interesante desde un punto de vista estético. [116,117] Otra alternativa a esta problemática consiste en el uso baldosas cerámicas que posean varios recubrimientos: uno en la zona superior que tenga una tonalidad dada, gracias a un pigmento, y que sea transparente a la radiación infrarroja; otro en la parte inferior que sea capaz de reflejar dicha radiación y por último un sustrato cerámico. [105,118,119] Estos materiales son aptos para su aplicación en tejados, ya que además de ser reflectantes, presentan buenas características técnicas como son sus buenas propiedades mecánicas, que son inertes químicamente e ignífugos. El principal inconveniente que presentan está derivado de su procesamiento, ya que, al tratarse de, al menos, tres materiales diferentes, van a ser necesarios, al menos, tres procesos de sinterización diferentes, lo cual no es favorable de cara a su producción industrial. Otra consideración que deben tenerse en cuenta en azulejos cerámicos (teja o baldosa) es que, a pesar de conseguir un elevado albedo, al estar en contacto con el aire, pueden elevar su temperatura por conducción. Consecuentemente, dicho calor será transferido al interior del edificio. Para ello se puede emplear un sustrato poroso con el fin de reducir su conductividad térmica, sin embargo, sus propiedades mecánicas pueden verse negativamente afectadas [94]. Esta es la base de las espumas vitrocerámicas, típicos materiales porosos empleados para aislamiento del calor, en las cuales se consiguen conductividades térmicas bajas, inferiores a 0,50 W/mK en algunos casos . [120]

En la literatura hay muchos trabajos que tratan el procesamiento de los materiales para su aplicación en baldosas cerámicas, [121,122] la posibilidad de usar diferentes materias primas [123–125] o que estudian las nuevas tendencias. [126] Sin embargo, hay pocos trabajos en la literatura en los que se evalúan las propiedades térmicas en baldosas cerámicas, [94,122] así como de materiales basados en feldespatos que se emplean en éstas. [127,128] En la

Tabla **1.3** se incluyen valores de algunos de los parámetros térmicos anteriormente mencionados, para una serie de materiales empleados en la fabricación de baldosas cerámicas. Además, se incluyen también baldosas vitrocerámicas empleadas en aplicaciones de tipo "cool roof", así como materiales típicos empleados en aplicaciones reflectantes, como es el caso del ATH o el TiO_2, entre otros.

Material	α (m^2s^{-1})·10^{-6}	ρ (g/cm^3)	C ($Jg^{-1}K^{-1}$)	K (W/mK)	Referencias
Granito	1,90	2,87	0,72	4,00	[122]
Mármol	1,10	2,7	0,94	2,77	[122]
Terrazzo	1,00	2,58	0,79	2,12	[122]
Gres porcelánico	0,90	2,41	0,73	1,68	[122]
Plagioclasas	1,00	2,62-2,75	0,84	1,7-2,4	[103]
Cerámica roja	0,80	2,23	0,67	1,51	[122]
Cerámica blanca	0,50	1,67	0,65	0,59	[122]
Cool tile(β-wollanstonita y hardystonita)	-	1,94	-	0,61	[94]
Kaolinita	-	-	0,78-0,95	0,16-0,3	[128,129]
Porcelana	0,41	1,92	-	-	[127]
Arcilla roja	-	1,85	-	0,41	[130]
TiO_2	0,90-1,70	4,25	0,69	2,5-5	[131,132]
ATH	3,50-45,7	2,42	1,18	10-30	[133,134]

Tabla 1.3. Valores de las diferentes propiedades térmicas en materiales empleados en la fabricación de baldosas cerámicas: α (difusividad térmica); ρ (densidad); C (calor específico); K (conductividad térmica).

Por tanto, el estado del arte actual busca materiales cerámicos para la mejora en la eficiencia térmica en los edificios, con elevada emisividad y reflectancia solar, incluyendo el NIR, así como baja conductividad y difusividad térmica con el fin de mitigar el efecto isla de calor en las ciudades y aumentar simultáneamente el ahorro energético en las viviendas. Además, dichos materiales deben tener unas propiedades mecánicas de acuerdo con la norma y ser producidos de forma viable a escala industrial.

En resumen, existe un número creciente de aplicaciones donde la presencia de cristales de feldespatos puede suponer una ventaja respecto a las soluciones actuales. En estas aplicaciones es necesaria una modificación composicional y de la micro/nanoestructura que permita mejorar las prestaciones de los materiales cerámicos basados en feldespatos. En particular, se abre un campo de estudio basado en la obtención de propiedades funcionales basadas en materiales cerámicos obtenidos mediante procesos de ingeniería de feldespatos.

Capítulo 2.

Objetivos y/o hipótesis

Este trabajo se ha llevado a cabo en colaboración con la empresa Vidres S.A., con la que se establecieron una serie de objetivos a cumplir, dentro de un proyecto CDTI. Además, en esta tesis se ha querido ir un paso más allá estableciendo nuevos objetivos, con el fin de encontrar novedosas aplicaciones a esta nueva familia de materiales vitrocerámicos funcionales. Todo ello, apoyado en una caracterización exhaustiva a nivel estructural, microestructural y funcional.

El gran conocimiento acerca de los feldespatos minerales junto con las interesantes características que presentan, hace que sean muy empleados como materia prima en el sector cerámico industrial. A nivel de materiales sintéticos, existe una enorme variedad de composiciones por explorar, sin embargo, hasta la fecha, apenas se ha explotado su potencial. Las investigaciones se han centrado principalmente en el estudio de los procesos de síntesis y sólo existen unos pocos trabajos en los que se evalúan sus propiedades mecánicas, dieléctricas o luminiscentes. [9,10,51,72] Teniendo en cuenta el amplio rango de posibilidades que ofrecen los materiales vitrocerámicos y siendo posible la ingeniería de su microestructura por medio del control de su composición y del proceso de desvitrificación, parece interesante intentar desarrollar una nueva familia de materiales que aúne los puntos fuertes que caracterizan a ambos sistemas. A todo ello, se le añade la incorporación y optimización de ciertas propiedades por medio del uso de la nanotecnología, apenas extendida en el sector de los esmaltes cerámicos.

Por todo ello, y teniendo en cuenta el estado del arte anteriormente expuesto, el **objetivo principal** establecido para esta tesis doctoral es **el desarrollo de una nueva familia de materiales vitrocerámicos, basados en cristalizaciones de feldespatos con una microestructura singular, dotados de funcionalidades inusuales de cara a su uso en aplicaciones potenciales.**

Este objetivo se abordará mediante un método de procesado que opta por una ruta cerámica convencional, empleando precursores y tratamientos térmicos que puedan ser aplicados a nivel industrial, con el fin de cumplir con los requisitos de sostenibilidad y viabilidad económica.

Para desarrollar de forma completa este objetivo principal, se han planteado una serie de objetivos parciales que se exponen a continuación:

1. Obtención de esmaltes vitrocerámicos con cristalizaciones de feldespatos mediante un proceso de síntesis rápido, sencillo, sostenible, reproducible y fácilmente escalable en el sector cerámico industrial.

2. Optimización de la composición de los materiales precursores, frita y caolín, así como el proceso de sinterización llevado a cabo, con el fin de obtener una elevada densificación, elevada cristalinidad, baja porosidad y de diseñar una microestructura en el material vitrocerámico que maximice las propiedades de los esmaltes obtenidos.

3. Establecer los mecanismos de cristalización de esta nueva familia de materiales vitrocerámicos micro-nanoestructurados.

4. Estudiar exhaustivamente la estructura y la micro-nanoestructuración desarrollada, combinando técnicas de microscopía y espectroscopia avanzadas que permitan correlacionar la información obtenida.

5. Estudiar la mejora de diversas propiedades, enumeradas a continuación, gracias a la estructura y la microestructura diseñadas, de cara al uso de dichos materiales en diferentes aplicaciones:

    - Evaluación de las propiedades dieléctricas.
    - Evaluación de las propiedades mecánicas.
    - Evaluación de las propiedades luminiscentes.
    - Evaluación de las propiedades termorreflectantes.

6. Correlacionar las diferentes propiedades funcionales obtenidas y/o mejoradas con las variaciones en la estructura y microestructura, teniendo en cuenta el efecto de las nanopartículas y de los defectos introducidos en la estructura de estos materiales vitrocerámicos.

Por tanto, con esta agrupación de objetivos se pretende abordar un estudio completo y sistemático de la nueva familia de materiales vitrocerámicos diseñados, correlacionando todos los resultados obtenidos, de forma que se logren comprender los mecanismos físicos y químicos que subyacen a los fenómenos observados. Así mismo, se podrá definir el rango de aplicaciones en el que estos materiales tienen cabida, tanto en la cerámica tradicional como en la exploración de nuevos campos.

Capítulo 3.

Preparación de materiales

Durante este trabajo de investigación de la tesis doctoral se han realizado diversas modificaciones composicionales con el fin de obtener y estudiar dos composiciones extremas dentro del grupo de las plagioclasas. Por un lado, un material vitrocerámico con un contenido mayoritario de cristalizaciones de un feldespato cálcico, anortita, y, por otro lado, con la presencia de una fase sódica mayoritaria, albita. Es importante destacar que, a lo largo de esta tesis doctoral, especialmente en las publicaciones, se hace referencia a estos materiales como anortita o albita, respectivamente. Esta nomenclatura es la empleada en el sector cerámico para hacer referencia a materiales de tipo feldespato ricos en cristalizaciones de aluminosilicatos cálcicos ($CaAl_2Si_2O_8$) o sódicos ($NaAlSi_3O_8$). Sin embargo, cuando se aborda el problema desde un punto de vista mineralógico, es necesario el análisis composicional del material de forma más minuciosa. Como se explicó anteriormente en la introducción, las plagioclasas son soluciones sólidas con composiciones variables de sodio y calcio dentro del sistema albita-anortita. Sintetizar de forma pura estás fases es extremadamente complejo, por ello, mineralógicamente hablando, es necesario emplear la terminología de plagioclasa, especificando típicamente el contenido en anortita presente.

Las muestras empleadas para la elaboración de las publicaciones adjuntas fueron aquellas que presentaron las mejores propiedades, esto es, una mayor densificación, menor porosidad y una micro-nanoestructuración más homogénea, con el fin de obtener las mejores propiedades funcionales estudiadas, así como maximizar el efecto de la microestructura en las mismas, teniendo en cuenta los conceptos anteriormente explicados en la introducción y su correlación.

Para alcanzar las condiciones idóneas se variaron los siguientes parámetros:

- *El contenido en óxidos de las fritas precursoras* se modificó dentro de un rango de composiciones que se detallan a continuación:

  - entre un 45 % y un 68 % de SiO_2.
  - entre un 15 % y un 27 % de Al_2O_3.
  - entre un 4,5 % y un 13 % de CaO.
  - entre un 0 % y un 9 % de SrO.
  - entre un 1 % y un 5,5 % de Na_2O.

- entre un 1 % y un 5 % de K_2O.
- entre un 0 % y un 2 % de B_2O_3.
- entre un 0 % y un 14 % de ZrO_2.
- y entre un 0% y un 5 % de MgO, BaO y ZnO.

En la frita de albita se probaron composiciones con y sin ZrO_2 con el fin de determinar si éste actuaba como agente nucleante de la plagioclasa sódica. Finalmente, se determinó que no influía en la cristalización de ésta, mientras que la presencia de SrO_2 si era fundamental, tal y como se explica en el trabajo "***Study of the Crystallization in fast sintered Na-rich plagioclase glass-ceramic***".

Finalmente, las composiciones empleadas aparecen expresadas en la

Tabla 3.1:

Óxidos (% en peso)	SiO_2	ZrO_2	SrO	Na_2O	K_2O	Al_2O_3	ZnO	CaO	**Otros***
Frita albita	51,63	-	8,05	2,68	1,46	21,14	1,10	10,47	3,48
Frita anortita	47,33	8,03	-	5,06	1,7	19,23	4,72	12,97	0,97
Caolín	55,49	-	-	-	1,21	42,48	-	0,17	0,65

Tabla 3.1. Composición química de la frita precursora de albita y anortita y el caolín empleado para sintetizar los materiales vitrocerámicos del trabajo presente, expresado cómo % en peso De los óxidos equivalentes. La proporción de los componentes minoritarios < 1 % en peso es incluida en otros: TiO_2, Fe_2O_3, P_2O_5, MgO, PbO.

- *Determinación del tratamiento térmico, modificando tanto la temperatura como el ciclo de sinterización.* A partir de los ensayos de microscopía de calefacción llevados a cabo para una muestra de albita y anortita (Figura 3.1), se consideraron diferentes tratamientos de sinterización de las piezas cerámicas, variando tanto la duración como la temperatura de estos. A 1100 ºC ambos feldespatos cristalizan, tal y como muestran los ensayos de microscopía de

calefacción presentados a continuación. Se realizaron tratamientos a temperaturas de 1160 ºC, 1180 ºC y 1220 ºC, alcanzando una buena densificación para el caso de las muestras de albita, sin embargo, las de anortita no densificaban completamente. Por tanto, se determinó que es necesario alcanzar una temperatura de 1220 º C para densificar correctamente ambos materiales de forma simultánea y obtener la microestructura deseada, obteniendo una micro-nanoestructuración más homogénea. El tiempo de mantenimiento para el tratamiento térmico se varió en 6 minutos, 10 minutos, 1 hora y 2 horas. A mayor tiempo de mantenimiento se observó una microestructura ligeramente más refinada, sin embargo, a partir de un tiempo, las diferencias observadas ya eran insignificantes, por lo que se decidió que el tratamiento térmico a 1220 ºC con un mantenimiento de 6 minutos era el óptimo de cara a su aplicación industrial, permitiendo un ahorro energético considerable con respecto al resto de tratamientos.

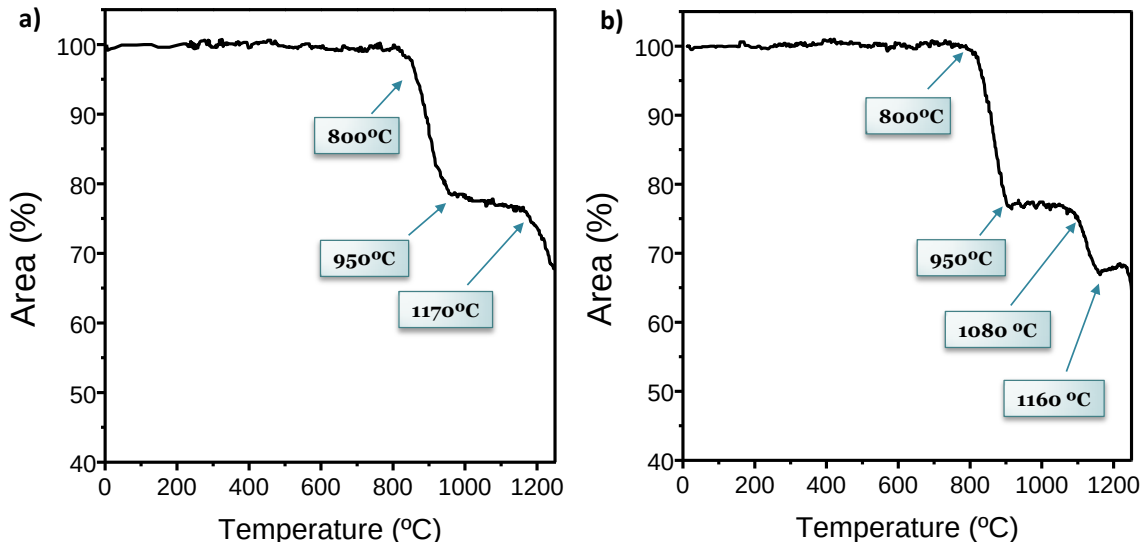

Figura 3.1. Microscopía de calefacción para una muestra vitrocerámica de: **a)** albita; **b)** anortita.

Por tanto, tras el análisis minucioso de las características estructurales de las muestras preparadas, para este trabajo de investigación se eligieron las muestras tratadas a 1220 ºC durante 6 minutos con una tasa de calentamiento de 30 ºC/min. El proceso experimental llevado a cabo está comprendido por las etapas mostradas en la Figura 3.2**:**

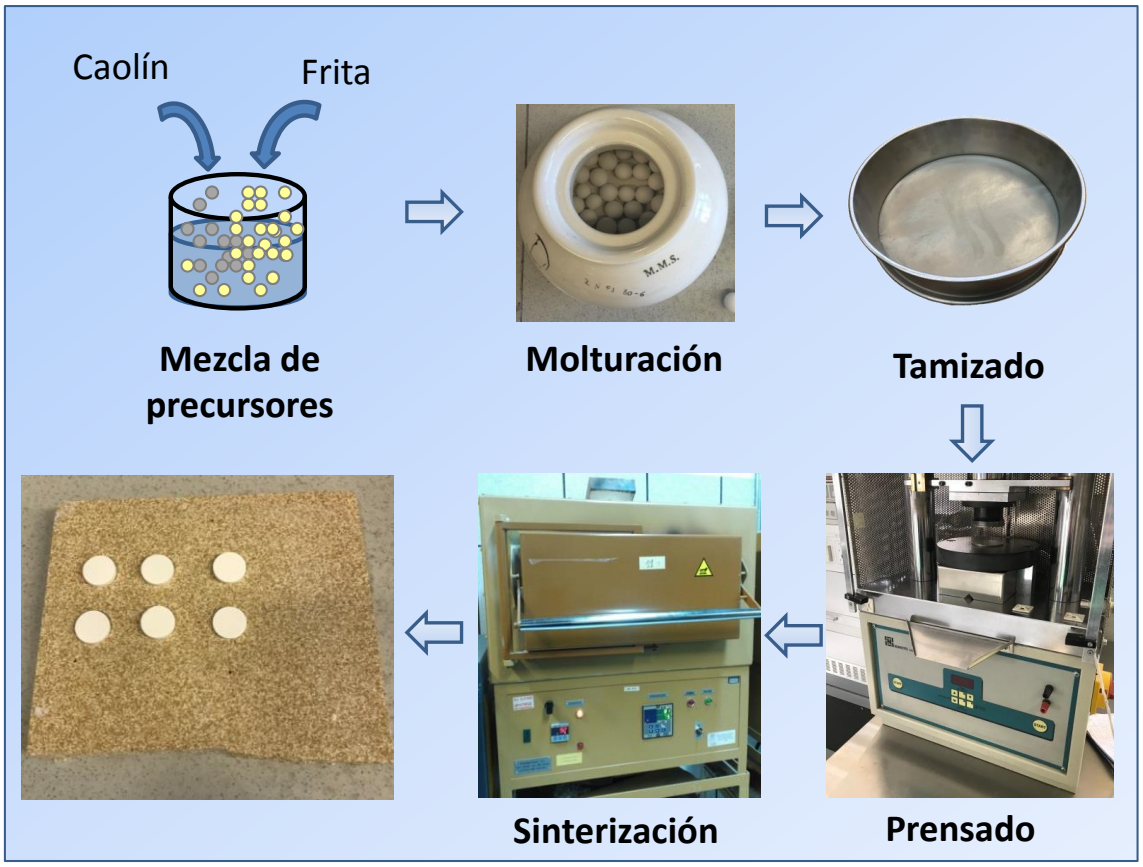

Figura 3.2. Proceso experimental llevado a cabo para la preparación de los materiales vitrocerámicos desarrollados.

En primer lugar, se procedió a realizar la mezcla de los precursores, frita y caolín, en una proporción en peso de 90:10, respectivamente. A continuación, con el fin de homogeneizar los precursores, se procedió a la molturación en un molino de bolas de alúmina durante 20 min con un 37 % en peso de agua. El material preparado fue secado a 60 ºC durante 24 horas y el polvo obtenido fue tamizado a través de un tamiz de 100 µm. Posteriormente se realizó un prensado uniaxial a 39,2 MPa. Tras el proceso de sinterización a 1220 ºC durante 6 min, el aspecto de las muestras obtenidas se puede observar en laFigura 3.2.

Capítulo 4.

Resultados

Los resultados principales de este trabajo de Tesis Doctoral se han recogido en forma de publicaciones científicas, las cuales se recogen a continuación. Se han dividido en dos grandes bloques. En el primero de ellos se aborda el estudio estructural y microestructural de los materiales diseñados, estando formado por dos publicaciones, mientras que el segundo se centra en el estudio de las propiedades de estos (mecánicas, dieléctricas, luminiscentes y termorreflectantes) y está formado por las siete publicaciones restantes.

BLOQUE 1

Este bloque está comprendido por los artículos de investigación "***Study of the Crystallization in fast sintered Na-rich plagioclase glass-ceramic***" (artículo 1) y "***Structural insights of hierarchically engineered feldspars by confocal Raman microscopy***" (artículo 2), en los cuales se estudia exhaustivamente la estructura y microestructura del material vitrocerámico rico en cristalizaciones de plagioclasa sódica. En el **artículo 1**, se analiza a fondo el mecanismo de cristalización y la micro-nanoestructuración desarrollada. Para ello, se emplearon experimentos de quenching, diferentes técnicas de análisis químico (ATD/TG y microscopía de calefacción), de caracterización estructural (XRD, XPS, RMN) y de caracterización microestructural (microscopías como FE-SEM, TEM y HRTEM). Además, se analizan los entornos atómicos del Si, mediante RMN, con el fin de determinar el grado de orden/desorden en la distribución de Si,Al en las posiciones tetraédricas de la red del feldespato.

En el **artículo 2,** se realiza un análisis estructural y composicional por medio de Espectroscopia Raman Confocal. En primer lugar, se pretende determinar la composición de la plagioclasa desarrollada, así como analizar el espectro vibracional en las zonas nanoestructuradas y en las microestructuradas, con el fin de poder discriminarlas gracias a posibles diferencias en respuesta de los fonones correspondientes. Por otro lado, se realiza un estudio de la dependencia estructural con la temperatura hasta 600 ºC, con el objetivo de analizar el efecto de la activación térmica en la evolución de la distribución de Si,Al y en la movilidad catiónica del sistema, tanto a nivel microscópico (por medio de espectroscopia Raman) como a gran escala (por medio de XRD). Por último, mediante espectroscopia de dispersión Rayleigh se pretendió estudiar procesos de exsolución, los cuales son habituales en los feldespatos minerales.

ARTÍCULO 1. Study of the Crystallization in fast sintered Na-rich plagioclase glass-ceramic

E. Enríquez, V. Fuertes, M.J. Cabrera, J. Seores, D. Muñoz, B.Galiana, J. F. Fernández.

Ceramics International, 45 (7), A, 2019, 8899-8907

Factor de impacto: 3,057 (según JCR Edition Science 2017).

Ceramics International 45 (2019) 8899–8907

Contents lists available at ScienceDirect

Ceramics International

journal homepage: www.elsevier.com/locate/ceramint

Study of the crystallization in fast sintered Na-rich plagioclase glass-ceramic

E. Enríquez[a,*,1], V. Fuertes[b,1], M.J. Cabrera[a], J. Seores[a], D. Muñoz[a], B. Galiana[c], J.F. Fernández[b]

[a] Centro tecnológico Vidres, S.L., Ctra. Onda, Km 3.4, 12540, Villareal, Castellón, Spain
[b] Electroceramics Department, Instituto de Cerámica y Vidrio, CSIC, Kelsen 5, 28049, Madrid, Spain
[c] Physics Department, Universidad Carlos III de Madrid, Av. Universidad 40, 28911, Leganés, Madrid, Spain

ARTICLE INFO

Keywords:
Glass-ceramic
Plagioclase feldspar
Micro-nanostructure
Crystallization processes
Fast sintering

ABSTRACT

A dense, ~94% of crystalline phase, glass-ceramic based on Na-rich plagioclase feldspar crystallizations has been obtained by a fast sintering process for the first time. By using Sr^{2+} and Ca^{2+} as nucleating agents, a unique hierarchical micro-nanostructure is developed in a fast sintering process at 1220 °C. In this work, a thorough study about crystallization processes of this novel material has been extensively carried out through thermal quenching experiments and supported by DTA/TG, Hot stage microscopy, XRD, FE-SEM, TEM/HRTEM and XPS measurements. The study reveals that crystallization takes place in two steps during the sintering process. Microcrystals nucleate on heating at temperatures > 900 °C, while nanocrystals start nucleating at the dwelling temperature, 1220 °C. However, it is during holding and cooling time when nanostructures zones grow, and the unique highly crystalline micro-nanostructure is developed. Structural and compositional analysis supported by NMR, shows the main presence of Q_4(nAl) albite-like sites and in lesser extent anorthite-like sites, corroborating the formation of a sodic plagioclase structure. The analysis of Si neighbours indicates that chemical environment presents a slight Si/Al disorder at short range.

1. Introduction

Feldspars are widely used in ceramic industrial applications, due to their high alumina content and its abundance in the earth's crust. Most of the products used on a daily basis are made with feldspar raw materials, such as glass for protection, fiberglass for insulation, floor tiles and tableware, among others. Feldspars are very interesting natural mineral due to their excellent properties, such as high Mohs hardness and chemical inertness. Feldspars are basically classified into two groups, plagioclases and alkali feldspars. The first one is a solid solution between albite ($NaAlSi_3O_8$) and anorthite ($CaAl_2Si_2O_8$) end members, while the second one is a solid solution between K-feldspars ($KAlSi_3O_8$) and albite. Feldspars are usually integrated in igneous rocks and, therefore, they have many impurities and intermediate compositions. Feldspar synthesis is still a challenge to obtain pure phase materials under controlled conditions to tailor properties [1–3].

The crystallization processes are of great relevance in the feldspar synthesis. In magmatic rocks, crystallization strongly depends on the cooling rate, pressure, geological time and the abundance of liquid media. The presence of high amount of water can produce great compositional changes in the feldspars minerals [4]. Feldspar synthesis based on hydrothermal process is commonly attempt to obtain pristine particles with complex processes [5–8]. The sol-gel methods are also used to synthesize crystalline feldspar particles [9]. The most common way to synthetize feldspars is following the ceramic procedure of frits. A frit is a ceramic composition that has been melted in a special melting oven and quenched to form a glass. However, the further thermal treatment of frits developed a typical porcelain structure in which feldspar crystallization occurs in a continuous glassy matrix [1,2]. Feldspars find several difficulties to crystallizes from its melts, and thus, the use of seeds is usually necessary to produce feldspars by this route [4,10]. The processing route became more complex when a high crystalline glass-ceramic is pursuit, since larger thermal treatments are required and in some extent it is combined with vacuum systems [2,11].

A glass-ceramic material is usually obtained by controlled devitrification process, which consists in cooling a glass below its melting temperature, in which a nucleation process is produced followed by crystal growth. Sometimes, nucleation and crystallization can coexist when their corresponding temperatures are close enough. In these situations, the glass-ceramic formation is optimum, since there is a large presence of nuclei where the crystals can grow, creating a fine microstructure. The crystal growth rate strongly depends on the fusion entropy that for anorthite, albite and orthoclase are 72.2, 46.3 and 36.0 J/Kmol, respectively [12]. Therefore, Albite feldspar has quite lower

* Corresponding author.
E-mail address: esther@icv.csic.es (E. Enríquez).
[1] These authors contributed equally to this work.

https://doi.org/10.1016/j.ceramint.2019.01.219
Received 29 November 2018; Received in revised form 25 January 2019; Accepted 28 January 2019
Available online 29 January 2019

crystal growth rate ($\approx 10^{-10}$ ms^{-1}) than anorthite ($\approx 10^{-4}$ ms^{-1}). Moreover, albite crystal growth is produced at lower range of temperatures (1000-1100 °C) regarding anorthite (1200-1300 °C). These characteristics make it necessary to use nucleating agents to accelerate the crystallization process of the albite. The presence of nucleating agent in form of seeds would produce an heterogeneous nucleation due to larger amount of boundaries [4,13]. However, it was demonstrated that ZrO_2 seeds do not favor the crystallization of albite feldspars [14]. On the other hand, selected cations as Zr, Ca or Sr, can act as nucleating agents following a homogeneous nucleation process. Albite feldspar is an alkali aluminosilicate quite difficult to obtain as single phase, both naturally and synthetically, since the presence of other cations apart from Na^{1+}, such as Ca^{2+} and K^{1+}, favors the simultaneous formation of anorthite and orthoclase feldspars, respectively. For these reason, the use of seeds having isomorphs crystal structure than albite, such as anorthite, is often needed [4,13,15]. Besides, Sr^{2+} can act as nucleating agent to form strontium feldspar ($SrAl_2Si_2O_8$) which would favor the albite or anorthite crystallization. However, in the anorthite crystallization is less probable since it requires higher temperatures, ~1400 °C [12]. An approximation to the problem may be to deal with sodic plagioclases that are materials which present albite as a major component and anorthite as minor one. Recently, a high dielectric strength response of albite-based glass-ceramics is reported [16]. The excellent insulator properties are based on their unique micro-nanostructure that consists of isolated micrograins surrounded by nanostructured regions forming a hierarchical microstructure. Such hierarchical microstructure serves to tailor properties of the glass-ceramics as thermal diffusivity [15] and wear resistance.

Thus, in this work, the objective is to study the crystallization process that occurs in synthetic plagioclase-based glass-ceramic with high albite content processed by a fast sintering process. The glass-ceramic materials are obtained from a glass frit. With the aim of deepening in the heating and cooling steps and therefore, in crystallization and devitrification process, DTA/TG and quenching experiments were carried out. Compositional and microstructural analysis of quenched and sintered samples by XRD, FE-SEM, TEM and HRTEM is combined with structural characterization by XPS and NMR and reveals that crystallization of the Na-rich plagioclase occurs in two steps.

2. Experimental procedure

2.1. Sample preparation

The glass ceramic based on Na-rich plagioclase feldspar was prepared following a fast sintering process easily adaptable for the tile industry [18,19]. Firstly, a composition melted in a furnace at 1450-1500 °C and then, water quenched to form the frit precursor. Once obtained the frit, it was homogenized with kaolin (Molcasa) in a weight proportion 90/10, in an alumina ball miller during 20 min with 37 wt% of water. Then, the resulted material was dried in an oven at 80 °C and sieved by a 63 μm sieve. The powder obtained was pressed in pellets of ~10 mm in thickness, at 400 kg/cm^2 of pressure. Finally, samples were thermally treated in an industrial furnace at 1220 °C with dwelling time of 6 min with a heating and cooling rate of 30 °C/min. The composition of the final material is expressed in term of equivalent oxides in Table 1. The minority components of the composition (providing from the raw materials) having concentrations < 1 wt% (B_2O_3, TiO_2, P_2O_5, Fe_2O_3, MgO, BaO, ZnO) are included in the term "others".

Table 1
Composition of studied glass ceramic and glaze expressed as equivalent oxides. The minority components are all included in others (B_2O_3, TiO_2, P_2O_5, Fe_2O_3, MgO, BaO, ZnO).

Oxides wt. %	SiO_2	ZrO_2	Al_2O_3	CaO	Na_2O	SrO	K_2O	ZnO	Others
Frit	54.67	1.24	22.63	7.73	2.14	7.20	1.44	1.27	2.96
Kaolin	55.49	–	42.48	0.17			1.21		0.65

In order to study the crystallization degree during the densification process at selected temperatures, a thermal quenching process was carried out. For this purpose, powder pellets were prepared following the procedure explained above, and they were heated up to 800 °C, 900 °C, 1100 °C and 1200 °C, temperatures at which the sample was extracted and immersed quickly in cold water to freeze the structure obtained at those temperatures.

2.2. Characterization

Thermal behavior of the glass-ceramic was studied by means of differential thermal analysis (DTA) and thermogravimetric (TG) analysis using a Thermo-Analyzer Netzch STA 409 with a temperature controller Netzch TASC 414/2 being the reference α-Al_2O_3. Hot-stage microscopy was also carried out by a Leica Leitz microscope. Both measurements were made in the range 30–1250 °C with a heating rate of 10 °C/min in air atmosphere.

Microstructural characterization was studied by means of Field Emission Scanning Electron Microscopy (FESEM) using a Hitachi S-4700. Polished samples were chemically etched with 5 vol% of HF with the aim of removing the glassy phase to reveals the microstructure. In addition, the crystalline phases formed were identified by using X-ray diffraction (XRD) technique in a diffractometer Bruker D8 Advance with Cu Kα radiation, 40 kV and 40 mA, in sintered samples. The identification of the crystalline phases was carried out by the comparison with the JCPDS patterns, and the glassy phase content was obtained through the integration of the areas corresponding to the glassy and crystalline phases by means of the diffraction software Bruker's Diffrac.Eva.

Transmission electron microscopy (TEM) was performed at 200 keV on Philips Tecnai F20. Samples were prepared in cross-section by standard sample preparation methods, mechanical thinning and argon ion milling to electron transparency. High resolution TEM (HRTEM) images were also acquired to study the local crystalline quality. Electron diffraction pattern and diffraction pattern simulations after fast Fourier transform (FFT) of HRTEM images were also used.

X-ray photoelectron spectroscopy (XPS) was carried out by an X-ray photoelectron spectrometer (XPS, K-Alpha, Thermo Scientific). Samples were deeply polished before measuring in order to be able to study the internal part of the materials. Prior to analysis, the samples were cleaned by ion bombardment with an Ar^+ beam (2 kV) for 5 min. A monochromatic Al K_α (1486.6 eV) source running at a voltage of 12 kV with a pass energy of 40 eV was used for high-resolution region scans and 200 eV for survey scans; finally, for charge correction a 1 point scale with the C 1s peak shifted to 284.60 eV was used.

Structural characterization at short range was made by solid state MAS nuclear magnetic resonance (NMR) on the powders obtained by milling the sintered samples at room temperature. ^{29}Si MAS NMR spectra were recorded on a Bruker AV-400-WB spectrometer equipped with 4 mm MAS probe and operating at 79.49 MHz by a simple pulse of π/2 at 50 KHz. Relaxation time was of 60s, spectral width of 40 kHz and 2 h of accumulation time with a spinning rate of 10 kHz were taken. Kaolin (−91.2 ppm) was used as secondary reference with respect to TMS as primary reference.

3. Results and discussion

3.1. Thermal evolution of the crystallization in Na-rich plagioclase glass-ceramic formation

In order to analyze the thermochemical reactions that occurs during the thermal treatment firstly, DTA-TG measurements and hot stage microscopy of the frit and kaolin mixture were made (Fig. 1a and b, respectively. DTA-TG results reveal two endothermic peaks related to

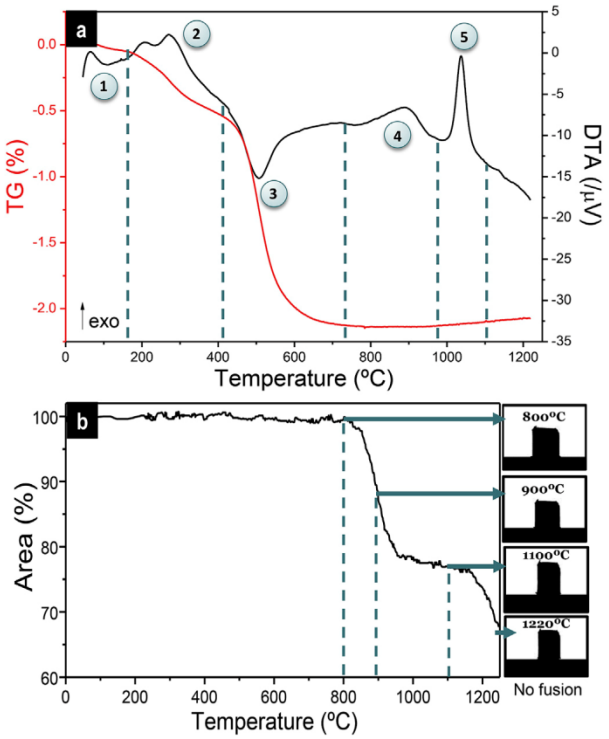

Fig. 1. a) DTA-TG of frit - kaolin (90%–10%) mixture from room temperature (RT) to 1220 °C; b) Hot stage microscopy of this material in the same temperature range of a).

the adsorbed water loss up to ~150 °C (region 1) and organic-based processing additives that burn out from 300 °C to 400 °C with an associated weight loss of 0.5% (region 2). A relevant endothermic peak is observed at ≈500 °C (region 3) corresponding to the structural water dihydroxylation of Kaolin that transform into metakaolin along with a mass loss of ≈2% [20]. Also associated with metakaolin, an exothermic peak appears at ≈900 °C (region 4), which corresponds to an aluminum-silicon spinel or pre-mullite type crystals attributed to a transformation of the SiO4 groups combine with the AlO6 groups to form the Al–Si spinel phase, precursor of the mullite phase [21,22]. Finally, an exothermic process corresponding to the albite-rich feldspar crystallization occurs at ≈1040 °C (region 5). These two exothermic processes correlated with crystallizations do not have associated a loss of weight. In addition, the cooling curve is also measured in order to check if any thermal or structural process occurs during this period. However, the resolution obtained does not reveal any significant process and the curve is omitted.

According to this information, hot stage microscopy is carried out from room temperature up to 1220 °C, in order to determine the influence of different thermal processes of the Na-rich feldspar formation (Fig. 1b). At 800 °C it is possible to observe the beginning of the first material shrinkage, with a 13% of reduction of its effective area, up to 900 °C. At 800 °C the glaze powders started to shrink with a low rate, indicating a mechanism associated with low mass transport due to the reaction of the metakaolin with the particles of frit [20]. The shrinkage rate decreases drastically at 960 °C, indicating a change of the mass transport mechanism. The decreasing of shrinkage rate in glaze materials is typical of the appearance of crystalline phase that evolved from the glassy phase. The devitrification of frit particles seems to be in the origin of such change. At 1150 °C the material begins to soften, however, as it is seen in the hot stage microscopy image the material does not melt in the studied temperature range.

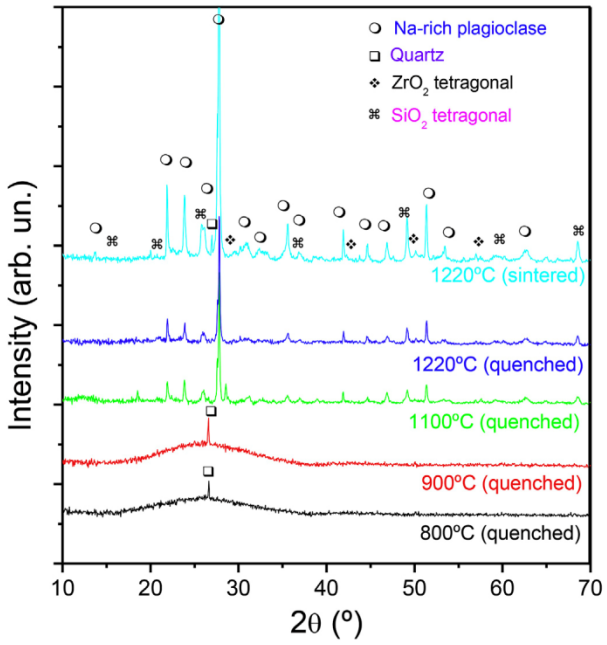

Fig. 2. XRD pattern of the quenched samples at 800 °C, 900 °C, 1100 °C and 1220 °C in comparison with the sample sintered at 1220 °C with a dwell time of 6 min.

Therefore, attending to these results, the temperatures of interest defined for specific thermally treatments and thermal quenching are 800 °C (beginning of the process), 900 °C (in the middle of the sintering process), 1100 °C (crystallization range) and 1220 °C (before the melting point). The samples obtained are structurally characterized by XRD (Fig. 2) and microstructural analyzed by FESEM (Fig. 3). Quenched samples are compared with the material sintered at 1220 °C with a dwell time of 6 min.

The XRD patterns (Fig. 2) show that a thermal treatment up to 900 °C the material is still amorphous presenting a wide band at low 2θ angles, and quartz (JCPDS card no. 00-046-1045) traces as crystalline phase. This quartz trace comes from the kaolin raw material. Hence, at these temperatures, the frit is still in the vitreous phase and the nucleation and crystallization of the glasses have not occurred. At 1100 °C, the slowest shrinkage rate temperature range during the sintering observed in the hot stage microscopy curve, the plagioclase crystallization has already produced, and it is possible to observe the well-defined XRD pattern (JCPDS card no. 00-041-1480), with very low amount of glassy phase. In addition, other minority phases appear: zircon (JCPDS card no. 00-003-064), quartz (JCPDS card no. 00-046-1045) and tetragonal SiO_2 (JCPDS card no. 00-013-0026). Finally, for quenched sample treated at 1220 °C, the XRD pattern is very similar to the one quenched at 1100 °C, however the diffraction peak intensities increase, which indicates crystal growth. In the XRD pattern of the sample sintered at 1220 °C 6 min it is possible to observe the Na-rich plagioclase diffraction pattern with higher crystallinity. In a Na-rich plagioclase (a solid solution between albite and anorthite), albite is the major phase (> 50%) and anorthite appears in less content. Therefore, it is easy to conclude that the Na-rich plagioclase crystallization starts at temperatures > 900 °C, and the crystallinity of the sample rises with the temperature increase, reducing, in consequence, the glassy phase content in the sample.

FESEM micrographs (Fig. 3a–f) corroborate the information extracted from XRD and can also provide more information about nucleation and crystallization. Fig. 3a shows the sample quenched at 800 °C where the frit grains are still visible, with sizes up to 20 μm. The

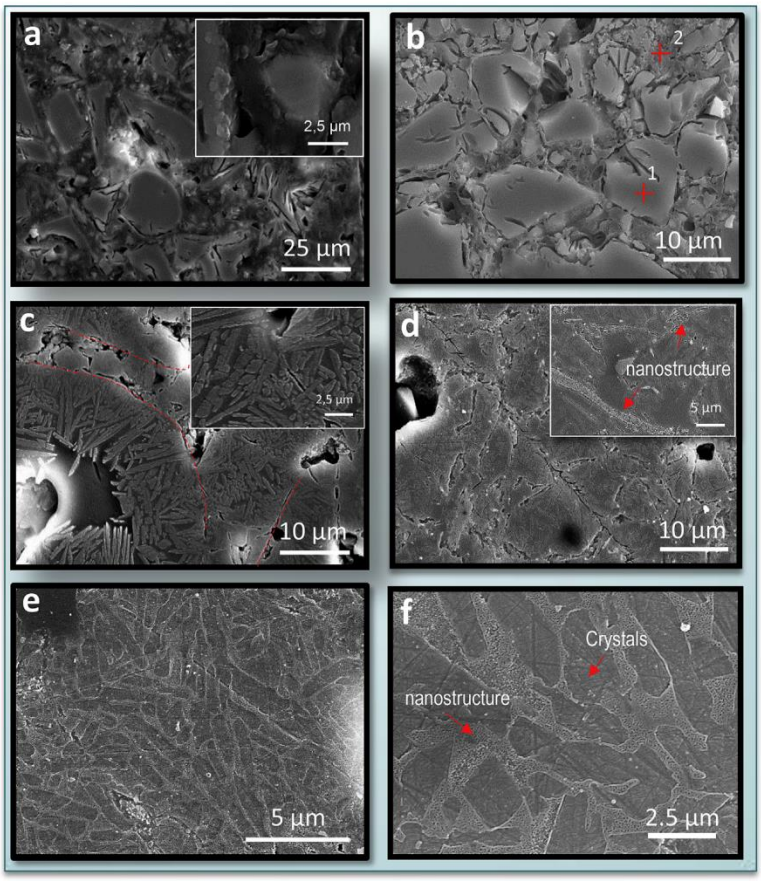

Fig. 3. FESEM micrographs at different magnifications of the Na-rich glass-ceramic feldspar quenched at a) 800 °C; b) 900 °C; c) 1100 °C; d) 1220 °C. In e), f) and sintered at 1220 °C with a dwell time of 6 min.

Table 2
Composition in equivalent oxides of the albite-rich glass quenched at 900 °C, obtained from EDX analysis.

	Na_2O	MgO	Al_2O_3	SiO_2	K_2O	CaO	ZnO	SrO	ZrO_2
Frit region (Point 1)	2.99	0.86	18.06	56.21	0.82	7.60	1.03	7.34	5.10
Glassy region (Point 2)	1.97	0.44	20.79	61.58	1.64	7.88	–	4.81	0.88

frit grains are surrounded by a glassy phase formed from the reaction of the metakaolin and the frit. Therefore, at this temperature the feldspar structure has not crystallized yet. At 900 °C (Fig. 3b), the structure becomes slightly more homogeneous and the frit reacts locally with the surrounding glassy phase. As temperature increases, the reaction of metakaolin with the frit particles produces the diffusion of the necessary cations to form the albite-rich feldspar. An EDX analysis was carried out in this sample in order to understand the composition distribution. In Fig. 3b, two points are marked where the analysis was carried out, a frit grain (point 1) and a vitreous region (point 2). The composition distribution is presented in Table 2, in terms of equivalent oxides. As seen, the Al_2O_3 and SiO_2 percentages indicate the presence of silicoaluminates in the surrounding glassy phase. However, the relevant information is given by the percentages of Na, Ca and Sr. The amount of Ca is very similar in both regions (points 1 and 2), nevertheless, the amount of Na and Sr varies. In the frit grain the amounts of Na and Sr are larger than in the surrounded liquid phase, indicating the cations competence between both elements: Sr^{2+} begins to replace Na^+ in the feldspar structure due to a greater electronic affinity, releasing Na cations from the glassy phase, which will tend to create albite-rich crystals, as it was discussed above.

Fig. 3c shows the microstructure formed at 1100 °C (crystallization region in hot stage microscopy curve), where long albite-rich crystals (up to 10 µm) have been formed inside the frit grains thanks to release of Na^+ cations in the previous step, according to the XRD results. These albite-rich crystals grow in radial direction inside the former frit grain, due to a high nucleation rate at the grain boundaries (marked with red dash lines in Fig. 3c). Therefore, the crystals growth is limited by the former frit grain size and it is also possible to observe glassy phase surrounding the formed microcrystals. When thermal treatment temperature reached up to 1220 °C (Fig. 3d), the boundaries between the former frit regions disappear and the microcrystals growth is more homogeneous. In addition, some nanostructures regions begin to appear as it can be seen in the inset of Fig. 3d, marked with red arrows. Fig. 3 e and f shows the micrographs at different magnifications of the glass-ceramic sintered at 1220 °C 6 min. As it may be seen a dual microstructure, long albite-rich microcrystals (≈5 µm) are homogeneously distributed in the sample, surrounded by nanocrystals regions) which isolate the micrograins. The glassy phase residue is located at the nanoregions.

The chemical composition used in this work (Table 1) possesses lower content of Na than Ca, which would lead to expect the formation of anorthite-rich feldspar instead of albite-rich one. However, the main phase obtained in this material corresponds to a sodic plagioclase, in

which albite is the major crystalline phase, as previously supported by the XRD patterns, Fig. 2. Moreover, the percentage of glassy phase, extracted from this XRD pattern by the diffraction software Bruker's Diffrac. Eva, is as low as ≈ 6%, which indicates the formation of a highly crystalline Na-rich feldspar glass-ceramic.

In this system, strontium probably acts as glass network disruptor, that is, the Sr^{2+} ions are introduced between Si/Al tetrahedra in Na^{+} positions of the glass network system, where oxygen defects are more common, since its charge is electronically more compatible. Accordingly, during the sintering process, these sodium cations are available to form crystals, especially in areas around nucleating agents.

Thus, two conditions favor the formation of a Na-rich plagioclase with larger content of albite than anorthite crystals, despite the lower content of sodium in the frit composition: a) the albite and anorthite glass seeds; and b) Sr^{2+} cations acting as glass network disruptor, favouring the ejection of Na^{1+} cations from glassy matrix and the consequent crystallization of sodium-rich crystals, mainly due to a cationic competition. As known, cation diffusion in the melting liquid is quite relevant in the nucleation and crystallization processes, since the cations mobility influences the composition of the final crystals [4]. For this reason, as sodium ions have larger mobility than calcium ions, formation of a Na-rich plagioclase is favoured.

With the aim of obtaining a detailed phase and morphological characterization of the dual microstructure of glass-ceramic sintered at 1220 °C, TEM and HRTEM measurements were performed. In Fig. 4a it is observed a TEM image showing the presence of microcrystal and a nanostructured region having nanoparticles in a glassy matrix. The nanoparticles size is quite homogeneous with an average diameter between 30 and 40 nm. Fig. 4b illustrates a HRTEM image performed in the boundary between a microcrystal (top left corner) and glassy-phase of the nanostructured region. The microcrystal is perfectly crystalline and the corresponding FFT pattern is showed in Fig. 4c. The crystallographic planes are indexed and the spots have been identified as (001) with an interplanar distance of 0.6780 nm and (002) planes with an interplanar distance of 0.3391 nm. These determined values are slight higher than those for pure albite, i.e. 0.6387 nm for (001) and 0.3194 nm for (002) [23]. This experimental data correlated with the existence of calcium and strontium in the Na-rich plagioclase structure that is responsible for the distortion of crystallographic planes. To observe the limits of the crystalized region, and inverse mask has been applied to the FFT image, selecting the (001) and (002) spots (Fig. 4c). Yellow colour in Fig. 4d represents zones with higher crystallinity while blue ones correspond to amorphous areas, where glassy-phase is located. A chemical disaggregation of the crystalline feldspar it is observed at the interphase in which Si/Al tetrahedral ring of the feldspar structure by breaking the structure in the basal plane perpendicular to the (001) crystalline direction. This fact allows explaining the dual microstructure formation mechanism as follow: during sintering process, elongated microcrystals start nucleating at 1100 °C (as it was observed by quenching experiments in Fig. 3). Microcrystals initially have straight edges, however glassy phase begins etching differentially the grain edges, which lead to form irregular curved edges (Fig. 3e and f) after being completed the sintering cycle. Finally, the nanoparticles nucleated in the surrounding glassy-phase due the compositional enrichment.

Therefore, according to these results, it is possible to conclude that albite-rich crystals are formed at temperatures > 900 °C, at which they still coexist with large amount of glassy phase that favors the cations diffusion. At 1100 °C long albite-rich crystals with straight edges are nucleated inside the frit grains, while glassy phase is surrounding them. Such crystals start being dissolved by glassy phase, forming irregular curved edges. Then, the nucleation of this glassy phase begins to form the nanoregions at ≈1220 °C around the microcrystals. These nanoregions continue growing and propagating throughout the sample during the dwell period, and probably during the cooling, which leads to the formation of the dual microstructure observed in the sample

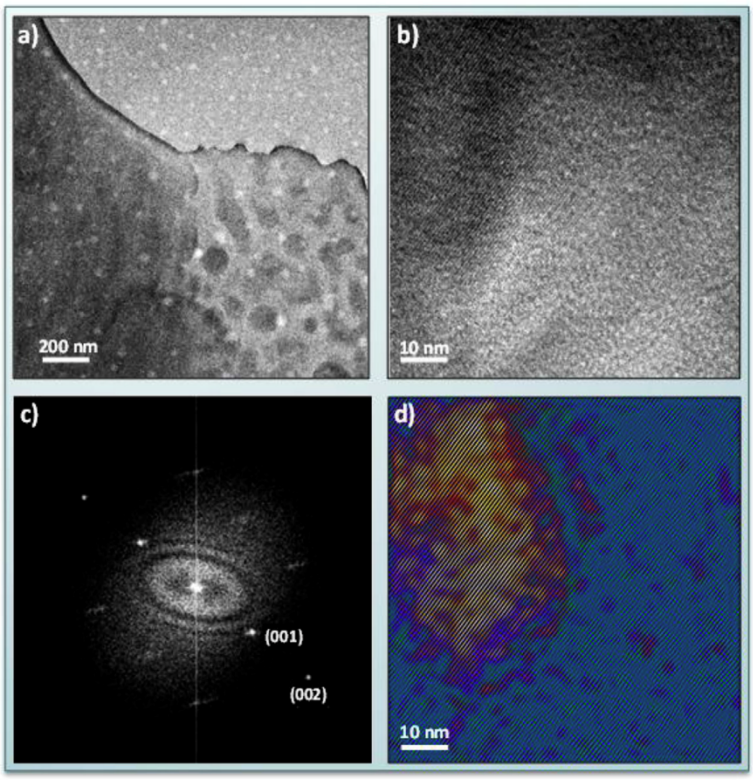

Fig. 4. a) TEM image of the Na-rich plagioclase glass-ceramic where nanoparticles/glassy matrix (right side) and a part of a microcrystal (left side) can be identified. **b)** HRTEM image of the interphase between the microcrystal and the glassy matrix. **c)** FFT microcrystal. The spots have been identified as (001) and (002) planes of an albite-rich structure. **d)** Inversed image achieved by selecting (001) and (002) spots of FFT image gathered on figure c). Yellow color represents zones with higher crystallinity while blue ones correspond to amorphous areas, where glassy phase is located. (For interpretation of the references to colour in this figure legend, the reader is referred to the Web version of this article.)

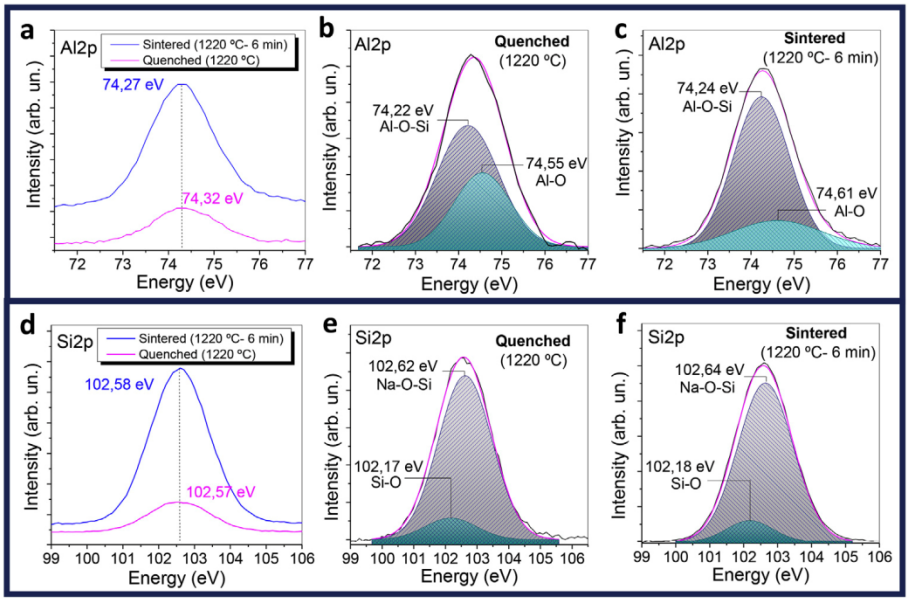

Fig. 5. High resolution XPS spectra of Al 2p (**a**, **b** and **c**) and Si 2p (**d**, **e** and **f**) for Na-rich plagioclase glass-ceramic sintered at 1220 °C, quenched or with a dwell time of 6 min. Deconvolution of each spectrum is shown in **b** and **e** for the complete sintered glass-ceramic and in **c** and **f** for quenched glass-ceramic.

subjected to the complete sintering cycle. Moreover, the glassy phase has been reduced to 6%, forming a highly crystalline albite-rich glass-ceramic. In addition, the nanoregions located around the crystals stop its growth during the cooling process, obtaining crystals with lower sizes, as seen in Fig. 3 e and f.

3.2. X-ray photoelectron spectroscopy (XPS) measurements

XPS gives information about the composition, chemical and electronic state of the element present in the material surface. However, in this work, samples were polished before measuring in order to be able to study the internal structure of the glass-ceramics and the formation reactions. Fig. 5 shows the high resolution XPS spectra of Al 2p (Fig. 5 a, b and c) and Si 2p (Fig. 5d, e and f) of Na-rich plagioclase glass-ceramic sintered at 1220 °C, both quenched and with 6 min dwelling, respectively. Fig. 5a presents the comparison of Al 2p signal of both samples having similar binding energy, which agrees well with typical values of sodium and calcium aluminosilicate feldspars (74.1–74.4 eV) [24,25], although binding energy for Al 2p signal slightly shifted (0.05 eV) in vitreous network. Fig. 5b and c shows the deconvolution of the Al2p signal for the quenched sample and the sintered one at 1220 °C 6 min, respectively, where it is observed two main contributions corresponding to the aluminosilicate bindings (~74.20 eV) and the octahedral aluminum oxide (~74.60 eV) [24,26]. The XPS spectra indicate that quenched glass-ceramic possesses larger contribution of oxide bindings (Al−O) than glass-ceramic sintered with a dwelling time of 6 min. These results corroborate that crystallization progress during the dwelling temperature and the cooling step of the sample. This larger contribution of aluminum oxide in the quenched Na-rich plagioclase may be related to the binding energy shifting of the total contribution of Al 2p signal. Additionally, there is a strong relationship between the coordination number of Al and the binding energy, that is, as larger the coordination number is, higher the binding energy will be. For this reason, octahedral aluminum oxide with a coordination number of 6, has larger binding energy than Al 2p signal in tetrahedra of $NaAlSi_3O_8$ and in lesser extent of $CaAl_2Si_2O_8$, where Al has coordination number of 4.

In the case of Si 2p signal, both the quenched and the sintered samples also possess similar binding energies (Fig. 5d). The deconvoluted spectra (Fig. 5e and f) show two main contributions associated with albite feldspar at 102.6 eV and with tetrahedral Si−O at 102.3 eV [27]. Both contributions are similar in relative proportion, which indicates that the major part of Si bonds corresponds to the formation of the Na-rich plagioclase feldspar and a small part to tetrahedral Si, probably corresponding to the glassy phase. Therefore, the Na−O−Si formation does not be largely affected by the quenching process, being formed these bonds before the cooling process of the thermal treatment. Signal position of main chemical species and FWHM for the XPS spectra are summarized in Table 3.

Fig. 6 shows high resolution XPS spectra of O 1s (Fig. 6 a and b) and Na1s (Fig. 6 c and d) for Na-rich plagioclase sintered at 1220 °C, quenched and with a dwell time of 6 min. In Fig. 6a it is observed a single peak for O 1s in both samples, however, lower binding energy (531.34 eV) is registered in quenched sample regarding the 6 min sintered (531.64 eV). In addition, the FWHM of these samples also evolves, being wider in the 6 min sintered glass-ceramic. These changes are related with oxygen coordination environments in each structure, being narrower when oxygen coordination is lower [26,28].

Table 3
Signal position of main chemical species and full width at half maximum (FWHM) of XPS spectra for both Na-rich plagioclase, sintered at 1220 °C, quenched and 6 min.

Sample sintered at 1220 °C	Al 2p		Si 2p		O 1s		Na 1s	
	Position (eV)	FWHM (eV)	Position (eV)	FWHM (eV)	Position (eV)	FWHM (eV)	Position (eV)	FWHM (eV)
Quenched	74.32	1.64	102.57	1.99	531.34	2.28	1070.83	1.81
6 min	74.27	1.64	102.58	1.93	531.64	2.35	1071.57	1.96

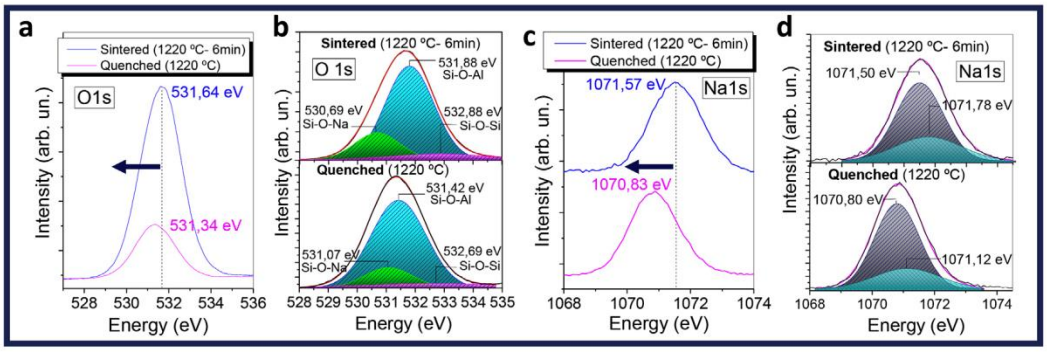

Fig. 6. High resolution XPS spectra of O 1s (**a** and **b**) and Ca 2p (**c** and **d**) for Na-rich plagioclase glass-ceramic sintered at 1220 °C, quenched or with a dwell time of 6 min. The corresponding deconvolution of each spectrum for both samples is shown in **b)** and **d)**.

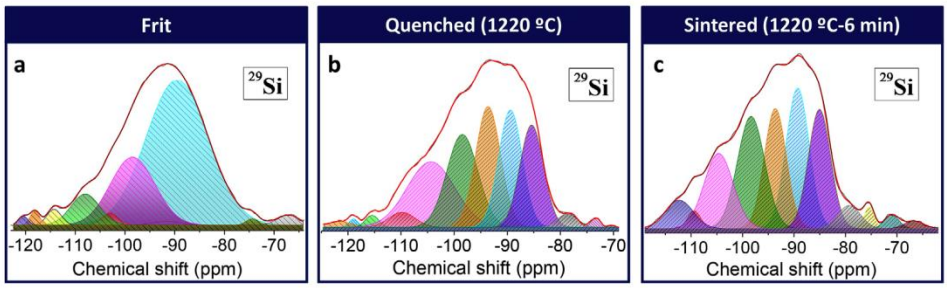

Fig. 7. ^{29}Si NMR spectra for **a)** the precursor frit; **b)** the quenched glass-ceramic at 1220 °C and **c)** the sintered glass-ceramic at 1220 °C 6 min. Deconvolution of ^{29}Si NMR spectrum of the frit shows the different polymerization state of Q_n units according to assignment of Table 4. In the case of quenched and sintered glass-ceramic, b) and c) respectively, the different Si neighbours are obtained and detailed in Table 5.

In the sodium aluminosilicate system, it is possible to find three components of O 1s signal, that is, three different oxygen environments, corresponding to Si−O−Si (~533 eV), Si−O−Al (~532 eV) and Si−O−Na (~531 eV). Fig. 6b shows the deconvolution of the O 1s signal in these 3 components for each sample, where it is possible to observe that the Si−O−Si bond suppose a low contribution in the system, since the main contribution is due to the Si−O−Al and Si−O−Na bonds. Sintered glass-ceramic at 1220 °C 6 min possesses larger proportion of Si−O−Na bonds than the quenched sample, which indicates higher crystallization of the Na-rich feldspar, and a wider FWHM, Table 3. This is also reflected in the chemical shift to lower binding energies of the quenched plagioclase, that indicates weaker bonds and therefore, lower feldspar crystallization. Fig. 5c shows the XPS spectra of Na 1s signal of both samples, where it is observed a significant shift to lower binding energies (0.74 eV) for quenched sample. This energy binding shift corroborates the nature of bonds and the crystallinity of the sample, that is, disorder structures as glass has lower binding energies than ordered crystalline phases. In addition, samples with non-bridging oxygens (NBO) also present lower binding energies. In Fig. 6d it is shown the deconvolution of the Na 1s peak, resulting two main contributions, one corresponding to the NBO (lower energies) and another one corresponding to modifying Na ions needed for charge balance during the process (higher energies) [29]. The Na 1s signal is placed in albite feldspars at 1072 eV [30,31], therefore, the albite-rich glass-ceramic sintered at 1220 °C 1 h fit this binding energy due to its higher crystallization, in comparison with the quenched sample that is a glassy phase, as it was discussed in section 3.2.

Therefore, as conclusions, XPS spectra of both samples with different thermal treatments present similar Al 2p and Si 2p binding energies and FWHM, indicating the formation of a sodium-rich aluminosilicates in both compounds, although Al 2p signal reveals larger amount of aluminosilicate bonds in the 1220 °C 6 min sintered sample. In case of O 1s and Na 1s signals, the binding energy is lower and the FWHM is shorter for quenched sample in comparison with sintered samples, indicating lower crystallinity and higher non-bridging bonds. These results suggest that the formation of the albite glass-ceramic, with high feldspar crystallinity requires a dwell sintering time and the cooling process to obtain both the dual microstructure and the high crystallinity.

3.3. NMR characterization

With the aim of deepening in the crystallization process undergone by the glass-ceramic and obtaining more precise information at short range, both compositionally and about order/disorder studies of the sintered feldspars NMR measurements were carried out.

^{29}Si has spin 1/2 and therefore does not suffer quadrupolar interactions, which makes it suitable to obtain information about electronic environment around Si sites. Fig. 6 shows the ^{29}Si NMR spectrum for the precursor frit (Fig. 7a), the quenched glass-ceramic at 1220 °C (Fig. 7b) and the sintered glass-ceramic at 1220 °C 6 min (Fig. 7c). ^{29}Si NMR spectrum of the frit exhibits a broad band in the range from −65 to −125 ppm with a maximum at ~ -92 ppm. This fact indicates that the frit might be mainly formed by a non-ordered calcium aluminosilicate in a glass structure having a Si/Al ratio between 1 and 2 [32]. Spectrum deconvolution allows distinguishing the different polymerization state in which silicon is found in the glass network. Peak positions are tabulated in Table 4 as well as the area contribution of each one and the corresponding Q_n species involved. Several works show that tetrahedra in glasses appear in more than one polymerization state, as occurs in our case [33]. Chemical shift values in the range from −66 to −74 ppm are assigned to Q_0 units in the ^{29}Si NMR spectrum. ^{29}Si NMR bands in the range −75 to −82 ppm correspond to Q_1 units and in the range −84 to −86 ppm correspond to Q_2 units. Q_3 units appear in the range of −90 to −101 ppm, while Q_4 groups provide ^{29}Si NMR peaks in the range from −103 to −120 ppm [34,35]. The area for each ^{29}Si NMR peak (Table 4) indicates that Q_3 species dominate the spectra, contributing with more than 85% of the total area.

In the plagioclase solid solution, the ordered end members, low albite and anorthite, have three resolved peaks in the ^{29}Si NMR

Table 4
Chemical shift (ppm), area contribution (%) and Q_n unit assignment for each deconvoluted band of the ^{29}Si NMR spectrum for the frit, plotted in Fig. 7a.

Chemical shift (ppm)	Area contribution (%)	Q_n unit assignment
−67.1	1.6	Q_0
−73.9	0.6	Q_0
−89.5	64.5	Q_3
−91.7	0.7	Q_3
−98.5	21.6	Q_3
−103.0	1.4	Q_4
−108.0	6.4	Q_4
−114.3	1.6	Q_4
−118.1	1.0	Q_4
−120.5	0.6	Q_4

Table 5
Chemical shift (ppm), area contribution (%) and site assignment for each deconvoluted band of the ^{29}Si NMR spectrum for the quenched glass-ceramic at 1220 °C and the sintered one at 1220 °C 6 min, plotted in Fig. 7b and c, respectively. Deconvoluted bands show the different Si neighbours in each sample. (*) indicates an anorthite-like site. Rest of tabulated positions between −89.3 ppm and −112.3 ppm corresponds to albite-like sites.

Quenched glass-ceramic		Sintered glass-ceramic		Site assignment
Chemical shift (ppm)	Area contribution (%)	Chemical shift (ppm)	Area contribution (%)	
–	–	−66.7	0.9	Q_0 unit (glass)
−70.3	0.1	−71.0	1.2	Q_0 unit (glass)
−73.3	0.6	–	–	Q_0 unit (glass)
–	–	−75.4	1.3	Q_1 unit (glass)
−78.6	1.7	−79.3	3.3	Q_1 unit (glass)
−85.4	15.8	−85.0	16.8	Q_4(4Al) (*)
−89.4	18.1	−89.3	20.5	T_2 (3Al)
−93.6	19.6	−93.6	16.7	T_{2m} (2Al)
−98.5	18.7	−98.3	19.2	T_{20} (1Al)
−104.4	20.3	−104.6	13.7	T_{1m} (1Al)
−109.8	2.6	−109.4	1.5	Q_4 unit (glass)
–	–	−112.3	4.9	T_1 (0Al)
−115.5	1.1	–	–	Q_4 unit (glass)
−119.0	0.5	–	–	Q_4 unit (glass)
−121.6	0.9	–	–	Q_4 unit (glass)

spectrum, corresponding to T_{1m},T_{20} and T_{2m} tetrahedral sites [36]. Generally, ^{29}Si NMR peaks in the range from −81 ppm to −92 ppm are characteristic of anorthite structure while peaks in the range from −92 ppm to −112 ppm are associated to low albite structure [37]. ^{29}Si NMR spectrum for 1220 °C sintered 6 min and quenched glass-ceramic exhibit a broad band approximately covering the ranges of −60 to −120 ppm and −70 to −125 ppm, respectively, indicating, therefore, that both albite and anorthite structures contributes to these spectra. In order to analyze in detail, ^{29}Si NMR spectra for both samples, deconvolution was carried out and the ^{29}Si NMR peaks were tabulated in Table 5. Area contribution of each one and the corresponding assignment are also included in the table.

In Fig. 7c, it might be observed the presence of five prominent peaks for the 1220 °C 6 min sintered glass-ceramic associated to Q_4 units and another six minor bands placed at both extremes of the spectrum. ^{29}Si NMR peak at ~ -85 ppm is associated to Q_4(4Al), typical of anorthite-like sites [36,37]. ^{29}Si NMR peak at ~ -89 ppm is also usually associated to Q_4(4Al) sites but overlaps with T_2(3Al) site of albitic structures, typically placed in the −87 to −91 ppm range in plagioclases [37]. The rest of main peaks placed at −93.6, −98.3, −104.6 ppm matches well with albite-like sites corresponding to T_{2m} (2Si, 2Al), T_{20} (3Si, 1Al) and T_{1m} (3Si, 1Al) positions, respectively [36–38]. In general, chemical shifts are strongly affected by composition [37]; thus, taking into account chemical shifts reported in the literature for different plagioclases [36] and peak positions obtained in this work (see Table 4), it may be concluded that the glass-ceramic synthetized is a sodic plagioclase with a composition between an oligoclase (> An23) and labradorite (An < 50) [36].Moreover, it is worth mentioning that chemical shifts may slightly differ from reported values because of the presence of some amount of Si/Al disorder and other elements in the starting frit, as strontium and in lesser extent potassium, which distortion the lattice, change bond distances and thus modify resonances. For this reason, composition might not be exactly defined. Considering the results previously discussed and that the area contribution of the peak at ~ −89 ppm is ~20%, the most prominent one, it is highly probable that this resonance, principally correspond to T_2(3Al) site of albite structure although a small contribution of Q_4(4Al) sites may also take place, overlapping it. Besides, another ^{29}Si NMR peak less intense associated to an albite-like site is found at −112.3 ppm, corresponding to T_1(0Al) site. Triclinic albite has four crystallographic non-equivalent tetrahedral positions known as T_{1o}, T_{1m}, T_{2o}, and T_{2m}. In the most ordered state, low albite, Si is placed in T_{1m},T_{2o} and T_{2m} sites while Al in T_{1o} and ^{29}Si NMR spectrum exhibit three bands of equal intensity, as it was discussed before [37]. However, the presence of additional broader peaks in Fig. 7b, with different intensity and higher overlapping indicate that Si neighbours have changed regarding an ordered state [39]. Moreover, the presence of T_2(3Al) and T_1(0Al) sites in albite-like domains corroborate that a slight Si, Al disorder distribution is presented. The rest of the peaks tabulated give a small contribution to ^{29}Si NMR spectrum and might be associated to the parent glass, according to Table 4 and the previous discussion of Fig. 6a. It is noticed mainly the presence of Q_1 units with a whole area contribution of 4.6% and in lesser extent Q_0 and Q_4 species with an area contribution of 2.0% and 1.5% respectively (see Table 5).

Quenched sample (Fig. 7b) exhibits approximately the same resonances registered in the sintered glass-ceramic (Fig. 7c) except for the presence of Si in T_1(0Al) positions, which confirms that the Na-rich plagioclase structure is formed on the heating, as it was previously discussed in section 3.2. Moreover, it presents a slight lower occupancy in T_2(3Al) sites in addition to the lack of T_1 (0Al) sites, which suggest that once glass-ceramic is complete sintered, larger degree of Si/Al disorder is favoured. Disorder in feldspars may cause the formation of larger amount of structural defects as Al−O−$\bar{}$Al or Si−O−Si linkages [40], two of the main luminescent centres in feldspars [41].Regarding glass site assignments, it is observed as the main area contribution is of Q_4 units, with a 5.1%, and in lesser extent Q_0 and Q_1 species, with 0.7% and 1.7%, respectively. However, in the sample complete sintered the main contribution is of Q_1 units, which clearly indicates that a reorganization of structural elements in the crystallized plagioclase lattice occurs during devitrification process.

In other works, it has been established that a change in the Si−O bond length of 0.001 Å produces difference in the chemical shift of ca. 1 ppm and a change of 1° in the Si−O−T (T = Si,Al) bond angle led to chemical shift changes of 0.3–0.9 ppm. Moreover, it can be established that the chemical shift observed between Si resonances indicates that, as expected, bonds are slightly modified after devitrification process on the cooling.

Thus, by means of NMR it is corroborated that a synthetic Na-rich plagioclase with low content of glassy phase and a certain Si, Al disorder have been obtained by means of compositional design and fast sintering treatment following a ceramic route. A sintering treatment at 1220 °C with a dwell time of 6 min and further cooling process, promotes a dual microstructure having a hierarchical ordering by combining devitrification of micro regions and high nucleation of crystals at the nanoregions. This unique microstructure opens the engineering of feldspar as high crystalline glass ceramic to tailor properties in which nanocrystal and microcrystal coexists.

4. Conclusions

In this work it is presented for the first time a synthetic Na-rich

plagioclase glass-ceramic obtained by a conventional ceramic procedure. Both, the chemical composition, using Sr and Ca as nucleating agents, and a fast sintering process lead to develop a unique highly crystalline and dual micro-nanostructure glass-ceramic.

The crystallization process reveals that crystallization of the Na-rich plagioclase occurs in two steps. Firstly, microcrystals devitrify on heating, in the range of 900–1100 °C, while nanocrystals start nucleating at 1220 °C in the glassy regions between microcrystals. Sintering treatment at 1220 °C for 6 min is required to develop a higher presence of nanoparticles and therefore to obtain a hierarchical micro-nanostructure of the glass-ceramic. Finally, ^{29}Si NMR measurements mainly show the contribution of Q_4(nAl) albite-like sites and in lesser extent some glass and anorthite-like sites, corroborating the formation of a sodic plagioclase structure. Analysis of Si environments for quenched glass-ceramic at 1220 °C and sintered at 1220 °C 6 min reveal that Si is placed in T1(0Al) sites only for the sintered sample, which suggest an increase of Si/Al disorder at short range after thermal treatment because of a structural reorganization during devitrification process.

This work may serve as a reference for future works in the field of glass-ceramic, since it demonstrates as microstructure could be engineered through a suitable crystallization process, which might be applied in the future to other glass-ceramic materials in order to tailor functionalities.

Acknowledgments

The authors express their thanks to the MINECO project MAT2017-86450-C4-1-R, and project CDTI of CTV for their financial support. Dra. E. Enriquez is also indebted to MINECO for a "Torres Quevedo" contract (ref: PTQ-14-07289), which is co-financed with European Social Funds.

References

[1] S.P. Chaudhuri, Crystallization of glass of the system - SiO, K20(Na20) - a1203, Ceram. Int. 8 (1982) 27–33.
[2] T.A. Khabas, V.V. Klimova, S.I. Starosvetskiy, A.P. Vasilyeva, M.A. Zvigintsev, Crystal phase formation in colored leucite-reinforced glass-ceramics for dental restorations, Inorg. Mater. Appl. Res. 8 (2017) 186–193, https://doi.org/10.1134/S2075113317010191.
[3] W. Flehmig, The synthesis of feldspars at temperature between 0°-80° C, their ordering behaviour and twinning, Contrib. Mineral. Petrol. 65 (1977) 1–9.
[4] I. Parsons, Feldspars and Their Reactions, Springer. Science + Business Media, B.V., Edinburgh, 1994, https://doi.org/10.1180/minmag.1995.059.397.23.
[5] J. Yuan, J. Yang, H. Ma, C. Liu, C. Zhao, Hydrothermal synthesis of analcime and hydroxycancrinite from K-feldspar in Na $_2$ SiO $_3$ solution: characterization and reaction mechanism, RSC Adv. 6 (2016) 54503–54509, https://doi.org/10.1039/C6RA08080D.
[6] E.S. Derkacheva, M.G. Krzhizhanovskaya, R.S. Bubnova, Thermal behavior of reedmergnerite NaBSi3O8 and searlesite NaBSi2O5(OH)2, Glas. Phys. Chem. 43 (2017) 459–463, https://doi.org/10.1134/S0087659617050030.
[7] S. Su, H. Ma, X. Chuan, Hydrothermal synthesis of zeolite A from K-feldspar and its crystallization mechanism, Adv. Powder Technol. 27 (2016) 139–144, https://doi.org/10.1016/j.apt.2015.11.011.
[8] E. Nyankson, J.K. Efavi, A. Yaya, G. Manu, K. Asare, R.Y. Abrokwah, Synthesis and characterisation of zeolite-A and Zn-exchanged zeolite-A based on natural aluminosilicates and their potential applications, Cogent Eng (2018) 200–202, https://doi.org/10.1080/23311916.2018.1440480.
[9] I. Buljan, C. Kosanovic, D. Kralj, A novel synthesis of nano-sized mullite from aluminosilicate precursors, J. Alloy. Comp. 509 (2011) 8256–8261, https://doi.org/10.1016/j.jallcom.2011.05.099.
[10] C. Liu, Epitaxy in the Crystallization of Feldspar Gels and Glasses, University Microfilms International, 1993, https://doi.org/10.1557/PROC-346-721.
[11] T.Y. Sablina, N.L. Savchenko, A.G. Mel'nikov, S.N. Kul'kov, Vacuum sintering of a ceramic based on zirconium dioxide, Glas. Ceram 51 (1994) 198–201, https://doi.org/10.1007/BF00682584.
[12] C. Liu, S. Komarneni, R. Roy, Epitaxy in the crystallization of feldspar gels and glasses, MRS Proc 346 (1994) 721, https://doi.org/10.1557/PROC-346-721.
[13] C. Liu, S. Komarneni, R. Roy, Crystallization of anorthite-seeded albite glass by solid-state epitaxy, J. Am. Ceram. Soc. 75 (1992) 2665–2670, https://doi.org/10.1111/j.1151-2916.1992.tb05486.x.
[14] P.H. Ribbe, H.D. Megaw, W.H. Taylor, R.B. Ferguson, R.J. Traill, The albite structures, Acta Crystallogr. B 25 (1969) 1503–1518, https://doi.org/10.1107/S0567740869004262.
[15] U. Selvaraj, C.L. Liu, S. Komarneni, R. Roy, Epitaxial crystallization of seeded albite glass, J. Am. Ceram. Soc. 74 (1991) 1378–1381, https://doi.org/10.1111/j.1151-2916.1991.tb04115.x.
[16] V. Fuertes, M.J. Cabrera, J. Seores, D. Muñoz, J.F. Fernández, E. Enríquez, Hierarchical micro-nanostructured albite-based glass-ceramic for high dielectric strength insulators, J. Eur. Ceram. Soc. (2018), https://doi.org/10.1016/j.jeurceramsoc.2018.02.009.
[18] J.J. Reinosa, D.M.Y. Marero, A. Del Campo, M.Á. De La Rubia, J.F. Fernández, Chemical analysis with high spatial resolution by rutherford backscattering and Raman Confocal spectroscopies: surface hierarchically structured glasses, J. Am. Ceram. Soc. 96 (2013) 1783–1788, https://doi.org/10.1111/jace.12397.
[19] J.J. Reinosa, F. Rubio-Marcos, E. Solera, M.A. Bengochea, J.F. Fernández, Sintering behaviour of nanostructured glass-ceramic glazes, Ceram. Int. 36 (2010) 1845–1850, https://doi.org/10.1016/j.ceramint.2010.03.029.
[20] D.O. Obada, D. Dodoo-Arhin, M. Dauda, F.O. Anafi, A.S. Ahmed, O.A. Ajayi, The impact of kaolin dehydroxylation on the porosity and mechanical integrity of kaolin based ceramics using different pore formers, Results Phys 7 (2017) 2718–2727, https://doi.org/10.1016/j.rinp.2017.07.048.
[21] L. Carbajal, F. Rubio-Marcos, M.A. Bengochea, J.F. Fernandez, Properties related phase evolution in porcelain ceramics, J. Eur. Ceram. Soc. 27 (2007) 4065–4069, https://doi.org/10.1016/j.jeurceramsoc.2007.02.096.
[22] J.J. Reinosa, B. García-Baños, J.M. Catalá-Civera, J.F. Fernández, A step ahead on efficient microwave heating for kaolinite, Appl. Clay Sci. 168 (2019) 237–243, https://doi.org/10.1016/j.clay.2018.11.001.
[23] P.H. Ribbe, H.D. Megaw, W.H. Taylor, R.B. Ferguson, R.J. Traill, The albite structures, Acta Crystallogr. Sect. B Struct. Crystallogr. Cryst. Chem. 25 (1969) 1503–1518, https://doi.org/10.1107/S0567740869004262.
[24] J. Wang, Z. Wang, L. Yang, G. Yang, C. Miao, P. Lv, Natural albite as a novel solid basic catalyst for the effective synthesis of biodiesel: characteristics and performance, Energy (2017), https://doi.org/10.1016/j.energy.2017.11.086.
[25] R. Golovchak, M.J. Davis, P. Vullo, A. Astashkin, L. Nichols, A. Ingram, H. Jain, The Charge State of Titanium Ions in Pd-Doped Ti: CMAS Glass and Glass-Ceramics, (2017), pp. 2568–2581, https://doi.org/10.1111/jace.14791.
[26] M. Todea, E. Vanea, S. Bran, P. Berce, S. Simon, XPS analysis of aluminosilicate microspheres bioactivity tested in vitro, Appl. Surf. Sci. 270 (2013) 777–783, https://doi.org/10.1016/j.apsusc.2013.01.178.
[27] X. Cui, Y. Cheng, H. Lin, F. Huang, Q. Wu, Y. Wang, Size-dependent abnormal thermo-enhanced luminescence of ytterbium-doped nanoparticles, Nanoscale (2017), https://doi.org/10.1039/C7NR04575A.
[28] M.F. Hochella, G.E. Brown, Aspects of silicate surface and bulk structure analysis using X-ray photoelectron spectroscopy (XPS), Geochem. Cosmochim. Acta 52 (1988) 1641–1648, https://doi.org/10.1016/0016-7037(88)90232-3.
[29] H. Bach, D. Krause, Analysis of the Composition and Structure of Glass and Glass Ceramics, Springer Science & Business Media, Mainz, Germany, 2014.
[30] H. Seyama, M. Soma, X-ray photoelectron spectroscopic study of the effect of heating on montmorillonite containing sodium and potassium cations, Clay Clay Miner. 34 (1986) 672–676.
[31] W. Wang, J. Cong, J. Deng, X. Weng, Y. Lin, Y. Huang, Developing effective separation of feldspar and quartz while recycling tailwater by HF pretreatment, Minerals 8 (2018) 1–15, https://doi.org/10.3390/min8040149.
[32] S. Lee, J. Stebbins, The degree of aluminum avoidance in aluminum silicate glasses, Am. Mineral. 84 (1999) 937–945, https://doi.org/10.2138/am-1999-5-630.
[33] A.R. Allu, S. Balaji, D.U. Tulyaganov, G.C. Mather, F. Margit, M.J. Pascual, R. Siegel, W. Milius, J. Senker, D.A. Agarkov, V.V. Kharton, J.M.F. Ferreira, Understanding the formation of CaAl2Si2O8 in melilite-based glass-ceramics: combined diffraction and spectroscopic studies, ACS Omega 2 (2017) 6233–6243, https://doi.org/10.1021/acsomega.7b00598.
[34] O. V Filonenko, V.S. Kuts, M.I. Terebinska, V. V Lobanov, Quantum chemical calculation of 29Si NMR spectrum of silicone dioxide fullerene-like molecules, Chem. Phys. Technol. Surf. 6 (2015) 263–268, https://doi.org/10.15407/hftp06.02.263.
[35] K.J.D. MacKenzie, E.S. Mark, Multinuclear Solid-State NMR of Inorganic Materials, (2002).
[36] R.J. Kirkpatrick, R.A. Kinsey, K.A. Smith, D.M. Henderson, E. Oldfields, High resolution solid-state sodium-23, aluminum-27, and silicon-29 nuclear magnetic resonance spectroscopic reconnaissance of alkali and plagioclase feldspars, Am. Mineral. 70 (1985) 106–123.
[37] R.J. Kirkpatrick, M.A. Carpenter, W.H. Yang, B. Montez, 29Si magic-angle NMR spectroscopy of low-temperature ordered plagioclase feldspars, Nature 325 (1987) 236–238, https://doi.org/10.1038/325236a0.
[38] W.H. Yang, R.J. Kirkpatrick, D.M. Henderson, High-resolution 29Si, 27Al and 23Na NMR spectroscopic study of Al-Si disordering in annealed albite and oligoclase, Am. Mineral. 71 (1986) 712–726.
[39] L. Sanchez-Muñoz, L. Nistor, G. Van Tendeloo, J. Sanz, Modulated structures in KAlSi3O8: a study by high resolution electron microscopy and 29Si MAS-NMR spectroscopy, J. Electron. Microsc. 47 (1998) 17–28, https://doi.org/10.1093/oxfordjournals.jmicro.a023555.
[40] Andrew Putnis, The crystal structure of minerals II- silicates, An Introd. to Miner. Sci, 1992, pp. 141–184, , https://doi.org/10.1017/CBO9781139170383.
[41] M. Pagel, V. Barbin, P. Blanc, D. Ohnenstetter, Cathodoluminescence in Geosciences, Springer-Verlag Berlin Heidelberg GmgH, New York, 2000.

ARTÍCULO 2. Structural insights of hierarchically engineered feldspars by Confocal Raman Microscopy.

V. Fuertes, A. del Campo, J. F. Fernández, E. Enríquez.

Journal of Raman Spectroscopy, 50 (5), 2019, 741-754.

Factor de impacto: 2,879 (según JCR Edition Science 2017).

Received: 26 October 2018 | Revised: 10 December 2018 | Accepted: 11 December 2018

DOI: 10.1002/jrs.5556

RESEARCH ARTICLE

WILEY Journal of RAMAN SPECTROSCOPY

Structural insights of hierarchically engineered feldspars by confocal Raman microscopy

V. Fuertes de la Llave[1] | A. del Campo[1] | J.F. Fernández[1] | E. Enríquez[2]

[1] Departamento de Electrocerámica, Instituto de Cerámica y Vidrio, Madrid, Spain

[2] Centro tecnológico Vidres, Castellón, Spain

Correspondence
Víctor Fuertes de la Llave, Departamento de Electrocerámica, Instituto de Cerámica y Vidrio, CSIC, Kelsen 5, 28049, Madrid, Spain.
Email: vfuertes@icv.csic.es

Funding information
European Social Fund, Grant/Award Number: CDTI (IDI-20130894) CDTI (IDI-20161120) MAT2017-86450-C4-1-R, Torres Quevedo contract (ref: PTQ- 14-07289); MINECO, Grant/Award Numbers: PTQ-14-07289, IDI-20161120, IDI-20130894 and MAT2017-86450-C4-1-R

Abstract

A structural and compositional characterization of fast-sintered Na-rich feldspar is carried out by means of the confocal Raman microscopy. The analysis of the main Raman modes (ν_a = 512 cm^{-1} and ν_b = 480 cm^{-1}) determines that feldspar crystallizations correspond to a sodic-plagioclase group, with an anorthite proportion estimated of 25–45%. The presence of alkali and alkaline earth in the formulated composition leads to albite type feldspar with slightly Al–Si disordered distribution in tetrahedral sites. Raman shift of the main Raman mode ν_a reveals differences in crystal stresses between nanograins and micrograins. The Rayleigh light-scattering microscopy shows up lamellar domains of ~2–3 μm resulting from unmixing by spinodal decomposition. Combining Raman spectroscopy and X-ray diffraction versus temperature significant structural changes are confirmed. This structural change correlates with a stress release and thermally activated conduction. This research gives fundamental understanding of structure, chemical composition, and micro-nanostructure of engineered glass–ceramics, which may allow tailoring them: for example, to modulate spinodal decomposition regions and interphases.

KEYWORDS

engineered, feldspars, feldspars, glass–ceramics, Rayleigh light-scattering microscopy, spinodal decomposition

1 | INTRODUCTION

Recently, a novel glass–ceramic material based on Na-rich albite type feldspar has been sintered having a high crystallinity, >94%, following a conventional ceramic process.[1–3] This material possesses a hierarchical micro-nanostructure in which nanostructured regions isolate micrograins. Nanostructured regions contain nanograins and rest of vitreous phase. All of these features favour scattering processes of phonon, photon, and electron in the material, which are the origin of low thermal conductivity, high ultraviolet, visible, and near infrared reflectivity[2] and the largest breakdown strength reported for a glass–ceramic material.[1,3] However, to a whole understanding of the excellent thermal, optical, and electric properties a complete characterization of the feldspar under study is necessary. The characterization of feldspars requires specifications of its chemical composition, the symmetry of the structure, and a characterization of the Al–Si order which may undergoes significant changes in the system when changes in temperature or pressure are produced.[4–6]

Regarding structure, it is important to know that albite ($NaAlSi_3O_8$) and anorthite ($CaAl_2Si_2O_8$) are the end-members of plagioclase feldspars. The framework of albite consists of rings of four tetrahedra, where each tetrahedron is centred by a Si^{4+} or an Al^{3+}, being the ratio Si^{4+}:Al^{3+} of 3:1. Each oxygen atom is located at the corners of each tetrahedron and links two tetrahedra. Albite

may be found with a triclinic (space group $C\bar{1}$) or monoclinic structure (space group C2/m), in which Al–Si order–disorder varies. In triclinic structure four symmetrically nonequivalent sites exists, designated as $T_1(0)$, $T_1(m)$, $T_2(0)$, and $T_2(m$; Figure 1), and only two in the monoclinic structure (T_1 and T_2). In the most ordered structure, known as low albite (Figure 1), which belongs to triclinic pinacoidal crystal system, Al is placed in $T_1(0)$ positions. However, albite has also three different high-temperature polymorphs, where Al and Si are distributed among the tetrahedral sites. When temperature increases, the disordering process begins; Al starts migrating to $T_1(m)$, $T_2(0)$, and $T_2(m)$ sites. In a perfect disorder state, 25% of Al is placed in $T_1(0)$ positions, and the other 75% is equally distributed between $T_1(m)$, $T_2(0)$, and $T_2(m)$ sites. The completely disordered triclinic albite is known as *high albite*, which stays triclinic despite being heated. Then, *analbite* is topochemically monoclinic ($T_1(0) = T_1(m) \geq T_2(0) = T_2(m)$), but still topologically

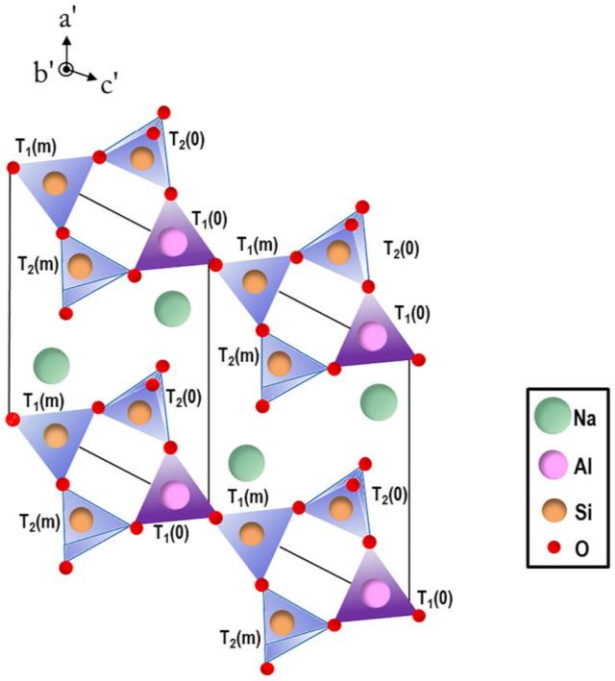

FIGURE 1 Low albite structure formed by rings of four tetrahedra, where each tetrahedron is centred by Si (orange atoms) or Al (pink atoms), with a Si/Al ratio of 3:1. Each oxygen atom (red atoms) links two tetrahedra. Sodium atoms appear in green. In triclinic structure, four symmetrically nonequivalent sites exists, labelled as $T_1(0)$, $T1(m)$, $T_2(0)$, and $T_2(m)$. In the most ordered structure, Al is in $T_1(0)$ sites. Regarding the Cartesian system XYZ, X-axis forms an angle of about 2° with the crystallographic axis, Y-axis approximately coincides with the b crystallographic axis, and Z-axis is almost perpendicular to the ab plane at ~26° from the C-axis. Adapted from the studies of Senderov and Meneghinello, Alberti, and Cruciani.[7,8] [Colour figure can be viewed at wileyonlinelibrary.com]

triclinic and undergoes a reversible phase transformation to monoalbite at 980°C (at 0.0001 GPa). Finally, *monoalbite*, which is the monoclinic and completely disordered polymorph that undergoes a symmetry change, but no change in composition.[4,7–11] In contrast, anorthite has a Si:Al ratio of 1:1 and an essentially Al–Si ordered structure (with space group $I\bar{1}$) except above 2000°C, at which disorder occurs ($C\bar{1}$ symmetry).[12] Al/Si distribution has been intensively studied in feldspars by X-ray diffraction (XRD), through the analysis of peak position[13–17] for reflections 2θ (131) and 2θ(1–31).

Concerning chemical composition, alkali feldspars have chemical compositions that form a solid solution, principally between the two end member of the compositions of orthoclase ($KAlSi_3O_8$) and albite ($NaAlSi_3O_8$), whereas plagioclase does it between the two end member of compositions of albite ($NaAlSi_3O_8$) and anorthite ($CaAl_2Si_2O_8$). In the case of intermediate plagioclases from albite to anorthite, substitution of Ca^{2+} and Al^{3+} by Na^+ and Si^{4+} takes place, as anorthite content increases, which has to maintain local charge balance and be compatible with Al–Si ordering scheme.[12] In this case, some disorders are typically presented, and for that reason, the structure of a Na-rich plagioclase might be considered to be similar to the albite structure shown in Figure 1 but with a higher population of aluminum in $T_1(m)$, $T_2(o)$, and $T_2(m)$ than in a low albite in addition to some distortion of angles and lengths of the bonds.[4] The synthesis of a pure phase feldspar is of high complexity, and if minerals are used as precursor, feldspar particles in a glass matrix are obtained.

When a solid solution is cooled below the solvus temperature, the phase separation, also termed exsolution or unmixing, occurs because is a more energetically favourable process.[12] Exsolution may occur by a process called spinodal decomposition compositional fluctuations whose amplitude grows by uphill diffusion.[18] Spinodal decomposition is an atomic level mechanism that leads to a coherent intergrowth of the phases involved. It has been used in a wide range of materials to improve their physical properties such as the following: thermoelectric materials, polymers, magnetic materials, and glasses, as well as feldspars.[12,19–23] If the end members have noticeably different structures, exsolution occurs by nucleation and growth of the exsolved phase.[24]

Compositional changes and Al–Si order in feldspars may act separately on the same sample; therefore, in a given sample, the degree of order and the composition must be determined to fully characterize the sample and develop new applications. Engineering materials based on synthetic feldspar with technological and industrial interest must require tailoring properties by both control of the chemical composition and the Al/Si order.

However, microstructure also plays a relevant role in material properties that also point out to evaluate the composition and order of feldspar in terms of microstructural analysis. For such reason, new techniques as the confocal Raman microscopy (CRM) are required in the study of engineered feldspars.

Raman spectroscopy is a powerful non-destructive characterization tool that is fast, offers high resolution, gives structural and electronic information, and allows phase identification of the material.[25] This technique when it is combined with confocal microscopy is also useful for measuring residual stresses in terms of Raman shift variation of the Raman modes[26] as well as determining the phase coexistence in complex systems. By using Raman spectroscopy and knowing accurately the microstructure, subtle spectrum alterations can be correlated with nanocrystals and microcrystals in the sample. Additionally, Raman measurements with temperature allow investigating phenomena such as Al, Si-O tetrahedral distortions due to Al, Si disorder, phase transitions or alkali/alkaline earth site ordering, and local distortion of Si-Al-O network.[4,5] Using the elastic scattering of light, areas with slight differences in refractive index or density might be discriminated in a sample, as a source of optical contrast, which allows to obtain more information about the chemical composition.[27–32]

In this context, the aim of this work is to further characterize the sintered Na rich-based glass–ceramic, paying especially attention to fundamental aspects such as chemical composition and thermal effect in Al–Si ordering of micro and nanocrystals regions. For this purpose, the CRM of sintered feldspars is used to discriminate between phonon response in the micro and nanostructured regions. Local compositional variations are studied by means of Rayleigh light-scattering spectroscopic microscopy, in order to evidence the formation of unmixing domains. Finally, the spectra evolution with temperature is used to reveal the possible Al–Si order–disorder.

2 | EXPERIMENTAL PROCEDURE

2.1 | Sample preparation

The Na-rich glass–ceramic material was prepared by a conventional ceramic process as described in previous works.[1] Chemical composition of precursors, Kaolin, and frit, is expressed in terms of equivalent oxides in Table 1. Composition having a ratio of 0.1 Kaolin and 0.9 frit were homogeneously mixed and then die pressed in disks of 2 mm in diameter, at 40 MPa. After pressing, the disks were thermally treated in an industrial furnace at 1220°C for 6 min with a 30°C min^{-1} heating rate, in a fast sintering cycle of 55 min in total. Once sintered, disks thickness was reduced to ~300 μm by polishing.

2.2 | Characterization

The powder XRD analyzes were recorded on an X'Pert PRO PANalytical diffractometer using Cu Kα radiation, 45 kV, 40 mA. Scan was carried out from 20 to 35° 2θ with a scan step size of 0.017° using a fast X'Celerator detector and an accumulation time of 500 s. Sample spinning and atmospheric air were used during the measurements. Measurements on heating were carried out from 40to 600°C in steps of 60°C.

Microstructural characterization was studied by means of field emission scanning electron microscopy (FESEM) S-4700, with a resolution of 1.5 nm at 15 kV). Grain size was evaluated by an image analyzer system Leika Qwin from micrographs of a representative surface. Raman spectroscopy using a Confocal Raman Microscope (Witec ALPHA 300RA) with a Nd: YAG laser light source (532 nm) in p-polarization was used. Optical resolution of this confocal microscope is, approximately, 250 and 700 nm in the longitudinal and transversal directions, respectively. Raman spectra were recorded in the spectral range of 0–1175 cm^{-1} by using a grating of 1,800 lines per millimetre resulting in a spectral resolution of the system below 0.02 cm^{-1}. Samples were mounted on a piezo-driven scan platform with a positioning accuracy of 3 nm in lateral and 1 nm in vertical directions. The reflected laser light at each point was collected using a multimode optical fibre of 25 μm in diameter by a very sensitive charge-coupled device detector. Raman images of sample were measured with a size 50 × 50 μm and each image content 130048 Raman spectra. Raman measurements at RT were performed using objectives of 20x and 100x with a numerical aperture of 0.40 and 0.95, respectively. In situ high-temperature Raman spectra were collected with the objective of NA 0.40, varying

TABLE 1 Composition of the glass–ceramic expressed as equivalent oxides

Oxides (wt%)	SiO_2	ZrO_2	SrO	Na_2O	K_2O	Al_2O_3	ZnO	CaO	Other*
Frit	54.67	1.24	7.20	2.14	1.44	22.63	1.27	7.73	1.68
Kaolin	55.49	—	—	—	1.21	42.48	—	0.17	0.65

Note. The minority components are all included in others.

*Others: TiO_2, Fe_2O_3, P_2O_5, MgO, and PbO. Each one lower than 1 wt%.

the temperature from 25 to 595°C with a heating rate of 2°C/min by using a LNP95 heating and cooling system from Limkam. Argon gas was used in order to purge the sample chamber and avoid condensation in the upper lid of the window surface. The acquired spectra were analyzed by using Witec Project 2.02 program and Witec Control Plus Software. To discriminate nanocrystals and microcrystals Raman band differences, a scanning with a fibre of 100 μm in diameter was carried out, and the exact band positions was obtained by fitting the peaks to Lorentzian function. Rayleigh light-scattering measurements were carried out by using the objective of 100x and the same Confocal Raman Microscope equipment previously explained, but the filter was removed during the measurement to gather photons elastic scattered. Detection is made by a back-illuminated 1,024 × 127 pixel charge-coupled device camera operating at −60°C. Raman images in this mode were measured with a size of 4 × 4 μm and 10 × 10 μm, and 130048 spectra for each image. Raman spectroscopy was used to analyze both the microstructural and the compositional characteristics. Elastic and inelastic scattering were used. The dominant type is elastic scattering or Rayleigh scattering, which does not involve energy transfer in the scattering event, and consequently, the scattered light has the same wavenumber as the incident light. The other type of scattering, inelastic one, takes place when energy is transferred in the scattering process, and the scattered light has a different wavenumber from the incident light. The position of the Raman shift peaks of each phase is very sensitive to the tensile or compression stress inside of the matrix in which is immersed.

3 | RESULTS AND DISCUSSION

3.1 | Structural analysis by XRD versus temperature

With the aim of exploring if the plagioclase-based glass–ceramic undergoes structural changes at long scale upon heating, XRD measurements with temperature were carried out. Figure 2a shows the XRD patterns in the range 21–34° 2θ for the plagioclase-based glass–ceramic upon heating from room temperature to 580°C, for different selected temperatures. Plagioclase was determined to be the major phase of the glass–ceramic, as shown the XRD pattern of Figure S1a. In the inset of Figure 2a, it might be observed that a shift ~0.5° towards lower 2θ occurs as temperature increases. This fact confirms an expansion of the crystal lattice at long-range scale accordingly with the thermal expansion of the material. At selected temperatures (Figure 2b), a study of Al, Si-O tetrahedral

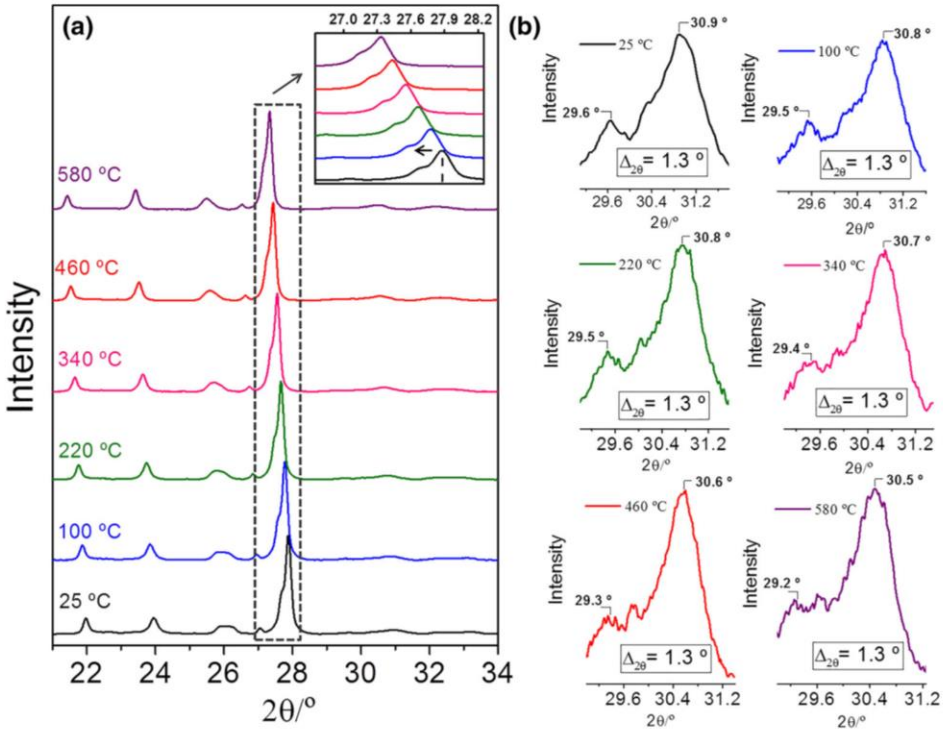

FIGURE 2 (a) X-ray diffraction patterns upon heating from room temperature until 580°C for a plagioclase-based glass–ceramic in the range 21–34° 2θ. The inset shows an X-ray peak shift towards lower 2θ as temperature increases; (b) enlargement of X-ray diffraction patterns showing in more detail the diffraction peaks (131) and (1–31) for each temperature. The value of $\Delta_{2\theta} = 2\theta_{(131)} - 2\theta_{(1-31)}$ is included for each temperature [Colour figure can be viewed at wileyonlinelibrary.com]

distortions with temperature might be carried out through the analysis of the diffraction peak positions for 2θ reflections (131) and (1–31) [13–16]. At room temperature, the diffraction peak (131) locates at 29.6° whereas (1–31) locates at 30.9°, which fits well with data reported in literature for low plagioclases.[33] The difference between both reflections, $\Delta_{2\theta}$, remains with a constant value of 1.3° 2θ during all the heating range, indicating that Al/Si distribution is not apparently modified by heating in this temperature range. As consequence, no significant structural changes are observed when the material is heating, which indicates a good stability for applications in which temperatures up to 600°C are involved.

3.2 | Micro-nanostructural characterization of the fast-sintered glass–ceramics

Figure 3a–c shows the FESEM micrographs of the polished and chemically etched glass–ceramic at different magnifications. In Figure 3a, the presence of localized microporosity is observed. Figure 3b and 3c reveals the hierarchical micro-nanostructure formed by elongated microcrystals surrounded by nanocrystal regions and separated from each other by glassy phase, which is located at the boundary. In the enlargement of Figure 3c, the nanostructured region marked may be elaborately observed.

In Figure 3d, a histogram is presented showing the nanocrystals diameter (violet), in addition to the width (red) and length (green) of the elongated microcrystals, measured from Figure 3b. The diameter size of nanocrystals range from 10 to 20 nm and microcrystals possess large grains, having 0.8–3 μm in length, 0.4–0.6 μm in width and aspect ratios in the range of 2–5. In addition, to further characterize the sample and obtain information about the composition of the fast-sintered glass–ceramic, an energy-dispersive X-ray spectroscopy (EDX) analysis is carried out (Figure S1b and Table S1) in a microstructured, a nanostructured, and a glassy phase region. EDX analysis evinces that glassy phase is richer in calcium than micro and nanoregions. Taking into account the larger amount of calcium than sodium in the precursors, it might be expected that the final composition was richer in calcium instead than in

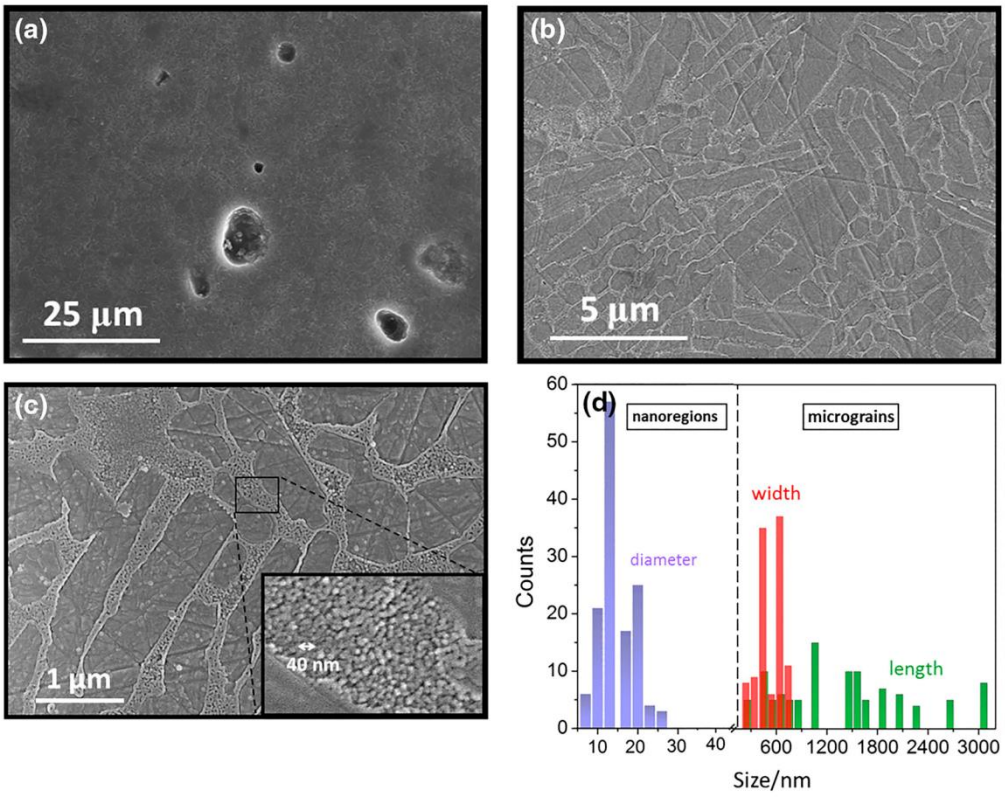

FIGURE 3 (a-c) Field Emission Scanning Electron Microscopy micrographs of the fast-sintering glass–ceramic sample at different magnifications. The enlargement showed in (c) display the detail of the nanostructured region. (d) Histogram showing the nanocrystals (violet) diameter as well as the width (red) and length (green) of elongated microcrystals [Colour figure can be viewed at wileyonlinelibrary.com]

sodium (Table S1). However, SrO plays an important role in the compositional evolution because it acts as glass network disruptor, favouring the formation of the sodium-rich aluminosilicate during the devitrification process, although the frit[34] only has a 2% of Na_2O. Thus, a considerable amount of calcium from the precursor frit goes into the glass formed although some considerable amount of it is presented in the crystallized structure, as it will be determined more precisely by the analysis of Raman spectrum in the next section.

3.3 | Confocal Raman microscopy of glass–ceramic feldspar

3.3.1 | Phase identification and Raman modes description

Figure 4 shows a confocal optical micrograph for the glass–ceramic feldspar in a representative area of the sample. It is possible to observe a similar surface than the one previously shown by FESEM (Figure 3). In the selected square marked in the micrograph, a Raman scanning was performed, which allows obtaining Raman image with the phase distribution (Figure 4b). It is possible to distinguish the major phase (depicted in red) identified as sodic plagioclase feldspar and a region of ~10 μm in diameter that correspond to pure albite phase (depicted in blue). In fact, from SEM–EDX analysis of supporting information, it is inferred that plagioclase is non-stoichiometric. This crystal of pure albite only appears in this scanned region, but it cannot be considered as widespread along the sample. Moreover, two grains, one of zircon (depicted in yellow) and another one of quartz (depicted in green) are also identified. The average Raman spectra of the Na-rich plagioclase and albite phases are represented in Figure 4c maintaining colours depicted in the Raman c image. Both Raman spectra present slight differences between each other, as it may be observed in Figure 4c. The albite phase has a Raman spectrum with two well-defined main Raman modes. This phase presents a similar spectrum to a pure albite mineral phase and agrees with the patterns obtained from RRUFF database for albite (R050253-3); for that reason, it is referred as albite crystal in this work. On the contrary, these Raman modes show a different relative intensity for the sodic plagioclase phase, which is the main crystallization of the glass–ceramic.

In general, Raman modes assignment in feldspars (included in Figure 4c) might be separated in five groups as follows: (a) Raman modes below 200 cm^{-1} are cage-shear modes; (b) Raman modes between 200 and 400 cm^{-1} are rotation–translation modes of the rings; (c) ring-breathing modes between 400 and 520 cm^{-1}; (d) deformation modes between 600 and 900 cm^{-1}; and (e) vibrational stretching modes between 900 and 1200 cm^{-1}

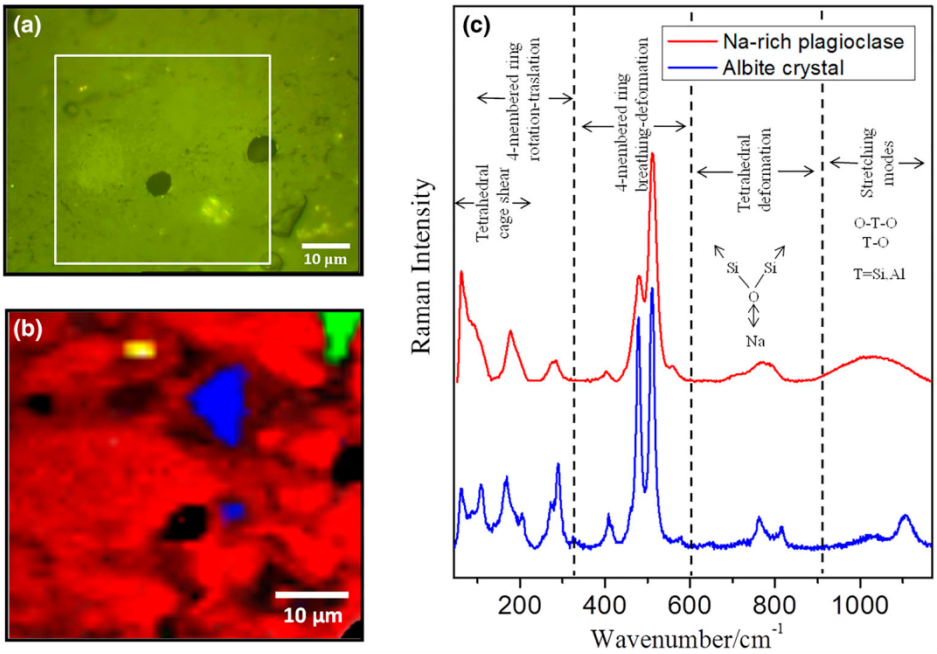

FIGURE 4 (a) Confocal optical micrograph of fast-sintered glass–ceramic; (b) Raman image of the selected area in (a) in which main phases are depicted in colours: Na-rich plagioclase as the major phase in red, albite crystal in blue and two grains of quartz in green and zircon in yellow; (c) Raman spectra of Na-rich plagioclase and albite crystal phases, including the vibrational assignment (adapted from the study of McKeown[11]) [Colour figure can be viewed at wileyonlinelibrary.com]

[7]. Raman spectrum of feldspars is easily recognized by the presence of two or three peaks located between 450 and 515 cm^{-1}. Only two Raman modes are observed in this range, at ca. 480 cm^{-1} (ν_b) and ca. 512 cm^{-1} (ν_a) for the sodium rich plagioclase phase and at ca. 479 cm^{-1} (ν_b) and ca. 509 cm^{-1} (ν_a) for the albite crystal, which indicates that the Si–O–Si and Si–O–Al bond angles are distributed in approximately two groups that give rise to these two Raman modes.[35] ν_b is mainly assigned to tetrahedral ring compression–expansion within the ***ab*** plane, and ν_a is assigned to a compression–expansion of four-membered ring along ***c***,[11] also contributing the translation of Na along ***ab*** plane and ***a***-axis, respectively, according to the system depicted in Figure 1.[7] Peak position of the strongest Raman mode has an inverse correlation with the size of the four-membered ring of tetrahedra. In the case of albite (Ab) end-member, this peak is typically placed at ~508 cm^{-1}, while in anorthite (An) end-member is placed at ~505 cm^{-1}. As it has been discussed, in the case of the Na-rich plagioclase-based glass–ceramic, this peak is at ca. 512 cm^{-1}, which indicates that the size of the four-membered tetrahedral rings is smaller than the corresponding one for albite end member.

By means of XRD, it is possible to determine the chemical composition[36,37]; however, the resolution of the obtained XRD diffractograms does not allow to attempt such procedure (see Figure S1a). Thus, further analyzes are required in this material by other techniques with larger resolution, as CRM. Bersani et al.[38] have recently reported a method to estimate the plagioclase composition taking into account the difference between the Raman shift of the most intense Raman mode ($\Delta_{ab} = \nu_a$-ν_b) and the linewidth or FWHM of the strongest one (Γ_a). Bersani et al.[38] observed that samples with $\Delta_{ab} < 27$ cm^{-1} have an anorthite content of >60 mol% whereas samples with $\Delta_{ab} > 27$ cm^{-1} have an anorthite content of <60 mol%. In the present work, $\Delta_{ab} = 32$ cm^{-1}, which would indicate that An is <60 mol%. In this regime, it can be applied in Equation 1. [38]

$$\text{An (mol\%)} = 4.26(24)\cdot\Gamma_a - 31.9(4.0) \quad (1)$$

Using $\Gamma_a = 18$ cm^{-1} in Equation 1, anorthite content of ~45 mol% is obtained. By means of this approximation, the deviation of the measurements in intermediate plagioclases is estimated to be up to 10%. To determine more accurately the composition of the sintered glass–ceramic, the peaks width and positions of the Raman spectra are compared with some plagioclases with different content of anorthite reported in the literature.[35,38] Thus, from a mineralogical point of view, the composition of the fast-sintered glass–ceramic is placed between an oligoclase (~An25) and an andesine (~An45).[35] As it was previously discussed, SrO plays an important role in the compositional evolution, favouring the formation of a sodium-rich aluminosilicate during the devitrification process. For this reason, the fast-sintered glass–ceramic is referred as Na-rich plagioclase feldspar-based or sodic plagioclase-based material.

The Raman modes description included in Table 2 explains briefly the main contributions to the atomic displacements based on attributions made in previous works.[7,8,11,39] Direction of motions follows the system depicted in Figure 1. Raman modes of the Na-rich plagioclase feldspar discussed in Figure 4c are included in Table 2 in the column of plagioclase micrograin; this designation will be discussed later in the manuscript. Most of these Raman modes tabulated in Table 2 vary regarding Raman modes for albite crystal, and some of them even do not appear, as it can be observed in Figure 4c and Table 2. Moreover, the broad Raman bands observed from 700 to 1170 cm^{-1} suggest the overlap of several internal vibration modes.[11] These differences observed may be caused by several factors such as compositional Al/Si disorder and the fact that plagioclase phase crystallize with a hierarchical microstructure (Figure 3). Moreover, the presence of rest of glassy phase at the nanoregions could produce stress gradient that contributed also to modification of Raman modes. Sodium plagioclases might be approximately considered as slightly disordered albite phase because the increase of Ca^{2+} and Al^{3+} over Na^{+} and Si^{+4}creates a structural disorder equivalent to the disorder introduced by annealing a low albite at higher temperature to produce an intermediate albite.[4] The disorder increase leads to change T–O (T = Si,Al) bonds regarding albite structure[4] and therefore modifying the wavenumber of Raman modes. However, although wavenumber of Raman modes is modified, their origin could be considered the same[7,11] because albite structure approximately remains unalterable,[4] as it is observed in Table 2. Comparing the results of this work with results reported by Tribaudino, Gatta, Aliatis, Bersani, and Lottici,[40] it can be concluded that only slight disorder exists at microscopic scale.

There are Raman shift differences in the Raman modes between the micrograins and the nanoregions. These differences require evaluating in more detail the microstructural dependence of the Raman modes with the composition.

3.3.2 | Microstructural characterization

According to the microstructure of the fast-sintered glass–ceramic[1] (Figure 3a) different distribution of stress could

TABLE 2 Raman modes measured for albite crystal and sodic plagioclase glass-ceramic for micrograins and nanoregions

Albite crystal (cm^{-1})	Sodic plagioclase micrograin (cm^{-1})	Sodic plagioclase nanoregions (cm^{-1})	Mode description
61.7	*61.7*	64.7	Translation of Na^+ along ***a*** and rigid rotation of SiO_4 tetrahedra[7]
87.7	*91.6*	91.6	Translation of Na^+ along ***a*** and rigid rotation of AlO_4,SiO_4 tetrahedra[7]
108.4	—	—	Overall structural compression–expansion in **bc** plane[11]
168.8	—	—	Na^+ translations and tetrahedral cages deformations[7]
—	177.8	178.1	Na^+ translations in tetrahedral cages||**b**[7]
204.5	—	—	Rigid translation of tetrahedra and Na + motion along **b** [7]
271.6	—	—	Tetrahedral cage rotation breathing[11]
290.5	280.2	280.8	Tetrahedral cage shear[11]
408.5	—	—	Deformation of AlO_4 tetrahedra[11]
478.2	479.7	479.7	Tetrahedral ring compression–expansion within the ***ab*** plane and Na translation along ***ab***[11]
509.3	511.7	510.7	Compression–expansion of four-membered ring along ***c*** and Na translation along ***a***[11]
761.4	771.5	771.5	Bending deformation of $T_2(0)$, $T_2(m)$ tetrahedra[7,11]
815.4	—	—	Si–O–Si bending[11]
1027.3	1027.9	1020.6	Antisymmetric stretching of the $T_1(m)$ and $T_2(0)$
1105.7	—	—	Antisymmetric stretching for all the SiO_4 tetrahedra[7]

Note. A short Raman mode description is also included, being explained the main contributions to the atomic displacements involved in the corresponding Raman modes.

be expected. These differences should generate subtle alterations in Raman spectrum. In order to identify the vibrational spectrum of both nanocrystals and microcrystals in this glass–ceramic material, a thorough scanning with a fibre of higher resolution (100 μm) was carried out, in a selected area of Figure 4.

Raman spectra in cyan and red of Figure 5a are respectively assigned to the nanoregions and micrograins, as it will be then discussed, and their Raman peaks are tabulated in Table 2. This assignment is made after analyzing the whole spectra of the dual microstructure. Some slight differences might be observed between each other, such as little differences of intensity in some Raman modes between nanoregions and micrograins. The strongest Raman mode, ν_a, is analyzed in detail in both Na-rich phases. It is noticed a red shift of the nanograins (ν_a at 510.7 cm^{-1}) regarding the micrograins (ν_a at 511.7 cm^{-1}), as it can be observed in Figure 5c and Table 2. Raman shifts of ν_a vary from 510.7 to 512 cm^{-1} are plotted in a Raman shift image, Figure 5b. Nanoregions represent zones that undergo a tensile stresses whereas microcrystal represents regions that undergo a compressive stresses.[26] The Raman shift image shows regions with higher Raman shift (yellow-orange coloured), which are bigger and can be associated to the micrograin regions of Figure 3, whereas lower Raman shift regions (cyan-green coloured) are more connected to the nanostructured regions of the fast-sintered glass–ceramics. The red shift of ν_a observed for nanocrystals is in agreement with tensile stress of small grains in glassy matrix that possesses a lower thermal expansion coefficient than the feldspar crystal. Taking into consideration that ν_a is related to compression–expansion of four-membered ring along **c**-axis and Na translation along ***a*** direction (according to the axis depicted in Figure 1), it may be concluded that tetrahedra in nanostructured areas experience an expansion in ***c*** direction whereas microstructured areas undergo a compression in this direction, all together with the corresponding translation of Na along ***a*** direction. On the contrary, the second strongest in intensity Raman mode, ν_b, remains unalterable, and therefore, tetrahedral rings

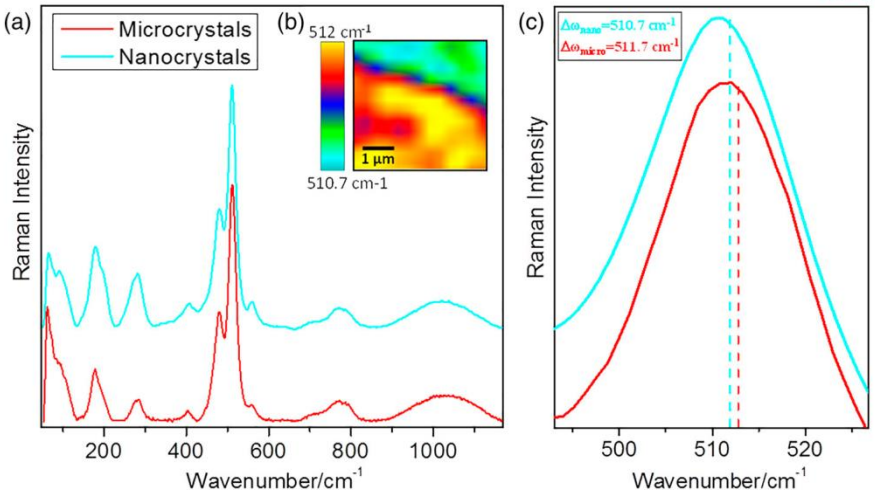

FIGURE 5 (a) Raman spectra of micrograins (red curve) and nanoregions (cyan curve); (b) Raman shift image of ν_a which varies from 510.7 to 512 cm^{-1} in a selected area of Figure 4a. Yellow-orange coloured zones are associated with micrograin regions while cyan-green coloured one to nanoregions. Nanocrystals suffer a red shift regarding microcrystals because of the tensile stress underwent by being immersed in the glassy phase, according to the microstructure of Figure 3; (c) enlargement of (a), showing the main Raman mode ν_a in detail, for both micrograins and nanoregions [Colour figure can be viewed at wileyonlinelibrary.com]

have no differences in ***ab*** plane between microcrystals and nanocrystals, being only affected ***c*** direction. Moreover, attending to the Raman shift variations inside of the micrograins, Figure 5b, additional compositional variations in addition to microstructural stresses generated in fast-sintered glass–ceramic feldspar can be intuited. This fact will be discussed in more detail in the following section.

3.3.3 | Rayleigh light-scattering microscopy

Exsolution processes are common in feldspars and very interesting to study because sometimes, interfaces formed between the separated phases improve the final properties of the composite material, as occurs in the case of spinodal decomposition.[41] The result of unmixing is a lamellar aggregate formed for lamellas with variable composition. These differences in composition produce changes in the refractive index, which may be used to identify them.[28]

Rayleigh light-scattering microscopy is attempted to verify if Raman shift variations observed might be caused by compositional differences or might be corresponded to stresses gradients. Figure 6a illustrates a Rayleigh image taken inside a micrograin that shows a striped pattern with bright and brown zones. Taking into consideration that refractive index for Ca-feldspars in the three-dimensional space (n_x = 1.57, n_y = 1.58, and n_z = 1.59) is higher than for Na-feldspars (n_x = 1.53, n_y = 1.53, n_z = 1.54),[42] it may be expected that Ca-rich domains will have a higher intensity of scattered light and thus will have lighter colours in Figure 6a and 6b

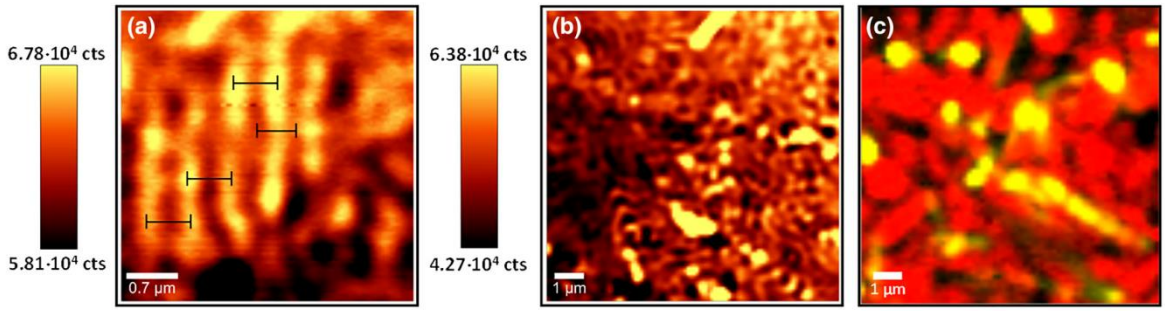

FIGURE 6 Rayleigh light-scattering microscopy images for: (a) micrograin region showing a striped pattern, and (b) nanostructured regions showing a sinusoidal disordered pattern. Lighter zones represent Ca-rich domains while darker zones Na-rich domains. (c) Raman image of (b) showing that in nanostructured areas zircon grains (in yellow) with different morphology and size are preferentially placed, in addition to Na-rich plagioclase phase (in red) [Colour figure can be viewed at wileyonlinelibrary.com]

than Na-rich domains. This pattern is typical of spinodal modulations with a periodicity of ~550 nm, Figure 6a. In lower symmetry minerals, only one or two compositional modulations are observed as occurs in feldspar with triclinic structure.[12] Unmixed domains are almost periodic and alternate zones with higher and lower refractive index produced by the compositional changes. The orientation of spinodal modulations is defined by the need of minimizing the elastic strain energy and hence corresponds to elastically soft orientations in the crystal. This spinodal decomposition observed confirms that effectively some compositional variations occur inside of microcrystals and for that reason Raman shift of ν_a mode varies up to 0.5 cm^{-1}, Figure 5b.

Figure 6b shows a Rayleigh image taken in a nanostructured region. On the contrary, in the nanostructured region, the bright and brown region does not form a pattern. In addition, the presence of black regions in which the Raleigh light-scattering is quite low and forms an incipient-disordered pattern. The differences between patterns indicate that spinodal decomposition occurs at the micrograins and therefore could be associated with the devitrification of the frit particles during the sintering process. Moreover, the presence of bright areas in the nanostructured region could be also related to phases of higher refraction index.

Raman image with higher resolution was taken in the nanostructured area of Figure 6b, and it confirms the presence of zircon grains with different morphology and size (Figure 6c). From this analysis, it seems that zircon grains are preferentially placed in nanostructured regions instead of inclusion in micrograins.

Lamellae pattern is microscopically observed only in some regions of the sample, being the size of the domains ~2–3 μm.[4] According to literature, lamellar structures in plagioclase feldspars are presented for three composition ranges: An_{1-25} (peristerite intergrowth), An_{46-60} (Bøggild intergrowth), and An_{67-90} (Huttenlocher intergrowth).[4] Information previously obtained by Raman spectroscopy indicates that this glass–ceramic material is a sodic plagioclase with ~25–45% of anorthite (~75–55% of albite). Therefore, the average percentage of anorthite in the sample is ~25–45%, and only some local regions may have different content, forming an intergrowth of peristerites or Bøggild, as it is illustrated in Figure 6. These findings would allow us tailoring the composition of the glass–ceramic by modifying the sintering cycle or/and the initial composition, to obtain more extended regions with spinodal decomposition. As a result, properties can be improved, and new one can be discovered, thanks to phenomena derived from interaction between both interphases such as phonon and photon scattering.

3.3.4 | Structural dependence with temperature: Raman spectroscopy

Raman spectroscopy versus temperature upon heating up to 595°C in steps of 15°C is attempted to determine if structural modification exists at local scale; in spite of at large scale, it does not occur, as reveals the result obtained from XRD versus temperature. Raman spectra for both micrograins and nanostructured regions are shown in Figure 7.

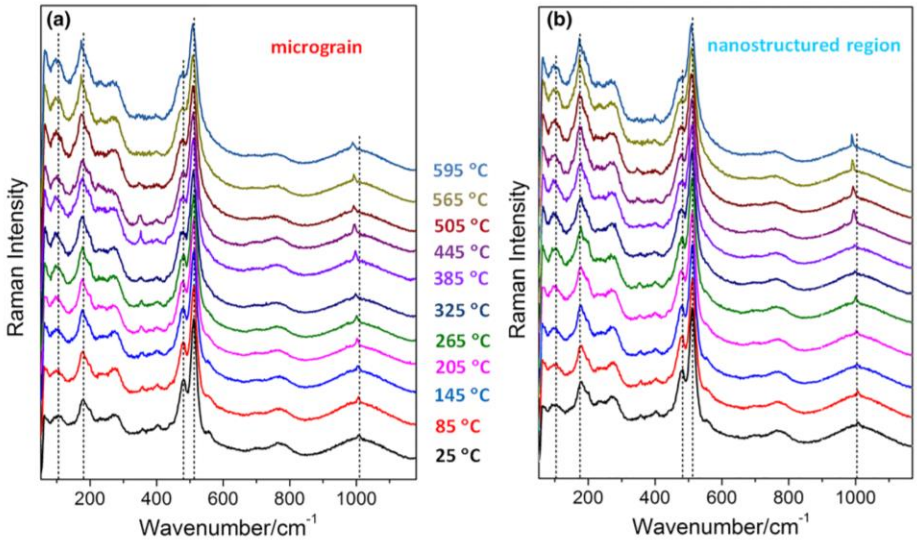

FIGURE 7 Raman spectra upon heating from room temperature up to 595°C for fast-sintered glass–ceramic feldspar in: (a) a micrograin and (b) nanostructured region [Colour figure can be viewed at wileyonlinelibrary.com]

Identification of micrograin and nanostructured region in the Raman spectroscopy versus temperature is obtained by the Raman shift of ν_a previously discussed. Raman modes situated at ca. 63 cm^{-1}, ca. 105 cm^{-1}, and ca. 179 cm^{-1} undergo a noticeable increase of their intensity, probably due to the increased thermal population effects, as reported McKeown[11] for a crystalline albite sample. By contrast, the Raman shift of these Raman modes is hardly modified. According to Table 2, in these Raman modes are involved cage-shear movements in which rotations of tetrahedral along with Na^+ translation take place. Taking into account that the electrical conductivity mechanism o of this material occurs by a hopping mechanism [1], it may be established that the temperature increase activates the diffusion process of cations with high mobility, such as Na^+ or Ca^{2+}, which strongly enhance the cage-shear modes of this material.[1,43] Raman modes between 600 and 900 cm^{-1} are softened, and therefore, the raise of temperature only reduces the force constant of the bond for tetrahedra as correspond to the increase in thermal agitation of the crystal. The broad Raman band from ~900 to 1165 cm^{-1}, in which several vibrational stretching modes of tetrahedral overlap is also slightly softened. Additionally, the zircon antisymmetric mode, located at ca. 1009 cm^{-1}, becomes to be better defined with temperature. However, the Raman modes most sensitive to temperature are the main Raman peaks, ν_a and ν_b, which undergo a red shift and a peak broadening as a consequence of lattice expansion. As reported McKeown,[11], e such Raman peak broadening, and possibly, the mode frequency shifts, are explained by the significant increase of the atomic thermal vibration parameters as temperature increases.

In sodic plagioclases, linewidth of ν_b is sensitive to changes in Al/Si order/disorder processes.[38] Therefore, a detailed study of the peak broadening evolution with temperature allows obtaining information about the order/disorder state on a local scale. Figure 8a and 8b show the peak broadening for micrograin and nanostructured regions versus temperature. It might be observed that ν_a undergoes a larger peak broadening ($\Delta\Gamma_a$) with temperature in nanograins ($\Delta\Gamma_a$~6 cm^{-1}) than in micrograins ($\Delta\Gamma_a$~4 cm^{-1}), as well as in the Raman mode ν_b (Figure 8b), where the peak broadening ($\Delta\Gamma_b$) is ~8.5 cm^{-1} in the nanograins and ~6.5 cm^{-1} in micrograins. Peak broadening of Raman mode ν_a may be fitted to a parabolic expression, as it is observed in Figure 8a, following a multi-phonon interaction, which is based on an harmonic approximation with the temperature dependence showed in Equation 2 [4]:

$$\gamma_a = AT + BT^2 \quad (2)$$

Where γ_a is the damping factor and measured through $\Delta\Gamma_a$, A and B are constants of the fitting, and T is the temperature. The damping factor for ν_a in the microcrystals and nanocrystals is very similar, $\gamma_{micro} = 6.01{\cdot}10^{-3}\ T + 1.95{\cdot}10^{-6}\ T^2$ and $\gamma_{nano} = 8.56{\cdot}10^{-3}\ T + 3.28{\cdot}10^{-6}\ T^2$, taking into account that the error of the fitting is ~3% for microcrystals and ~2% for nanocrystals. A similar temperature dependence was observed by Salje[5] in a previous work for an Amelia low albite sample and an analbite sample.

Peak broadening of Raman mode ν_b, which is more sensitive to ordering–disordering processes, follow a different trend, as it is observed in Figure 8b. It may be

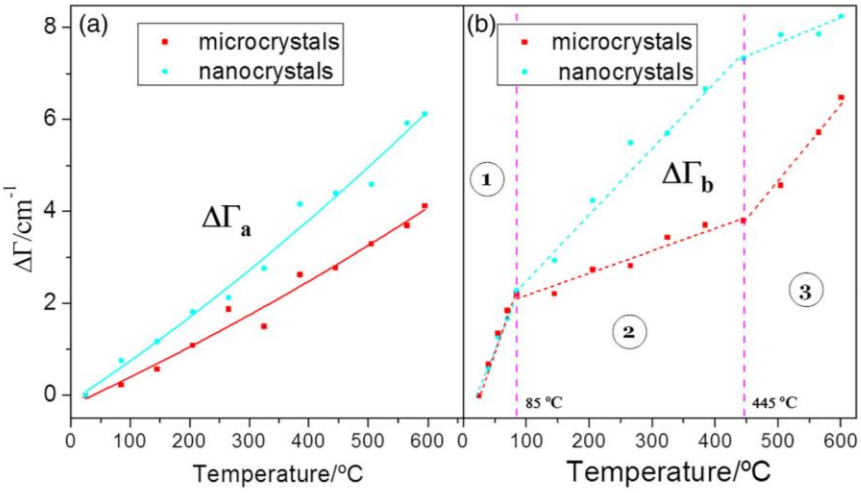

FIGURE 8 Peak broadening ($\Delta\Gamma$) versus temperature (°C) for the main Raman modes, ν_a and ν_b; (a) $\Delta\Gamma_a$; (b) $\Delta\Gamma_b$, respectively, in microcrystals (red squares) and nanocrystals (cyan circles) because of the temperature effect. $\Delta\Gamma_a$ might be fitted to a quadratic equation, while $\Delta\Gamma_b$ to three linear equations because of the presence of three regions well differentiated [Colour figure can be viewed at wileyonlinelibrary.com]

observed three regions well-differentiated where $\Delta\Gamma_b$ approximately follows a linear trend in each one. In this case, the damping factor of this mode, γ_b, might be fitted to Equation 3:

$$\gamma_b = C + DT \quad (3)$$

Where C and D are fitting constants, which take different values as a function of the temperature interval. For microcrystals, $\gamma_{micro} = -0.84 + 3.80\cdot10^{-2}\ T$ for $25°C \leq T \leq 85°C$, $\gamma_{micro} = 1.69 + 5.17\cdot10^{-3}\ T$ for $85°C \leq T \leq 445°C$, and $\gamma_{micro} = -4.12 + 1.78\cdot10^{-1}\ T$ for $445°C \leq T \leq 600°C$. For nanocrystals, $\gamma_{nano} = -0.93 + 3.86\cdot10^{-2}\ T$ for $25°C \leq T \leq 85°C$, $\gamma_{nano} = 1.18 + 1.47\cdot10^{-2}\ T$ for $85°C \leq T \leq 445°C$, and $\gamma_{nano} = 5.17 + 5.37\cdot10^{-3}\ T$ for $445°C \leq T \leq 600°C$. These results might be summed up as follows: The peak broadening of both, microcrystal, and nanocrystal follows the same trend up to 85°C (region 1 in Figure 8b), even overlapping both fittings. From this temperature, $\Delta\Gamma_b$ grows faster in nanocrystals than in microcrystals in all the temperature range, as occurred for mode ν_a (Figure 8a). Moreover, it is noticed that the behaviour undergone by nanocrystals in region 2 is the same as the behaviour undergone by microcrystals in region 3. The same occurs in region 3, where nanocrystals exhibit a slope approximately equal than microcrystals in region 2. Therefore, these results reveal that $\Delta\Gamma_a$ has a similar behaviour in microstructured and nanostructured regions and it may be understood in a harmonic approximation. However, $\Delta\Gamma_b$ shows that temperatures affect both regions in a different way and different contributions should be considered, although the vibrational behaviour with temperature might be understood in a linear approximation.

The annealing effect in albite samples is widely studied in literature.[5,11] However, our system is more complex, as it was previously discussed because of the following: the considerable amount of Ca^{2+} and in lesser extent K^+, which introduces some Al/Si disorder; hierarchical microstructure; and the presence of other minor phases such as glassy phase, zircon, and quartz. The peak broadening observed, up to 10 cm^{-1}; it is not excessive to be attributed to a purely disorder process where Al–Si–O tetrahedral distortions are presented, in comparison with other feldspars reported in the literature[5,8] or with others minerals like nesosilicates.[44] Michel, Colomban, Abolhassani, Voyron, and Kahn-Harari[44] reported that the difference of the FWHM between a sillimanite (fully ordered) and a germanium mullite (disordered) was higher than 20 cm^{-1}.Therefore, Al–Si disorder does not seem to be the main source of such broadening. This suggests that changes of stresses in the system (see red shifts of Figure 7) between microcrystals and nanocrystals as well as the mobility of cations,[5] mainly Na and Ca, play an important role when temperature activates their diffusion mechanism, namely, concerning to tetrahedra in the ab plane, because it has been proved that ν_b is more sensitive to temperature changes. In previous work,[1] it was proved that this material undergoes an increase of conductivity from ~400°C, which is based on an ionic conduction mechanism where sodium cations are the dominant charge carriers although calcium cations also contribute. Thus, mobility of alkali and alkaline-earth cations seem to be the main source of such broadening in region 3 (Figure 8b) although the readjustment of structural stresses may also contribute to this region and mainly to region 2. Moreover, several authors reported that a displacive phase transition occurs in alkali-feldspar[5,6] at about 200–250°C. Salje[5] observed a marked break of the Raman intensity versus temperature at 250°C, for ν_a and ν_b, in a fully disordered albite. The same study is carried out in the Na-rich plagioclase-based glass–ceramic, and it is showed in Figure S2. In our work, a linear temperature dependence of the intensity is observed in all the temperature range studied. This can indicate that any displacive transition takes place in the temperature range measured, up to 600°C. However, this kind of transition only occurs in fully disordered samples. In Section 3.1 and 3.3.1, it was observed that Si–Al distribution is only slightly disordered at large scale and at microscopic scale. Therefore, it is confirmed that only small Si–Al disorder exists, and any transition is expected at higher temperature.

Comparing these values with other results reported in albite natural samples under annealing,[5,8] it is observed a completely different behaviour indicating that the unique hierarchical micro-nanostructure of fast-sintered engineered feldspar along with considerable compositional variations, and the presence of different phases provides a different phonon scattering processes than in mineral feldspar.

4 | CONCLUSIONS

Fast-sintered Na-rich feldspar-based glass–ceramic has been thoroughly studied both structurally and compositionally by CRM. According to the features of the Raman spectra, a sodic-plagioclase is determined to be the major crystallization, with an anorthite proportion of 25–45%, and with Al–Si slightly disordered distribution in tetrahedral sites. A red shift of 1 cm^{-1} for the main Raman mode, ν_a, is observed in nanograins regarding micrograins, which is attributed to tensile stresses generated in nanostructured regions by the occurrence of glassy phase. XRD and Raman spectroscopy versus

temperature does not show structural changes at a large scale upon heating, up to 600°C, but it does at microscopic scale, mainly related to stress release and thermal activation of electrical conductivity mechanism. Moreover, it is observed that main Raman modes, ν_a and ν_b, undergo a more complex behaviour in comparison with albite-type mineral. In fast-sintered feldspars, several factors are revealed: the hierarchical microstructure; the presence of minor phases such as glassy phase, zircon, and quartz; and the considerable amount of divalent cations (Ca^{2+}, Sr^{2+}) and in lesser extent K^+, which introduces Al/Si disorder in tetrahedral sites. Furthermore, Rayleigh light-scattering microscopy shows that unmixing processes occur by spinodal decomposition, forming lamellar domains ~2–3 μm.

This research provides fundamental insight of structure, chemical composition, and micro-nanostructuration in fast-sintered feldspars, which might allow tailoring their unique properties. Moreover, the findings show a strategy in order to modulate spinodal decomposition regions and interphases in engineered feldspar, with a view to future applications in electrical, optical, and mechanical field.

ACKNOWLEDGEMENTS

The authors express their thanks to the MINECO (Spain) project MAT2017-86450-C4-1-R, and projects CDTI (IDI-20130894 and IDI-20161120) for their financial support. Dra. E. Enriquez is also indebted to MINECO for a "Torres Quevedo" contract (ref: PTQ- 14-07289), which is co-financed with European Social Funds. The authors also thank to Dr. A. Moure for the scientific discussion carried out about results explained in this manuscript.

ORCID

V. Fuertes de la Llave https://orcid.org/0000-0003-2201-1360

REFERENCES

[1] V. Fuertes, M. J. Cabrera, J. Seores, D. Muñoz, J. F. Fernández, E. Enríquez, *J. Eur. Ceram. Soc.* **2018**, *38*, 2759.

[2] E. Enríquez, V. Fuertes, M. J. Cabrera, J. Seores, D. Muñoz, J. F. Fernández, *Sol. Energy* **2017**, *149*, 114.

[3] V. Fuertes, M. J. Cabrera, J. Seores, D. Muñoz, J. F. Fernández, E. Enríquez, *J. Eur. Ceram. Soc.* **2019**, *39*, 376.

[4] I. Parsons, Feldspars and their reactions, **1994**.

[5] E. Salje, *Phys. Chem. Miner.* **1986**, *13*, 340.

[6] Y. Yang, Z. P. Wang, Z. Z. Tian, Q. K. Xia, G. W. Li, *Phys. Chem. Miner.* **2016**, *43*, 111.

[7] I. Aliatis, E. Lambruschi, L. Mantovani, D. Bersani, S. Andó, G. Diego Gatta, P. Gentile, E. Salvioli-Mariani, M. Prencipe, M. Tribaudino, P. P. Lottici, *J. Raman Spectrosc.* **2015**, *46*, 501.

[8] I. Aliatis, Vibrational dynamics and structure of natural feldspars.

[9] E. E. Senderov, *Phys. Chem. Miner.* **1980**, *6*, 251.

[10] E. Meneghinello, A. Alberti, G. Cruciani, *Am. Mineral.* **1999**, *84*, 1144.

[11] D. A. McKeown, *Am. Mineral.* **2005**, *90*, 1506.

[12] A. Putnis, An introduction to mineral sciences, **1992**, pp. 141–184.

[13] R. T. Downs, R. M. Hazen, L. W. Finger, *Am. Mineral.* **1994**, *79*, 1042.

[14] D. B. Stewart, P. H. Ribbe, *Am. J. Sci.* **1969**, 444.

[15] C. T. Pnbwttt, S. Surnol, J. J. Paprrp, *Am. Mineral.* **1976**, *61*, 2.

[16] H. Kroll, W. F. Mfiller, *Phys. Chem. Miner.* **1980**, *5*, 255.

[17] H. Kroll, *Am. Mineral.* **1980**, *65*, 449.

[18] E. P. Favvas, A. C. Mitropoulos, *J. Eng. Sci. Technol. Rev.* **2008**, *1*, 25.

[19] J. Androulakis, C. H. Lin, H. J. Kong, C. Uher, C. I. Wu, T. Hogan, B. A. Cook, T. Caillat, K. M. Paraskevopoulos, M. G. Kanatzidis, *J. Am. Chem. Soc.* **2007**, *129*, 9780.

[20] K. Sato, H. Katayama-Yoshida, P. H. Dederichs, *Jpn. J. Appl. Phys.* **2005**, *44*, Part 2, 28.

[21] D. Julthongpiput, W. Zhang, J. F. Douglas, A. Karim, M. J. Fasolka, *Soft Matter* **2007**, *3*, 613.

[22] M. Suzuki, T. Tanaka, *High Temp. Mater. Process.* **2012**, *31*, 323.

[23] M. Goldstein, *J. Am. Ceram. Soc.* **1965**, *48*, 126.

[24] M. A. Carpenter, *Contrib. To Mineral. Petrol.* **1980**, *71*, 289.

[25] C. M. Álvarez-Docio, J. J. Reinosa, A. Del Campo, J. F. Fernández, *J. Alloys Compd.* **2019**, *779*, 244.

[26] J. J. Reinosa, A. del Campo, J. F. Fernández, *Ceram. Int.* **2015**, *41*, 13598.

[27] S. Su, P. H. Rrssn, *Am. Mineral.* **1986**, *71*, 1393.

[28] L. Sánchez-Munõz, A. Del Campo, J. F. Fernández, *Sci. Rep.* **2016**, *6*, 1.

[29] N. N. Boustany, S. A. Boppart, V. Backman, *Annu. Rev. Biomed. Eng.* **2010**, *12*, 285.

[30] M. Havel, P. Colomban, *Compos. Part B Eng.* **2004**, *35*, 139.

[31] M. Havel, P. Colomban, *J. Raman Spectrosc.* **2003**, *34*, 786.

[32] P. Colomban, M. Havel, *J. Raman Spectrosc.* **2002**, *33*, 789.

[33] I. Y. Borg, D. K. Smith, Geological Society of America Memoirs, **1969**, pp. 639–641.

[34] E. Enríquez, J. F. Fernández, M. Á. García, M. J. Cabrera, J. Seores, F. J. Villar, J. J. F. de Mora, Pat *EP15382162.4*.

[35] J. J. Freeman, J. John, K. E. Alian Wang, L. A. H. Kuebler, *Can. Mineral.* **2008**, *46*, 1477.

[36] J. V. Smith, *Mineral. Mag.* **1955**, *31*, 47.

[37] J. Goodyear, *Mineral. Mag.* **1954**, *30*, 306.

[38] D. Bersani, I. Aliatis, M. Tribaudino, L. Mantovani, A. Benisek, M. A. Carpenter, G. D. Gatta, P. P. Lottici, *J. Raman Spectrosc.* **2018**, *49*, 684.

[39] M. Zhang, B. Wruck, A. Graeme Barber, E. K. H. Salje, M. A. Carpenter, *Am. Mineral.* **1996**, *81*, 92.

[40] M. Tribaudino, G. D. Gatta, I. Aliatis, D. Bersani, P. P. Lottici, *J. Raman Spectrosc.* https://doi.org/10.1002/jrs.5490

[41] M. U. Kim, J. P. Ahn, H. K. Seok, E. Fleury, H. J. Chang, D. H. Kim, P. R. Cha, Y. C. Kim, *Met. Mater. Int.* **2009**, *15*, 193.

[42] H. L. Alling, *J. Geol.* **2015**, *62*, 360.

[43] M. S. I, M. M. A. Jones, D. Palmer, *Phys. Chem. Miner.* **2004**, *31*, 313.

[44] D. Michel, P. Colomban, S. Abolhassani, F. Voyron, A. Kahn-Harari, *J. Eur. Ceram. Soc.* **1996**, *16*, 161.

SUPPORTING INFORMATION

Additional supporting information may be found online in the Supporting Information section at the end of the article.

How to cite this article: Fuertes de la Llave V, del Campo A, Fernández JF, Enríquez E. Structural insights of hierarchically engineered feldspars by confocal Raman microscopy. *J Raman Spectrosc.* 2019;50:741–754. https://doi.org/10.1002/jrs.5556

Structural insights of hierarchically engineered feldspars by Confocal Raman Microscopy

V. Fuertes*[1], A. del Campo[1], J. F. Fernández[1], E. Enríquez[2]

[1]Dept. Electrocerámica, Instituto de Cerámica y Vidrio, CSIC, Kelsen 5, 28049, Madrid, Spain.

[2]Centro tecnológico Vidres, S.L., Ctra. Onda, Km 3.4, 12540 Villareal, Castellón, Spain

Supporting information

Figure S1a shows the XRD pattern of the glass-ceramic studied. The major phase presented is a plagioclase phase, while tetragonal SiO_2 is also identified. Plagioclase phase may correspond to a Na-rich plagioclase (JCPDS Card no. 00-041-1480) or a Ca-rich plagioclase (JCPDS Card no. 00-041-1481). Due to the similarity of both XRD patterns and the overlap of XRD peaks, it cannot be precisely identified by this technique if the major phase is a sodium-rich (albite) or a calcium-rich (anorthite) plagioclase. To overcome difficulties in phase identification, Confocal Raman Microscopy is used in the manuscript, since it allows discriminating between both compositions.

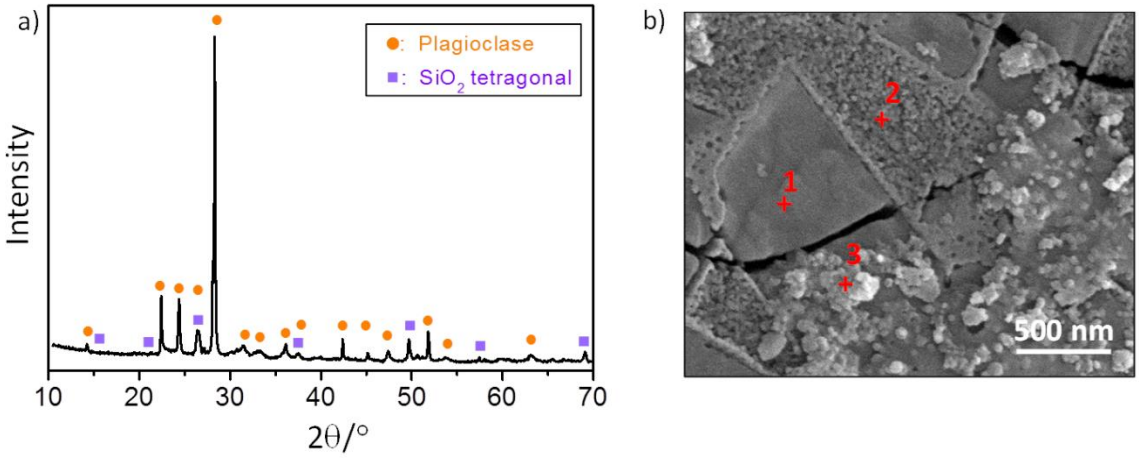

Figure S1. **a)** XRD pattern and **b)** FESEM micrograph for the fast-sintering glass-ceramic sample. EDX analysis was carried out in a microregion, a nanoregion and in a glassy-phase region, which correspond with the marked points in b), respectively. Oxide composition (%) is included in table S1.

Figure S1b shows a FESEM micrograph in a zone of the sample in which a microregion, a nanoregion and a glassy-phase region can be observed. Chemical etching was not carried out in a region of the sample, in order to accurately analyse the composition of glassy phase. The EDX analysis in the marked points of figure S1b, reveals that the oxide composition (table S1) of the glassy phase (point 3) is richer in CaO than the micro (point 1) and nanostructured region (point 2), while Na_2O is around the triple in the last two regions. Therefore, although the precursor frit has a higher amount of CaO than Na_2O, it is favoured the crystallization of a Na-rich plagioclase instead of a Ca-rich one, after devitrification process, thanks to the presence of SrO in the precursor frit, which acts as lattice disruptor. From these results, it is inferred that plagioclase is non-stoichiometric. Thus, part of the calcium of the frit goes into the glass formed and part is presented in the crystallized structure, since the Na-rich plagioclase formed has a composition between an oligoclase (~An25) and an andesine (~An45), as it is determined by Raman spectroscopy in the manuscript.

Point	*Na_2O*	*MgO*	*Al_2O_3*	*SiO_2*	*K_2O*	*CaO*	*ZrO_2*	*SrO*	*ZnO*	*TiO_2*
1 (micrograin)	4.62	-	25.04	60.60	1.52	2.79	0.25	3.74	1.13	0.31
2 (nanoregion)	4.99	0.86	23.06	62.21	0.82	2.60	0.10	4.34	1.02	-
3 (glassy phase)	1.27	0.47	21.73	59.32	0.69	9.50	0.40	6.62	-	-

Table S1. Oxide composition (wt%) obtained by EDX in points 1-3 marked in figure S1b.based glass-ceramic.

Figure S2 shows the evolution of Raman intensity vs Temperature for Raman modes ν_a and ν_b in the microcrystals (figure S2a,b) and in the nanocrystals (figure S2c,d) from room temperature up to 595 ºC. It can be observed that Raman intensity shows in both cases linear temperature dependence, approximately, in the same way of the equation 3 of the manuscript. In the inset of figures S2a-d, the parameters of the fitting might be observed. Despite fluctuation of some values due to possible experimental errors, any significant change is observed in the linear behaviour displayed. This, according to previous experiments of Salje [5], can indicate that any displacive transition takes place in the temperature range measured, up to 600 ºC. However, this kind of transition only occurs in fully disordered samples. In section 3.1 and 3.3.1 in the manuscript, it was observed that Si-Al distribution is only slightly disordered at large scale and at microscopic scale, by comparing the results of this work

with results reported by M.Tribaudino et al. [41]. Therefore, it can be concluded that only slight disorder exists and any transition is expected.

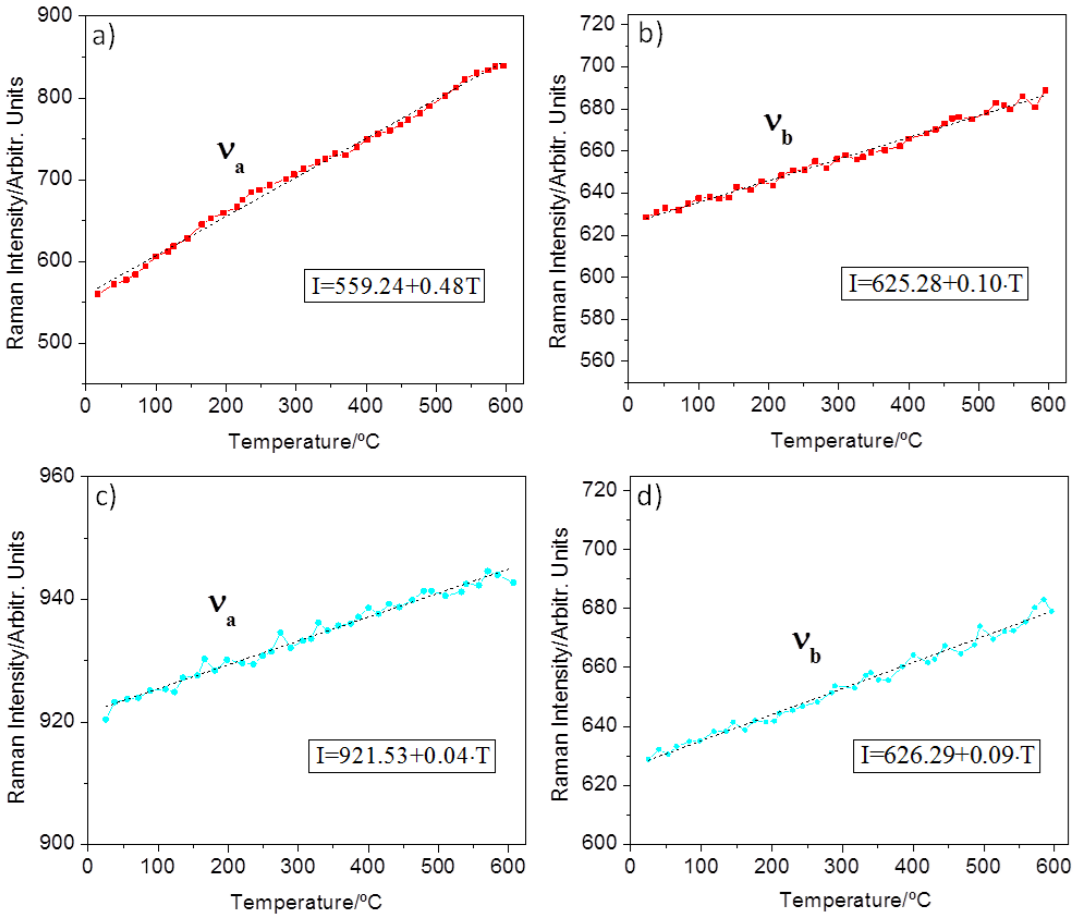

Figure S2. Raman intensity (arbitr. units) vs Temperature (ºC) for Raman modes ν_a and ν_b in **a,b)** microcrystals (red squares) and **c,d)** nanocrystals (cyan circles). The Raman intensity approximately shows linear temperature dependence in the two main Raman modes of the fast sintered glass-ceramic.

BLOQUE 2

El estudio estructural y microestructural realizado en el bloque 1 abre paso a la caracterización sistemática de las propiedades y su correlación con las características estructurales y microestructurales determinadas. Por tanto, en el bloque 2, se procedió al estudio de las propiedades dieléctricas, mecánicas, termorreflectantes y luminiscentes.

En primer lugar, en los artículos de investigación "***Enhanced Wear Resistance of Engineered Glass-ceramic by Nanostructured Self-lubrication*** (artículo 3) y "***High impact resistance of new glass-ceramics tiles***" (artículo 4), se realiza un estudio de las propiedades mecánicas de los materiales vitrocerámicos desarrollados con el fin de corroborar las mejoras introducidas en su respuesta mecánica con respecto a materiales cerámicos convencionales, debido a la microestructura diseñada, de cara a su aplicación en pavimentos. El artículo 3 se centra en el estudio de la resistencia a la flexión, la dureza Vickers, el módulo de Young, la resistencia a la fractura y las propiedades tribológicas (desgaste y coeficiente de fricción). La superficie desgastada de las muestras fue analizada mediante SEM y perfilometría óptica de no contacto, con el fin de revelar el papel que juegan las zonas nanoestructuradas y las microestructuradas en el comportamiento experimentado. En el artículo 4 se estudió otro factor relevante de cara a la aplicación de dichos esmaltes vitrocerámicos en pavimentos, como es la resistencia al impacto. Para ello se analizó la superficie dañada de una baldosa vitrocerámica micro-nanoestructurada y se comparó con una a la que se le incorporó un granulado y con una baldosa convencional, con el fin de determinar la influencia de la microestructura y la rugosidad en la resistencia al desgaste.

En segundo lugar, en los artículos "***Hierarchical micro-nanostructured albite-based glass-ceramic for high dielectric strength insulators"*** (artículo 5) y "***Microstructural study of dielectric breakdown in glass-ceramics insulators"*** (artículo 6) se realizó un estudio del comportamiento dieléctrico de los materiales vitrocerámicos diseñados. El artículo 5 aborda un minucioso estudio del comportamiento eléctrico del material vitrocerámico rico en cristalizaciones de plagioclasa sódica. Éste fue examinado por medio de medidas de impedancia compleja (constante dieléctrica, factor de pérdidas y módulo eléctrico complejo), medidas en corriente continua y alterna y, por último, ensayos de ruptura dieléctrica a temperatura ambiente. En el artículo 6, se extendió el estudio de ruptura dieléctrica hasta una temperatura de 200 ºC, en ambos materiales vitrocerámicos. Con el fin de establecer un modelo de ruptura dieléctrica, se

analizó el punto en el que se produjo la ruptura y los alrededores, tanto con espectroscopia Raman Confocal, como con SEM-EDX.

En el trabajo "***New strategy to mitigate urban heat island effect: Energy saving by combining high albedo and low thermal diffusivity in glass ceramic"*** *(artículo 7)*, se evaluaron las propiedades termorreflectantes. Las propiedades térmicas evaluadas fueron la conductividad térmica, el calor específico y la difusividad térmica; mientras que el comportamiento óptico fue evaluado gracias a medidas de blancura, de reflectancia (en el rango UV-Infrarrojo cercano), de reflectancia solar y medidas de simulación solar. Además, se evaluó el posible ahorro energético que se conseguiría al aplicar dichos materiales vitrocerámicos por medio de un demostrador escalado.

Por último, en los trabajos "***Enhanced Luminescence in Rare-earth free Fast Sintering Glass-ceramic"*** (artículo 8) y "**Tunable UV/blue Luminescence in Rare-earth Free Glass-ceramic Phosphor**" (artículo 9) se realiza un estudio detallado de la luminiscencia en las matrices vitrocerámicas de tipo plagioclasa sódica. En el artículo 8 se mide la luminiscencia de dicho material vitrocerámico mediante fotoluminiscencia y catodoluminiscencia, comparándola con la de un mineral con similar composición. Con el objetivo de determinar la influencia de la estructura y de la microestructura en el comportamiento luminiscente observado, se realizó un estudio por medio de XRD, SEM, TEM, HRTEM y RMN. Finalmente, en el artículo 9, se estudió cómo la modificación química de elementos estructurales influye en este tipo de matrices luminiscentes, de cara a poder modular la intensidad y la longitud de onda de emisión.

ARTÍCULO 3. Enhanced Wear Resistance of Engineered Glass-ceramic by Nanostructured Self-lubrication

V. Fuertes, M.J. Cabrera, J. Seores, D. Muñoz, J. F. Fernández, E. Enríquez.

Materials & Design, 168, 2019, 107623.

Factor de impacto: 4,525 (según JCR Edition Science 2017).

Materials and Design 168 (2019) 107623

Contents lists available at ScienceDirect

Materials and Design

journal homepage: www.elsevier.com/locate/matdes

Enhanced wear resistance of engineered glass-ceramic by nanostructured self-lubrication

V. Fuertes [a,*], M.J. Cabrera [b], J. Seores [b], D. Muñoz [b], J.F. Fernández [a], E. Enríquez [b]

[a] Dept. Electrocerámica, Instituto de Cerámica y Vidrio, CSIC, Kelsen 5, 28049 Madrid, Spain
[b] Centro tecnológico Vidres, S.L., Ctra. Onda, Km 3.4, 12540 Villareal, Castellón, Spain

HIGHLIGHTS

- Novel micro-nanostructured glass-ceramics obtained by a fast sintering processing route.
- Hierarchical micro-nanostructure extremely improves mechanical properties.
- Wear mechanism undergone is unlike other glass-ceramics, like a polishing process.
- Nanocrystals work as solid lubricants, reducing surface damage suffered.
- Very promising candidates to be used in high-performance self-lubricating applications.

GRAPHICAL ABSTRACT

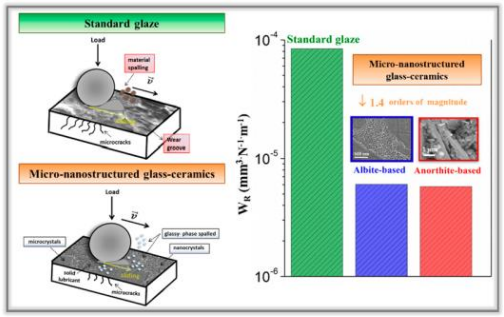

ARTICLE INFO

Article history:
Received 29 October 2018
Received in revised form 25 January 2019
Accepted 25 January 2019
Available online 15 February 2019

Keywords:
Wear
Solid lubricant
Micro-nanostructure
Glass-ceramic
Hardness
Fracture toughness

ABSTRACT

A new kind of micro-nanostructured glass-ceramic based on albite and anorthite crystallizations, >90%, has been obtained following a fast sintering processing route. Flexural strength values up to 111 MPa and microhardness values of 9.5 GPa are measured, supposing an improvement of ~60% regarding current glazes for ceramic floor tiles for high transit areas. The hierarchical micro-nanostructuration of these glass-ceramics favour crack deflection, which implies a reduction of brittleness in these materials and a consequent increase of fracture toughness of ~40% regarding a standard glass-ceramic. Tribological properties are also evaluated, showing a decrease in the friction coefficient (μ) of ~36% and a surprising reduction of the wear rate (W_R) larger than one magnitude order, in both micro-nanostructured glass-ceramics, concerning a standard one. Worn tracks analysed by Multi-Mode Optical Profilometry and FE-SEM measurements revealed that nanocrystals present in the microstructure work as solid lubricants, favouring body sliding over their surface and noticeably reducing μ, W_R and the surface damage suffered. Wear mechanism undergone by both glass-ceramics is unlike other glass-ceramics, similar to a polishing process, without any apparent material spalling. All of these findings make the micro-nanostructured materials very promising candidates to be used in high-performance self-lubricating applications.

1. Introduction

Glass-ceramics are materials which consist of crystalline phases with a residual glassy matrix, produced through controlled crystallization of parent glasses. Glass-ceramics are characterized by high thermal and chemical stability, good optical properties, low closed porosity and

* Corresponding author.
E-mail address: vfuertes@icv.csic.es (V. Fuertes).

https://doi.org/10.1016/j.matdes.2019.107623

good mechanical properties (e.g machinability, high hardness and high resistance to abrasion) [1]. Since the discovery of glass-ceramic materials in the early 1950s, a great variety of compositions and microstructures with specific technological properties have been developed [2]. The different functionalities discovered in glass-ceramics have allowed them to be used in several applications such as household appliances [3], industrial [4], optical [5], biomedical [6], environmental [7], electrical insulating [8] and in architectural applications (e.g buildings, pavements etc) [4,9], among others.

One of the extended and massive uses it is as glaze in ceramic tile industry, for instance on floors in high transit areas, in which the demand to considerably increase wear resistance is one of the main challenges in this sector. In addition to sustainability criteria, saving repair time and replacement costs are critical aspects to consider for these applications. Actually, standard glazes have low abrasive resistance and easily loses its surface characteristics, such as brightness, colour and superficial texture [10]. To overcome these drawbacks in the ceramic tile industry, new engineered products showing better resistance to wear by abrasion and higher surface hardness than traditional glass-ceramics are required [10–13].

Wear resistance is a complex mechanism which may be affected by many factors, such as physical properties (hardness, fracture toughness, Young's modulus, flexural strength …) [14] and features of phase composition and microstructure (crystal size, porosity, secondary phases or crystallinity among others) [15–17]. Therefore, to be able to understand the wear behaviour, a thorough mechanical study of the materials is required in order to know the influence of the different variables involved. In this sense, the complexity of glass-ceramics has prevented the knowledge of the main parameters that limit its wear resistance, and therefore, the solutions to their limitations.

In the last years, development of nanotechnology and nanoscience has allowed the improvement and creation of new materials with unique properties in the ceramic sector [18]. Regarding mechanical properties, reinforced materials with nanoparticles exhibit higher mechanical strength and resistance to wear because of their larger specific surface area that favours load transfer from bulk counterparts [19]. It is demonstrated that nanoparticles used as additives for different ceramic matrices, typically SiC, SiO_2, Al_2O_3, $ZrSiO_4$, ZrO_2, TiO_2 or ZnO, provide an enhancement of mechanical properties, mainly in wear resistance [18–22]. However, the use of nano-materials is limited in practice, by different reasons: the high price of nanoparticles affects the final cost of the product; the technical problems of manipulating large amount of nanoparticles; and the uncertainty in nano-toxicological risks. Nevertheless, glass-ceramics materials obtain their reinforced phases from the nucleation from the parent glass during the thermal treatment [23]. Thus, the in situ formation of nanostructured glass-ceramic materials, avoiding the handling of nanoparticles, may overcome these drawbacks. J.J Reinosa et al. [24] and H. Man et al. [25] obtained nanostructured glass-ceramic glazes based mainly on pyroxene and anorthite crystallizations, respectively. However, little attention has been paid to the characterization of their properties. Therefore, the incorporation of nanostructured materials in the ceramic sector is relatively recent and is a fairly unexplored field.

Gleiter [26] reported that conventional polycrystalline ceramics might become ductile if their grain size is reduced to nanometers. Zabinski et al. [27] reported that lubrication is possible by engineering the microstructure of oxides. In this work, it is showed that nanocrystalline structures may enhance grain boundary sliding and contribute to plastic deformation and low friction. Glass-ceramic materials are suitable to be engineered, because their microstructure might be easily tailored by modifying chemical composition of the precursors and through the control of nucleation and crystal growth during the crystallization step, in which sintering process play a vital role [1,10]. In fact, the controlled crystallization of glazes has proved to be the most effective and economical way of obtaining high-quality mechanically resistant floor tile [28]. In recent works, two polycrystalline glass-ceramic materials based on micro-nanostructured albite and anorthite crystallizations have been synthetized by a facile and conventional ceramic process [8,29]. These novel glass-ceramics, consist of a combination of microcrystals and nanocrystals along with high crystallinity, >90%, that reveals an engineering material offering a unique microstructure for the study of mechanical performance.

In this context, the aim of this work is to design a new glass-ceramic material with a micronanostructure and high crystallinity and easily tailored with the aim of improve mechanical properties regarding other materials of ceramic industry. Thus, a new family of glass-ceramic materials has been obtained [29,30]. In order to reveal these improvements, measurements of flexural strength, Vickers hardness, Young's modulus, fracture toughness and wear resistance are included in this study. Observations of worn surface by SEM and non-contact optical profilometry revealed the relevance of nanocrystals in the surprising enhancement of wear resistance. All of these findings obtained are compared with a standard glass-ceramic (with similar chemical composition and conventional microstructure) used for high transit floor tile, showing a remarkable improvement of mechanical behaviour in these novel glass-ceramics. Finally, it was established a new phenomenological wear model for micro-nanostructured glass-ceramics which, according to authors´ knowledge, it has never done before in such detail in any glass-ceramic material for tile applications.

2. Experimental procedure

2.1. Sample preparation

Both glass-ceramics were prepared by a conventional ceramic process previously reported in which the composition was quenched from the high temperature melt to form a frit [8]. The precursors used, kaolin (Molcasa, $d_{50} = 5.34\ \mu m$) and frit, were mixed in a weight proportion of 10/90, respectively, with a milling process in an alumina ball mill for 20 min with 37 wt% of water [24,31]. The frits compositions expressed in term of equivalent oxides are shown in Table 1. The main difference between anorthite and albite frits is the use of different nucleating agents, mainly ZrO_2 and SrO, respectively, which favour in different ways the crystallization of both phases. SrO is a crystal lattice disruptor which favours the formation of the sodium aluminosilicate after devitrification process, although the frit only has ~3% of Na_2O. Moreover, Zirconium oxide is a nucleating agent, and it is used in higher percentage in the composition without SrO. Table 1 also shows the chemical composition of a standard commercial glaze for comparative purposes. This standard glaze is a conventional matte shine glaze for high transit applications. The composition of the standard glaze is similar in feldspars composition, calcium-rich plagioclase, although with significant lower crystallinity, ~ 44% (see Fig. S1c in supporting

Table 1
Chemical composition of the albite, anorthite and standard precursor frits expressed as equivalent oxides. The minority components (<1 wt%) are all included in others. *Others: mainly minority oxides are TiO_2 and Fe_2O_3.

Oxides wt%	Albite	Anorthite	Standard
SiO_2	51.63	47.33	43.70
ZrO_2	–	8.03	4.07
SrO	8.05	–	3.28
Na_2O	2.68	5.06	1.50
K_2O	1.46	1.70	1.52
Al_2O_3	21.14	19.23	32.20
ZnO	1.10	4.72	2.14
CaO	10.47	12.97	2.98
B_2O_3	1.40	–	1.50
P_2O_5	0.84	–	2.88
MgO	1.04	0.62	1.63
BaO	–	–	2.12
Others*	0.21	0.33	–

information). After mixing and milling, the materials prepared were dried at 60 °C for 24 h and sieved under 100 μm, achieving monomodal particle size distributions with $d_{50} = 6.72$ μm for albite-based glass-ceramic and $d_{50} = 7.52$ μm for anorthite-based glass-ceramic. Then, the powder was pressed at 40 MPa by a rectangular die for flexural strength measurements, obtaining samples of 80 mm × 30 mm × 5 mm. Both albite and anorthite-based glass-ceramics are self-supported glazes and not required a porcelain stoneware support as the standard glaze does. Finally, pressed samples were thermally treated in an industrial furnace at 1220 °C for 6 min with a 30 °C min^{-1} heating rate, in a rapid cycle of 55 min [8,29]. Samples were carefully adjusted in size and shape for the rest of measurements to be fitted in the corresponding equipment. Besides, for Vickers indentation samples were diamond polished before measurements.

2.2. Characterization

Flexural strength (σ_f) was determined by three points flexural method, ISO 10545-4, using a Universal Instron Machine [32]. The measurement was carried out in bars with an outer span of 60 mm and a displacement rate of 0.5 mm min^{-1}.

Young's modulus (E) and hardness (H) were measured at room-temperature by depth sensing indentation (Zwick/Roell, Zhu 2.5, Germany), using a Vickers diamond indent and four indentation loads of 0.5 N, 1 N, 5 N and 10 N. Resolution for load cell is 1 mN and lateral resolution of 2 μm. The load and the penetration depth were continuously and simultaneously recorded during each test. Young's modulus was obtained from the unloading branch and hardness from the peak load and the indentation area measured on the optical microscope. Nine indentations were made for each material and the results presented correspond to the average. Fracture toughness (K_{IC}) was estimated by using Eq. (1), proposed by Nihiira [33], one of the experimental expressions most used:

$$K_{IC} = 0.067 \cdot \left(\frac{E}{H_V}\right)^{2/5} \cdot H_V \cdot a^{1/2} \cdot \left(\frac{c}{a}\right)^{-3/2} \quad (1)$$

where a and c are parameters determined by geometrical factors of the indentation imprint (Fig. 2).

Dry sliding tests were performed by a UMT3 tribometer (Bruker Nano Inc., formerly CETR, USA) using linear reciprocating ball-on-plate tests in order to evaluate tribological properties, friction and wear behaviour, of materials examined. The balls used as counter bodies were commercial Al_2O_3 spheres (10.3 mm diameter, Saint Gobain) and the plates had the corresponding surface of the materials. Tests were carried out at 20 ± 2 °C and 20–30% of relative humidity with the following parameters: stroke length of 3 mm, frequency of 20 Hz (0.03 m·s^{-1}), sliding distance of 75 m, a normal applied load of 6 N. For Al_2O_3 sphere, a normal load of 6 N on a 10.3 mm diameter ball corresponds to a Hertzian contact pressure of 561 MPa, 538 MPa and 578 MPa for albite-based glass-ceramic, anorthite based glass-ceramic and standard glaze, respectively. Three tests were carried out for each material and data represented are their average. Friction coefficient, μ, was continuously registered during the tests. The wear volume loss of the plates (W_V) was calculated by using Eq. (2):

$$W_V = \Delta x \cdot A + \pi \cdot \frac{d^2}{8} \cdot W_l \quad (2)$$

where Δx is the nominal stroke, A is the cross section area beneath the 2D curves, and d and W_l are the width and depth of the wear tracks, respectively [34]. Eq. (2) is formed by two terms, where the first one considers the central zone of the wear tracks according to the ASTM G133 standard. The second term is a correction factor that takes into account W_V in the two edges of the track [35]. A stylus profiler (Dektak XT, Bruker, Germany) was employed to measure the 2D wear track profiles, as stated the ASTM G133 standard [36]. Wear rate (W_R) was estimated by using Archard equation [35] (Eq. (3)).

$$W_R = \frac{W_V}{F_N \cdot l} \quad (3)$$

where F is the normal force applied and l the sliding distance.

Microstructural characterization of worn surfaces was studied by means of Field Emission Scanning Electron Microscopy (FESEM) using a Hitachi S-4700, with a resolution of 1.5 nm at 15 kV; and with a ZETA-20 Multi-mode Optical Profiler, which also was used to register the surface profile in worn and unworn surfaces and to measure a and c parameters in Vickers indentation imprints.

3. Results and discussion

3.1. Micro-nanostructure characterization of engineered glass-ceramics

Fig. 1a and b shows the characteristic micro-nanostructuration of albite-based glass-ceramic where elongated albite microcrystals (~1–3 μm in length) are surrounded by nanocrystal regions (diameter size of 10 to 20 nm). Micrograph of Fig. 1c and d shows the presence of elongated anorthite crystals having 5–10 μm in length. The anorthite microstructure also reveals the presence of ZrO_2 particles with spherical morphologies having 100–300 nm in diameter which tend to be placed at the feldspar crystal edges. Zircon crystals are irregular in shape with grains in the range of 0.5–2 mm, and appear forming aggregates located also at the feldspars crystal edges. Nanostructured regions are located between the large feldspar microcrystals. Fig. 1e shows the microstructure of the standard glaze used for comparative purposes. It can be observed the expected presence of anorthite-rich microcrystals (according to XRD pattern of Fig. S1c), of up to 20 μm in length, in a vitreous matrix. Glassy phase content in standard glaze is considerably larger than in the novel glass-ceramics (Figs. 1a–d and S1). Moreover, nanometric ZrO_2 grains and submicronic $ZrSiO_4$ appear in anorthite-based glass-ceramic (Fig. 1c–d) that could contribute to reinforce the material.

3.2. Mechanical performance: flexural strength and hardness response

Flexural strength values for anorthite-based glass-ceramic are ~111 ± 10 MPa while in albite-based glass-ceramic is ~83 ± 8 MPa. These values of flexural strength are higher than reported values for conventional glazes on porcelain ceramic bodies, σ_f ~60 MPa, or in porcelain bodies with sodium and potassium feldspar, σ_f ~51–53 MPa [37]. Recently, Barrachina et al. [38] have reported improved values of σ_f of 96 MPa for a porcelain stoneware tile with a glass-ceramic glaze based on anorthite crystallizations, comparable with the values obtained in this work. It is worth remembering that the micro-nanostructured glass-ceramics used in the present study are self-supported. The improvement of flexural strength regarding conventional materials might be mainly attributed to the characteristic micro-nanostructure of these micro-nanostructured glass-ceramic materials. Differences observed in flexural strength between albite and anorthite-based glass-ceramics may be due to the presence of dispersed crystalline phases in the case of anorthite-based glass-ceramic, mainly $ZrSiO_4$ (micrometric size) and ZrO_2 (nanometric particles) (see Fig. S1a and b in supporting information), which are typically used to provide opacity to the glaze and enhance mechanical properties [1,39]. These results evince that flexural strength of these micro-nanostructured glass-ceramics meet the new requirements to be used in tile industry.

Vickers indentation tests for loads of 0.5 N, 1 N, 5 N and 10 N are carried out in both, the standard glaze with a similar composition (see Table 1 and Fig. S1c in supporting information) and the micro-nanostructured albite and anorthite-based glass-ceramics. Fig. 2a–c show optical micrographs of Vickers indentation imprints for each

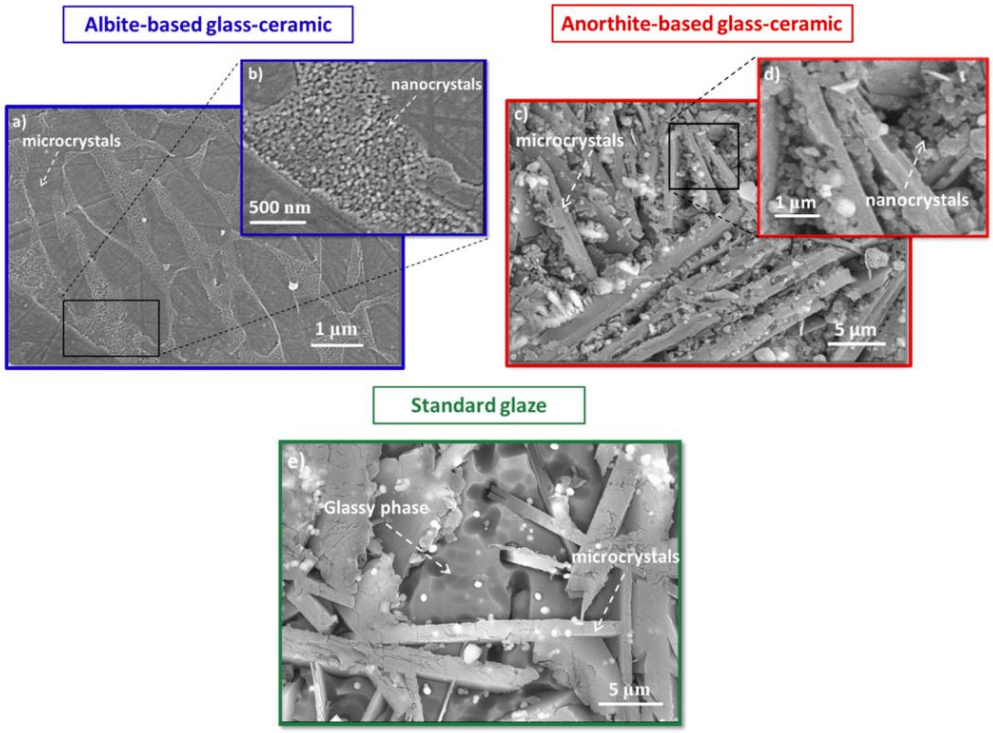

Fig. 1. FESEM micrograph of: a) albite-based glass-ceramic sample; b) an enlargement of the previous picture, showing the nanocrystals in more detail; c) anorthite-based glass-ceramic sample; d) an enlargement of the previous picture; e) standard glaze. Nanocrystals, microcrystals and glassy phase are labelled and indicated by arrows.

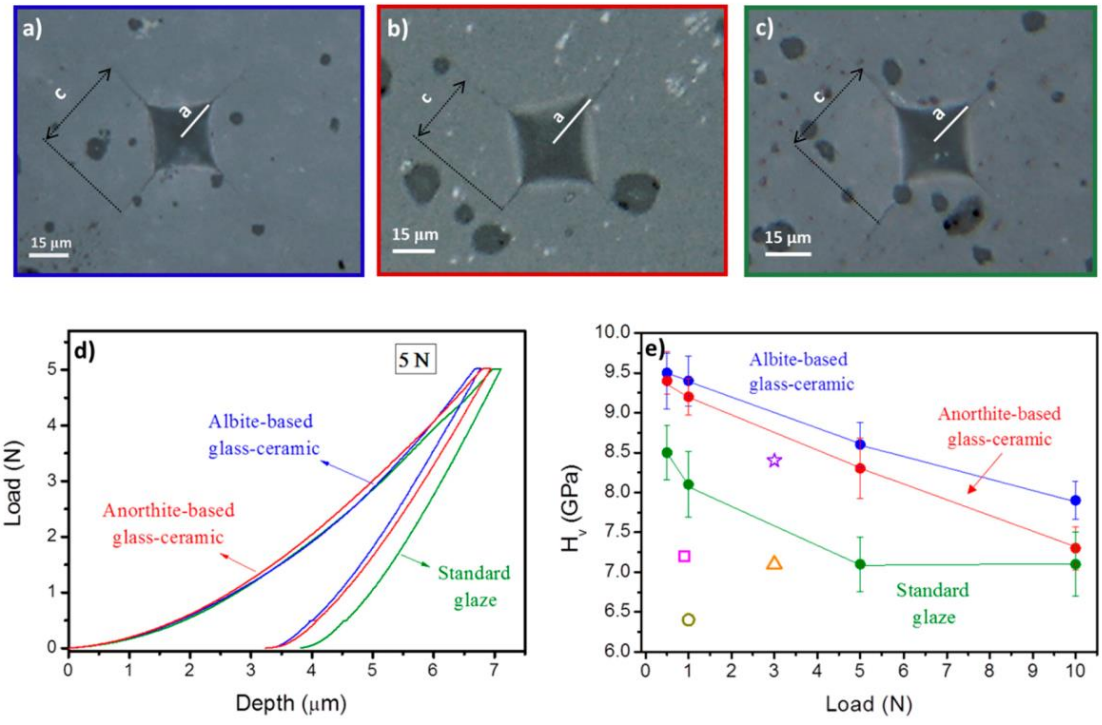

Fig. 2. Optical micrographs showing indentation imprint for a load applied of 5 N in a) albite-based glass-ceramic (blue colour); b) anorthite-based glass-ceramic (red colour) and c) the standard glaze (green colour). For each Vickers indentation imprint *a* and c distances are indicated. d) Loading–unloading curves for each material for a load applied of 5 N. e) Hardness values vs load in micro-nanostructured glass-ceramics (red and blue solid circles) are compared with measured values of standard glaze (green solid circle) and the best reported values in literature for different glass-ceramic glazes (empty symbols) based on: cordierite (violet star) and mullite (orange triangle) [12], CaO-MgO-SiO_2-Al_2O_3 system (dark yellow circle) [40] and CaO-MgO-SiO_2-Al_2O_3-ZrO_2 system (pink square) [41]. The drawn lines are guides for the eyes. (For interpretation of the references to colour in this figure legend, the reader is referred to the web version of this article.)

material studied for a load applied of 5 N, which was chosen as a representative example. The corresponding *a* and *c* parameters that characterize the Vickers indentation imprints are marked in each micrograph. The corresponding load versus penetration depth curves for these indentations, depicted in Fig. 2d, allow analysing the different mechanical response of each material. The rest of loading-unloading curves for loads applied of 0.5 N, 1 N and 10 N might be found in Fig. S2 of supporting information.

Examining loading-unloading curves of Figs. 2d and S2, an indentation size effect (ISE) is observed [42–44]. Changes in the shape and depth of the indentation curve may indicate changes in the elastic recovery of the material involved [43]. Loading curves approximately follow the same tendency in the three materials for each indentation load (see Figs. 2d and S2). For all loads, the unloading curves of the standard glaze are slightly shifted regarding both micro-nanostructured glass-ceramics (ranging from 0.2 μm at 0.5 N) and up to 0.5 μm at 10 N. The area under load-unload curve for the standard material increases in relation to the micro-nanostructured glass-ceramics, which means that a larger amount of energy is stored after the loading and, consequently, an increase of the work of indentation in the material, indicating that the novel glass-ceramics are harder than the standard material [45].

Analysing the unloading curves, Vickers microhardness and Young's modulus may be obtained, which values are tabulated in Table S1 in supporting information. The general trend observed for the three materials is a decrease of these both values as indentation load increases. Young's modulus values obtained, in the range 66–78 N (see Table S1 in supporting information), are compared with reported values in literature of 73 GPa for porcelain stoneware tiles with addition of glass-ceramic in the system K_2O-CaO-MgO-SiO_2-Al_2O_3 [46] or 61 GPa for a glass-ceramic tile with nepheline and forsterite as major phases [47]. According to values of Table S1, ISE for elastic modulus in both glass-ceramics is more considerable at high loads, mainly ≥10 N. This fact can be due to it is achieved a limit load value for glass-ceramics that produces the sudden breakdown of microcrystals, increasing the deformation of the material, and, therefore a decrease of the Young's modulus occurs. However in the case of the standard glaze, load independent microhardness regime is reached at 5 N [48].

Hardness measured by Vickers indentation is often reported as a materials property; however, the measured value is strongly affected by the load of indentation as it was previously discussed and it can be observed in Fig. S2 and Table S1. For that reason, in Fig. 2e hardness vs load is plotted for these novel micro-nanostructured glass-ceramics and compared with the values of the standard glaze evaluated in this work, as well as the best reported values in literature for different glass-ceramic glazes. The largest values of H_V are determined for albite based-glass ceramic for any indentation load, reaching values of up to 9.5 GPa. An increase of the hardness up to 18% regarding the standard glaze for indentation loads up to 5 N is observed. Hardness of anorthite-based glass-ceramic also registers noticeable values, showing an enhancement of hardness up to ~14%. In both cases an improvement of H_V is observed regarding the standard material with similar oxide composition but lower crystallinity and different microstructure. However, at 10 N, the hardness of glass-ceramics decreases, equated to the standard glaze, due to the breakdown of microcrystals, as it is explained before. It is important to note that the standard material chosen for comparative purposes provide high mechanical performance that it is superior to other conventional materials, as it might be seen in Fig. 2e.

From data of literature plotted in Fig. 2e, it might be concluded that H_V has been improved ~ 7% regarding the best value found in literature for a cordierite-based glass-ceramic [12], and ~59% in relation to a traditional one used in tile industry [41]. However, the low thermal expansion coefficient of cordierite based glass-ceramic is however a serious limitative factor for their potential use in ceramic tile because the stoneware support have a large thermal expansion coefficient and therefore the glaze will be under tensile stress that is detrimental for their performance.

Despite the importance of durability in ceramic for tile applications, the literature is not conclusive about the main parameters to be considered about this issue. Crystalline phases usually present in glass-ceramics used as tile glazes, are mainly cordierite, anorthite, mullite, zircon, celsian, wollastonite or diopside, because of their good mechanical behaviour [1,12]. In this work, in addition of anorthite, another crystalline phase based on feldspar crystallizations, albite, has been synthetized, despite the difficulty of being artificially obtained with such purity. In fact, this material shows not only the best behaviour for the three materials analysed, but the best hardness reported in the literature, according to the best of our knowledge.

Considering the values of flexural strength obtained in Section 3.1 and values of hardness in Table 2, it may be confirmed that $H_V > 3\sigma_F$. This is the typical behaviour of ceramics, which are brittle materials that exhibit high hardness and relatively low strength [49]. Hardness represents, in some way, the ability of the surface to withstand scratches and cuts, and is also related to the resistance to impacts and other kind of stresses generated at normal working conditions for tiled floors. Therefore, it is a very important characteristic which conditions the durability of ceramic surfaces. These obtained results clearly evince that surface hardness of ceramic tile materials could be enhanced by using these novel glass-ceramics. Vickers micro-hardness of glass-ceramic glazes depends on several factors such as the type and amount of crystalline phases, surface porosity and microstructure. Therefore, as it was mentioned in Section 3.1, the improvement of mechanical response in both micro-nanostructured glass-ceramics regarding the standard glaze (with similar chemical composition) may be attributed to combination of several factors such as crystallinity, porosity, secondary phases and microstructure. It is well known that the presence of more crystallinity, >90% in both glass-ceramics, enhances mechanical properties [50].

Porosity was evaluated in previous works [8,51], obtaining for albite glass-ceramic a porosity of ~3.2% with an average pore size of 3.9 ± 0.2 μm, and for anorthite glass-ceramic, ~6.7% with an average pore size of 5.4 ± 0.4 μm. In the case of the standard material analysed the determined porosity is ~3.1% with an average pore-size of 17.8 ± 0.6 μm. The percentage of porosity achieved in the three materials is similar, slightly larger for anorthite-based glass-ceramic. However there are considerable differences in the pore size, being quite large for standard glaze. It is well known that as pore size increases mechanical behaviour is worsened, as it is observed in other works [52,53], but the differences in the porosity are low enough between the three materials in study to be established as a key differentiating factor.

The other factor to be considered is the presence of several polycrystalline phases with different sizes. In the case of anorthite-based glass-ceramic the presence of zircon and zirconia might help to increase the hardness of the final material [1,23,39]. However, albite-based glass-ceramic hardly has secondary phases and it presents the best hardness value. This suggests that microstructure, in fact micro-nanostructure, plays an essential role and strongly determines the good performance exhibited. The presence of a hierarchical micro-nanostructure may favour load transfer from microcrystals to nanocrystals, resulting in an improvement of the mechanical strength of both glass-ceramics [18].

Finally, fracture toughness was calculated by means of Eq. (1), obtaining K_{IC} values of 2.1 $MPa{\cdot}m^{1/2}$ for both micro-nanostructured glass-ceramics and 1.5 $MPa{\cdot}m^{1/2}$ for the standard glaze, at indentation load of 10 N. This supposes an increase of K_{IC} up to 40% in both glass-

Table 2
Wear volume (W_V) and wear rate (W_R) for a conventional glaze and new glass-ceramics developed.

Sample	W_V (mm^3)	W_R ($mm^3/N{\cdot}m$)
Standard glaze	$3.5{\cdot}10^{-2}$	$8.4{\cdot}10^{-5} \pm 4.9{\cdot}10^{-8}$
Micro-nanostructured albite glass-ceramic	$3.7{\cdot}10^{-3}$	$6.1{\cdot}10^{-6} \pm 9.9{\cdot}10^{-9}$
Micro-nanostructured anorthite glass-ceramic	$3.4{\cdot}10^{-3}$	$5.8{\cdot}10^{-6} \pm 4.9{\cdot}10^{-9}$

ceramics regarding the standard material tested (Table S1 of supporting information). Indentation load below 5 N did not cause cracking of any sample and therefore, K_{IC} was not calculated. Gómez-Tena et al. [54] reported values of K_{IC} for different ceramic tile glazes for an indentation load of 9.8 N. In that work, K_{IC} calculated was, 0.74–1.41 $MPa{\cdot}m^{1/2}$ for some earthenware wall tiles and 0.66–1.3 $MPa{\cdot}m^{1/2}$ for some vitrified floor tiles. A value of 1.6 $MPa{\cdot}m^{1/2}$ was reported by Carbajal et al. [55] for a standard porcelain stoneware and of 2.0 $MPa{\cdot}m^{1/2}$ for a porcelain which glassy matrix was reinforced with stresses induced by quartz grains. Comparing these data of the literature with values obtained in both glass-ceramics from this work, an increase of K_{IC} in the range 5–72% is noticed. Fracture toughness is a quantitative way of expressing a material's resistance to brittle fracture when a crack is present. Thus, this increase registered indicates that by micro-nanostructure engineering an improvement of toughening is obtained. The hierarchical micro-nanostructured glass-ceramics are characterized by having nano and microstructured regions which suppose the presence of higher amount of grain boundaries regarding a traditional material. Since grain boundaries have weaker atomic bonding within the interfacial area, when a crack appears, it preferentially propagates along these paths of lower fracture energy, being deflected at each grain boundary. With a reduction of the grain size, number of grain boundaries increases and the number of such events significantly increases. In that case, as occurs in both micro-nanostructured glass-ceramics, more energy is required to propagate the cracks and consequently the materials will be more fracture resistant, favouring cracks deflection (see Fig. S3 in supporting information) [56,57]. As it can be seen in Fig. S3, both micro-nanostructured glass-ceramics displays a more tortuous and deflected crack path than the standard glaze tested. Such increased crack-path tortuosity is a major contributor to the higher fracture toughness (Table S1) of these engineered glass-ceramics. Apart from these excellent characteristics, other important mechanical aspects have to be considered, as resistance against abrasive wear, which will be discussed in following sections.

3.3. Relevance of the micro-nanostructure on tribological performance

An adequate knowledge of tribological properties is a key factor to take into consideration when a glaze is considered for floor tile applications, since they are often installed in areas suffering a strong wear by pedestrian traffic. Tribological properties were evaluated for a relative humidity of 20–30%, a standard value used for applications of ceramic tiles. Humidity can modify the friction coefficient and wear and to evaluate this influence, further studies should be done, as it is reported in other works [58]. However, in this work, the study was carried out in the range explained before. In Fig. 3 is depicted the friction coefficient (μ) (Fig. 3a) and the wear rate calculated by Eq. (3) (Fig. 2b) for the standard glaze previously considered (green colour), albite-based (blue colour) and anorthite-based (red colour) glass-ceramics. Friction coefficient of both glass-ceramics displays considerable lower values during the all sliding distance regarding the standard material. In both cases friction coefficient slightly increases as sliding distance increases while in standard glaze remains approximately constant. It could be assumed that this effect is due to surface roughness, since it is well known that it affects friction at the beginning of the tests and after some sliding distance [59]. However, the average surface roughness measured for the three materials is 3.8 ± 0.9 μm, 1.7 ± 0.5 μm and 2.2 ± 0.7 μm, for albite-based, anorthite-based glass ceramics and for the conventional glaze, respectively, which are very similar. Therefore, it is possible to conclude that surface roughness possess a low influence in the results. However, the differences in μ evolution are very noticeable. Nevertheless, microstructure of the glass-ceramics seems to play an important role regarding the conventional glaze, as it was also previously observed for microhardness and fracture toughness. As it was reported in previous works, the presence of nanocrystals may contribute to plastic deformation, mainly due to dislocation motion is favored, as well as the decrease of friction coefficient [26,27]. Moreover, the spherical shaped nanoparticles, in general, favour effects of sliding due to their rolling action contact area and consequently increase the lubricating behaviour of the material [60]. Both features are essential to reduce friction coefficient and wear in the glass-ceramics developed in this work.

Friction coefficient values at 75 m (which equated to 25,000 cycles for a stroke length of 3 mm) for albite-based glass-ceramic, anorthite-based glass-ceramic and standard glaze are 0.43, 0.49 and 0.66 respectively. As a consequence of this decrease in the friction coefficient in both micro-nanostructured glass-ceramics, ~36% after 75 m of sliding distance, the wear rate is surprisingly ~1.4 orders of magnitude lower in relation to the standard glaze (Fig. 3b). Values of wear rate and wear volume obtained from the test are collected in Table 2, showing an enhanced reduction of the wear volume in these novel glass-ceramics regarding the standard one. Comparing these values of wear rate with other ceramic glazes of the literature, it is also observed a noticeable improvement in W_R. Pina-Zapardiel et al. [61] reported a high wear resistance glaze based on glaze produced by using sepiolite with

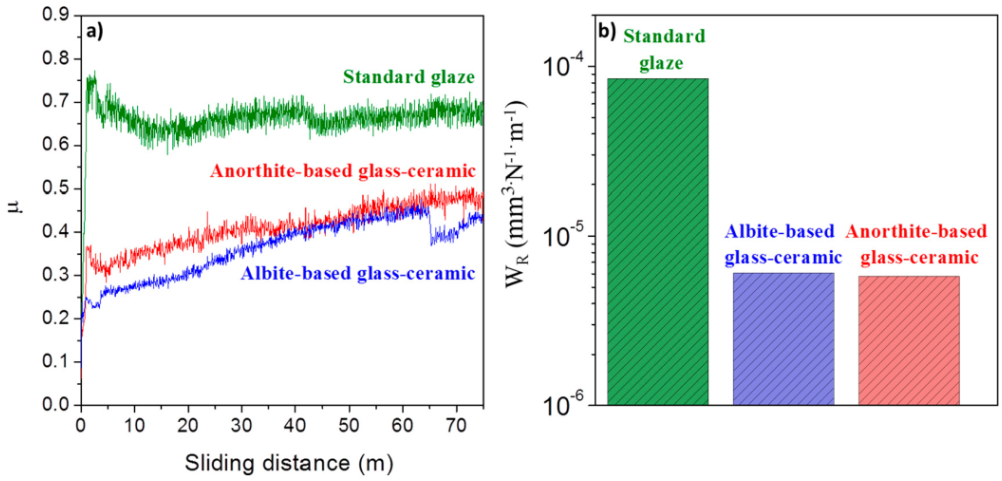

Fig. 3. a) Friction coefficient (μ) vs sliding distance and b) wear rate (W_R) for standard glaze (green colour), albite-based (blue colour) and anorthite-based (red colour) glass-ceramics. Wear rate plotted in y-axis of b) is represented in logarithmic scale in order to clearly evince that wear rate in both micro-nanostructured glass-ceramics is 14 times lower regarding the standard glaze. (For interpretation of the references to colour in this figure legend, the reader is referred to the web version of this article.)

dispersed zircon nanoparticles that achieved values of $1{\cdot}10^{-5}$ $mm^3/N{\cdot}m$. Heo [62] published W_R values of $9{\cdot}10^{-3}$ $mm^3/N{\cdot}m$ for a traditional whiteware and values of $4{\cdot}10^{-2}$ $mm^3/N{\cdot}m$ for two transparent glazes with ~70 wt% of SiO_2, ~20 wt% of Al_2O_3 and variable content of calcium, sodium and potassium oxides. In comparison with all of these values, wear resistance in both micro-nanostructured glass-ceramics developed in this work, is significantly improved, decreasing W_R up to half order of magnitude regarding the best of cases described in literature.

In order to deepen the role played by the microstructure in these micro-nanostructure glass-ceramics, tested surfaces were analysed by Multi-Mode Optical Profilometry (Fig. 4a–c) and FE-SEM (Fig. 4d–i). Fig. 4a and b show the worn surfaces of the new glass-ceramics materials after the test, where it is possible to observe that both micro-nanostructures remain smooth, without apparent cavities due to abrasion process, despite the mechanical contact of the Al_2O_3 counter body with the surface of the samples. Nevertheless, in the standard glaze, the aspect of worn surface after abrasive wear is totally different, showing empty cavities produced by material spalling. Surface profiles depicted as insets in Fig. 4a–c, display marked differences in depth between worn and unworn areas for the three materials analysed, verifying the wear process. Wear process in micro-nanostructured glass-ceramics is not as severe as in the case of the standard glaze: in worn areas of albite-based and anorthite-based glass-ceramics, depth is <4 μm and ~2 μm, respectively, while in the conventional glaze is ~25 μm, indicating the larger wear of the surface. In addition, in the standard material it may be observed some empty cavities due to the large material spalled, which well agrees with the larger W_R and μ previously discussed. The area of wear tracks measured by a profiler is as low as $\sim10^{-3}$ mm^2 in both albite and anorthite-based glass-ceramics, while in the standard glaze is $\sim10^{-2}$ mm^2.

By means of FE-SEM, both worn and unworn surfaces are analysed in more detail. Unworn zone of albite-based glass-ceramic (Fig. 4d) exhibits the presence of a smooth layer of glassy phase covering the micro and nanocrystals. In Fig. 4e, the characteristic microstructure of this glass-ceramic is clearly revealed as result of the wear process, which acts as a polishing process [8], where the presence of microcrystals surrounded by the nanocrystal regions is observed. In the inset of Fig. 4e, it could be seen some nanostructured areas slightly eroded, as a direct consequence of the abrasion wear undergone, as well as some small debris particles might be identified randomly distributed on the surface of the sample and small grooves, <500 nm in length.

In the case of anorthite-based glass-ceramic (Figs. 4b, f and g), a similar behaviour is observed. In the unworn surface (Fig. 4f) some elongated anorthite microcrystals are covered by nanoparticles and by extent glassy phase. Fig. 4g shows the worn part of the sample in which microcrystals may be clearly observed after the abrasion suffered, displaying the characteristic microstructure of this material, previously reported [29]. In contrast, surface of the conventional glaze exhibits a completely different aspect (Fig. 4c), presenting empty cavities and less smooth surface because of the larger spalling of material (Fig. 4h and i). In the higher magnification FESEM micrograph (Fig. 4i) it could

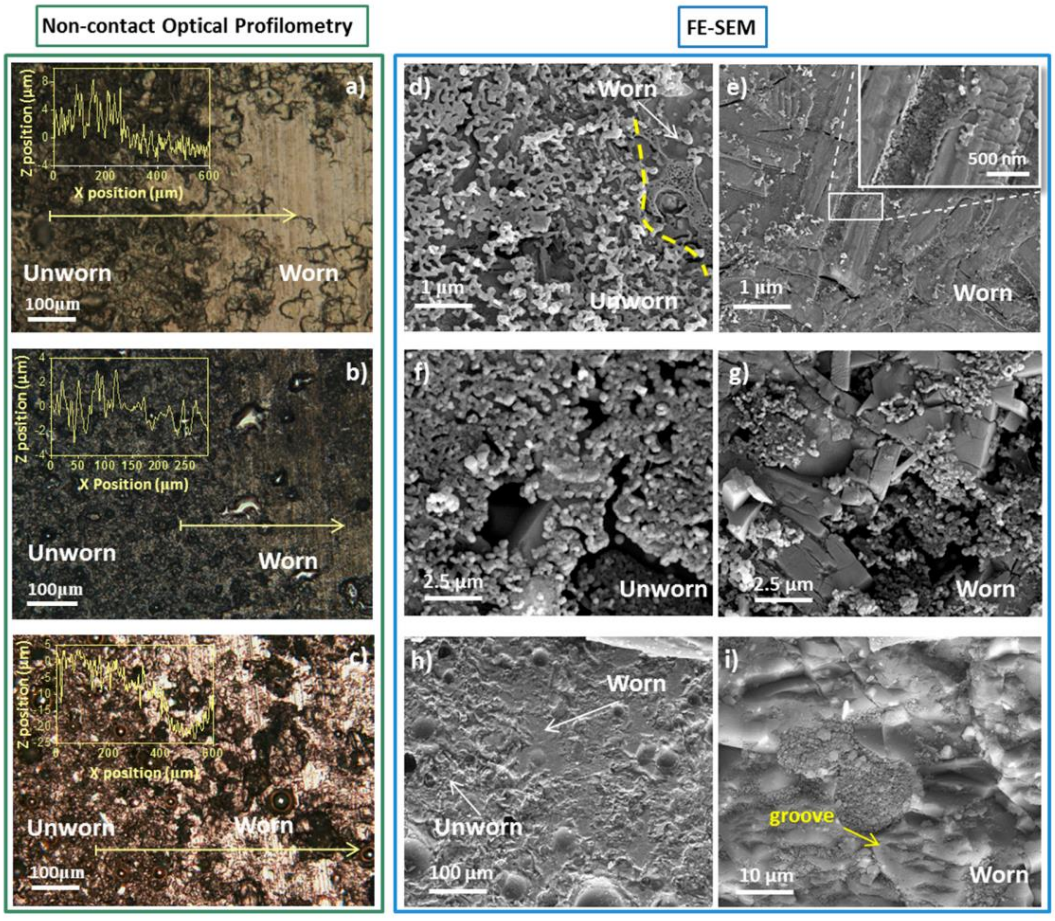

Fig. 4. Multi-mode optical profilometry (left column in green), showing optical images of worn and unworn areas and surface profiles carried out along the yellow arrow (insets), and FE-SEM micrographs (right columns in blue) for albite (a, d, e) and anorthite (b,f, g) based glass-ceramics and for a conventional glaze (c, h, i). (For interpretation of the references to colour in this figure legend, the reader is referred to the web version of this article.)

be noticed some plastic deformation grooves more noticeable than in micro-nanostructured glass-ceramics, of around 10 μm in length, a larger content of debris material and, in general, a much more damaged surface [63]. Moreover, in this case, the wear does not reveal any nanostructured area, which seems to be the decisive factor between the wear behaviour developed in both micro-nanostructured materials regarding the non-nanostructured one. From these analyses, it may be concluded that nanocrystals plays a vital role reducing wear in glass-ceramics, since nanocrystals seem to work as solid lubricants, favouring the sliding when a body comes into contact with the glass-ceramic surface. As consequence, the friction coefficient of the material is highly reduced and therefore, a surprisingly lower wear rate is obtained.

Wear process in these micro-nanostructured glass-ceramics and in a standard glaze might be phenomenological modelled (Fig. 5). When abrasion process starts in glass-ceramics, firstly, the glassy phase that, usually, is covering the surface of the material, is removed. In high crystallinity glass-ceramics, this glassy phase forms a very smooth layer because of the low vitreous phase content of the samples. Once glassy phase is removed from the surface, contact with crystals begins. In the case of micro-nanostructured glass-ceramics, nanoparticles regions form a resistant barrier with strong interfacial bondings which hinder the wear of the material when a body takes contact with its surface. These nanoparticles are progressively peeling-off because of the abrasion and favour the sliding over the glass-ceramic surface, which therefore reduce the friction coefficient acting as a self-lubrication process. The reduction of the contact area with microcrystals along with the nanocrystals distribution, considerably help to reduce the wear rate in the micro-nanostructured glass-ceramics, as well as the size of the wear track registered. In contrast, in the standard glaze surface, the larger amount of glassy phase produces greater amount of landslides of both the microcrystals and the vitreous phase, which also generates larger microcracks and deeper wear grooves, as a consequence of greater material spalling. This gives rise to a strongly damaged surface and a bigger wear track regarding glass-ceramics, as it is observed in Fig. 5a and b.

Considering the area produced by the wear indent and for the load applied of 6 N, the pressure generated in albite or anorthite-based glass-ceramics is ~6 GPa, while in the standard material tested is ~0.6 GPa (see supporting information for more details). These means that both glass-ceramics may withstand pressures of one magnitude order larger than the conventional material. In addition, the pressure exerted by an average person (~80 kg and typical dimensions of a foot of ~27 × 10 cm^2) or by loading/unloading heavy machine (5000 kg and ~0.53 × 0.20 m and ~0.13 × 0.20 m of front and rear tire) is ~0.002 GPa and ~0.2 GPa, respectively. Therefore, these new glass-ceramic materials would withstand the high pressures which usually undergo high transit soils, in particular the ones related to heavy machinery.

Attending to all the excellent mechanical properties analysed such as flexural strength, microhardness, fracture toughness, Young's modulus and wear resistance, it might be concluded that these novel materials are very suitable to be used in floor tile applications such as high pedestrian traffic applications where also support machinery traffic (e.g airports, supermarkets, shopping or entertainment large areas…), which, because of their beneficial properties, will enable a considerably improvement of mechanical behaviour regarding commercial products and significantly longer service life time. Besides, they may allow cost and energy saving, since these glass-ceramics are obtained by an easy conventional ceramic process successfully scaled up and using a sinterization cycle which only takes ~55 min. Moreover, the in situ development of micro-nanostructure of such materials acting as self-lubrication concept can be translated into other engineered ceramic materials that can thus benefit from an improvement in its mechanical properties, and in particular in their wear resistance.

4. Conclusions

A new glass-ceramic family with high crystallinity and a unique micro-nanostructure has been successfully designed. These engineered glass-ceramics results in a simultaneous improvement of flexural strength, microhardness, fracture toughness and tribological properties regarding standard materials used in tile industry. These novel materials show the highest microhardness reported for a glaze, up to 9.5 GPa, which supposes an enhancement of ~60% in relation to a traditional floor tile glaze and ~7% regarding the best reported value in literature for a glass-ceramic material. The hierarchical micro-nanostructuration of these glass-ceramics favours crack deflection, which implies a reduction of brittleness and a consequent increase of fracture toughness of ~40% regarding a standard glass-ceramic. Tribological properties showed a decrease in the friction coefficient of ~36% and in the wear rate of one magnitude order in relation to a standard glaze tested.

The analysis of worn and unworn surfaces of the samples reveal that nanocrystals work as solid lubricants, favouring body sliding over their surface and consequently reducing the friction coefficient, the wear rate and noticeably the damage suffered. In contrast, the absence of nanostructured areas in standard glazes causes a huge surface damage and remarkable material spalling.

All of these findings make hierarchical micro-nanostructured glass-ceramics very promising candidates to be used in high performance self-lubricating applications, being suitable for high pedestrian traffic applications and also supporting machinery traffic, which will enable a considerably improvement of mechanical behaviour and durability of

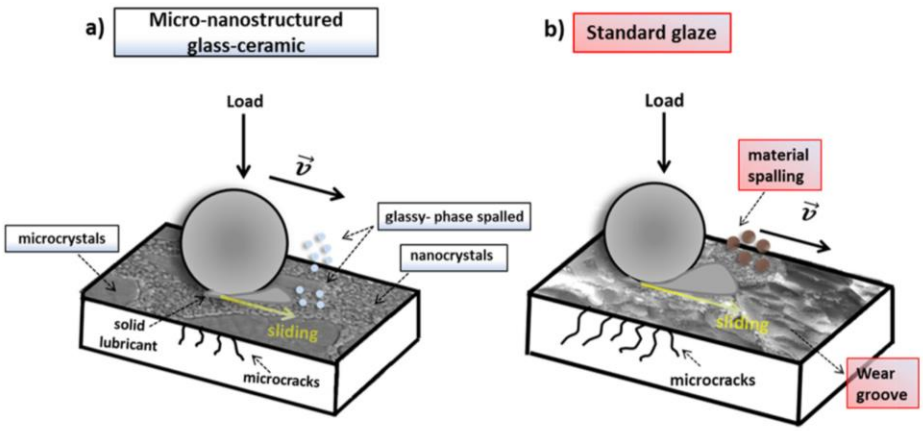

Fig. 5. a) Micro-nanostructured glass-ceramic after wear test, showing a hardly non-damaged surface thanks to the sliding favored by nanocrystals which work as solid lubricants; b) standard glaze after wear test, showing a damaged surface with wear grooves because of the large material spalling.

tiles. This work may serve as a reference for future works in the field of enhancement of wear resistance in brittle materials, because illustrates as microstructural engineering of glass-ceramic materials allow producing novel materials with improved mechanical performance.

CRediT authorship contribution statement

V. Fuertes: Investigation, Methodology, Formal analysis, Writing - original draft, Writing - review & editing. **M.J. Cabrera:** Funding acquisition. **J. Seores:** Funding acquisition. **D. Muñoz:** Funding acquisition. **J.F. Fernández:** Supervision, Conceptualization. **E. Enríquez:** Supervision, Conceptualization.

Acknowledgements

The authors express their thanks to the MINECO (Spain) project MAT2017-86450-C4-1-R, and projects CDTI (IDI-20130894 and IDI-20161120) for their financial support. Dra. E. Enriquez is also indebted to MINECO for a "Torres Quevedo" contract (ref: PTQ- 14-07289), which is co-financed with European Social Funds. The authors also thank J. Llorente and D. Soriano for their contribution to test of tribological properties and indentation tests, respectively.

Declarations of interest

V. Fuertes and J. F. Fernández declare no competing financial interest. M.J. Cabrera, J. Seores, D. Muñoz and E. Enríquez are employees of the company C.T. Vidres.

Data availability

The raw/processed data required to reproduce these findings cannot be shared at this time as the data also forms part of an ongoing study.

Appendix A. Supplementary data

See supporting information for more details of: XRD pattern of anorthite and albite based glass-ceramics and the standard glaze studied; loading–unloading curves for indentation loads of 0.5 N, 1 N, 5 N and 10 N; optical images from Multi-Mode Optical Profilometry showing differences in tortuosity and crack deflection; tabulated values of H, E and K_{IC} from indentation load vs penetration depth curves at different indentation loads; estimation of contact pressure for albite, anorthite-based glass-ceramics and the standard glaze. Supplementary data to this article can be found online at https://doi.org/10.1016/j.matdes.2019.107623.

References

[1] R. Casasola, J.M. Rincón, M. Romero, Glass-ceramic glazes for ceramic tiles: a review, J. Mater. Sci. 47 (2012) 553–582, https://doi.org/10.1007/s10853-011-5981-y.
[2] E.D. Zanotto, A bright future for glass-ceramics, Am. Ceram. Soc. Bull. 89 (2011) 609–612, https://doi.org/10.2217/fmb.11.55.
[3] H. Bach, D. Krause, Low Thermal Expansion Glass Ceramics, 2005https://doi.org/10.1007/3-540-28245-9.
[4] W. Höland, G. Beall, Glass–Ceramic Technology, 2012.
[5] R. Lisiecki, E. Czerska, M. Żelechower, R. Swadźba, W. Ryba-Romanowski, Oxyfluoride silicate glasses and glass-ceramics doped with erbium and ytterbium - an examination of luminescence properties and up-conversion phenomena, Mater. Des. 126 (2017) 174–182, https://doi.org/10.1016/j.matdes.2017.04.046.
[6] O. Bretcanu, S. Spriano, C.B. Vitale, E. Verné, Synthesis and characterization of coprecipitation-derived ferrimagnetic glass-ceramic, J. Mater. Sci. 41 (2006) 1029–1037, https://doi.org/10.1007/s10853-005-2636-x.
[7] R.D. Rawlings, J.P. Wu, A.R. Boccaccini, Glass-ceramics: their production from wastes-a review, J. Mater. Sci. 41 (2006) 733–761, https://doi.org/10.1007/s10853-006-6554-3.
[8] V. Fuertes, M.J. Cabrera, J. Seores, D. Muñoz, J.F. Fernández, E. Enríquez, Hierarchical micro-nanostructured albite-based glass-ceramic for high dielectric strength insulators, J. Eur. Ceram. Soc. 38 (2018) 2759–2766, https://doi.org/10.1016/j.jeurceramsoc.2018.02.009.
[9] I. Rozenstrauha, L. Krage, E. Lodins, V. Filipenkov, Functional properties of glass-ceramics for building application, Proc. 2nd Int. Conf. Adv. Constr. 2010, pp. 141–147.
[10] M.G. Rasteiro, T. Gassman, R. Santos, E. Antunes, Crystalline phase characterization of glass-ceramic glazes, Ceram. Int. 33 (2007) 345–354, https://doi.org/10.1016/j.ceramint.2005.10.002.
[11] C. Lira, A.P.N. de Oliveira, O.E. Alarcon, Sintering and crystallisation of CaO-Al2O3-SiO2 glass powder compacts, Glass Technol. 42 (2001) 91–96, https://doi.org/10.1016/j.ssi.2004.03.009.
[12] S. Ghosh, K.S. Pal, N. Dandapat, J. Ghosh, S. Datta, Glass-ceramic glazes for future generation floor tiles, J. Eur. Ceram. Soc. 33 (2013) 935–942, https://doi.org/10.1016/j.jeurceramsoc.2012.11.008.
[13] C. Ye, F. He, H. Shu, H. Qi, Q. Zhang, P. Song, et al., Preparation and properties of sintered glass-ceramics containing Au-Cu tailing waste, Mater. Des. 86 (2015) 782–787, https://doi.org/10.1016/j.matdes.2015.07.173.
[14] E. Medvedovski, Wear-resistant engineering ceramics, Wear. 249 (2001) 821–828, https://doi.org/10.1016/S0043-1648(01)00820-1.
[15] I.R. Sare, J.I. Mardel, A.J. Hill, Wear-resistant metallic and elastomeric materials in the mining and mineral processing industries—an overview, Wear. 250 (2001) 1–10, https://doi.org/10.1016/S0043-1648(01)00622-6.
[16] C.P. Doğan, J.a. Hawk, Role of composition and microstructure in the abrasive wear of high-alumina ceramics, Wear 225–229 (1999) 1050–1058, https://doi.org/10.1016/S0043-1648(99)00036-8.
[17] B.A. Latella, B.H. O'Connor, Effect of porosity on the erosive wear of liquid-phase-sintered alumina ceramics, J. Am. Ceram. Soc. 82 (1999) 2145–2149.
[18] M. Cain, R. Morrell, Nanostructured ceramics: a review of their potential, Appl. Organomet. Chem. 15 (2001) 321–330, https://doi.org/10.1002/aoc.153.
[19] J. Zhao, D. Xie, Effect of nanoparticles on wear resistance and surface hardness of a dental glass-ionomer cement, J. Compos. Mater. 43 (2009) 2739–2752, https://doi.org/10.1177/0021998309345341.
[20] W. Brostow, H. Lobland, N. Hnatchuk, J. Perez, Improvement of scratch and wear resistance of polymers by fillers including nanofillers, Nanomaterials. 7 (2017) 66, https://doi.org/10.3390/nano7030066.
[21] I. Journal, Influence of Nano-particle on the Wear behaviour of Thin Film Coatings A Review Influence of Nano-particle on the Wear behaviour of Thin Film Coatings, 13, 2018 4053–4058.
[22] H. Xiao, S. Liu, 2D nanomaterials as lubricant additive: a review, Mater. Des. 135 (2017) 319–332, https://doi.org/10.1016/j.matdes.2017.09.029.
[23] F.M. Bertan, O.R.K. Montedo, D. Hotza, C.R. Rambo, The effect of microstructural features on the mechanical properties of LZSA glass-ceramic matrix composites, Ceramica. 59 (2013) 351–359, https://doi.org/10.1590/S0366-69132013000300002.
[24] J. Reinosa, F. Rubio-marcos, E. Solera, F. Ferna, M.A. Bengochea, Sintering behaviour of nanostructured glass-ceramic glazes, Ceram. Int. 36 (2010) 1845–1850, https://doi.org/10.1016/j.ceramint.2010.03.029.
[25] H. Man, L. Hong-xia, Y. Xiu-jun, X. Hong-liang, Sintering and crystallization behaviour of nanostructured glass-ceramic glazes derived from industrial solid wastes, Glass Technol. Eur. J. Glass Sci. Technol. Part A 52 (2011) 169–174.
[26] H. Gleiter, Nanocyrstalline materials, Prog. Mater. Sci. 33 (1989) 223–315, https://doi.org/10.1016/0079-6425(89)90001-7.
[27] J. Zabinski, J. Sanders, J. Nainaparampil, S. Prasad, Lubrication using a microstructurally engineered oxide: performance and mechanisms, Tribol. Lett. 8 (2000) 103–116, https://doi.org/10.1023/A:1019187202237.
[28] M. Gajek, J. Partyka, Frits within a CaO-MgO-Al2O3-SiO2 system for glass-ceramic glazes: a comparison of laboratory and industrial applications, InterCeram Int. Ceram. Rev. 61 (2012) 283–285.
[29] E. Enríquez, V. Fuertes, M.J. Cabrera, J. Seores, D. Muñoz, J.F. Fernández, New strategy to mitigate urban heat island effect: energy saving by combining high albedo and low thermal diffusivity in glass ceramic materials, Sol. Energy 149 (2017) 114–124, https://doi.org/10.1016/j.solener.2017.04.011.
[30] V. Fuertes de la Llave, A. del Campo, J.F. Fernández, E. Enríquez, Structural insights of hierarchically engineered feldspars by confocal Raman microscopy, J. Raman Spectrosc. (2019) 1–14, https://doi.org/10.1002/jrs.5556.
[31] J.J. Reinosa, D.M.Y. Marero, A. Del Campo, M.Á. De La Rubia, J.F. Fernández, Chemical analysis with high spatial resolution by Rutherford backscattering and Raman confocal spectroscopies: surface hierarchically structured glasses, J. Am. Ceram. Soc. 96 (2013) 1783–1788, https://doi.org/10.1111/jace.12397.
[32] J.J. Reinosa, F. Rubio-Marcos, M.A. Bengochea, J.F. Fernández, Effect of fugitive phase addition on porosity evolution and properties of stoneware tiles, Adv. Appl. Ceram. 109 (2010) 219–224, https://doi.org/10.1179/174367509X12503626841514.
[33] K. Niihara, A fracture mechanics analysis of indentation-induced Palmqvist crack in ceramics, J. Mater. Sci. Lett. 2 (1983) 221–223, https://doi.org/10.1007/BF00725625.
[34] J. Llorente, B. Román-Manso, P. Miranzo, M. Belmonte, Tribological performance under dry sliding conditions of graphene/silicon carbide composites, J. Eur. Ceram. Soc. 36 (2016) 429–435, https://doi.org/10.1016/j.jeurceramsoc.2015.09.040.
[35] D. Klaffke, Fretting wear of ceramics, Tribol. Int. 22 (1989) 89–101, https://doi.org/10.1016/0301-679X(89)90169-2.
[36] ASTM G133-95, e1, Standard Test Method for Linearly Reciprocating Ball-on-Flat Sliding Wear, ASTM, International, West Conshohocken, PA, 2002www.astm.org.
[37] S.K. Das, K. Dana, Differences in densification behaviour of K- and Na-feldspar-containing porcelain bodies, Thermochim. Acta 406 (2003) 199–206, https://doi.org/10.1016/S0040-6031(03)00257-0.
[38] E. Barrachina, M. Esquinas, J. Llop, M.D. Notari, J.B. Carda, Development of a glass-ceramic glaze formulated from industrial residues to improve the mechanical properties of the porcelain stoneware tiles, Mater. Lett. 220 (2018) 226–228, https://doi.org/10.1016/j.matlet.2018.03.023.

[39] H. Kumchai, P. Juntavee, A.F. Sun, D. Nathanson, Effect of glazing on flexural strength of full-contour zirconia, Int. J. Dent. 2018 (2018)https://doi.org/10.1155/2018/8793481.
[40] B.E. Yekta, P. Alizadeh, L. Rezazadeh, Floor tile glass-ceramic glaze for improvement of glaze surface properties, J. Eur. Ceram. Soc. 26 (2006) 3809–3812, https://doi.org/10.1016/j.jeurceramsoc.2005.12.016.
[41] B.E. Yekta, P. Alizadeh, L. Rezazadeh, Synthesis of glass-ceramic glazes in the ZnO-Al2O3-SiO2-ZrO2 system, J. Eur. Ceram. Soc. 27 (2007) 2311–2315, https://doi.org/10.1016/j.jeurceramsoc.2006.08.009.
[42] Y.V. Milman, A.A. Golubenko, S.N. Dub, Indentation size effect in nanohardness, Acta Mater. 59 (2011) 7480–7487, https://doi.org/10.1016/j.actamat.2011.08.027.
[43] S.J. Bull, T.F. Page, E.H. Yoffe, An explanation of the indentation size effect in ceramics, Philos. Mag. Lett. 59 (1989) 281–288, https://doi.org/10.1080/09500838908206356.
[44] A. Ruiz-Moreno, P. Hähner, Indentation size effects of ferritic/martensitic steels: a comparative experimental and modelling study, Mater. Des. 145 (2018) 168–180, https://doi.org/10.1016/j.matdes.2018.02.064.
[45] J.B. Wachtman, W. Roger Cannon, M.J. Matthewson, Mechanical Properties of Ceramics, Second ed. John Wiley & Sons, Inc., 2009https://doi.org/10.1002/9780470451519.
[46] V. Biasini, M. Dondi, S. Guicciardi, C. Melandri, M. Raimondo, E. Generali, et al., Mechanical properties of porcelain stoneware tiles: the effect of glass-ceramic systems, Key Eng. Mater. 206–213 (2002) 1799–1802, https://doi.org/10.4028/www.scientific.net/KEM.206-213.1799.
[47] F. Andreola, M.I. Martín, A.M. Ferrari, I. Lancellotti, F. Bondioli, J.M. Rincón, et al., Technological properties of glass-ceramic tiles obtained using rice husk ash as silica precursor, Ceram. Int. 39 (2013) 5427–5435, https://doi.org/10.1016/j.ceramint.2012.12.050.
[48] D. De Graaf, M. Braciszewicz, H.T. Hintzen, M. Sopicka-Lizer, G. De With, The influence of the composition on (the load-dependence of) the microhardness of Y-Si-Al-O-N glasses as measured by Vickers indentation, J. Mater. Sci. 39 (2004) 2145–2149, https://doi.org/10.1023/B:JMSC.0000017777.05637.a6.
[49] P. Zhang, S.X. Li, Z.F. Zhang, General relationship between strength and hardness, Mater. Sci. Eng. A 529 (2011) 62–73, https://doi.org/10.1016/j.msea.2011.08.061.
[50] M. Guazzato, M. Albakry, S.P. Ringer, M.V. Swain, Strength, fracture toughness and microstructure of a selection of all-ceramic materials. Part II. Zirconia-based dental ceramics, Dent. Mater. 20 (2004) 449–456, https://doi.org/10.1016/j.dental.2003.05.002.
[51] V. Fuertes, M.J. Cabrera, J. Seores, D. Muñoz, J.F. Fernández, E. Enríquez, Microstructural study of dielectric breakdown in glass-ceramics insulators, J. Eur. Ceram. Soc. 39 (2019) 376–383, https://doi.org/10.1016/j.jeurceramsoc.2018.08.044.
[52] S. Kitouni, A. Harabi, Sintering and mechanical properties of porcelains prepared from algerian raw materials, CerâMica. 57 (2011) 453–460, https://doi.org/10.1590/S0366-69132011000400013.
[53] J.C. Le Huec, T. Schaeverbeke, D. Clement, J. Faber, A. Le Rebeller, Influence of porosity on the mechanical resistance of hydroxyapatite ceramics under compressive stress, Biomaterials. 16 (1995) 113–118, https://doi.org/10.1016/0142-9612(95)98272-G.
[54] M.P. Gómez-Tena, J. Gilabert, J. Toledo, M.J. Ibáñez, A. Muñoz, Determination of the wear resistance of traditional ceramic tile glazes using a pin-on-disk tribometer, Int. J. Surf. Sci. Eng. 5 (2011) 272–285, https://doi.org/10.1504/IJSURFSE.2011.044277.
[55] L. Carbajal, F. Rubio-Marcos, M.a. Bengochea, J.F. Fernandez, Properties related phase evolution in porcelain ceramics, J. Eur. Ceram. Soc. 27 (2007) 4065–4069, https://doi.org/10.1016/j.jeurceramsoc.2007.02.096.
[56] R. Daniel, M. Meindlhumer, W. Baumegger, J. Zalesak, B. Sartory, M. Burghammer, et al., Grain boundary design of thin films: using tilted brittle interfaces for multiple crack deflection toughening, Acta Mater. 122 (2017) 130–137, https://doi.org/10.1016/j.actamat.2016.09.027.
[57] C. Wang, K. Shi, C. Gross, J.M. Pureza, M. de Mesquita Lacerda, Y.W. Chung, Toughness enhancement of nanostructured hard coatings: design strategies and toughness measurement techniques, Surf. Coat. Technol. 257 (2014) 206–212, https://doi.org/10.1016/j.surfcoat.2014.08.018.
[58] J.K. Lancaster, A review of the influence of environmental humidity and water on friction, lubrication and wear, Tribol. Int. 23 (1990) 371–389, https://doi.org/10.1016/0301-679X(90)90053-R.
[59] K.J. Kubiak, T.W. Liskiewicz, T.G. Mathia, Surface morphology in engineering applications: influence of roughness on sliding and wear in dry fretting, Tribol. Int. 44 (2011) 1427–1432, https://doi.org/10.1016/j.triboint.2011.04.020.
[60] S. Shailesh Kumar, S. Chattopadhyaya, A. Pramanik, S. Kumar, N. Gupta, Influence of nano-particle on the wear behaviour of thin film coatings:a review, Int. J. Appl. Eng. Res. 13 (2018) 4053–4058.
[61] R. Pina-Zapardiel, A. Esteban-Cubillo, J.F. Bartolomé, C. Pecharromán, J.S. Moya, High wear resistance white ceramic glaze containing needle like zircon single crystals by the addition of sepiolite n-ZrO2, J. Eur. Ceram. Soc. 33 (2013) 3379–3385, https://doi.org/10.1016/j.jeurceramsoc.2013.05.033.
[62] S. Heo, S. Kim, U. Kim, J. Pee, Y. Han, S. Kim, et al., Tribological behavior of whiteware with different transparent glazes, J. Korean Ceram. Soc. 52 (2015) 186–191, https://doi.org/10.4191/kcers.2015.52.3.186.
[63] Y. Wang, S.M. Hsu, Wear and wear transition mechanisms of ceramics, Wear. 195 (1996) 112–122, https://doi.org/10.1016/0043-1648(95)06800-7.

Supporting information

Enhanced Wear Resistance of Engineered Glass-ceramic by Nanostructured Self-lubrication

V. Fuertes*[1], M.J. Cabrera[2], J. Seores[2], D. Muñoz[2], J. F. Fernández[1], E. Enríquez[2]

[1]Dept. Electrocerámica, Instituto de Cerámica y Vidrio, CSIC, Kelsen 5, 28049, Madrid, Spain.

[2]Centro tecnológico Vidres, S.L., Ctra. Onda, Km 3.4, 12540 Villareal, Castellón, Spain

S1. XRD pattern of anorthite, albite based glass-ceramic and standard glaze

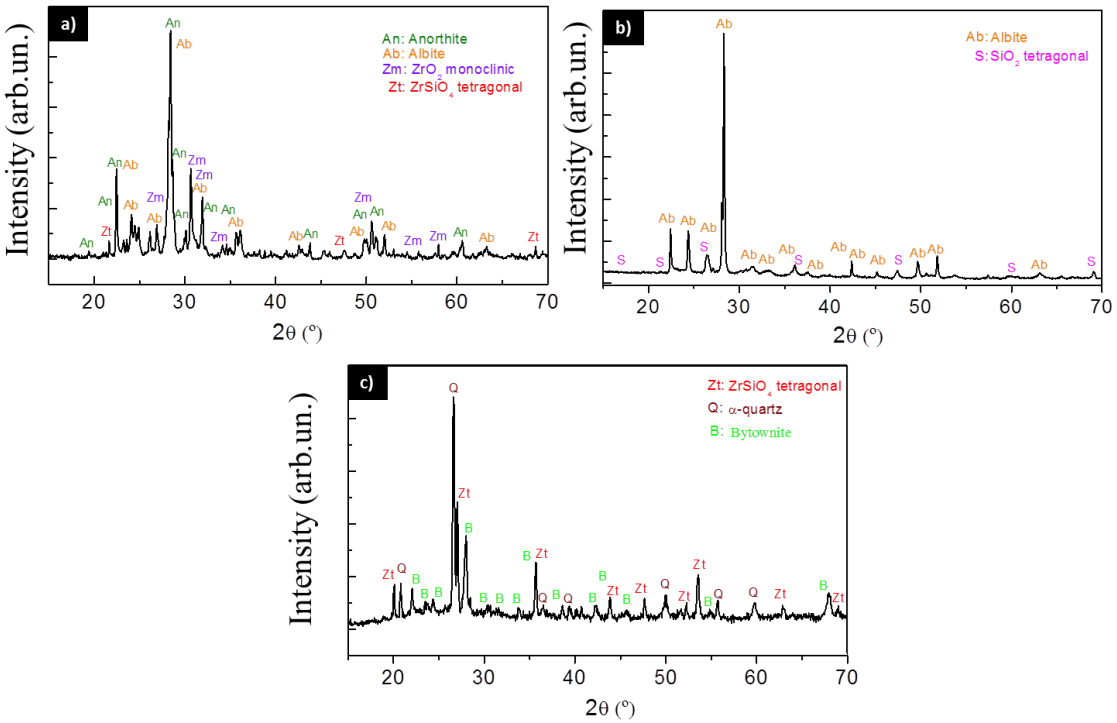

Figure S1. XRD pattern for **a)** anorthite and **b)** albite based glass-ceramics and for **c)** standard glaze studied in this work.

In figure S1 is plotted the XRD pattern for anorthite (figure S1a) and albite (figure S1b) based glass-ceramics and the standard glaze studied in this work (figure S1c). It might be observed the different phases present in each material, according to the legend. In the case of the standard material, noticeable content of quartz and zircon was found as well as bytownite, which is a calcium rich member of the plagioclase solid solution series of feldspar with a content of anorthite in the range of 70-90 %, and albite between 30 % and 10 %, respectively. This material was chosen due to the similar feldspars composition regarding albite and anorthite.

The broad band located between 15° and 35° 2θ allows us to estimate the glassy phase content present in the sample by means of the diffraction software Bruker's Diffrac. Eva. For anorthite sample it was estimated to be about 9 Vol. % and about 6 Vol. % in albite sample. This glassy phase content is lower than that in the standard glaze (∼56% Vol.% of glassy phase), which favour to improve the mechanical properties, as it is discussed in the manuscript.

S2. Loading-unloading curves for anorthite, albite-based glass-ceramic and standard glaze

Figure S2a-d show load versus penetration depth curves, obtained from Vickers indentation tests, measured for the standard glaze (green) and the micro-nanostructured albite (blue) and anorthite-based glass-ceramics at loads of 0.5 N, 1 N, 5 N and 10 N. In the manuscript only the loading-unloading curve for 5 N is presented, as a representative example of the rest of measurements.

Loading curves approximately follow the same tendency in the three materials for each indentation load *(figures S2a-d*). For all loads, the unloading curves of the standard glaze are slightly shifted regarding both micro-nanostructured glass-ceramics, increasing it as indentation load increases, which indicate a different mechanical response between each other. This difference in the penetration depth ranges from 0.2 μm (at 0.5N) up to 0.5 μm (at 10 N). This shift in the standard material tested in relation to the micro-nanostructured glass-ceramics is caused by a larger amount of energy stored after the loading which means that the novel glass-ceramics are harder than the standard material. From these curves, Vickers microhardness (H) and Young´s modulus (E) may be obtained. Values of H_V tabulated in table S1, verify as both micro-nanostructured glass-ceramics are harder than the standard one, as it was discussed previously.

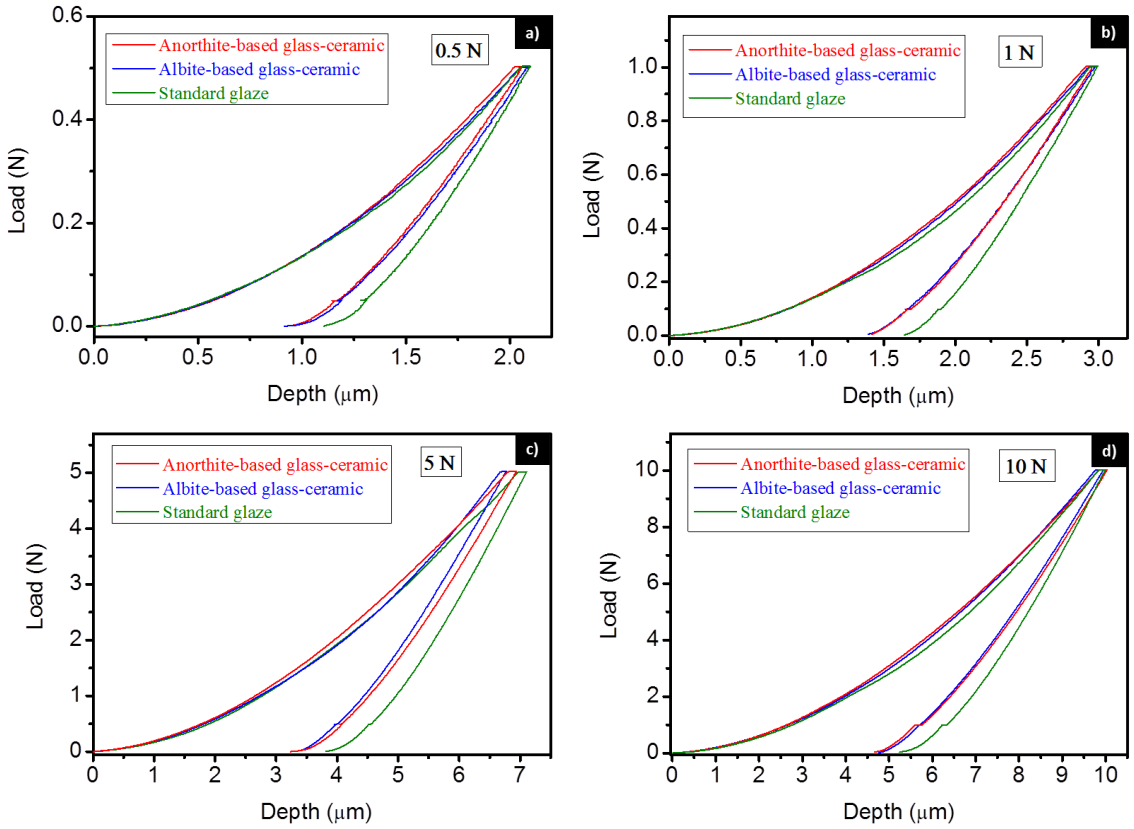

Figure S2. Loading–unloading curves for albite-based (blue colour), anorthite-based glass ceramics (red colour) and the standard glaze tested (green colour), for different indentation loads: **a)** 0.5 N; **b)** 1 N; **c)** 5 N and **d)** 10 N.

From loading-unloading curves of figure S2a-d, Vickers microhardness (H) and Young´s modulus (E) are obtained (table S1). The general trend observed in the values for both micro-nanostructured glass-ceramics is a decrease of them as indentation load increases, which is known as indentation size effect (ISE). In the case of the standard glaze tested, load independent microhardness and Young´s modulus regime is reached at 5 N. This increase of hardness in both micro-nanostructured glass-ceramics is mainly attributed to the unique micro-nanostructure designed, as it is deeply explained in the manuscript.

Materials	H (GPa)				E (MPa)				K_{IC} (MPa·m$^{1/2}$)	
	0.5 N	1 N	5 N	10 N	0.5 N	1 N	5 N	10 N	5 N	10 N
Albite-based glass-ceramic	9.5	9.4	8.6	7.9	77.5	76.4	75.6	66	2.1	2.1
Anorthite based glass ceramic	9.4	9.2	8.3	7.3	77.1	76.3	76.1	66.6	1.9	2.1
Standard glaze	8.5	8.1	7.3	7.3	77.2	73.2	73.9	74	1.5	1.5

Table S1. Calculated values of H and E from indentation load vs penetration depth curves in albite, anorthite-based glass-ceramics and the standard glaze, at different indentation loads: 0.5 N, 1 N, 5 N and 10 N. K_{IC} was only calculated for loads of 5 N and 10 N because for loads below 5 N any cracks in the samples were observed.

Moreover, from Vickers indentation imprints fracture toughness (K_{IC}) may be estimated by using eq.1, proposed by Nihiira, one of the experimental expressions most used and taking into account the characteristic of the indentation imprint (a and c parameters) as well as values of microhardness and Young's modulus of table S1.

$$K_{IC} = 0.067 \cdot \left(\frac{E}{H_V}\right)^{2/5} \cdot H_V \cdot a^{1/2} \cdot \left(\frac{c}{a}\right)^{-3/2} \quad (1)$$

K_{IC} was only calculated for loads of 5 N (figure 2a-c) and 10 N (not showed), because for loads below 5 N any cracks in the samples were observed. As occurred with hardness, K_{IC} is higher in both micro-nanostructured glass-ceramics, which is mainly attributed to the unique micro-nanostructure designed, since it may favour crack deflection, reducing brittleness.

S3. Multi-Mode Optical Profilometry of cracks

The hierarchical micro-nanostructured glass-ceramics (figure S3a) have nano and microstructured zones which suppose larger amount of grain boundaries regarding the standard glaze (figure S3b). Cracks generated after indentation test preferentially propagates along these grain boundaries, being deflected at each one. Consequently, both micro-nanostructured glass-ceramics displays a more tortuous and deflected crack path, as it is observed in figure S3a, than the standard glaze tested, which contribute to the increase of fracture toughness (table S1) concerning the standard glaze. At the bottom of figure S3, it is presented a schematic image which illustrates the crack deflection mechanism previously discussed.

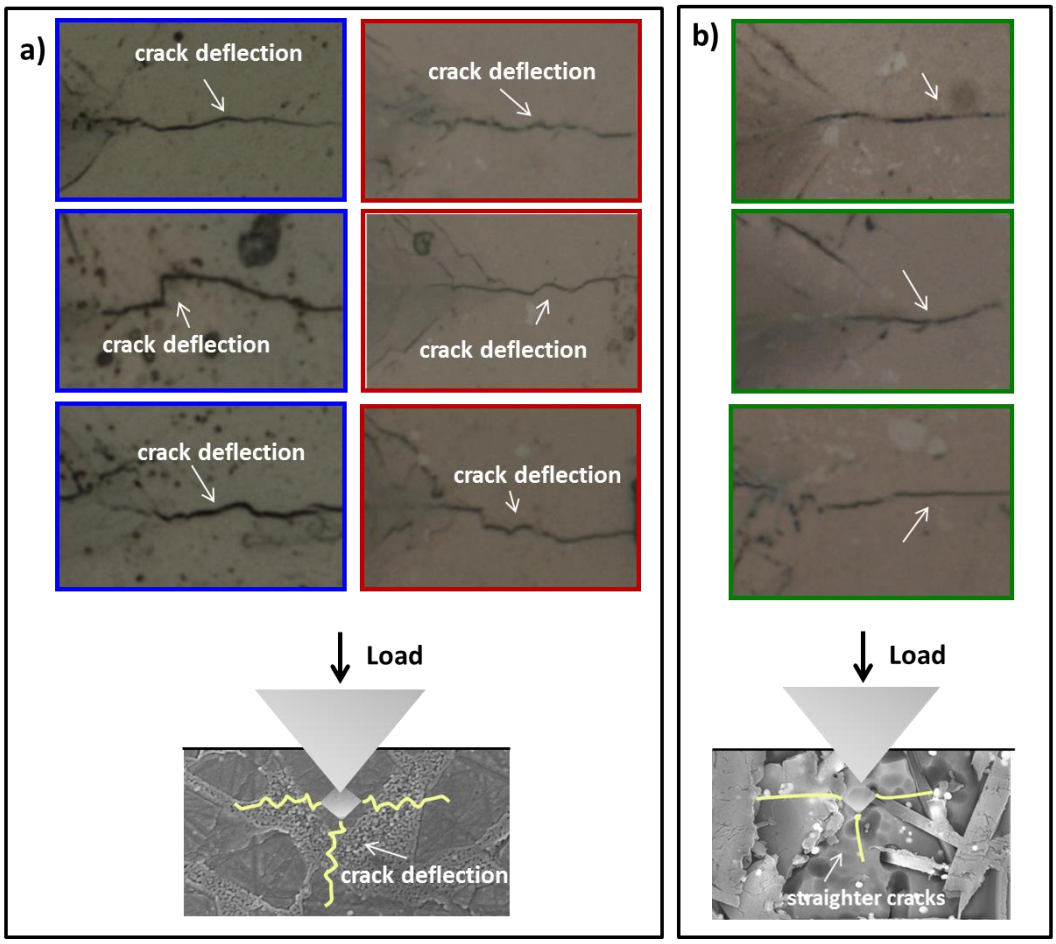

Figure S3. At the top, some optical images taken by Multi-Mode Optical Profilometry showing a more tortuous and deflected crack path in: **a)** albite (blue box) and anorthite-based glass-ceramic (red box) than in **b)** the standard glaze (green box). At the bottom, a schematic image illustrating the process observed in each case.

S4. Estimation of contact pressure

The contact pressure for albite, anorthite-based glass-ceramics and the standard glaze was estimated by eq.2 considering that the applied load was 6 N (F) and the area of wear tracks measured (S) by the profiler is ~10^{-3} mm^2 in both albite and anorthite-based glass-ceramics and ~10^{-2} mm^2 in the standard glaze.

$$P = \frac{F}{S} \quad (2)$$

ARTÍCULO 4. Absence of surface flaking in hierarchical glass-ceramic coating: high impact resistant ceramic tiles

E. Enríquez, V. Fuertes, M.J. Cabrera, Jaime Seores, D. Muñoz, J. F. Fernández

Journal of the European Ceramic Society, bajo revision (major revision).

Factor de impacto: 3,794 (según JCR Edition Science 2017).

Absence of surface flaking in hierarchical glass-ceramic coating: high impact resistant ceramic tiles

E. Enríquez*[1,2], V. Fuertes[1], M.J. Cabrera[2], Jaime Seores[2], D. Muñoz, J. F. Fernández[1]

[1]Dept. Electrocerámica, Instituto de Cerámica y Vidrio, CSIC, Kelsen 5, 28049, Madrid, Spain.

[2]Centro tecnológico Vidres, S.L., Ctra. Onda, Km 3.4, 12540 Villareal, Castellón, Spain

Abstract

The impact resistance method is a useful procedure to determine the tile resistance. While other works are focused on modifying the tile support to improve the impact resistance, in this work, a new glass-ceramic material was developed to used it as glaze coating in order to relax impact tensions. This material possesses a hierarchical nano-microstructure consisted of microcrystal surrounded by nanostructured regions having low glassy phase, which is considered responsible for tension relaxations. The resilience coefficient measured in conventional and glass-ceramic glazes presents little differences (0.85-0.88). However, impact damages on the surface are totally inhibited for glass-ceramic coating while the conventional one suffers great flaking. These damages were analyzed by Optical profilometry and FESEM to compare the impact resistance and to correlate it with its microstructure. The results confirm that the micro-nanostructured coating paves the way to improve impact resistance in ceramic materials where surface damage is a critical parameter.

*Corresponding author. Tlf:+34 91 735 58 40; Ext 1076. Fax: +34 91 735 58 43. E-mail address: esther@icv.csic.es (E. Enríquez)

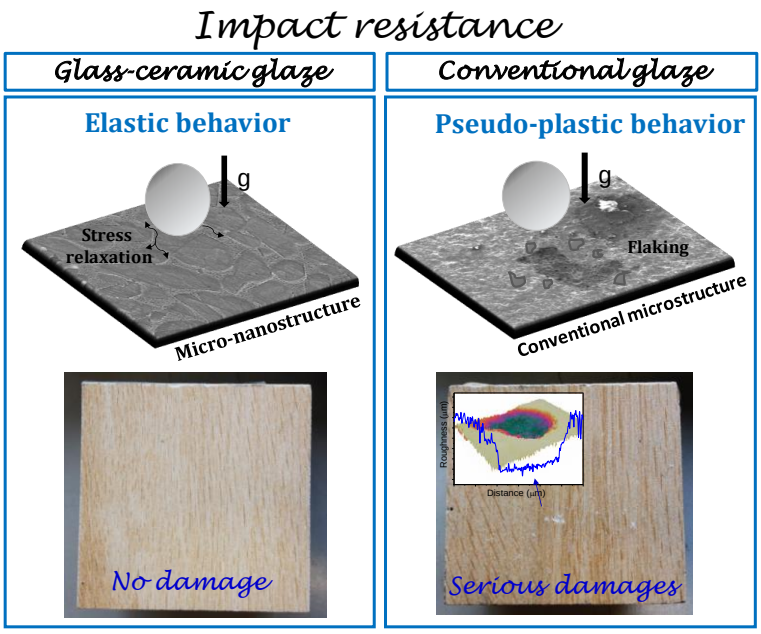

Keywords: Impact resistance; glass-ceramic; nano-microstructure; elastic behavior.

1. Introduction

Ceramic materials have excellent durability properties that make them suitable for application as building materials. One of the most critical aspects at present, consists in their low impact resistance, since they have good mechanical properties but they are brittle. In particular, for ceramic tile floors, the fall of a heavy object can cause the appearance of surface flaking. Moreover, the new manufacturing trends in ceramic tiles having enlarge sizes and low thickness, further complicates this problem, because it is well-known that the impact resistance strongly depends on the tile thickness, being more resistant as larger the thickness is. In fact, the British standard 1281:1966, stablishes the dropped height of the Steel ball (that is, the energy) appropriate for different glaze thicknesses [1,2] . The resistance to impact has been significantly improved in ceramic materials for armoring, where pre-stressed materials have been developed and composite materials with laminated and gradient composition using structural ceramics [3,4]. Improved glass-ceramic materials were also proposed for transparent armor applications [5].

These new requirements of the ceramic trade, make it necessary to improve the impact resistance response. The impact resistance method provides the coefficient of restitution which gives information about the inelastic deformation of the material. This coefficient is usually related with the surface damage produced by the ball impact. The impact resistance mainly depends on

the internal tension, superficial cracks, critical defects, the thickness and porosity of the material [6,7]. In this context, previous researches are focused on improving the impact resistance by adding Al_2O_3 particles [8,9], using microwave energy for the ceramic tiles processing [10], imitating layered structures observed in natural elements [11] or adding metallic nickel inclusions in a ceramic matrix [12]. Thus, most of the approaches are focused on improving mechanical properties of the ceramic tile body. It is also proposed to remove glaze coating for improving mechanical properties of ceramic tiles, since it is the most brittle layer [6]. In some cases, due to the difficulty of avoiding surface damages, new solutions have even been proposed, such as decorate the tile in bulk in order to hide flaking or cracks that can be produced by a collision.

In previous works, a glass-ceramic glaze based on Na-rich plagioclase has been developed, presenting a unique nano-microstructure [13,14], which improves glaze mechanical properties achieving excellent tribological properties, flexural strength and hardness response [15,16]. Consequently, in this work, two kind of samples were studied, a conventional tile (stoneware support, engobe and glassy glaze) and a novel tile where the glassy glaze has been substituted by this new engineered material, maintaining the conventional stoneware support and engobe, in order to improve impact resistance without the necessity of increasing its thickness. The difference observed in the impact damages are then correlated with the different composition, microstructure and properties of both samples, demonstrating the effectiveness of the glass-ceramic glaze.

2. Experimental procedure

2.1. Sample preparation

The glass-ceramic glaze based on Na-rich plagioclase feldspar was prepared by mixing the precursors, kaolin (Molcasa, d50 = 5.34 μm) and frit in a weight proportion of 10/90, respectively, with a milling process in an alumina ball mill for 20 min with 37 wt% of water [13], following the standard ceramic processing for the tile industry. In addition, a standard commercial glaze was also used for comparative purposes. Both materials were deposited on the same kind of porcelain stoneware support of ~1cm in thickness, through water falling deposition process and were thermally treated at 1220ºC-6min through a fast sintering process. In addition, an engobe layer of ~ 90 μm of thickness was deposited between the glaze and support in order to avoid dilatation and diffusion problems. The chemical compositions of glass-ceramic and conventional glazes, expressed in terms of equivalent oxides, are showed in Table 1. The crystalline phases of samples can be extracted from the XRD patterns shown in figure 1, where it is possible to

observe that glass-ceramic glaze is composed of Na-rich plagioclase and quartz, and conventional glaze is composed of quartz, zircon and bytownite (a calcium rich member of the plagioclase solid solution series of feldspar). The glassy phase of the conventional (~ 56 %) and the Na-rich plagioclase glass-ceramic (~6 %) glazes was calculated from the broad band located between 15° and 35° in the XRD patterns by means of the diffraction software Bruker's Diffrac. Eva. The porosity of samples is 8.3 % and 3.1 % for conventional and glass-ceramic glazes, respectively. In order to determine the roughness contribution to the impact resistance, a feldspar granulate was deposited on the top of the glass-ceramic glaze before sintering. Moreover, samples were decorated with wood motives by using inkjet printing, in such a way that, when damage occurs, this decorative coating is removed, leaving a more obvious imprint. Nevertheless, the images of the damage caused to undecorated samples can be seen in figure S2 of supporting information.

Oxides wt %	**Na-rich plagioclase**	***Conventional***
SiO_2	51.63	43.70
ZrO_2	-	4.07
SrO	8.05	3.28
Na_2O	2.68	1.50
K_2O	1.46	1.52
Al_2O_3	21.14	32.20
ZnO	1.10	2.14
CaO	10.47	2.98
B_2O_3	1.40	1.50
P_2O_5	0.84	2.88
MgO	1.04	1.63
BaO	-	2.12
*Others**	0.21	-

Table 1. Chemical composition of the Na-rich plagioclase glass-ceramic material and conventional glaze, expressed as equivalent oxides. The minority components (< 1 wt%) are all included in others. *Others: mainly TiO_2 and Fe_2O_3.

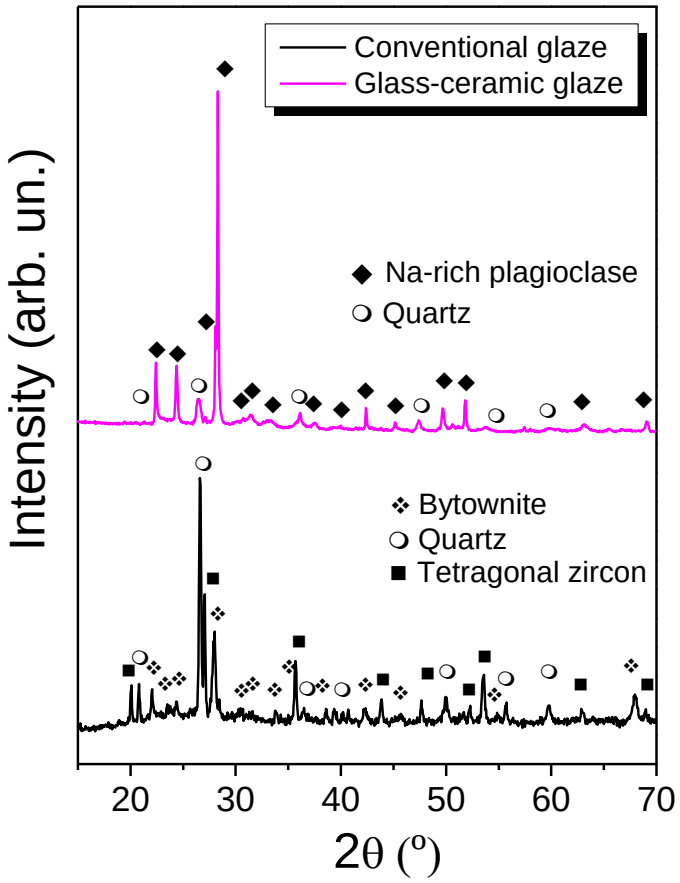

Figure 1: XRD pattern for Na-rich plagioclase glass-ceramic glaze and conventional glaze studied in this work.

2.2. Characterization

Chemical composition characterization was carried out by a X-Ray Fluorescence Spectrometer (Philips MagiX, equipped with a rhodium x-ray tube and beryllium window). The structural characterization of samples was performed by X-ray diffraction (XRD) in a diffractometer Bruker D8 Advance with Cu Kα radiation, 40 kV and 40 mA and the crystalline phases identification was carried out by comparison with JCPDS patterns. The glassy phase content was calculated through the areas integration by means of the diffraction software Bruker's Diffrac.Eva.

Impact test was carried out by Gabtec impact tower with a steel ball of 19.00 ± 0.05 mm in diameter, following the normative ISO 10545 [17], which is based on the rebound of the ball dropped from a height of 120 cm onto a tile fixed in a mortar support of 6 cm of thickness, applying weak impact energy (0.27J). A ceramic standard provided by the supplier was used for calibration. Samples should be of 75 mm x 75 mm dimensions and the measurements should be repeated for 5 specimens of each. This technique provides the coefficient of restitution (e) of studied materials, which gives information of the inelastic deformation of the material. That is, when e = 0, the collision between two materials is considered completely inelastic, and when e = 1, the collision is elastic (all the energy is conserved). However, this method does not measure the damage produced in the ceramic tiles after impact. For this purpose, ZETA-20 Multi-mode Optical Profiler was used to register the surface profile of the impact imprints of damaged samples. According to the French Standard 3515 of CSTB for glazed tiles, the surface damage can be classified into different levels:

- Level 0: None visible damage on the tile surface.
- Level 1: Circular lines around the impact. No radial cracks or flaking of material.
- Level 2: Radial cracks of l ≤ 5 mm in length. No flaking of material.
- Level 3: Radial cracks of 5 < l ≤ 10 mm. No flaking of material.
- Level 4: Radial cracks of l > 10 mm. No flaking of material.
- Level 5: Flaking of material.

The combination of both parameters, allow us to relate the resilient coefficient with the surface damage. In addition, microstructural characterization of samples was studied by means of Field Emission Scanning Electron Microscopy (FESEM) using a Hitachi S-4700, with a resolution of 1.5 nm at 20 kV.

3. Results and discussion

3.1. Microstructure of the studied glazes

Figure 2 shows the FE-SEM micrographs of conventional (figures 2a and d) and glass-ceramic (figures 2b and e) glazes, and of the granulated layer onto glass-ceramic glaze (figures

2c and f). Figures 2a, b and c show the distribution of the glazed and engobe layers and the stoneware support of each sample, where it is possible to extract the thickness of each one, which are in the range of 270 - 300 µm for glazes and 70 – 100 µm for engobe. In addition, in these figures, it is possible to verify the interface between the three layers, where it is observed that a correct match is produced between support-engobe and engobe-glaze, since no curvature or decoupling is produced. Moreover, the thermal expansion coefficient of both samples are very similar, 53·10-7 $ºC^{-1}$ for glass-ceramic glaze and 56·10-7 ºC-1 for conventional glaze, which match well with the engobe and the stoneware, that have thermal expansion of 70.8·10-7 $ºC^{-1}$ and 70.4·10-7 $^{ºC-1}$, respectively. Glazes should have slightly lower thermal expansion coefficient than the support that results in a slight compression of the glaze layer during the sintering. This fact improved the mechanical strength response of the glaze. However, the ceramic tile has a high planarity which indicates a low effect of the glaze on the support according to the requirements of the ceramic product. Conventional glaze presents a microstructure composed of elongated anorthite feldspars (up to 17 µm) along with quartz and zircon crystals, as seen in figure 2d. In addition, large amount of glassy phase is also observed. In the case of glass-ceramic glaze, it shows a dual nano-microstructure formed by Na-rich plagioclase microcrystals of up to 3 µm in length, surrounded by nanocrystals of the same material that provides a hierarchical micro-nanostructure (figure 2e). In this case, the glassy phase is located in the nanostructured region, and is much lower than in the conventional glaze. The granulates onto the glass-ceramic glaze form hillocks of up to 100 µm, as seen in figure 2c, making the surface rougher. The granulated microstructure is formed by elongated feldspars microcrystals of ≈ 12µm in length (figure 2f).

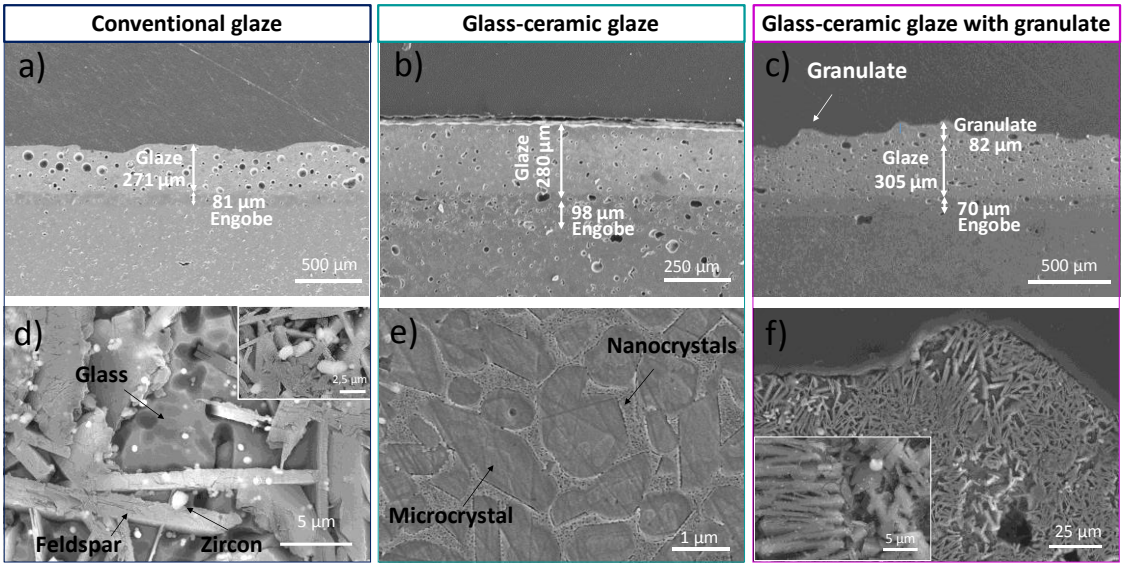

Figure 2: FE-SEM micrographs of conventional (**a** and **d**) and hierarchical glass-ceramic (**b** and **e**) glazes; granulate deposited onto glass-ceramic glaze surface (**c** and **f**).

3.2. Impact resistance test of glazes

The impact resistance test was carried out for the three samples and Table 2 shows the resilience coefficients along with the average roughness values. Roughness of conventional and glass-ceramic glazes are similar, but when granulates are deposited, roughness increases up to 40 times. The resilience coefficient values obtained are typical of stoneware tiles [2,18–20]. The hierarchical glass-ceramic glaze has a slightly larger resilience coefficient than the conventional one, however, they are very similar, indicating that the resilience of the tile depends more on the whole system (glaze-engobe-stoneware) than on the surface coating. That is, since the distribution of layers are the same, with similar thicknesses and the same composition for the support and the engobe, and, in addition, the interfaces of both samples are correctly matched, the average calculation of the resilient coefficient is similar. However, the glaze with granulates deposited onto the surface of the glass-ceramic coating, worsen its value showing that the surface roughness affects negatively the impact resistant, because it absorbs inhomogeneously the impact and concentrated the stress at the protruded regions. Therefore, from these results it is inferred that, in the same surface conditions, the resilience coefficient is more influenced by the bulk composition than by the surface coating.

Glaze coating	**Average surface roughness (μm)**	**Average resilience coefficient**	**Damage marks**
Conventional	17.9 ± 0.5	0.85 ± 0.02	Yes
Hierarchical glass-ceramic glaze	12.9 ± 0.5	0.88 ± 0.02	No
Hierarchical granulated glass-ceramic glaze	52.2 ± 0.5	0.80 ± 0.02	Yes

Table 2: Resilience coefficient of the conventional, hierarchically glass-ceramic and granulated glass-ceramic glazes, obtained by the impact resistant test.

On the other hand, it is also important to point out that, in this case, the damage produced by the ball impact is not clearly correlated with the resilience coefficient, since despite they have similar coefficient, conventional and glass-ceramic coatings present different surface damage degree. Figure 3 shows the images of the white glazes after the impact test (figures 3a and b) and the optical images when a dye (methylene blue) is used to highlight the damage (figures 3c, 3d, 3e, and 3f). As can be seen, conventional glaze undergoes severe damage with material flaking (level 5 according French Standard). The dye clearly reveals the ball impacts (figure 3c) which are more pronounced on the first rebound, and smaller on the seconds. Figure 3e shows an enlargement of the main damage where it is possible to observe that the glaze has been removed leaving a hole of more than 2000 μm in length. However, the glass-ceramic glaze does not present any damage (figure 3b) and when the dye is used (figure 3d), only a slight glaze coloring is produced, but not damages are revealed. The enlarged optical image (figure 3f) confirms these results, since a homogeneous surface is observed. The optical images of the decorated granulated glass-ceramic glaze, when a dye is used to reveal damages, can be seen in figure S1 of supporting information.

It is known, that the energy lost in the impact is related with the number and size of the flaky fragments [21]. In this case, the initial impact energy is low (0.27J) and the damage and flaky material is a very low proportion regarding the whole system (glaze – engobe – support). Therefore, the energy lost during the impact, which causes the flaking in the case of the conventional tile, is very low and does not significantly affect the ball rebound, resulting in no significant differences in the resilience coefficient. Nevertheless, the difference detected might be due to these energy differences. It is worth to remark the total absence of damage marks in the

tile where the hierarchical glass-ceramic material is used as coating, which would classify it as level 0 in damage regarding the French Standard 3515 of CSTB. This result is unusual because, up to know, the appearance of surface flaking is inherent to the brittle behavior of conventional glaze coating for stoneware tiles.

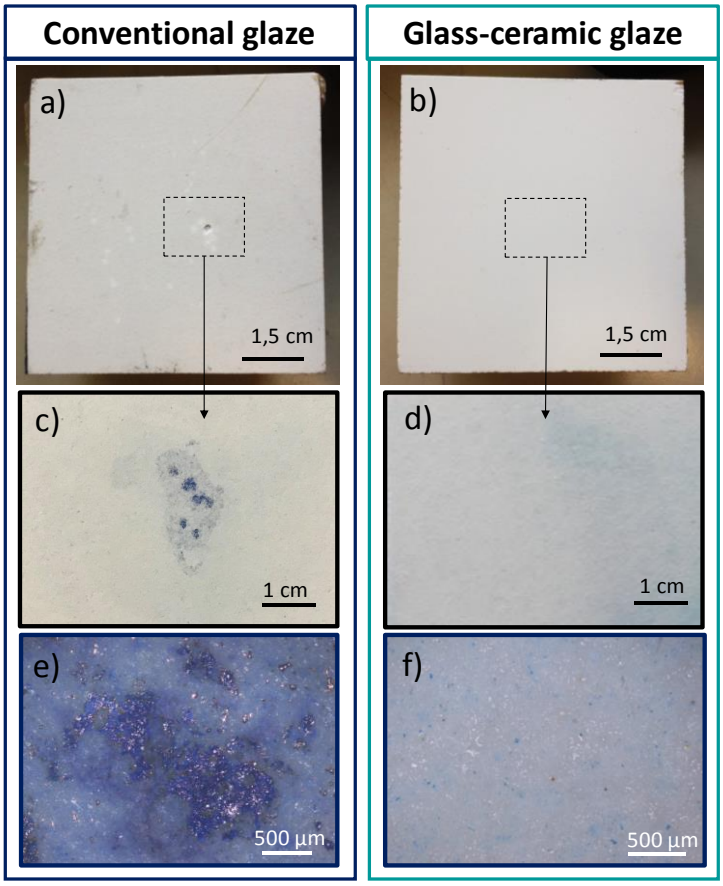

Figure 3: Images taken after impact test and optical images taken when a dye is used to reveal the damages in white conventional (**a, c** and **e**) and white hierarchical glass-ceramic (**b, d** and **f**) glazes, where it is possible to check the damage produced by the steel ball.

Figure 4 shows the images and the FESEM micrographs of conventional glaze (figures 3a and 3d), hierarchical glass-ceramic glaze (figures 3b and 3e) and granulated glass-ceramic glaze (figures 3c and 3f) with decorative motives, after the impact resistance test, where it is also possible to check the damage caused by the steel ball because of the contrast produced by the lack of decoration in the damage. The green and blue squares shown in the FESEM micrographs (figures 3d and 3f) represent the regions where a further analysis of the damage produced was carried out and will be shown later.

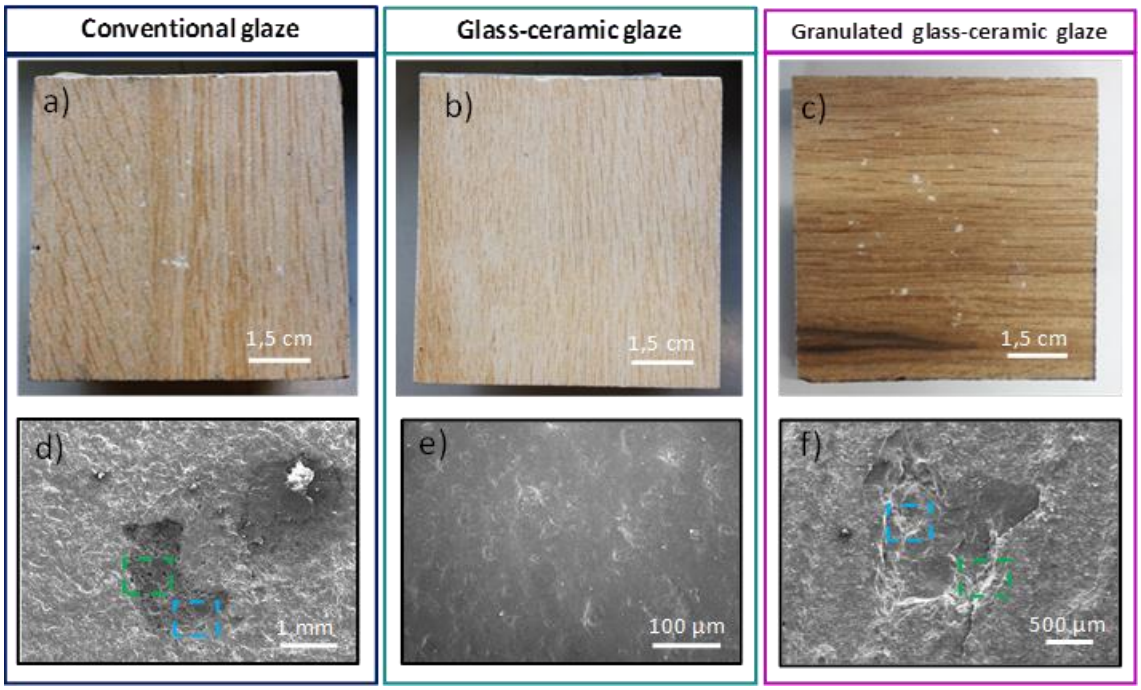

Figure 4: Images and FESEM micrographs of conventional (**a** and **d**), hierarchical glass-ceramic (**b** and **e**) and granulated glass-ceramic (**c** and **f**) glazes with decorative motives, after the impact resistance test, where it is possible to check the damage produced by the steel ball. The green and blue squares represent the regions where a further analysis of the damage produced was carried out.

Decorated conventional glaze coatings (figure 4a) are highly damaged and present abundant surface flaking (level 5 according French Standard) and shallower marks (level 1), produced by the successive ball impacts. It is clearly shown that the decoration has been removed by the impacts, leaving white enamel marks. However, in case of the hierarchical glass-ceramic coating, there is an absence of surface flaking and marks (level 0) (figure 4b), as occurred in the white glaze. The addition of granulates onto the glass-ceramic coating produces damage by the ball impact although the sizes of the marks are smaller than the ones produced in the conventional coating (figure 4c). The damages are studied in more detail in the FESEM micrographs. Figure 4e shows that the glass-ceramic coating has a homogeneous surface. Figure 4d shows the micrograph of the impact damages produced in the conventional glaze. There are observed two impact types, one more pronounced corresponding to the first impact, and other less significant, corresponding to secondary rebounds. The main surface flacking is ≈ 2300 µm in width. Figure 4f shows the main surface flaking caused by the ball impact on granulated glass-ceramic coating, where a short crack can be observed (lower than 5 mm, which corresponds to level 2 in French Standard), indicating the impact stress. The size of this damage is lower than in the conventional

coating, being ≈ 1300 µm in width (≈ 50% lower). The green and blue squares represent the regions where a further analysis of the damage produced was carried out, which can be seen in figure 5, where a comparison of the damage in conventional and granulated glass-ceramic glazes is performed.

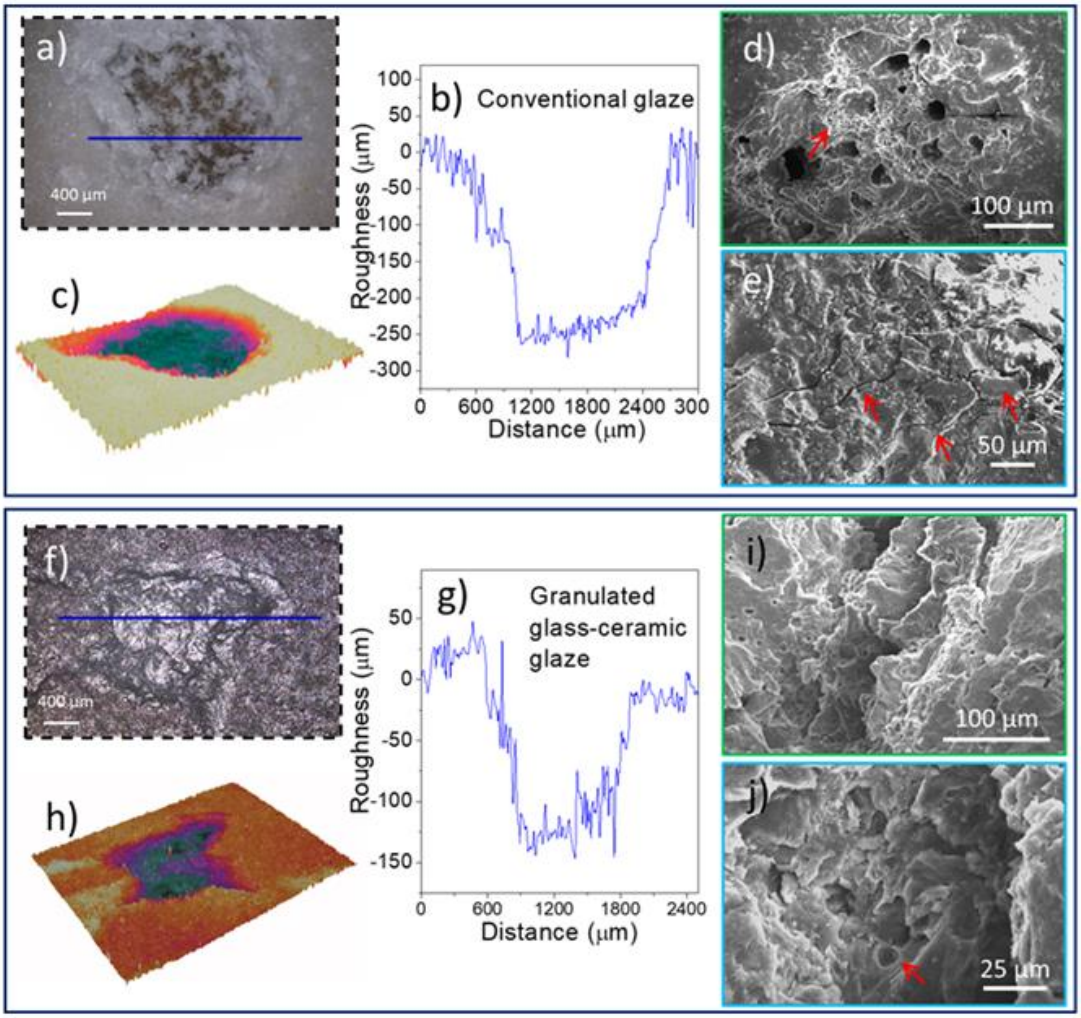

Figure 5: Damage produced by the ball impact into glazes: Optical image of the main hole generated by the ball during impact test for **a)** conventional and **f)** granulate onto glass-ceramics glazes; hole profile for **b)** conventional and **g)** granulate onto glass-ceramics glazes; 3D image of the surface flaking for **c)** conventional and **h)** granulate onto glass-ceramic glazes; FESEM micrographs of the main damage for **d)** and **e)** conventional and **i)** and **j)** granulate onto glass-ceramic glazes.

Figure 5a shows the optical image of the main damage produced in the conventional glaze where impact ring is formed with a total inner fragmentation of the ring [7,22]. The depth profile

(figure 5b) reveals that the surface flaking width is ≈ 2246 μm, in agreement with FESEM micrograph of figure 4d, and the depth is ≈ 269 μm, which is approximately the thickness of the coating. Therefore, the impact produces the total flaking of the glaze coating, as shown in figure 5a. In case of multilayered materials (as occurs in a glaze coating onto stoneware tile), the mechanical behavior is complex, since Hertzian and plastic behavior can coexist [23]. A 3D image of the surface flaking, figure 5c, shows that the maximum depth is located in the center of the impact (green region) and the depth is lower in the lateral regions, showing a conical shape corresponding to a Herztian cone [22]. An optical-profilometry image of a less prominent mark produced by the secondary ball bounces can be seen in figure S2a of the supporting information, which possess lower impact energy and, therefore, produce less damage, leaving a tiny circle imprint, in which an Herztian cone may also be produced [7]. For a further impact imprint analysis, at lower scale, FESEM analysis was carried out. The micrograph seen in figure 5d (corresponding to the green square in figure 4d) shows that the ball impact produces a delamination of the conventional glaze coating, which reveals inner pores, having 20 - 45 μm in width. Inside of some of these pores, residues of the fracture are accumulated and it is also possible to observe some chatter marks around the pore, indicating the friction direction (following the yellow arrow) as seen in figure S2b of supporting information, where it is also observed the gap left by some crystals that are ripped out during the impact test (marked with red arrows). In addition, in some damaged regions a delamination occurs at the interfaces between the vitreous matrix and the feldspar crystallizations, causing them to be exposed (red arrow), as observed in an enlarged micrograph in figure S2c of the supporting information. Figure 5e (corresponding to blue square in figure 4d) shows magnified surface flaking produced by the ball rebound, where cracks appear around the contact point, as hackle marks (red arrows) [22]. These cracks possess some forking, which indicates moderate stress in the material.

In the case of the granulated glass-ceramic glaze, the ball impact produces several damages where the decorative motives have been removed and also present fractured impact ring, as seen in figure 5f. The depth profile (figure 5g) reveals that the width of the surface flaking is ≈ 1397 μm and the depth is ≈ 150 μm. Therefore, despite the presence of granulate favors the damage generation in the glass-ceramic glaze coating, in which no damage is observed without granulate, the width and depth of the surface flaking is approximately 50% lower than the conventional coatings. Figure 5i shows an enlarged FESEM micrograph of the main surface flaking caused by the ball impact on granulated glass-ceramic coating (corresponding to green square in figure 4f), where it is observed that, in this case, the fracture is produced by

delamination through the hierarchical glass-ceramic material. The pores of this material are smaller, 5 - 10 μm in width, and less numerous than in the conventional glaze, therefore, their appearance after the impact does not suppose a threat to mechanical resistance. A short crack is observed in figure 5f that is magnified in figure S2c of supporting information. This isolated and short crack (l ≤5mm, level 2) does not present forking which indicates low impact stress. Finally, figure 5j shows a magnification of the damage area (blue square in figure 4f), where the gap left by some removed crystals is seen (red arrow). In this case, no fracture residues are observed.

In a homogeneous material, the ball impact produces a tensile stress in the contact surface between both objects and, when the critic load is achieved, the conical damage proportional to the applied load is produced. This behavior corresponds to the Hertzian mechanism. However, in a heterogeneous material with great amount of interfaces, which is the case that concerns us, the behavior is quite different. In this case, the maximum shear strain at the ball-surface contact is scattered in the deformation region and can produce a slight slump and some microcracks. If the applied load increases, these cracks can star to produce secondary cracks which would produce the damage [23–25]. This kind of behavior corresponds to a pseudo-plastic mechanism, in which, if the damage progresses, the material becomes detached. Therefore, the material's microstructure has an important influence in the impact resistance, so that homogeneous and heterogeneous materials follow mechanisms extremely different [21,26].

As discussed, neither of the two damaged glazes present clear radial cracks around the imprint ring, which indicates that these materials have a quasi-plastic behavior. The damage internal area is totally fractured and/or only short radial cracks appear [7,23,27]. In case of the hierarchical glass-ceramic glaze, under the same conditions, it behaves as an elastic material since it is able to relax the generated mechanical stress and, therefore, no surface flaking is produced. These differences can be explained by the different microstructures, since they generate difference in density, porosity and number of interfaces, which are largely demonstrated to be key for mechanical properties.

According to these results, it is possible to extract some conclusions about the relationship between the microstructure and the impact resistance of materials. The hierarchical glass-ceramic material possesses great amount of interfaces due to its singular micro-nanostructure, since its presents feldspar microcrystals surrounded by nanocrystals of the same composition, with low amount of glassy phase (only 6%), compared to the conventional glaze, as seen in figure 2 [13,14]. Since the shear stress may be relaxed through the grain boundaries, this distribution

makes that the impact stress is greater relaxed due to the larger amount of the grain boundaries in this micro-nanostructure, reducing the damage probability. Moreover, other factor that affects the impact resistance is the grain size, so that higher the grain size, higher the damage produced for the impact because it decreases the grain boundary number [25,26]. As showed above, hierarchical glass-ceramic glaze possesses microcrystals more than 5 times smaller than conventional one, along to the presence of the nanostructure. Additionally, the glassy phase favors the crack propagation, especially if it constitutes a continuous phase in the microstructure. Therefore, the low content of glassy phase in the glass-ceramic regarding to the conventional glaze, also favors the damage inhibition. The porosity also affects the impact resistance, being higher when porosity size and proportion decreases.

In case of granulated glass-ceramic glaze, it was observed that impact damage is produced despite the unique microstructure of this material. Therefore, it is concluded that the roughness of the surface greatly affects the impact resistance [20,21], since, when the roughness increases, the ball impacts in protruding parts, where all the stress load concentrates and the accumulated tension results in greater local damage. However, the impact damage is ≈ 50 % lower than in the conventional glaze, due to the presence of the hierarchical layer that reduces the stress, and therefore reduces the damage.

4. Conclusions

The hierarchical nano-microstructure present in the developed glass-ceramic glaze is the main responsible factor of improving the mechanical properties of the conventional stoneware tiles, since both glazes possess similar chemical composition and thermal expansion coefficient. This nano-microstructure favors higher stress relaxation by the larger amount of interfaces, lower porosity and less glassy phase that it possesses. These properties avoid the impact damages, keeping the resilience value. The application of this kind of glaze could suppose a great advantage in the ceramic field since the use of a hierarchical glass-ceramic coating can prevent from the damage in pavements, which expands its use in a large number of applications. Moreover, the hierarchical micro-nanostructured coating provides a new concept that could be applied to other ceramic materials in which the impact resistance is a critical parameter.

Acknowledgments

The authors express their thanks to the MINECO (Spain) project MAT2017-86450-C4-1-R, and project CDTI of CTV for their financial support. Dra. E. Enriquez is also indebted to MINECO

for a ‘‘Torres Quevedo’’ contract (ref: PTQ-14-07289), which is co-financed with European Social Funds.

References

[1] Specification for Glazed Ceramic Tiles and Tile Fittings for Internal Walls, British Standard, BS1281., (1966).

[2] R. Harrison, R. Brough, The impact resistance of ceramic tiles and flooring, in: Qualicer, Ceram Research, Stoke-on-Trent, UK, n.d.: pp. 143–154.

[3] L. Li, L. Cheng, S. Fan, X. Gao, Y.P. Xie, L. Zhang, A novel fabrication approach for impact resistance laminated ceramics, Mater. Des. 79 (2015) 26–31. doi:10.1016/j.matdes.2015.04.043.

[4] C.Y. Huang, Y.L. Chen, Design and impact resistant analysis of functionally graded Al_2O_3-ZrO_2 ceramic composite, Mater. Des. 91 (2016) 294–305. doi:10.1016/j.matdes.2015.11.091.

[5] T.B. Da Cunha, J.P. Wu, O. Peitl, V.M. Fokin, E.D. Zanotto, L. Iannucci, A.R. Boccaccini, Mechanical properties and impact resistance of a new transparent glass-ceramic, Adv. Eng. Mater. 9 (2007) 191–196. doi:10.1002/adem.200600237.

[6] C. Fragassa, F.V. de Camargo, A. Pavlovic, A.C. de F. Silveira, G. Minak, C.P. Bergmann, Mechanical characterization of gres porcelain and low-velocity impact numerical modeling, Materials (Basel). 11 (2018) 1–17. doi:10.3390/ma11071082.

[7] M. Dondi, G. Guarini, C. Melandri, M. Raimondo, C. Zanelli, Resistance to impact of porcelain stoneware tiles, Ceram. Int. 42 (2016) 5731–5736. doi:10.1016/j.ceramint.2015.12.104.

[8] M. Yasir, C. Zhang, W. Wang, Y. Jia, L. Liu, Enhancement of impact resistance of Fe-based amorphous coating by Al_2O_3 dispersion, Mater. Lett. 171 (2016) 112–116. doi:10.1016/j.matlet.2016.02.060.

[9] Q. Zhao, Y. Liang, Z. Zhang, X. Li, L. Ren, Effect of Al content on impact resistance behavior of Al-Ti-B_4C composite fabricated under air atmosphere, Micron. 91 (2016) 11–21. doi:10.1016/j.micron.2016.09.004.

[10] S. Ghosh, K.S. Pal, A.K. Mandal, N. Biswas, M. Bhattacharya, P. Bandyopadhyay, Cordierite based glass-ceramic glazed floor tiles by microwave processing, Mater. Charact. 95 (2014) 192–200. doi:10.1016/j.matchar.2014.05.023.

[11] Z. Wang, Y. Sun, H. Wu, C. Zhang, Low velocity impact resistance of bio-inspired building ceramic composites with nacre-like structure, Constr. Build. Mater. 169 (2018) 851–858. doi:10.1016/j.conbuildmat.2018.03.043.

[12] J.P. Best, M. Polyakov, D. Shinde, M.H. Colliander, J. Wehrs, J. Michler, M. Morstein, Ni nanocluster composites for enhanced impact resistance of multilayered arc-PVD ceramic coatings, Surf. Coatings Technol. 354 (2018) 360–368. doi:10.1016/j.surfcoat.2018.07.102.

[13] E. Enríquez, V. Fuertes, M.J. Cabrera, J. Seores, D. Muñoz, B. Galiana, J.F. Fernández, Study of the crystallization in fast sintered Na-rich plagioclase glass-ceramic, Ceram. Int. (2019) 0–1. doi:10.1016/j.ceramint.2019.01.219.

[14] V. Fuertes de la Llave, A. del Campo, J.F. Fernández, E. Enríquez, Structural insights of hierarchically engineered feldspars by confocal Raman microscopy, J. Raman Spectrosc. (2019) 1–14. doi:10.1002/jrs.5556.

[15] E. Enríquez, V. Fuertes, M.J.J. Cabrera, J. Seores, D. Muñoz, J.F.F. Fernández, New strategy to mitigate urban heat island effect : Energy saving by combining high albedo and low thermal diffusivity in glass ceramic materials, Sol. Energy. 149 (2017) 114–124. doi:10.1016/j.solener.2017.04.011.

[16] V. Fuertes, M.J. Cabrera, J. Seores, D. Muñoz, J.F. Fernández, E. Enríquez, Hierarchical micro-nanostructured albite-based glass-ceramic for high dielectric strength insulators, J. Eur. Ceram. Soc. (2018). doi:10.1016/j.jeurceramsoc.2018.02.009.

[17] C. Fragassa, Limits in application of international standards to innovative ceramic solutions, Int. J. Qual. Res. 9 (2015) 279–298.

[18] F. Pacheco-Vázquez, S. Dorbolo, Rebound of a confined granular material: Combination of a bouncing ball and a granular damper, Sci. Rep. 3 (2013) 3–9. doi:10.1038/srep02158.

[19] R. Jankowski, Theoretical and experimental assessment of parameters for the non-linear viscoelastic model of structural pounding, J. Theor. Appl. Mech. 45 (2007) 931–942.

[20] W.L. Walters, Determination of impact resistance by measurement of coefficient of restitution, in: Qualicer, 1996: pp. 231–238.

[21] F. Orgaz, T.G. del Río, A. Varela, J. F. Fernández, Dynamic Mechanical Behaviour of Thick Alumina Layers with Thin Tunneled Interfaces, Ceram. Trans. 215 (2010) 27–40.

[22] T. Ono, R.A. Allaire, Fracture Analysis, A Basic Tool to Solve Breakage Issues, Taiwan FPD Expo 2000. (2004) 1–9. http://www.new.corning.com/assets/0/391/2423/2437/2441/38FCE344-211C-454E-878C-2BD1A9105453.pdf.

[23] G. Silva, A. Munoz, C. Felíu, V. Cantavella, Ceramic tile mechanical behaviour impact, Proc. Qualicer. IV World Congr. Ceram. Tile Qual. (2002) 385–399.

[24] B.R. Lawn, Indentation of Ceramics with Spheres: A Century after Hertz, J. Am. Ceram. Soc. 81 (2005) 1977–1994. doi:10.1111/j.1151-2916.1998.tb02580.x.

[25] B.A. Latella, T. Liu, A.J. Atanacio, Effect of grain size on Hertzian contact damage in 9 mol% Ce-TZP ceramics, J. Eur. Ceram. Soc. 22 (2002) 1971–1979. doi:10.1016/S0955-2219(01)00527-1.

[26] A.R. Keller, M. Zhou, Effect of microstructure on dynamic failure resistance of t itanium diboride/alumina ceramics, J. Am. Ceram. Soc. 86 (2003) 449–457. doi:10.1111/j.1151-2916.2003.tb03320.x.

[27] A. Ball, H.W. McKenzie, On the low velocity impact behaviour of glass plates, Le J. Phys. IV. 4 (1994) C8-783-C8-788. doi:10.1051/jp4:19948121.

Supporting information

Absence of surface flaking in hierarchical glass-ceramic coating: high impact resistant ceramic tiles

E. Enríquez[1,2], V. Fuertes[1], M.J. Cabrera[2], Jaime Seores[2], D. Muñoz, J. F. Fernández[1]

[1]Dept. Electrocerámica, Instituto de Cerámica y Vidrio, CSIC, Kelsen 5, 28049, Madrid, Spain.

[2]Centro tecnológico Vidres, S.L., Ctra. Onda, Km 3.4, 12540 Villareal, Castellón, Spain

S1. Optical image of granulated glass-ceramic glaze.

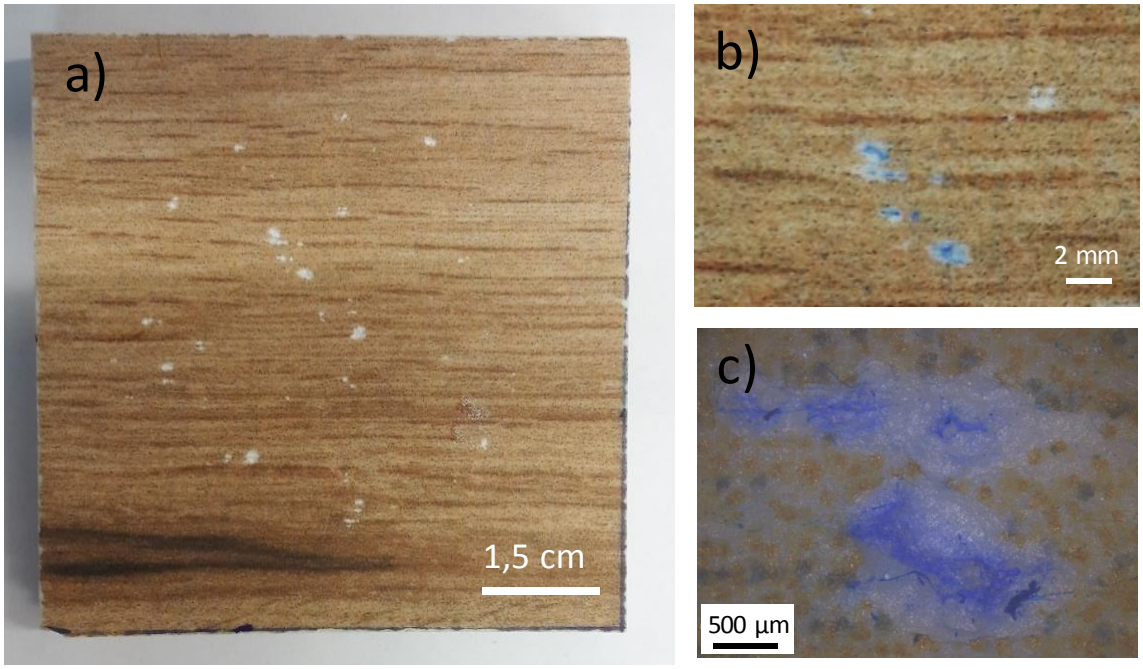

Figure S1: a) and **b)** Image of granulated glass-ceramic glaze; **c)** Optical image when a dye it is used to reveal the surface damage.

S2. Analysis of the damage produced after the impact test.

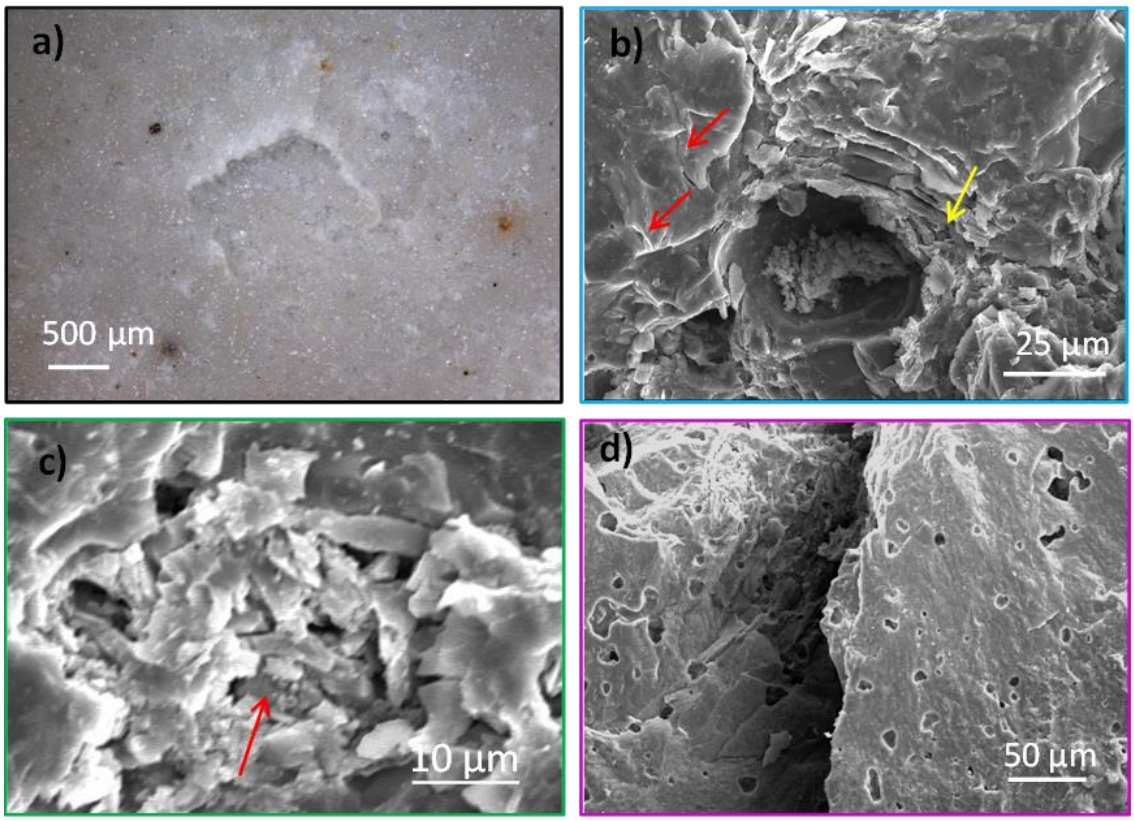

Figure S2: **a)** Optical-profilometer image of a less prominent mark produced by the secondary ball bounces in the conventional glaze coating; **b)** A pore revealed in the conventional glaze after the ball impact, that shows residues inside it and chatter marks around the pore, indicating the friction direction (following the yellow arrow). The gap left by some crystals that are ripped out during the impact test are marked with red arrows; **c)** Feldspars crystallization exposed after the impact; **d)** Magnification of the short crack appeared in the granulated glass-ceramic after the impact test (see figure 2f).

ARTÍCULO 5. Hierarchical micro-nanostructured glass-ceramic based on albite for high dielectric strength insulators

V. Fuertes, M.J. Cabrera, J. Seores, D. Muñoz, J. F. Fernández, E. Enríquez.

Journal of the European Ceramic Society, 38, 2018, 2759-2766.

Factor de impacto: 3,794 (según JCR Edition Science 2017).

Journal of the European Ceramic Society 38 (2018) 2759–2766

Contents lists available at ScienceDirect

Journal of the European Ceramic Society

journal homepage: www.elsevier.com/locate/jeurceramsoc

Original Article

Hierarchical micro-nanostructured albite-based glass-ceramic for high dielectric strength insulators

V. Fuertes[a,*], M.J. Cabrera[b], J. Seores[b], D. Muñoz[b], J.F. Fernández[a], E. Enríquez[a,b]

[a] Dept. Electrocerámica, Instituto de Cerámica y Vidrio, CSIC, Kelsen 5, 28049, Madrid, Spain
[b] Centro tecnológico Vidres, S.L., Ctra. Onda, Km 3.4, 12540, Villareal, Castellón, Spain

ARTICLE INFO

Keywords:
Glass ceramic
Ceramic electrical insulation
Dielectric properties
Complex impedance
Dielectric breakdown

ABSTRACT

A novel glass-ceramic material based on albite type Na-rich feldspar has been synthesized by conventional ceramic process. High crystallinity, > 94% Vol.% is obtained by fast sintering which allows energy saving processing. Albite is the main crystalline phase and tetragonal SiO_2 is a secondary phase. Electrical properties were examined by complex impedance, DC measurements, and dielectric breakdown test. Dielectric characterization shows a non-Debye type dielectric behavior with low dielectric constant, 4.6 at 1 MHz, low dielectric losses, ($\sim 10^{-3}$ at 1 MHz, and a large dielectric strength, ~60 kV/mm), that it is the largest value reported in ceramic insulators. Those dielectric properties are attained by the low glassy phase content in the samples and their unique micro-nanostructure. All these properties make this novel material a very promising candidate in the market of ceramic electrical insulator, highlighting for high-voltage applications.

1. Introduction

Electrical insulators are materials which block the flow of electric current. These materials are used in electrical equipment as insulators or insulation being their function to support or to separate electrical conductors without allowing current through themselves. The uses of it have increased in the last years because of the technology demand.

A kind of electrical insulators widely used currently is ceramic electrical insulators which are used in many microelectronic devices. Multifold insulator applications form part of automotive and aerospace sector, or home appliances. Ceramic insulators are also used for high-voltage applications, they are being one of the most important pieces used in power transmission as well as distribution lines between others [1–3]. The properties required for an insulator in this field of application are high resistivity, high dielectric strength, a low loss factor, good mechanical properties and dissipation of heat. One of the main limitations of these materials, mainly in high-voltage applications, is their dielectric breakdown, which prompts the loss of insulating properties and mechanical degradation of the material.

Dielectric strength for high-tension electrical insulation is currently limited to 30 kV/mm [4]. Only natural mica insulators provide larger dielectric strength values. Dielectric breakdown is related to scattering process and charge trapping in specific areas of the insulator material. Defects are considered as sites where polarizability is modified and where charge and energy localisation can occur. In ceramics, such defects can be porosity, crystallographic defects, lattice distortions, impurities, grain boundaries or interfaces with secondary phases [5]. Dielectric breakdown is strongly determined by micro-structure, playing the interfaces an important role since they are favourable places to charge trapping. Porosity and grain size are also some important variables to take into account [6]. It is reported in previous works that a low porosity and low grain size improve the breakdown resistance [7]. The amount of glassy phase presented in the glass-ceramic also affects the dielectric material behaviour, mainly the dielectric losses. High dielectric losses are registered in most of the glasses, so that, lower dielectric losses are expected in glass-free ceramics [8].

Albite ($NaAlSi_3O_8$) is the sodic end-member of plagioclase and alkali feldspar-group minerals. Albite may be found with an ordered or disordered structure. The ordered structure is known as low albite, which belongs to the triclinic pinacoidal crystal system. It framework consists of rings of four tetrahedron, where each tetrahedron is centered by a Si^{4+} or an Al^{3+}. Each oxygen atom is located at the corners of the tetrahedron and links two tetrahedron which are usually labeled as T1o, T1m, T2o and T2m. The completely disorder triclinic albite is known as high albite. Disordered albite undergoes a triclinic to monoclinic phase transition at about 980 °C, where the complete order is lost. In that case, albite framework is formed by two tetrahedral sites, i.e T1 and T2 [9,10]. Previous studies about the dielectric behavior and the conduction mechanism of feldspars at high temperature and high pressure showed an insulator behavior and suggested an ionic conduction as the

* Corresponding author.
E-mail address: vfuertes@icv.csic.es (V. Fuertes).

https://doi.org/10.1016/j.jeurceramsoc.2018.02.009
Received 19 December 2017; Received in revised form 30 January 2018; Accepted 3 February 2018
Available online 07 February 2018

dominant conduction mechanism [11–13].

In the last years, development of nanotechnology and nanoscience have allowed the improvement and creation of new materials with unique properties [3]. In this work, we have synthesized an albite-based glass-ceramic by fast firing processes that take ~55 min for the whole sintering cycle. The so obtained glass-ceramic possesses low porosity and a low glassy phase content, which is an important novelty regarding to standard dielectric materials such as glass ceramics, steatites or dielectric porcelains among others [4,14,15]. The unique micro-nanostructure of the albite-based glass-ceramic provide a high breakdown strength that is larger than that of the standard material used in this area [16]. All of these peculiar characteristics will favour numerous processes of phonon, photon and electron scattering in the material, achieving a low thermal conductivity, a high reflection of UV and IR radiation [17] and a good insulator behavior.

The present paper shows the results of an extensive study made on the dielectric properties of this micro-nanostructured albite, such as dielectric strength, dielectric constant, loss factor, complex electric modulus and DC/AC conductivity, trying to elucidate the influence of the microstructure in the dielectric behavior observed which can be of interest in the field of ceramic insulators.

2. Experimental procedure

2.1. Sample preparation

The glass ceramic was prepared by a conventional ceramic process followed in the tile industry [18,19]. The precursors used were kaolin (MOLCASA), with a particle size (D_{50}) of 5.34 μm, and frit in a weight proportion of 90/10, respectively. The frit, produced by Vidres S.A., was previously melted at 1500 °C (previously warmed at 900 °C and then directly brought under the dwell temperature) and water quenched [20]. The starting raw materials used for the preparation of this frit were potassium feldspar, quartz, dolomite, calcium carbonate, sodium feldspar, calcined alumina, strontium carbonate and zircon flour. The material composition expressed in terms of equivalent oxides is shown in Table 1. Homogenization of precursors was done by milling in an alumina ball mill for 20 min with 37 wt% of water [21]. The material prepared was dried at 60 °C for 24 h and the powder obtained was sieved through a sieve of 100 μm, achieving a particle size (D_{50}) of this material with a monomodal distribution centered at 6.72 μm. Green discs were pressed uniaxially at 39.2 MPa with different diameters accordingly to the characterization test specifications: samples of ~60 mm of diameter for dielectric constant and dielectric losses measurement at room temperature; and samples of ~10 mm for the rest of measurements. Then, samples were sintered in an industrial type furnace at 1220 °C for 6 min with a 30 °C min^{-1} heating rate, spending the sintering cycle only 55 min in being completed. This thermal cycle was chosen attending to the results obtained from the heating microscopy carried out to identify the sintering temperature of the samples. Different thermal treatments were evaluated in the range of 1000 °C–1250 °C, according to data obtained from Hot Stage Microscopy (varying the holding time and temperature). This single set of conditions was carefully chosen to adapt them to an industrial production process and to minimize porosity in the samples in order to improve mechanical behavior and dielectric strength (see Fig. S1a in section S1 of Supplementary information).

Table 1
Composition of the glass-ceramic expressed as equivalent oxides. The minor components are all included in other.

Oxides wt %	SiO_2	ZrO_2	SrO	Na_2O	K_2O	Al_2O_3	ZnO	CaO	Other
Frit	54,67	1,24	7,20	214	1,44	22,63	1,27	7,73	1,68
Kaolin	55,49				1,21	42,48		0,17	0,65

2.2. Characterization

Microstructural characterization was studied by means of Field Emission Scanning Electron Microscopy (FESEM) using a Hitachi S-4700. Metalographically polished samples were chemically etched with 5 vol% of HF with the aim of removing the glass phase to reveal the microstructure. The total porosity was evaluated by an image analyzer system Leika Qwin from micrographs of representative polished surfaces. In addition, the crystalline phases formed were identified by using X-ray diffraction (XRD) technique in a diffractometer Bruker D8 Advance with Cu Kα radiation, 40 kV and 40 mA. The identification of the crystalline phases was realized by comparison with the corresponding JCPDS cards, and the glassy phase content was obtained through the integration of the areas corresponding to the glassy and crystalline phases. In addition, the crystalline phase was calculated by the diffraction software Bruker's Diffrac.Eva which takes into account integrated intensities of the amorphous and crystalline contribution. Thermal characterization was carried out by thermogravimetric analysis (TGA) and differential thermal analysis (DTA) (Netzsch STA 409/C) up to 1000 °C with a heating rate of 10 °C/min in air atmosphere. Hot Stage Microscopy (Axel Hesse Instruments, Germany), was carried out from RT to 1500 °C in air atmosphere with a heating rate of 30 °C/min on a platinum substrate.

Dielectric measurements were carried out by an impedance analyzer (HP4294A, Agilent Technologies Inc., Santa Clara, CA). The frequency range was from 100 Hz to 10 MHz for dielectric constant and dielectric losses measurements at room temperature, for measurements of these magnitudes up to 800 °C using a 2 °C-min heating-cooling rate, for impedance measurements and for electric modulus. Arc obtained by Nyquist plot only were defined from 370 °C to 570 °C due to the resolution of the measurements and for this reason only arcs in this range appear plotted. The analysis of each circuits was carried out through Zplot software, based on the equations of circuits in the maximum of the arcs (ωRC = 1). DC and AC conductivity was measured by the same impedance analyzer from 30 °C to 750 °C. The measures were repeated in three samples in order to obtain an average, reducing the errors and assuring the reproducibility of the measures.

Finally, dielectric strength was evaluated by using a HV DC Power Supply 60 kV and 2.5 mA (Hipotronic, Brewster, NY) and following UNE-En iso standard no. 600,672 where > 10 disks, one face of which includes a hemispherical recess of 10°. Both sides of the disks were silver painted followed by thermal treatment at 750 °C. Samples were dried at 120 °C 2 h and then cooled down to Room Temperature in a desiccator. The discs were immersed into a dielectric medium (silicone oil).

3. Results and discussion

3.1. Microstructural characterization

Fig. 1a shows the XRD pattern of fast sintered glass-ceramic. The main phase identified in the glass-ceramic corresponds to albite feldspar. Albite is the major phase formed in our glass-ceramic when the material is sintered, although the frit only has a 2% of Na_2O. The addition of SrO plays a crucial role in the crystallization of albite phase, since SrO is a lattice disruptor which favours the formation of this sodium aluminosilicate after devitrification process [22]. The (131) and (1–31) reflections show the symmetry of the feldspar. In monoclinic albite only the (131) reflection appears in the XRD pattern. However, in triclinic albite, a splitting of this peak takes place. Inset of Fig. 1a shows the (1–31) and (131) reflections located at 30.1° and 31.2° 2θ, respectively, which agrees with literature data, JCPDS Card no. 01-084-0752 [23]. These data indicate the symmetry of the triclinic albite, that is, the most ordered Na-rich feldspar. In addition, SiO_2 crystalline phase appears in low concentrations. The broad band located between 15° and 35° 2θ allows us to estimate the glassy phase content present in the

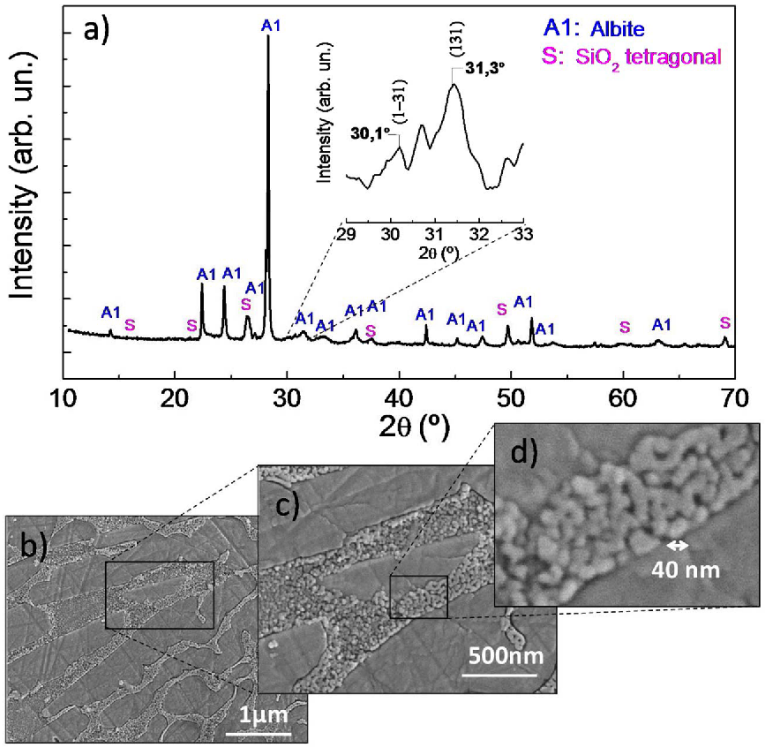

Fig. 1. a)XRD pattern of the sintered low albite glass ceramic and an enlargement between 29° - 33° which shows (1–31) and (131) reflections, corresponding to a triclinic structure. FESEM micrographs of the chemically etched, **b)** albite-based glass ceramic, and **c)** and **d)** enlargements of the previous pictures which show in more detail the formed nanostructure and albite microcrystals.

sample by means of the diffraction software Bruker's Diffrac.Eva, being this content ≈6% Vol. This glassy phase content is much lower than that in a conventional glaze (~35% Vol.% of glassy phase) [17]. Moreover, the narrow diffraction peaks of the XRD pattern show the high crystallinity of the material synthesized in spite of the fast thermal cycle. Therefore both the optimized composition and the processing allow obtaining this glass-ceramic.

Fig. 1b–d show FESEM micrographs of the sintered glass-ceramic material at different magnification. Fig. 1b shows the micro-nanostructure where elongated albite microcrystals are surrounded by nanocrystal regions. Fig. 1c–d shows the nanostructured region in detail.

3.2. Dielectric characterization

3.2.1. Dielectric permittivity and dielectric losses analysis

Complex impedance has been measured in order to determine the dielectric properties of the new glass ceramic. Fig. 2 shows the frequency dependence at 300 K of real part of complex dielectric permittivity (in blue) and dielectric losses (in red). The dielectric constant (ε′) remains approximately uniform in all frequency range measured, with values of 4.6–4.7. Dispersion in dielectric constant below microwave frequencies emerges from dipolar polarization effects and space charge or interfacial polarization. When an alternate field is applied, the material dipoles try to line up with the electrical field, where, for this range of frequencies, all the dipolar polarization mechanisms play an important role. The dielectric constant in albite-based glass-ceramic exhibits slight decrease when frequency increases up to $2{\cdot}10^6$ Hz, which indicates that electronic, ionic and molecular polarizability are practically suppressed [24]. Table 2 shows the ε′ values registered for some frequencies of interest. The values obtained for ε′ in this work are very close to the theoretical albite mineral permittivity (ε′ = 5–6 [8]) which along with XRD analysis, indicates the high purity of this Na-rich feldspar synthetized.

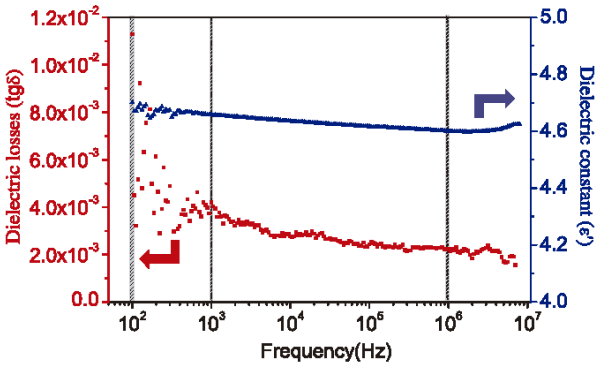

Fig. 2. Dielectric losses (tgδ) (left side) and dielectric constant (ε′) (right side) versus frequency for albite glass ceramic.

Dielectric losses (tgδ) at room temperature decrease as frequency increases [25]. The lack of a symmetric peak in tgδ as a function of frequency indicates a non-Debye dielectric behavior [26]. Losses in a dielectric material may have their origin in free-charge carrier movement or in a dipole orientation. Non-significant dielectric losses are registered in this glass ceramic material, about 10^{-3}, which may be motivated by a hardly activated polarization mechanism. Another important factor to take into account is the low presence of glassy phase in the material, which affects the dielectric behavior, mainly the dielectric losses. High dielectric losses are registered in most glasses, so that,

Table 2
Dielectric constant and dielectric losses at 100–Hz, 1000–Hz and 1 MHz, for albite glass ceramic.

Frequency f (Hz)	Dielectric constant, ε′	Dielectric losses, tgδ
100	4.7 ± 0.1	(11.30 ± 0.02)·10^{-3}
1000	4.7 ± 0.1	(4.20 ± 0.02)·10^{-3}
$1{\cdot}10^6$	4.6 ± 0.1	(2.23 ± 0.02)·10^{-3}

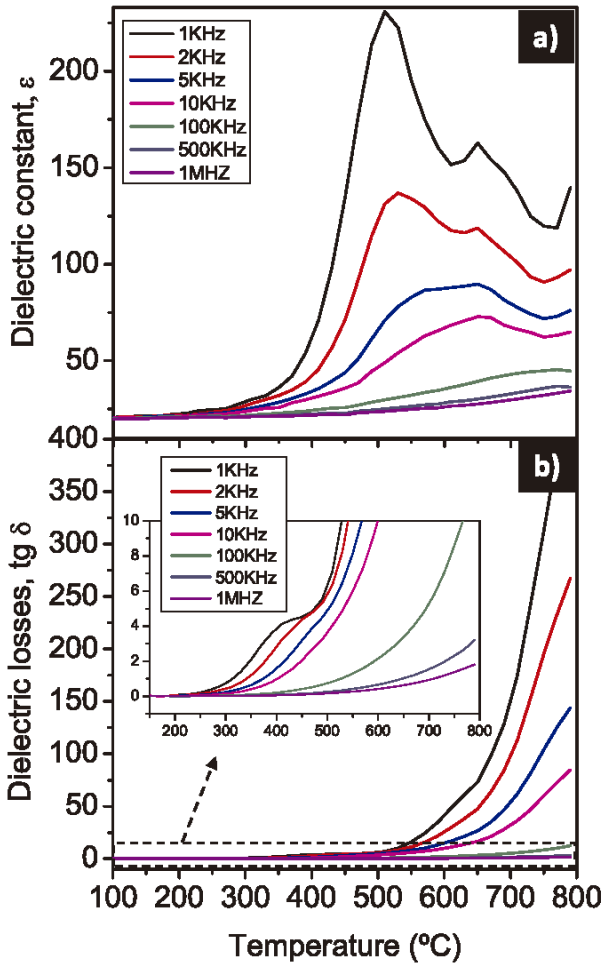

Fig. 3. Temperature dependence of a) the dielectric constant and b) dielectric losses for different frequencies, in the studied range for albite glass-ceramic.

lower dielectric losses are determined in this albite glass-ceramic [8]. These low values of dielectric constant are in the range of typical values at 1 MHz for alkali aluminosilicate porcelains ($\varepsilon \sim 5$–7 and $tg\delta \sim 1{\cdot}10^{-2}$), cordierite ($\varepsilon \sim 4.1$–$5.3$ and $tg\delta \sim (3$–$5){\cdot}10^{-3}$), steatite ($\varepsilon \sim 6$ and $tg\delta \sim (1$–$7){\cdot}10^{-3}$) or alkaline earth and zirconium aluminosilicate porcelains ($\varepsilon \sim 5$–12 and $tg\delta \sim (5$–$7){\cdot}10^{-3}$) between others [16]. Dielectric losses values are almost steady and also similar to values for others current glass-ceramic materials in the bibliography based on cordierite ($tg\delta$ up to $2{\cdot}10^{-3}$), barium aluminosilicate ceramics ($tg\delta \sim 5{\cdot}10^{-3}$) or magnesium aluminosilicates ($tg\delta \sim 9.5{\cdot}10^{-2}$) [27–29].

The dependence of the dielectric constant and dielectric losses behavior with temperature is also evaluated and it is shown in Fig. 3 for different frequencies. Fig. 3a shows that ε' exhibits a pronounced increase from 300 °C, which is more abrupt at lower frequencies due to the easier orientation of the dipoles with the applied electric field, appearing two clear peaks for frequencies ≤10 kHz. This increase in dielectric constant may be influenced by two phenomena: the larger mobility of sodium ions in this Na-rich feldspar material, and the associated phase transition, as occurs in ferroelectric materials [24]. To clear any doubts a thermogravimetric and a differential thermal analysis were carried out (see Fig. S2 in Supplementary info). It is well known, according to bibliography that a triclinic-monoclinic phase transition at 980 °C occurs in pure albite. In addition, other transitions related to change of order and disorder occurs below 750 °C. In this transition a change from low to high albite takes place, keeping triclinic structure [25,30,31]. However, highly pure albite is difficult to obtain and a little content of anorthite is probably formed due to the presence of Ca^{2+} in the composition, which is able to modify the phase transition temperature [30].

In response of DTA-TG data, any phase transition is undergone in this material and probably only an order-disorder phenomenon takes place in the feldspar, which usually has frequency dependence, as it is observed in Fig. 3. That process governs the electrical conductivity behavior observed, but it can also be influenced by the mobility of sodium ions or alkali earth ions present in the glassy phase. This glassy phase provides a free path to these mobile ions (Na^+, Ca^{2+}, …) to move and hence increase the conductivity of the system [4,32,33]. According to the literature, electrical conductivity in Na-rich alkali feldspars is based on an ionic conduction mechanism where sodium cations are the dominant charge carriers and migrate into interstitial sites within the aluminosilicate feldspar network [12]. Therefore, hopping processes of alkaline elements are responsible of electrical conductivity in albite. This process is thermally activated, like the order-disorder transitions in aluminosilicate framework, which is in agreement with the behavior shown in Fig. 3a, since alkali and alkaline earth cations migration is favoured when temperature increases [11,34,35]. In Fig. 3b, dielectric losses shows a strong dependence with temperature, raising its value as temperature increases, mainly at low frequencies which behaves as an increasing exponential. This behavior is, on the one hand, motivated by order-disorder processes, in which a migration of Al ions from T1o to T1m, T2o, and T2m positions occurs and, on the other hand, by the higher mobility of the alkali ions, such as Na^+, which increases conductivity as temperature increases, according to the hopping mechanism previously mentioned [36]. A dielectric losses increase will occur consequently, according to the expression (see Eq. (1)) which manages the dielectric losses for a dielectric material:

$$tg\delta = \frac{\varepsilon''(\omega)}{\varepsilon'(\omega)} = \frac{\sigma_{AC}(\omega)}{\omega\varepsilon(\omega)\varepsilon_0} \quad (1)$$

Where σ_{AC} is the AC conductivity and ε_0 the dielectric permittivity of the vacuum, $\varepsilon_0 = 8{,}85{\cdot}10^{-12}$ F/m. The glassy phase contributes mainly to this increase since it could present an electrical conductivity higher than that of the crystalline phase, because Alkali cations usually generate structural defects in the lattice suitable for conduction by hopping [37].Tg δ values decreases as frequency increases, as also occurred with the dielectric permittivity described previously, because the polarization mechanism plays an important role at lower frequencies [25,38].

3.2.2. Complex impedance measurements

Once the dielectric behavior of ε' and tg δ was studied, it would be interesting to characterize the material's electrical conduction, analyzing the different contributions and the conduction mechanisms. For this purpose, complex impedance measurements were analyzed. Fig. 4a shows the Nyquist plot for albite sample in the temperature range from 370 °C to 570 °C, which was the temperature range in which data could be successfully fitted to two semicircular impedance arcs. The low frequency semicircle corresponds to the grain boundary contribution whereas the higher frequency semicircle depicts the bulk effect, according to the values of capacitances obtained (see Table 3) [39]. Therefore, the first arc could be simulated as a double RC equivalent circuit, whereas the second arc is simulated as a simply one. These simulations allow obtaining the resistances and capacitances of each material contribution. The value of bulk resistance (R_b) and grain boundary resistance (R_{gb}) at different temperatures has been obtained from the intercept of the semicircular arc on the real axis (Z'). Resistance values, given in Table 3, undergo a decrease as temperature increases, for both bulk and grain boundary contributions, which indicate that albite has a negative temperature coefficient of resistance (NTCR). Then, albite, in contrast with metals, exhibits the characteristic

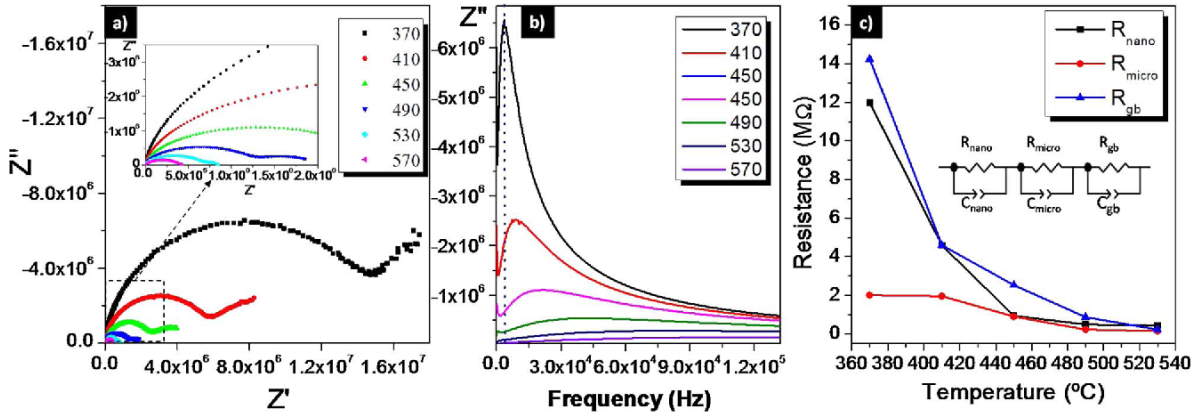

Fig. 4. a) Nyquist plot (Z″ vs Z′) of albite at different temperatures with equivalent circuit, **b)** Z″ vs frequency in the measured range of temperatures, and **c)** Resistance dependence with temperature for the contributions of grain boundaries, nanostructured albite regions and albite microcrystals.

Table 3
Resistance and capacitance values for albite obtained from Nyquist plot fitting. Resistance and capacitance values for both bulk contributions and for grain boundary are denoted as R_{b1}, R_{b2}, R_{gb} and C_{b1}, C_{b2}, C_{gb}, respectively.

Temperature (ºC)	R_{b1} (MΩ)	R_{b2} (MΩ)	R_{gb} (MΩ)	C_{b1} (pF)	C_{b2} (pF)	C_{gb} (nF)
370	11.98	2.01	14.25	5.50	9.10	0.46
410	4.59	1.96	4.60	8.73	6.01	0.68
450	0.94	0.90	2.53	7.52	7.65	2.92
490	0.49	0.23	0.87	9.52	7.85	5.20
530	0.44	0.14	0.23	9.79	9.28	4.55

behavior of semiconductor materials, as most ceramics do [35]. Both bulk contributions have a capacitance of the same magnitude order (pF), which suggests that they correspond to the same material. According to the micro-nanostructure of this glass-ceramic sample, it is possible to correlate both contributions with albite microcrystals and albite nanoparticles. It is well known that in nanomaterials, surface scattering processes play an important role in electrical conduction phenomena; therefore it is correct to assume that higher bulk resistance corresponds to nanostructure regions and that the lower bulk resistance corresponds to the microcrystalline regions.

Z″ values vs frequency graphs are plotted in Fig. 4b. It may be seen a peak up to 450 °C which shifts to higher frequencies as temperature increases and becomes wider. This widening of the peak suggests a temperature dependence of the involved relaxation process, as it was observed in Fig. 3. For temperatures > 450 °C only a slight overtone is presented.

Fig. 4c shows the resistance dependence with temperature for bulk and grain boundary of albite. As expected, the grain boundary exhibits higher resistance than the bulk in the temperature range of 370–490 °C, registering values of up to 14 MΩs. In a polycrystalline dielectric material, the resistivity of the grain boundaries may be much higher than that of the grains [39]. Therefore, the conduction current should be limited by the electrical properties of the grain boundaries. In this case, the conduction mechanism is called the grain-boundary-limited conduction [40]. In our case, there are a great number of grain boundaries in the material, on the one hand, micro-grains boundaries and on the other hand, nano-grains boundaries. Resistance values for grain boundaries (R_{gb}) are very close to values assigned to albite nanoparticles (R_{b1}), as it can be observed in Fig. 4c. Then, it may be stablished that overall resistance of the material is dominated by grain boundary components. Moreover the slight presence of remained vitreous phase is mainly located at the nanostructure region. This glassy phase seems to contribute to keep the nanostructuration of the albite and therefore to isolate percolation in microcrystals. The higher electrical resistivity of the albite nanostructure region is in this way a sum of the higher proportion of grain boundaries plus the secondary phase presence in spite of the higher conductivity of the glassy phase. So, albite nanostructuration has a great importance in the whole electrical response.

Modulus formalism is often used together with the impedance and permittivity formalisms to separate grain and grain-boundary effects. Since peak values are inversely proportional to their corresponding associated capacitances, the smaller capacitance should dominate in the electric modulus plots [41]. Since grains usually have smaller capacitance than the grain boundaries, as it was seen in Table 3, their response will be stronger in the modulus spectra. Therefore, complex modulus measurements and a comparative with impedance formalism will allow us to investigate more deeply the conduction process and the bulk contribution, as well as the relaxation processes involved in this material. Fig. 5 shows the bulk frequency dependence of the real and imaginary parts of the electric modulus for the temperature range previously studied. All the curves shift to higher frequencies with increasing temperature. It can be observed that the value of M′ is very low, close to zero for low frequencies, which may be due to the suppression of electrode polarization, and it increases as frequency increases, tending to an asymptotic value at 10 MHz, independently of temperature [42]. This tendency of saturation may indicate that the short range mobility of charge carriers contribute to reduce the conduction process and this implies a lack of a restoring force for the charge flow under the influence of a steady electric field [41,43].

The peak maxima of M″(Fig. 5) and Z″(Fig. 4b) vs frequency for each temperature of study appear at different frequencies, which is another indicative that the relaxation process in albite is of non-Debye type [44]. In addition, the maximum values of M" peak hardly depend on temperature, being it about $1.8{\cdot}10^{11}$, which implies that capacitances of grains and grain boundaries weakly depend on temperature. However, the relaxation peaks shift towards the higher frequency side with rise in temperature, which suggests that the relaxation is a thermally activated process [42].

The frequency region below the maximum of M″ curve determines the range in which charge carriers are mobile over long distances, being able to undergo successful hopping processes; while the region to the right of the peak indicates that ions are confined to their potential wells. That is, ions cannot overcome a voltage threshold and therefore they have short range mobility. This type of behavior suggests the existence of a temperature dependent hopping mechanism for electrical conduction [45,46].

Electric modulus was originally introduced to study space charge relaxation phenomena, but it is also widely used to analyze ionic conductivities in materials. For a pure conduction process, only one

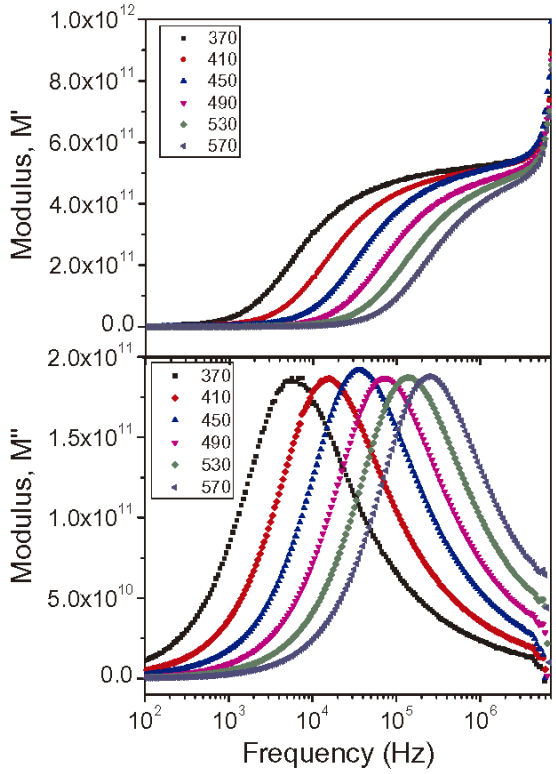

Fig. 5. Variation of real part (M') and imaginary (M'') part of modulus versus frequency at different temperatures.

relaxation peak is observed in the frequency spectra of M″ and no peak should appear in the corresponding plot of the imaginary part of dielectric constant, ε″, (see Fig. S3 in section S3 of Supplementary information), as it occurs in this work [47]. Therefore, it can be concluded that in AC, for that system, a conduction process takes place, based on a hopping mechanism as it was proposed above (Section 3.2.1). For a complete study, this AC conduction should be compare with DC measurements in order to evaluate the differences between both real conductions.

3.2.3. Electrical conductivity (DC and AC measurements)

Firstly, through real part of dielectric constant and dielectric losses values (plotted in Fig. 3) and taking into account Eq. (1) for a frequency of 1 MHz, AC conductivity was calculated and plotted in Fig. 6 (as σ_{AC}). As it was previously discussed, conductivity increases with temperature because albite exhibits a negative temperature coefficient of resistance,

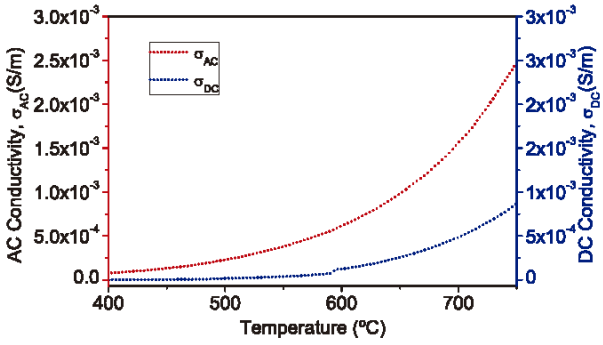

Fig. 6. AC conductivity (σ_{AC}) obtained by Eq. (1) and DC conductivity (σ_{DC}) vs Temperature, for albite glass ceramic.

taking values from $7{\cdot}10^{-7}$ S/m up to $8{\cdot}10^{-4}$ S/m in the temperature range showed.

DC conductivity was also evaluated from resistance measurements with increasing temperature, in the same range previously described. Because the equipment employed had not enough resolution for measurements below 400 °C, these data for DC and AC conductivity were omitted. It may be seen that σ_{DC} exhibits the same behavior than σ_{AC}, but it presents lower values in the measurement interval. For instance, σ_{DC} at 500 °C is $\sim 10^{-5}$ S/m, which is the same magnitude order of conductivity measured in some rock-forming minerals at this temperature, such as an alkali feldspar and olivine. In the case of quartz, σ_{DC} at 500 °C is $\sim 10^{-4}$ S/m, which shows the good insulator behavior of this synthetic albite-based glass-ceramic [48,49].

AC conductivity versus frequency, depicts in Fig. 7a, agrees well with Jonscher's power law (see Eq. (2)), where A and n, known as power law exponent, are fitting parameters of empirical nature [42,50].

$$\sigma_{AC} = \sigma_{DC} + A{\cdot}\omega^{n} \quad (2)$$

As both factors depend on temperature, the electrical conduction will be a thermally activated process as it may be seen in Fig. 7a, where curves show an upward shifting with temperature, as it was previously discussed.

Just plotting the log of AC conductivity as a function of log frequency, these parameters mentioned above can be obtained according to Eq. (2). The plateau region corresponds to the log of dc conductivity, which is nearly frequency-independent, followed by the high frequency domain where n can be calculated from the slope of the curve. This AC conductivity at higher frequency range is characterized by a frequency dependent behavior and it is referred in the plot as dispersive region, which gives us information about the chemical environment within the material [51]. Following that method, power law exponent values were obtained and plotted as a function of temperature in Fig. 7b.

The factor N represents the degree of interactions between mobile ions. N = 1 would indicate that the system behaves as a non-interacting Debye system. Values of n larger than 1 mean that the motions of species in the material undergo localized hopping movements. Finally, values of n lower than 1 indicate that charge carriers undergo a translational motion along with hopping events over long distances. As it may be seen in Fig. 7b, n decreases as temperature increases, which means that interaction between ions and the lattice increase progressively in our system, as a consequence of a temperature effect [52,53]. N values ranged from 0.41 to 0.06 in the evaluated temperature range, which indicates that albite glass ceramic of this work behaves far from a non-interacting Debye system and a hopping conduction mechanism over long distances is involved. Thus, the higher density of grain boundaries in the nanostructured region allows reducing overall resistivity in the obtained albite glass-ceramics by a fast firing process. This control of the hopping conduction mechanism limits the mobility of the carrier and could benefit the dielectric strength of the material.

3.2.4. Dielectric strength

As it has been checked by complex impedance measurements, the great number of grain boundaries from micro-grains, nano-grains and even interfaces with secondary phases play an important role in the dielectric behavior shown by this glass-ceramic material. As it was mentioned in the introduction, dielectric breakdown is strongly influenced by the micro-structure and it is expected that a prominent influence of this factor on the charge behavior occurs for a wide range of voltages. Therefore, dielectric breakdown measurements were carried out at room temperature according to UNE-En iso standard no. 600672-2, obtaining a dielectric strength > 59 kV/mm. However, in spite of the attempts made to maximize the applied field, most of the samples did not breakdown. Therefore, it could be concluded that the dielectric breakdown of the albite glass-ceramic processed by the fast firing route overcomes the ~60 kV/mm value. Table 4 summarizes a dielectric insulator data for conventional ceramic materials in comparison with

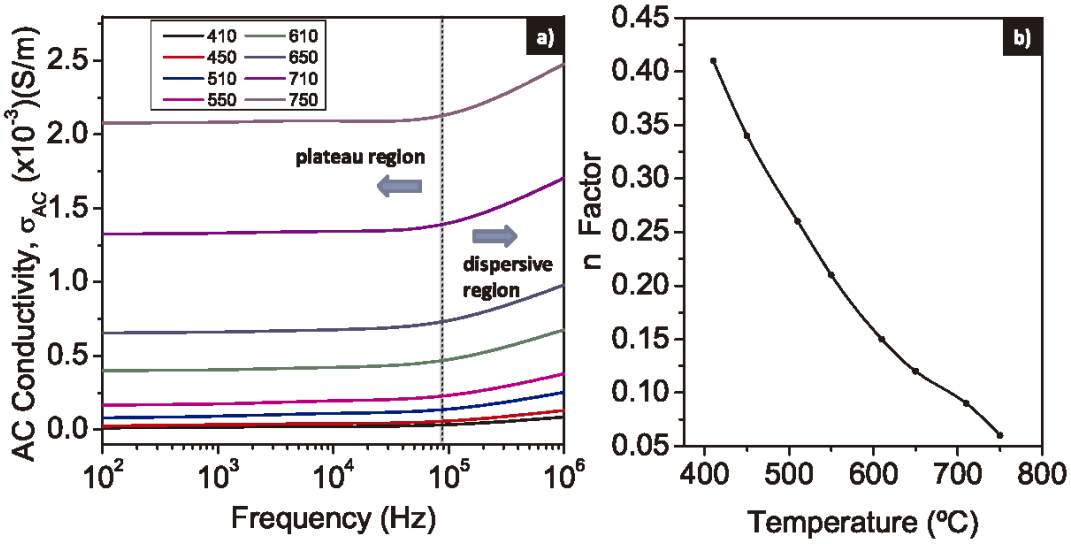

Fig. 7. a) Variation of AC conductivity (σ_{AC}) as a function of frequency in logarithmic scale at different temperatures, for albite glass ceramic, and b) Variation of power law exponent with temperature. These data were obtained from log σ_{AC} vs Temperature plot.

Table 4
Dielectric constant, dielectric losses at 1 MHz and dielectric strength for conventional ceramic materials and synthesized albite glass ceramic (*adapted from* [16]).

Material	ε (at 1 MHz)	tgδ (at 1 MHz)	Dielectric Strength (kV/mm)
99.9% Alumina	9.9	0.0002	17
99% Beryllia	6	0.001	13
Alkali aluminosilicate porcelains	5–7	0.012	20
Alkaline earth and zirconium aluminosilicate porcelains	5–12	0.005–0.007	10-20
Forsterite	7.9–11.9	0.003–0.007	7.9–11.9
Cordierite	4.1–5.3	0.003–0.005	10
Steatite	6	0.001–0.007	15
Zircon	8.0–9.6	0.001	6.3–11.5
Zirconia	12	0.01	~5
Quartz	3.8–5.4	0.0003	15–25
Mica	5.4–8.7	0.0002	39.5–79.1
Albite glass-ceramic	4.6	0.002	> 59

the albite glass-ceramic ones. The dielectric strength of this new glass-ceramic insulator overcomes those of the standard ceramic materials, being comparable with the mineral mica ones. This high-dielectric strength value achieved in albite glass material is strongly influenced by the unique micro-nanostructure of albite, according to the FESEM micrographs. The ability of the material to favour scattering processes and to avoid charge trapping in specific areas, mainly in grain boundaries, allows the material to reach higher dielectric strength values [54]. The hierarchical micro-nanostructure promotes the electron scattering, hindering charge accumulation in albite grain boundaries. Therefore, the potential energy barrier must be relatively low to allow electrons fluxing through grain boundaries, having designed a material with low trap density in the boundaries. On the other hand, glassy phase, which is more electrically conductive, is situated in the boundary between microcrystals and nanocrystals and it may favour the flux of electrons, avoiding the accumulation of charge in these zones and thus the diffusion takes place by hopping of electrons in the defect sites created in the lattice by alkali elements. All of this is supported by the information extracted from Jonscher's power law, which showed us that a translational motion of species along with hopping events over long distances take place in the system. Porosity is another important variable to take into account, since it is well known that low values of porosity lead to an improvement of the breakdown resistance. According to this, porosity was measured and resulted to be ~3.17% with an average pore size of 3.92 ± 0.20 μm, as it may be seen pore size distribution included in section S1 of Supplementary info (Fig. S1b and S1c).

In summary, all these data corroborate the good results of high-dielectric strength obtained for albite glass ceramic. Moreover, its low dielectric constant and dielectric losses have similar values or even lower than the values registered in other conventional ceramic materials such as steatite, cordierite, alumina or Alkali aluminosilicate porcelains, among others (see Table 4) [16]. These dielectric properties situate albite glass-ceramic as a very promising material for ceramic electrical insulator applications, mainly for high voltage insulation, highlighting that thermal cycle of sintering is considerably shorter (1 h duration) than the typical one for conventional ceramic materials that required higher temperatures and times (typically > 1200 °C and > 12 h of duration).

4. Conclusions

A glass ceramic material with high crystallinity, about 94%, has been designed by a fast sintering cycle from a conventional ceramic process. The analyzed dielectric behavior shows low dielectric constant and dielectric losses, with non-Debye type dielectric behavior and huge dielectric strength (~60 kV/mm). The unique hierarchical micro-nanostructure in which the nanostructured regions isolate microcrystals highly influences the dielectric properties of the material. This glass-ceramic material consists on polycrystalline hierarchically-structured albite in which scattering processes of charge carriers are favoured. Moreover, the hopping events of alkali ions from grains into defect sites, mainly localized in glassy phase located at the grain boundaries, avoid charge trapping at the interfaces. All of these characteristics make this material a very promising candidate in the market of ceramic electrical insulator for high-voltage applications, allowing an important save of energy in comparison with current standard materials for these applications.

Appendix A. Supplementary data

upplementary material related to this article can be found, in the online version, at doi:https://doi.org/10.1016/j.jeurceramsoc.2018.02.

009.

References

[1] A. Roula, K. Boudeghdegh, N. Boufafa, O. Aissa, Improving usual and dielectric properties of ceramic high voltage insulators, Cerâmica 55 (2009) 206–208, http://dx.doi.org/10.1590/S0366-69132009000200014.
[2] M.U. Ismail, H. Tsunatori, Z. Nakai, Preparation of mullite cordierite composite powders by the sol-gel method: its characteristics and sintering, J. Am. Ceram. Soc. 73 (1990) 537–543, http://dx.doi.org/10.1111/j.1151-2916.1990.tb06550.x.
[3] J.E. Contreras, E.A. Rodríguez, Nanostructured insulators – a review of nanotechnology concepts for outdoor ceramic insulators, Ceram. Int. 43 (2017) 8545–8550, http://dx.doi.org/10.1016/j.ceramint.2017.04.105.
[4] R. Adnan, Y.C. Chan, F. Islam, Structure–property relationship in high-tension ceramic insulator fired at high temperature, Mater. Sci. Eng. B 106 (2004) 132–140, http://dx.doi.org/10.1016/j.mseb.2003.09.005.
[5] J. Liebault, J. Vallayer, D. Goeuriot, D. Treheux, F. Thevenot, How the trapping of charges can explain the dielectric breakdown performance of alumina ceramics, J. Eur. Ceram. Soc. 21 (2001) 389–397, http://dx.doi.org/10.1016/S0955-2219(00)00186-2.
[6] E. Chibério da Silva, J.N. Gonçalves, P.H. da, S. Lima, P.H. Chibério, W. Acchar, U.U. Gomes, The influence of microstructure, temperature and sintering level on electric properties of electrical insulators obtained from raw materials of Rio Grande do Norte - Brazil, Mater. Sci. Forum. 881 (2016) 111–116, http://dx.doi.org/10.4028/www.scientific.net/MSF.881.111.
[7] M. Touzin, D. Goeuriot, C. Guerret-piécourt, D. Juvé, H. Fitting, Alumina based ceramics for high-voltage insulation, J. Eur. Ceram. Soc. 30 (2010) 805–817, http://dx.doi.org/10.1016/j.jeurceramsoc.2009.09.025.
[8] M.M. Krzmanc, M. Valant, D. Suvorov, A structural and dielectric characterization of NaxCa(1 − x)Al2 − xSi(2 + x)O8(x = 0 and 1) ceramics, J. Eur. Ceram. Soc. 25 (2005) 2835–2838, http://dx.doi.org/10.1016/j.jeurceramsoc.2005.03.151.
[9] J.R. Smyth, D.L. Bish, Crystal Structures and Cation Sites of the Rock-Forming Minerals, (1989), http://dx.doi.org/10.1002/gj.3350240110.
[10] D.A. McKeown, Raman spectroscopy and vibrational analyses of albite: from 25 °C through the melting temperature, Am. Mineral. 90 (2005) 1506–1517, http://dx.doi.org/10.2138/am.2005.1726.
[11] H. Hu, H. Li, L. Dai, S. Shan, C. Zhu, Electrical conductivity of albite at high temperatures and high pressures, Am. Mineral. 96 (2011) 1821–1827, http://dx.doi.org/10.2138/am.2011.3796.
[12] A. Jones, M.S. Islam, M. Mortimer, D. Palmer, Alkali ion migration in albite and K-feldspar, Phys. Chem. Miner. 31 (2004) 313–320, http://dx.doi.org/10.1007/s00269-004-0389-8.
[13] H. Hu, H. Li, L. Dai, S. Shan, C. Zhu, Electrical conductivity of alkali feldspar solid solutions at high temperatures and high pressures, Phys. Chem. Miner. 40 (2013) 51–62, http://dx.doi.org/10.1007/s00269-012-0546-4.
[14] K. Gasek, J. Partyka, M. Gajek, W. Panna, Characteristic of synthesis and transformations of hardystonite in willemite glass-crystalline glaze based on thermal analysis, J. Therm. Anal. Calorim. 125 (2016) 1135–1142, http://dx.doi.org/10.1007/s10973-016-5429-3.
[15] V. Bobnar, Processing of steatite ceramic with a low dielectric constant and low dielectric losses, J. Microelectron. Compon. Mater. 46 (2016) 100–105.
[16] Relva C. Buchanan, Ceramic Materials for Electronics, Third edition, (2004), pp. 525–526.
[17] E. Enríquez, V. Fuertes, M.J. Cabrera, J. Seores, D. Muñoz, J.F. Fernández, New strategy to mitigate urban heat island effect:Energy saving by combining high albedo and low thermal diffusivity in glass ceramic materials, Sol. Energy 149 (2017) 114–124, http://dx.doi.org/10.1016/j.solener.2017.04.011.
[18] J.J. Reinosa, D.M.Y. Marero, A. Del Campo, M.Á. De La Rubia, J.F. Fernández, Chemical analysis with high spatial resolution by rutherford backscattering and Raman confocal spectroscopies: surface hierarchically structured glasses, J. Am. Ceram. Soc. 96 (2013) 1783–1788, http://dx.doi.org/10.1111/jace.12397.
[19] J. Reinosa, F. Rubio-marcos, E. Solera, F. Ferna, M.A. Bengochea, Sintering behaviour of nanostructured glass-ceramic glazes, Ceram. Int. 36 (2010) 1845–1850, http://dx.doi.org/10.1016/j.ceramint.2010.03.029.
[20] E. Enríquez, V. Fuertes, M.J. Cabrera, J. Seores, D. Muñoz, J.F. Fernández, New strategy to mitigate urban heat island effect: energy saving by combining high albedo and low thermal diffusivity in glass ceramic materials, Sol. Energy 149 (2017), http://dx.doi.org/10.1016/j.solener.2017.04.011.
[21] N.M. Khalil, M.M.S. Wahsh, A. Gaber, The effect of albite additions on the sintering, phase compositions and microstructure of vitreous ceramic tiles, J. Ceram. Process. Res. 17 (2016) 478–484.
[22] E. Enríquez, J.F. Fernández, M.Á. García, M.J. Cabrera, J. Seores, F.J. Villar, et al., Glass-ceramic material of albite and/or anorthite exhibing warmth, Centro tecnológico Vidres-ICV (CSIC) (2016) PCT3261.1b.
[23] L.S. Muñoz, J.G. Guinea, S.L. Andrés, Caracterización estructural simple de feldespatos alcalinos: metodología de trabajo, Boletín La Soc. Española Cerámica Y Vidr 30 (1991) 69–79.
[24] M.F. Al-hilli, K.T. Al-rasoul, Characterization of alumino-silicate glass/kaolinite composite, Ceram. Int. 39 (2013) 5855–5862, http://dx.doi.org/10.1016/j.ceramint.2012.12.102.
[25] E. Ateia, M.A. Ahmed, A.K. El-Aziz, Effect of rare earth radius and concentration on the structural and transport properties of doped Mn-Zn ferrite, J. Magn. Magn. Mater. 311 (2007) 545–554, http://dx.doi.org/10.1016/j.jmmm.2006.08.014.
[26] A.K. Jonscher, Dielectric relaxation in solids, J. Phys. D Appl. Phys. 32 (1999), http://dx.doi.org/10.1088/0022-3727/32/14/201.
[27] Y. Yu, X. Hao, L. Song, Z. Li, L. Song, Synthesis and characterization of single phase and low temperature co-fired cordierite glass-ceramics from perlite, J. Non Cryst. Solids 448 (2016) 36–42, http://dx.doi.org/10.1016/j.jnoncrysol.2016.06.039.
[28] D. Wang, M. Han, M. Li, X. Yin, Effect of strontium doping on dielectric and infrared emission properties of barium aluminosilicate ceramics, Mater. Lett. 183 (2016) 223–226, http://dx.doi.org/10.1016/j.matlet.2016.07.113.
[29] A. Prasad, A. Basu, Dielectric and impedance properties of sintered magnesium aluminum silicate glass-ceramic, J. Adv. Ceram. 2 (2013) 71–78, http://dx.doi.org/10.1007/s40145-013-0045-1.
[30] H. Kroll, H. Bambauer, Diffusive and displacive transformations in plagioclase and ternary feldspar series, Am. Mineral. 66 (1981) 763–769.
[31] I. Parsons, Feldspars and Their Reactions, (1994), http://dx.doi.org/10.1180/minmag.1995.059.397.23.
[32] H.W. Zandbergen, M. Foo, Q. Xu, V. Kumar, R.J. Cava, Sodium ion ordering in NaxCoO2: electron diffraction study, Phys. Rev. B Condens. Matter Mater. Phys. 70 (2004), http://dx.doi.org/10.1103/PhysRevB.70.024101.
[33] O.R.K. Montedo, I.T. Alves, C.A. Faller, F.M. Bertan, D.H. Piva, R.H. Piva, Evaluation of electrical properties of glass-ceramics obtained from mill scale, Mater. Res. Bull. 72 (2015) 90–97, http://dx.doi.org/10.1016/j.materresbull.2015.07.040.
[34] H. Hu, C. Academy, H. Hu, Electrical Conductivity of Alkali Feldspar Solid Solutions at High Temperatures and High Pressures, (2017), http://dx.doi.org/10.1007/s00269-012-0546-4.
[35] R.M. Hazen, A. Navrotsky, Effects of pressure on order-disorder reactions, Am. Miner. 81 (1996) 1021–1035, http://dx.doi.org/10.2138/am-1996-9-1001.
[36] E. Meneghinello, A. Alberti, G. Cruciani, Order-disorder process in the tetrahedral sites of albite, Am. Miner. 84 (1999) 1144–1151.
[37] P.E. Le Bourhis, Glass: Mechanics and Technology, Wiley-VCH Verlag GmbH Co. KGaA, 2007, pp. 53–82, http://dx.doi.org/10.1002/9783527617029.
[38] D. Ravinder, A.V.R. Reddy, G.R. Mohan, Abnormal Dielectric Behaviour in Polycrystalline Zinc-Substituted Manganese Ferrites at High Frequencies Abnormal Dielectric Behaviour in Polycrystalline Zinc-Substituted Manganese Ferrites at High Frequencies, (2015), http://dx.doi.org/10.1016/S0167-577X(01)00404-9.
[39] D.C. Sinclair, A.R. West, B.J.T.S. Irvine, D.C. Sinclair, A.R. West, Electroceramics : Characterization by Impedance Spectroscopy, (1990), http://dx.doi.org/10.1002/adma.19900020304.
[40] F. Chiu, A review on conduction mechanisms in dielectric films, Adv. Mater. Sci. Eng. 2014 (2014), http://dx.doi.org/10.1155/2014/578168.
[41] A. Behera, N.K. Mohanty, S.K. Satpathy, B. Behera, P. Nayak, Investigation of complex impedance and modulus properties of Nd doped 0.5BiFeO3-0.5PbTiO3 multiferroic composites, Cent. Eur. J. Phys. 12 (2014) 851–861, http://dx.doi.org/10.2478/s11534-014-0523-2.
[42] V. Thakur, A. Singh, R. Punia, S. Dahiya, L. Singh, Structural properties and electrical transport characteristics of modi fi ed lithium borate glass ceramics, J. Alloys Compd. 696 (2017) 529–537, http://dx.doi.org/10.1016/j.jallcom.2016.11.230.
[43] T. Badapanda, R.K. Harichandan, S.S. Nayak, A. Mishra, S. Anwar, Frequency and temperature dependence behaviour of impedance, modulus and conductivity of BaBi4Ti4O15 aurivillius ceramic, Process. Appl. Ceram. 8 (2014) 145–153, http://dx.doi.org/10.2298/PAC1403145B.
[44] K. Ashok, M.B. Suresh, P. Sarah, Electrical Properties, Of Li and Nd doped SrBi4Ti4O15 ceramics, Int. J. Eng. Res. Technol. 2 (2013) 3299–3307.
[45] K.P. Padmasree, D.K. Kanchan, A.R. Kulkarni, Impedance and Modulus Studies of the Solid Electrolyte System 20CdI2–80[xAg2O–y(0.7V2O5–0.3B2O3)], Where 1 < x/y < 3 vol. 177, (2006), pp. 475–482, http://dx.doi.org/10.1016/j.ssi.2005.12.019.
[46] N. Cu, Z. Fe, Complex impedance and electric modulus studies of magnetic ceramic Ni0.27Cu0.10Zn0.63Fe2O4, J. Adv. Ceram. 4 (2015) 217–225, http://dx.doi.org/10.1007/s40145-015-0152-2.
[47] M. Singh, A. Mahajan, N. Gupta, R.K. Bedi, Study of junction charge transport properties of boron subphthalocyanine chloride thin film, Electrochim. Acta 11 (2015) 118–126, http://dx.doi.org/10.1007/s13391-014-4097-3.
[48] V.P. Il'ina, Feldspar material from karelia for electrical engineering, Glas. Ceram. (Engl. Transl. Steklo I Keramika). 61 (2004) 195–197, http://dx.doi.org/10.1023/B:GLAC.0000043092.46042.20.
[49] H. Mizutani, H. Kanamori, Electrical conductivity of rock-forming minerals at high temperature, J. Phys. Earth 15 (1967), http://dx.doi.org/10.4294/jpe1952.15.25.
[50] B. Behera, P. Nayak, R.N.P. Choudhary, Impedance spectroscopy study of NaBa2V5O15 ceramics, J. Alloys Compd. 436 (2007) 226–232, http://dx.doi.org/10.1016/j.jallcom.2006.07.028.
[51] A.K. Jonscher, The "universal" dielectric response, Nature 267 (1977) 673–679, http://dx.doi.org/10.1038/267673a0.
[52] K. Majhi, K.B.R. Varma, Dielectric Relaxation in CaO– Bi2O3–B2O3 Glasses vol. 97, (2010), pp. 89–97, http://dx.doi.org/10.1111/j.1744-7402.2009.02438.x.
[53] B.M. Greenhoe, M.K. Hassan, J.S. Wiggins, K.A. Mauritz, Universal Power Law Behavior of the AC Conductivity Versus Frequency of Agglomerate Morphologies in Conductive Carbon Nanotube-Reinforced Epoxy Networks, (2016), pp. 1918–1923, http://dx.doi.org/10.1002/polb.24121.
[54] M. Touzin, D. Goeuriot, C. Guerret-piécourt, D. Juvé, H. Fitting, Alumina based ceramics for high-voltage insulation, J. Eur. Ceram. Soc. 30 (2010) 805–817, http://dx.doi.org/10.1016/j.jeurceramsoc.2009.09.025.

Hierarchical micro-nanostructured albite-based glass-ceramic for high dielectric strength insulators

V. Fuertes*[1], M.J. Cabrera[2], J. Seores[2], D. Muñoz[2], J. F. Fernández[1], E. Enríquez[1,2]

[1]Dept. Electrocerámica, Instituto de Cerámica y Vidrio, CSIC, Kelsen 5, 28049, Madrid, Spain.

[2]Centro tecnológico Vidres, S.L., Ctra. Onda, Km 3.4, 12540 Villareal, Castellón, Spain

Supplementary information

S1. Hot stage microscopy and porosity characterization

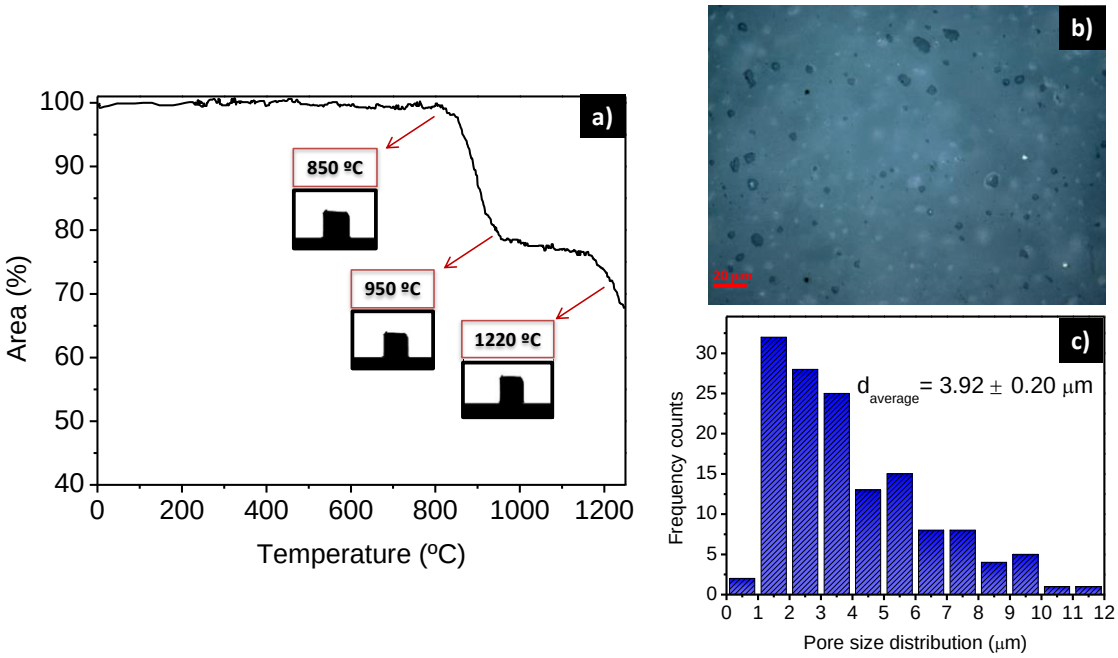

Figure S1. **a)** Hot Stage Microscopy for albite-based glass-ceramic, **b)** representative albite-based glass-ceramic micrograph in which porosity was estimated, and **c)** pore size distribution with an average pore diameter of 3.92 ±0.20 μm calculated from b).

Hot Stage Microscopy was carried out to identify the temperature at which samples will be sintered. Figure S1a shows several temperatures of interest at which an area loss is observed. The heating rate employed was 30 ºCmin-1 which allows us to simulate an industrial sintering cycle. Sinterization takes place from 950 ºC up to 1250 ºC and from this point melting occurred. Taking into account these results, albite was sintered at different temperatures in this interval,

varying the holding time from 6 min to 1 hour. Figure S1b shows the total porosity evaluated by an image analyser system from a micrograph of the sample sintered at 1220 ºC for 6 min, which was chosen as the optimum thermal treatment, showing the least proportion of pores and allowing to save a considerable amount of energy. The rest of temperatures studied were rejected owing to a larger amount of pores which is well known that make mechanical properties and dielectric strength worse. In the figure S1b can be seen a representative micrograph which shows a low pore percentage, about 3.17 %, with a mean diameter of 3.92±0.20 μm as it is depicted in the pore size distribution of figure S1c.

S2. Thermogravimetric and differential thermal analysis.

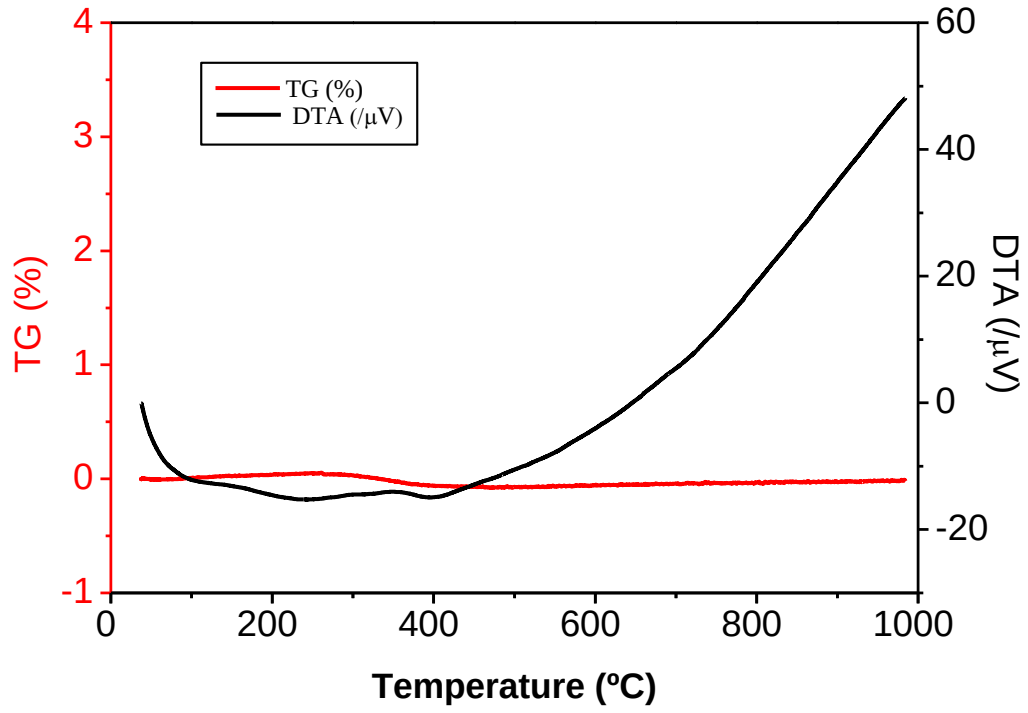

Figure S2. Thermogravimetric and differential thermal analysis for albite glass-ceramic sintered at 1220ºC.

A DTA-TG does not indicate any phase transition of the glass ceramic material in the measured range. The sample does not exhibit any mass loss and the DTA does not show any exo or endothermic peak that indicates some temperature process. The slightly increase of voltage from 600ºC indicates that probably, a phase transition from triclinic to monoclinic structure will occur at

temperatures above 1000ºC. Therefore, below 750ºC order disorder processes should have undergone, which contribute strongly to dielectric behaviour observed.

S3. Frequency dependence of the imaginary part of dielectric constant.

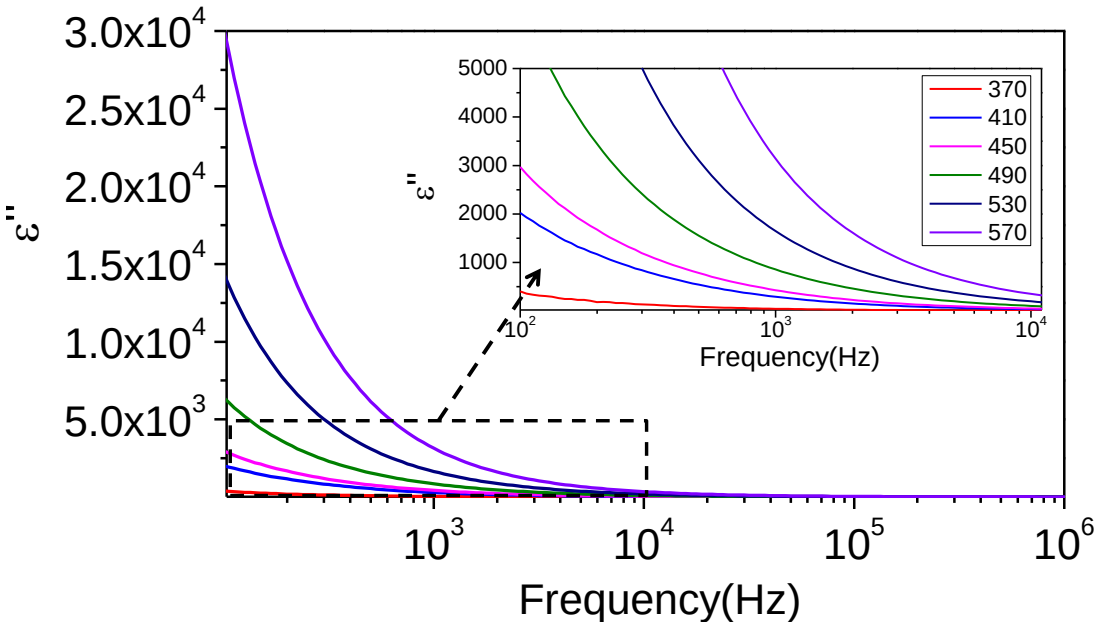

Figure S3. ε'' vs frequency for albite glass-ceramic in the temperature range studied.

Imaginary part of the dielectric constant shows higher values for higher temperatures (figure S2). As frequency increases a decrease in ε'' occurs, reminding a decreasing exponential behaviour. From 10^4 Hz, the difference between all the curves is less prominent. Any peak is observed in the plot, which indicates that a pure conduction process takes place, based on a hopping mechanism, as it was described in the manuscript.

ARTÍCULO 6. Microstructural study of dielectric breakdown in glass-ceramics insulators

V. Fuertes, M.J. Cabrera, J. Seores, D. Muñoz, J. F. Fernández, E. Enríquez.

Journal of the European Ceramic Society, 39, 2019, 376-383.

Factor de impacto: 3,794 (según JCR Edition Science 2017).

Journal of the European Ceramic Society 39 (2019) 376–383

Contents lists available at ScienceDirect

Journal of the European Ceramic Society

journal homepage: www.elsevier.com/locate/jeurceramsoc

Original Article

Microstructural study of dielectric breakdown in glass-ceramics insulators

V. Fuertes[a,*], M.J. Cabrera[b], J. Seores[b], D. Muñoz[b], J.F. Fernández[a], E. Enríquez[a,b]

[a] Dept. Electrocerámica, Instituto de Cerámica y Vidrio, CSIC, Kelsen 5, 28049, Madrid, Spain
[b] Centro tecnológico Vidres, S.L., Ctra. Onda, Km 3.4, 12540, Villareal, Castellón, Spain

ARTICLE INFO

Keywords:
Glass-ceramics
Ceramic electrical insulation
Dielectric breakdown
Aluminosilicates
Feldspars

ABSTRACT

Novel glass-ceramic materials based on Na and Ca-rich feldspar crystallizations with a hierarchical micro-nanostructure shown the largest dielectric strength, > 57 kV/mm, reported at room temperature in ceramic insulators, due to a large amount of interfaces that favor scattering processes of charge carriers. Dielectric breakdown tests with temperature indicated they withstood up to 200 °C, with dielectric strengths of 30 kV/mm and 44 kV/mm for anorthite and albite-based glass-ceramics, respectively. These values are even larger than the ones obtained at room temperature for most of the current ceramic insulators. Microstructural characterization and micro-Raman spectroscopy carried out after breakdown allow determining the dielectric breakdown mechanisms. Glass phases in the surroundings of the crater because of local melting and fast cooling are identified. These results make feldspar based glass-ceramics suitable for electrical insulator applications at room and high temperature. Moreover, dielectric breakdown mechanism may allow tailoring new high insulating application in the future.

1. Introduction

Ceramic materials are chemically stable, refractory, wear-resistant and have good mechanical and physical properties. For that reason their use in many applications in different fields is becoming increasingly widespread [1–4]. Most of ceramics are good insulators, both thermal and electrical. One of the main applications of ceramics is as electrical insulators, being the ability of withstanding high voltages an essential requirement for some applications in the field of electrical engineering and solid state electronics [3,5–7].

Electronics market has been changing very rapidly over recent years and new devices are demanded to be smaller, faster and more energy-efficient than before. One of the main problems of a higher performance electric devices is the heating produced during the operation time. The high temperatures generated in a device may wear them out and make useless. Insulating materials are needed in integrated circuit devices, but they need to withstand high temperatures without a significant deformation to have a high volume resistivity and high strength [8]. A machinable glass-ceramics can meet these requirements and solve heat-generation problems in new electronic devices because they are chemically stables until high temperatures, they can operate well at these temperatures and, unlike metals, they will not creep or deform. However, the main limitation of ceramic or glass-ceramic materials in these high-voltage applications is the dielectric breakdown, which leads to the loss of insulating properties [9]. Dielectric breakdown depends on multiple factors in addition to the applied voltage, such as room temperature and material properties like temperature durability and thermal conductivity [10,11]. A failure in the insulation of an electronic device, in a high-voltage system or a similar application can cause important damages. As temperature increases, the insulating properties of the ceramic material deteriorate because charge transport is activated [12]. For this reason, since materials properties are strongly influenced by temperature, a thorough analysis of their thermal behaviour must be carried out, in order to guarantee the safety of systems.

Dielectric breakdown mechanism in solids is principally intrinsic (electronic or avalanche) or thermal [13–15]. If a voltage is applied for a short time, about 10^{-8} s, the dielectric strength increases fast up to a limit, known as the intrinsic electric strength. Intrinsic breakdown is very difficult to identify and may be classified in electronic and avalanche breakdown. The first one takes place when an electric field is applied and promotes electron from conduction to valence band repeatedly, leading to breakdown. Avalanche or streamer breakdown occurs when electrons in the dielectric, accelerated sufficiently by the electric field applied, are able to liberate bounded electrons from the lattice atoms. Repetition of this process results in an electron avalanche [10,13,16]. Moreover, the electric field applied generates a conduction current which heats the material. When this heat generated is greater than the heat dissipated by the material, thermal breakdown happens.

* Corresponding author.
E-mail address: vfuertes@icv.csic.es (V. Fuertes).

https://doi.org/10.1016/j.jeurceramsoc.2018.08.044
Received 6 June 2018; Received in revised form 18 August 2018; Accepted 28 August 2018
Available online 30 August 2018

In a previous work it has been studied the dielectric properties of a new glass-ceramic material, carefully designed with a low content of glassy phase and based on micro-nano structured albite crystallization with very promising dielectric properties [17] (see Fig. S1a Supplementary information). Nanostructure favours scattering processes of charge carriers which leads to have a dielectric breakdown strength > 59 kV/mm, the largest dielectric strength reported at room temperature in ceramic insulators, low dielectric constant (ε = 4.6 at 1 MHz) and low dielectric losses (~10^{-3} at 1 MHz), at room temperature. On account of these significant results, a study of the dielectric strength as a function of the temperature is of great interest. In view of the previous great dielectric properties, highlighting for dielectric strength similar to natural mica, another feldspar glass-ceramic material based on anorthite crystallization was also synthesised by the same procedure [18]. The anorthite based glass-ceramics also possesses a characteristic micro-nano structure formed by several phases in order to keep scattering processes for both, phonons and charge carriers (see Fig. S1b Supplementary information).The electrical conductivity in Na and Ca-rich feldspars depends on thermal activate hopping of sodium and calcium ions, respectively, as the main responsible of conduction mechanism [19,20]. Ca^{2+} has a slight less mobility than Na^{+} and therefore ionic conduction should be lower, which should improve the insulator behaviour of anorthite glass-ceramics in comparison with albite glass-ceramics. However, dielectric breakdown is a complex process in which several factors should be taken into account, such as porosity, crystallographic defects, lattice distortions, impurities, grain boundaries or interfaces with secondary phases [17,21]. Therefore, dielectric strength has to be analyzed in detail, considering mainly the breakdown mechanism which may lead to understand accurately the processes involved in the glass-ceramic.

The aim of this work is to study deeply the behaviour of this new family of glass-ceramic materials with temperature (up to 200 °C), by exploring the high voltage effect and trying to elucidate the involved breakdown mechanism. For this purpose, the study was supported by SEM and micro-Raman spectroscopy measurements in order to analyse the breakdown point and the surrounding area to identify what may occur in the material during dielectric breakdown, which, according to the best of our knowledge, it has never done before in such detail in any glass-ceramic materials.

2. Experimental procedure

2.1. Sample preparation

Both glass-ceramics were prepared by a conventional ceramic process [22]. The precursors used were mixed: kaolin (Molcasa), with a particle size d_{50} = 5.34 μm, and frit in a weight proportion of 10/90, respectively. After the mixing, a milling in an alumina ball mill for 20 min with 37 wt% of water was carried out [22,23]. The frits compositions expressed in term of equivalent oxides are shown in Table 1. The homogenized compositions were dried at 60 °C for 24 h and sieved under 100 μm, achieving monomodal particle size distributions with d_{50} = 6.72 μm for albite-based glass-ceramic and d_{50} = 7.52 μm for anorthite-based glass-ceramic. Then, the obtained powders were pressed in a circular die at 39.2 MPa. Finally, pressed samples were thermally treated in an industrial furnace at 1220 °C for 6 min with a 30 °Cmin^{-1} heating rate, in a rapid cycle of 55 min [17,18]. The main difference between anorthite and albite frits is the presence of ZrO_2 and/or SrO, respectively, which play a crucial role in the crystallization of both phases. SrO is a lattice disruptor which favours the formation of the sodium aluminosilicate after devitrification process, although the frit only has a 2% of Na_2O. However, Zirconium oxide is a nucleating agent and it is used in higher percentage in the composition without SrO [24].

Table 1
Composition of the albite and anorthite frits expressed as equivalent oxides. The minority components are all included in others. *Others: TiO_2, Fe_2O_3, P_2O_5, MgO, PbO each one lower than 1 wt%.

Oxides wt %	SiO_2	ZrO_2	SrO	Na_2O	K_2O	Al_2O_3	ZnO	CaO	Others*
Albite	54.15	2.18	7.13	2.12	1.43	22.42	1.26	7. 66	1.65
Anorthite	47.33	8.03	–	5.06	1.70	19.23	4.72	12.97	0.96

2.2. Characterization

Dielectric strength was evaluated in a Faraday cage for safety precautions by using a HV DC Power Supply 60 kV and 2.5 mA (Hipotronic, Brewster, NY) and following UNE-En ISO standard no. 600672-2 where > 10 disks, one face of which includes a hemispherical recess of 10°. Both sides of the disks were silver painted and dried at 120 °C for 2 h and then cooled down to room temperature in a desiccator. Samples were immersed in a silicon oil bath to minimize surface currents and flash over during high voltage measurements. The temperature of the sample was homogenized while it was heated on a stirring hot plate. The silicon oil employed might be warmed up to 230 °C without degradation and losing of insulation properties. The bath temperature was controlled by an Hg thermometer located inside of it. Measurements were carried out increasing gradually the voltage in steps of 1 kV/s, 3 kV/s and 5 kV/s and in each step the current was cut off to allow the sample cooling and avoid a possible thermal breakdown. The application of current was carried out following: 1) in each step the current was cut off to allow the sample cooling and 2) by increasing current continuously, in order to check if the breakdown may be produced by a possible thermal breakdown. This procedure was repeated until dielectric breakdown occurred which was identified by a sudden huge increase of the current accompanied by the appearance of sparks and crackling.

Microstructural characterization after dielectric breakdown was studied by means of Field Emission Scanning Electron Microscopy (FESEM) using a Hitachi S-4700, with a resolution of 1.5 nm at 15 kV; and with high resolution micro-Raman spectroscopy (Witec ALPHA 300RA) with a laser excitation Nd:YAGa 532 nm and objective 100× (NA = 0.9). The acquired spectra were analyzed with the Witec Project 2.02 program. Raman image of albite and anorthite samples was measured with 14 μm × 8 μm and 160 μm × 180 μm of size respectively, and 130,048 spectra for each image. Polished samples were chemically etched with 5 vol% of HF with the aim of partially removing the glass phase to reveal the microstructure.

3. Results and discussion

3.1. Dielectric breakdown measurements at high temperature

In previous works, dielectric strength at room temperature was measured for albite glass-ceramic, obtaining values > 59 kV/mm [17]. Now, dielectric breakdown at room temperature for anorthite-based glass-ceramic is also tested in order to compare them, achieving a dielectric strength > 57 kV/mm. Therefore, both glass-ceramic materials present similar dielectric strength at room temperature, due probably to the similar composition and micro-nanostructure.

In this work, dielectric breakdown measurements are carried out as a function of temperature for both materials according to UNE-En ISO standard no. 600672-2, in view of the good dielectric strength registered in albite and anorthite glass-ceramic at room temperature. It is expected that the dielectric strength decreases with the increasing of temperature due to the rise of the electron mobility which promotes the losing of insulating properties. In several works it has been reported that the ramp rate of the applied voltage might affect the measured dielectric breakdown strength, because as voltage increases charge injection in the material increases which may affect conduction process

[5,25]. For this reason, voltage ramp rates of 1 kV/s, 3 kV/s and 5 kV/s were considered. After measurements, it can be concluded that the voltage ramp rates used in the tests have no significant effect on the breakdown strength and therefore effects due to e.g. space charge accumulation cannot be noticed [5,25]. Both glass-ceramic materials withstood temperatures up to 200 °C, independently of the rate of voltage rise and the cooling process above commented, which suggest an electronic process [5]. Albite and anorthite glass-ceramics resulted in a dielectric strength up to 44 kV/mm and 30 kV/mm, respectively. This difference between both materials observed at high temperatures cannot be correlated in principle to the lower mobility of Ca^{2+} in anorthite based glass-ceramics. The glassy phase content is a relevant factor for such behavior, ca. 6% in albite samples and ca. 9% in anorthite samples (see Fig. S1c in Supplementary information) [17,18]. In the kind of glass-ceramic system studied as well as in others such as porcelain or cordierite glass-ceramics, glassy phase has a slightly higher conductivity than crystalline phase, dominating conduction process [5,26]. Charge carriers can be transported more easily along the glassy network, undergoing no significant blocking effect and favouring dielectric breakdown [26,27]. Therefore, a higher amount of glass will lead to a higher conductivity of the system and will facilitate dielectric breakdown. In addition, the widespread presence of other crystalline phases in anorthite based glass-ceramics, such as monoclinic ZrO_2 ($\sigma \sim 10^{-3}$S/m) or tetragonal $ZrSiO_4$ which have larger conductivities than anorthite (below 10^{-7}S/m), at room temperature, could contribute to the overall conductivity and therefore favours the dielectric breakdown. Moreover, the porosity of samples is measured since it is a parameter that also strongly affects the breakdown resistance of the materials. Porosity resulted to be ~3.2% with an average pore-size of 3.9 ± 0.2 μm for albite glass-ceramic and 8.7% with an average pore-size of 5.4 ± 0.4 μm for anorthite glass-ceramic [17]. Therefore, the porosity is slightly higher in anorthite, which also account for the decreasing in the dielectric strength. All these factors contribute to the whole electrical conductivity of these glass-ceramics, leading to reach lower values of dielectric strength in anorthite than in albite-based glass-ceramic. In a previous work, a negative temperature coefficient of resistance (NTCR) was proved for albite-based glass-ceramic and therefore, as temperature increases, a reduction of resistivity in the material takes place [17]. This semiconductor-like behaviour registers in both glass-ceramic materials causes a decreasing of insulating properties with the increase of the temperature because of a modification in the charge transport. Anyway, both materials have a huge dielectric strength at 200 °C, even higher than dielectric strength of several conventional materials at room temperature [17]. The dielectric strength values obtained for these new glass-ceramics at 200 °C overcome the values registered in the bibliography for alumina based ceramics with a certain amount of anorthite, in the range of 9–16 KV/mm at 250 °C [12], which makes these both material very promising candidates in the market of ceramic electrical insulator highlighting for high-voltage applications.

3.2. Scanning electron microscopy of breakdown channels

After dielectric breakdown process, the samples are analyzed by SEM in order to determine the microstructural evolution. Fig. 1a and b and their enlargements (c and d) show the micrographs for anorthite and albite-based glass-ceramic, respectively. In both glass-ceramics materials it may be seen an irregular shape of the main crater formed after breakdown test and the twisting cracks that propagate from the crater due to the stress and thermal dilatation produced during the dielectric breakdown. The propagation of these cracks may be favoured by the presence of glassy phase placed in the grain boundaries of these materials, which is more conductive than the crystalline phase, as it was previously discussed. Moreover, the presence of some particles of other minor phases, as zircon, which hinder the progress of the cracks in one way, causing the twisting observed. In both cases, EDX analysis reveals compositional differences between the surrounding area of the cracks and far from this region. EDX analysis for anorthite (see Table 2) shows the presence of a high amount of SiO_2 in regions near to the crater, points 1 and 3 (Fig. 1a and c), which indicates a glass formation due to the melting material because of the locally high temperatures reached during the breakdown for the sudden increase of a high current, and the immediately fast cooled. In regions farther from the crater center, less amount of SiO_2 is detected because this area is less affected by dielectric breakdown. These different compositions are summarized in the Table 3 which presents that the silica content decreases as we move away from the crater: 92.57%, 78.77% and 61.48% for points 1, 3 and 4, respectively. In a farther zone, point 2, a higher content of CaO is observed in addition to Al_2O_3 and SiO_2 that should correspond to the crystallization of the major phase, anorthite. A certain amount of NaO is also found, because of the formation of albite as a minor phase, as seen in the XRD in Fig. S1c of Supplementary information [18]. In the case of albite glass-ceramic (see Table 2) the chemical analysis reveals again a higher amount of silica, > 80%, in the closest zone to the crater (surroundings of point 5 in Fig. 1d). In point 6 (Fig. 1d), 8.51% of NaO is registered which should come from albite phase crystallization as the main phase, as well as a minor amount of K_2O and CaO, which may form different minor phases difficult to identify. To overcome difficulties in phase identification, confocal Raman microscopy is used and showed in the next section.

3.3. Confocal Raman microscopy

To deepen in the study of the dielectric breakdown and to analyze in more detail the phases formed in the surroundings of the crater, samples are characterized by confocal Raman microscopy. Fig. 2a shows an optical image from the confocal microscope for albite-based glass-ceramic in the surrounding of the breakdown crater where it is observed a crack propagated from the main crater. In the selected area marked in this image, a Raman image is formed by using the color code of the different identified phases in the analyzed area (Fig. 2b). It is possible to distinguish four main phases identified as: albite feldspar (pink), the major one located far from the crater; zircon (yellow), located between albite crystals: an aluminosilicate glass (blue) formed just in the surroundings of the crater; and silica glass (cyan) close to the crater, in the area between the aluminosilicate glass and albite crystals. The Raman spectra of the different phases are presented in Fig. 2c with the same color codes as the Raman image. Albite and zircon phases agree with the patterns obtained from RRUFF database for albite (R050253-3) and zircon (R050203) minerals which allowed us to corroborate the formation of these phases. Moreover, the main Raman modes for albite-based glass-ceramic and zircon are identified and match with Raman modes reported in the bibliography [28,29]. The Raman image shows that close to the main breakdown crater an aluminosilicate glass material is formed due to the great heat generated during the breakdown as well as another kind of silica glass. In farther regions from the crater, zircon and albite phases are found, corresponding to the original material.

Therefore, the new phases formed, as a consequence of the melting processes reached because of dielectric breakdown, have been identified as different forms of silicate glasses. This new glasses formation is due to the great diffusion of cations during the melting process, even its vaporization, which changes the original composition. That confirms the hypothesis that a glass is formed due to the fast cooling process after melting as a consequence of dielectric breakdown, corroborating the information discussed in the Section 3.2 The aluminosilicate phase undergoes an important Raman shift along the surroundings of dielectric breakdown. The Raman shift accounts for a relevant stress gradient during the melting that could also promote compositional variations by the high mobility of alkali ions in the molten which produces the inhomogeneity observed. Fig. 2d shows three single spectra taken in different point of the crater surroundings (marked in

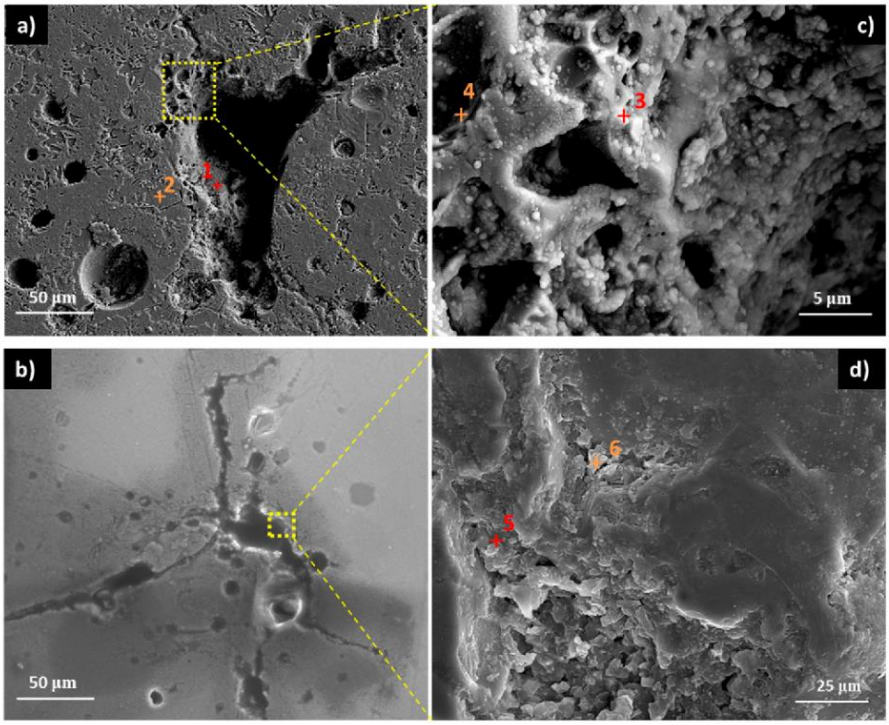

Fig. 1. Micrographs of breakdown crater, showing cavities and twisting cracks formed in **a)** and **c)** anorthite-based glass-ceramic and **b)** and **d)** albite-based glass-ceramic.

Table 2
Oxide composition obtained by EDX in points 1–6 marked in Fig. 1 for anorthite and albite based glass-ceramic.

	Point	Na_2O	Al_2O_3	SiO_2	K_2O	CaO	ZrO_2
Anorthite	1	1.47	3.24	92.57	–	2.72	–
	2	6.27	19.64	49.64	3.86	12.44	8.15
	3	2.21	10.30	78.77	2.90	5.82	
	4	3.89	19.52	61.48	–	7.25	7.86
Albite	5	1.65	8.66	84.70	0.72	2.85	–
	6	8.51	21.73	58.06	1.08	3.91	–

Fig. 2b) where it is possible to observe the red-shift of the Raman modes as being further away from the crater. This spectrum presents three main bands. In the range of 278–289 cm^{-1} two Raman modes are observed: one at 278 cm^{-1} that has been reported in a glass system with a composition of $5Na_2O{\cdot}20CaO{\cdot}5Al_2O_3{\cdot}\ 60SiO_2$ and it is related to the vibration of Ca^{2+} cations; and a shoulder at 222 cm^{-1} which is can be related to the vibration of Na^+ [30]. In a glass system composed by a mixture of nepheline ($NaAlSiO_4$) and anorthite ($CaAl_2Si_2O_8$) it was observed a blue shift (to higher wavenumber) of this Raman mode as anorthite content increased while the nepheline content was reduced as occurs in our case [31].

In the inset of Fig. 2d it may be observed an enlargement of the second Raman mode, the dominant symmetric stretch ν_s (T–O–T) Raman band, for the three Raman single spectra, where T represents Si or Al. This Raman mode is shifted between 492-505 cm^{-1} and it is related to the motions of bridged oxygen in T–O–T linkages [30]. In a crystal and in a glass the frequency of this Raman band is sensitive to the size of TO_4 rings which form the structures. Materials with four-membered rings have the ν_s (T–O–T) mode above 500 cm^{-1}, such as albite or anorthite crystals and anorthite glass, while materials with six-membered rings have Raman bands below 480 cm^{-1}, such as nepheline glasses [31]. Zones in the Raman image with a blue shift in the aluminosilicate glass formed should have a higher content of anorthite glass and therefore an increase in four-membered ring concentration, while zones with a red shift in the range 492–505 cm^{-1} would indicate a reduction of a four-membered ring concentration at the expense of an increase of the six-membered ones, which may indicate the formation of nepheline according to the literature and in agreement with the Na_2O content detected previously by SEM-EDX [31].

Finally, the third broad Raman band which appears at high frequencies, ~850–1000 cm^{-1}, is related with the antisymmetric-stretching modes of the bridging oxygens and the cations which form the network. In some points, as point 1 and 2, this Raman band registers stronger blue shifts which could probably be attributed to that the Si:Al ratio of the different species formed is varying, indicating that in these points higher content of Na/K-aluminosilicate feldspar is formed, while in the regions as point 3 more nepheline and anorthite should be crystallized, which agrees well with the results explained above for the other two Raman bands [31,32].

Another silicate glass is identified in a widespread region close to the crater and marked with a cyan color in the Raman image 2b. These Raman bands indicate the presence of an amorphous glass different of the aluminosilicate glass previously discussed. Two broad Raman bands are observed in the ranges of 400–600 cm^{-1} and 900–1100 cm^{-1}. According to the bibliography, these Raman bands correspond to the vibration modes of a silicate glass with a low content of Al_2O_3, such as a soda-lime silicate glass, which agrees well with the results obtained from EDX analysis in Table 2 [33]. The Raman band centred at ~500 cm^{-1}, known as D_1 band, correspond to a defect mode associated to breathing vibrations of oxygen atoms in four-membered rings; and it has a shoulder at 560 cm^{-1}, which is attributed to Si–O–Si symmetric stretching vibration mode of Q_3 species. The Raman band at ≈1000 cm^{-1} corresponds to symmetric Si–O stretching vibrations of the silicate tetrahedral units with three, two and one non-bridging oxygen atoms, usually defined as Q_1, Q_2, Q_3 species respectively [33,34].

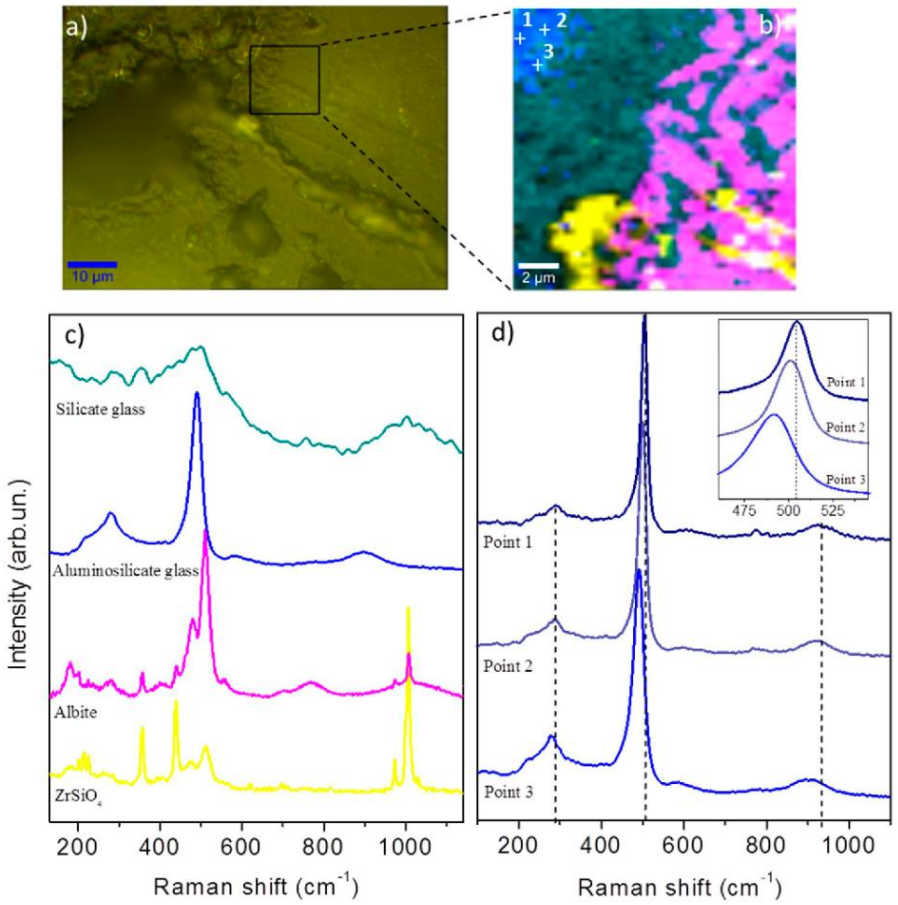

Fig. 2. a) Optical image of albite-based glass-ceramic in the surrounding of dielectric breakdown crater; **b)** Raman image of the selected area in a), shown a phase evolution from the crater to outward, distinguishing four phases represented by color codes as denotes in c); **c)** Raman spectra of albite (in pink), zircon (in yellow), aluminosilicate glass (in blue) and silicate glass (cyan); **d)** three single Raman spectra taken in the aluminosilicate phase, marked as 1, 2 and 3 point in Fig. 2b. The inset shows the shift undergone by ν_s (T-O-T) Raman mode, showing stress variations in the breakdown crater zone. (For interpretation of the references to colour in this figure legend, the reader is referred to the web version of this article).

Therefore, thanks to micro-Raman spectroscopy it can be concluded that some new phases are formed because of the dielectric breakdown in the surroundings of the breakdown channel for albite-based glass-ceramic: a silicate glass similar to a soda-lime silicate glass and a heterogeneous aluminosilicate glass which presents a high content of silica and calcium, being anorthite glass the main component, but also a slight content of sodium and probably potassium, which may also favour nepheline and orthoclase formation after the melting during dielectric breakdown and the immediate fast cooling process.

For anorthite-based glass-ceramic a similar confocal Raman microscopy study is carried out. Fig. 3a shows an optical image from the confocal microscope for anorthite-based glass-ceramic in the surrounding of the breakdown crater where it may be observed some cracks propagated from the main crater as occurred in albite-based glass-ceramic. In the selected area marked in Fig. 3a a Raman scanning is performed. In the Raman image of Fig. 3b, it is possible to distinguish also four phases identified as: feldspar (red), the major one located around the crater and the cracks; zircon (yellow), randomly located along feldspar crystals; an aluminosilicate glass (blue) formed just in the surroundings of the crater; and a different silicate glass (cyan) also close to the crater. The Raman spectra of the different phases are presented in Fig. 3c with the same color codes as the Raman image.

The phases observed in this anorthite sample agree with those previously obtained for the albite-based glass-ceramic. In the inset of Fig. 3c is showed an enlargement of the D_1 band for two single spectra taken in the aluminosilicate glass phase in the points marked in Fig. 3b. The dash line of the inset shows that, as being further away from the crater, there is a red-shift of the D_1 band, which indicates a decrease of the force constant associated to the breathing vibrations of oxygen atoms in four-membered rings. The change in force constant is due to compositional variations, as it was explained above for albite-based glass-ceramic (Fig. 2). The similarities in Raman modes and the overlapping of Raman shift of some of them represent an additional difficulty to determine the composition of the major phase which corresponds to a Na/Ca-rich feldspar [28,35]. The correlation of EDX result and the Raman red shift of the D1 band allow determining the materials evolution during the dielectric breakdown process. It is worth mentioning that this evolution is similar in both glass-ceramics under study. So, it is a common scenario under the appearance of dielectric breakdown in these high resistance insulators that involved the microstructure evolution of the material.

3.4. Dielectric breakdown mechanism

The mechanism of dielectric breakdown in this new family of glass-ceramics may be explained as follows: The rise of the input voltage increases the number of electrons which accumulated at the sample surface promoting an increase of charge carrier population in conduction band and a sudden conduction current in the material. Because of the Joule effect, the temperature undergoes a huge increase in the material during the breakdown, reaching temperatures of the glass melting point. The chemical composition determined by EDX analysis (Table 2) in the closest point to the breakdown crater analysis of residual silicate glass, shown that it is a glass with ≈90% of SiO_2, therefore and accordingly to the phase diagram [36], the reached temperature should be above 1500 °C. Fig. 4 shows a mechanism scheme of the dielectric breakdown, where the irregular shape of the crater is observed, which differs from the usual circular cavity formed

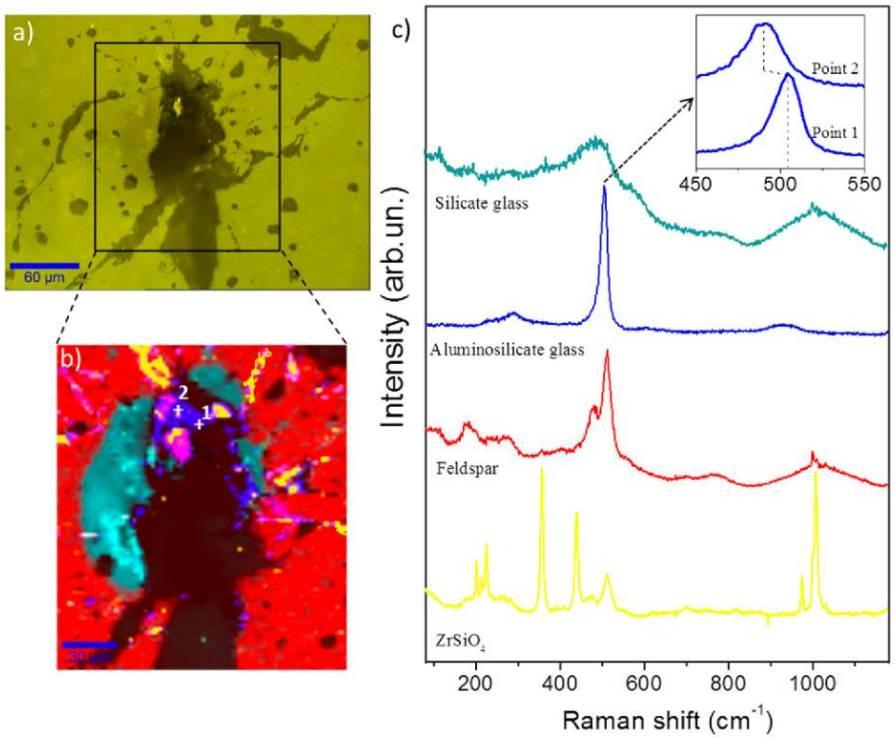

Fig. 3. a) Optical image of anorthite-based glass-ceramic in the surrounding of dielectric breakdown crater; **b)** Raman image of the selected area in a), shown a phase evolution from the crater to outward, distinguishing four phases represented by color codes as denotes in c); **c)** Raman spectra of feldspar (in red), zircon (in yellow), aluminosilicate glass (in blue) and silicate glass (cyan); in the inset the enlargement of D_1 band region for two single Raman spectra taken in 1 and 2 marked points in figure b). (For interpretation of the references to colour in this figure legend, the reader is referred to the web version of this article).

after dielectric breakdown in Al_2O_3 [21] or the typical fracture produced in insulator glasses [37]. The closest areas of the crater would present higher temperatures (marked by red color) and the existence of microcrystals, nanocrystals, glassy phase and other minority phases, with different thermal expansion coefficients, would cause an inhomogeneous dissipation of heat (marked by orange and yellow zones). This heat dissipation would produce stresses around the crater (represented in the scheme with τ_{ij} vectors and blue arrows) generating strains and twisting cracks around the crater. In addition, the molten region favour cation drag, in particular those with higher mobility such

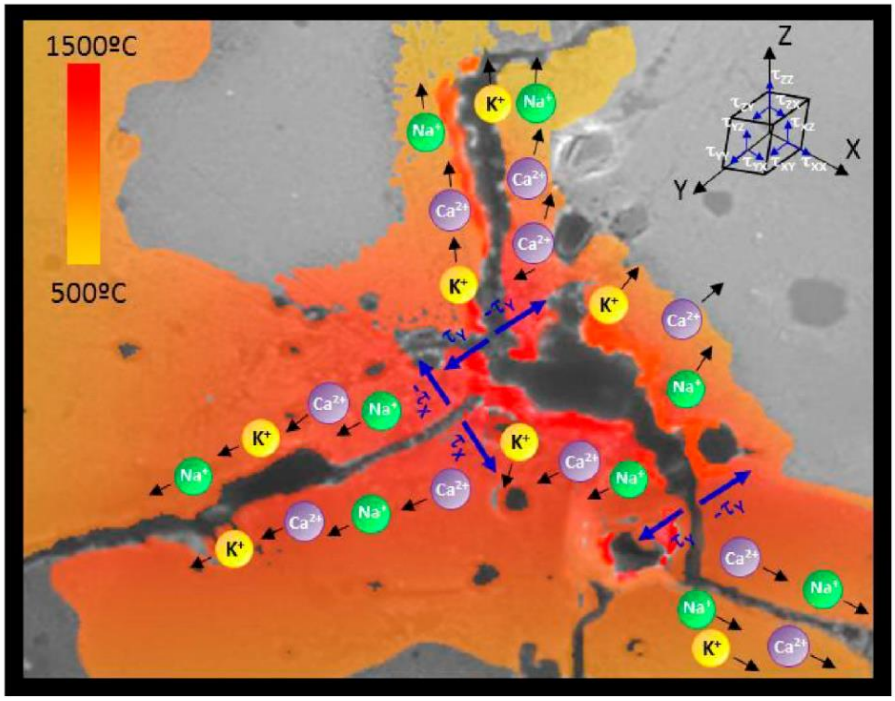

Fig. 4. Diagram of the dielectric breakdown mechanism proposed, where cations diffusion, stress (indicated by blue arrows) and temperature gradient (according to the temperature scale) are depicted. (For interpretation of the references to colour in this figure legend, the reader is referred to the web version of this article).

as Na, Ca or K, migrating to the surroundings of the crater, as it is depicted in Fig. 4. Therefore, after fast cooling, the compositional variation is reached as confirmed by the confocal Raman microcopy analysis (Figs. 2 and 3) [38].

The dielectric breakdown leaves as a result a crater from which appear cracks that advance irregularly in the material. These cracks occur as consequence of the thermal stress. The crater and cracks would resemble a Vickers indentation imprint (see Fig. S2a and b in Supplementary information) which correspond to a plastically-deformed region underneath the indenter during the fracture toughness testing. The Vickers indentation produces as well cracks that emanate radially outward and downward from the indentation. The differences in crack length between the indentation and the dielectric breakdown indicate a relevant difference in the stress supported by the material. In order to evaluate the dielectric breakdown extent, we will consider the electric power dissipated per unit of time in the immediate moment of dielectric breakdown. Thus, the pressure generated in the sample by this electric force may be estimated by combination of:

$$P = \frac{F}{surface} \quad (1)$$

$$W = F \cdot d = \Phi \cdot t \quad (2)$$

$$\Phi_{electric} = I.V \quad (3)$$

where, P is the pressure generated by a force F applied over a surface. W is the work realized by a force F which generates a dielectric displacement d. The dielectric displacement is equivalent to the electric power Φ generated as consequence of that work per unit of time t. When this electric power is generated by an electric current I and an electric potential voltage V, as in the case of dielectric breakdown, electric power is referred as $\Phi_{electric}$. For our case V is 22 kV, the voltage in the moment of dielectric breakdown, I is the sudden current registered in the ammeter when the glass-ceramic starts conducting which corresponds with 1 mA and d is the length of the crater and taken as **2a** (see Fig. S2a in Supplementary information). Combining these equations, the pressure generated during the dielectric breakdown results in ~688 TPa (detail calculations are explained in the Supplementary information). This huge value of pressure justifies the fact that samples break after dielectric breakdown event, showing the crater observed in Fig. 4. In the dielectric breakdown, a stress is generated in the material as a consequence of high current and high temperatures reached, which produced the perforation of the glass-ceramics and the twisting cracks observed in the micrographs (Fig. 1b and 4), because of the stress accumulated (marked in Fig. 4 with blue arrows). In the case of a Vickers indentation, the stress would be generated by a mechanical force applied over the material surface, which has similar effect in the mechanical response of the material, causing cracking as occurs by an extreme rise in temperature. In comparative terms, it may be calculated the pressure applied by a mechanical force (by a Vickers indentation) and by an electric force (by dielectric breakdown). Considering a normal load of 10 N and measuring the Vickers imprint (Fig. S2b in the Supporting information), the pressure obtained by using Eq. (1) is ~6 GPa. This pressure generated by a normal Vickers indentation is $\sim 10^5$ times lower than the obtained during the dielectric breakdown. This estimation allows determining the huge pressure concentrated in the small area of the crater in comparison with an indenter during the toughness test.

The above describe mechanism for dielectric breakdown of the studied glass-ceramic materials highlights the higher performance of these materials. Their present superior mechanical and physical properties are combined with a simple manufacturing process. In comparison with current glass insulators, the glass-ceramic materials dielectric breakdown is not as destructive as the case of glass insulators [39], where the explosive breakage of the insulator occurs. This fact, would favor the exploration of new applications in which glass insulators fails to provide a higher performance and an enhancement of safety.

4. Conclusions

Two glass-ceramic materials have been designed by fast sintering following a conventional ceramic process. In both glass-ceramics highlight the characteristic high crystallinity, ~91% Vol.% and ~94% Vol.% for anorthite and albite respectively, which strongly conditions their good insulator behavior. A huge dielectric strength, over 59 kV/mm and 57 kV/mm at room temperature for albite and anorthite respectively, along with the unique micro-nanostructure, carefully designed, motivated a deep study of this phenomena. Dielectric breakdown tests with temperature showed that both glass-ceramic withstood temperatures up to 200 °C. Anorthite and albite glass-ceramics resulted in a dielectric strength of up to 30 kV/mm and 44 kV/mm respectively, independently of the rate of voltage rise and the cooling process which suggest an electronic origin of the dielectric breakdown mechanism.

The effects of the dielectric breakdown have been exhaustively studied, for the first time in such detail in a glass-ceramic material, in order to better understand the process. The crater resulted from the dielectric breakdown was microstructurally characterized by FE-SEM. EDX and confocal Raman microscopy allowed to identify the presence of a Ca/Na/K-aluminosilicate glass in the surroundings of the crater and an amorphous silicate glass, because of the local melting and fast cooling of the glass-ceramic during dielectric breakdown. Conventional glass-ceramic materials present a larger amount of glassy phase which increases the length of the free path of mobile ions, such as Na^+, Ca^{2+} or K^+, and increases the conductivity, anticipating dielectric breakdown event. The high crystallinity of albite and anorthite-based glass-ceramics and their characteristic polycrystalline hierarchically structure favor scattering processes of charge carriers which lead to delay dielectric breakdown regarding conventional ceramics. All the results reported place both materials in a very good position in the market of ceramic electrical insulator for room and high temperature insulation applications and even for integrated circuit devices. Also gives us essential information about the possible mechanism and causes of dielectric breakdown which may allow tailoring these materials in order to improve, even more, the excellent dielectric strength of both glass-ceramic materials.

Acknowledgments

The authors express their thanks to the MINECO (Spain) project MAT2017-86450-C4-1-R, and projects CDTI (IDI-20130894 and IDI-20161120) for their financial support. Dra. E. Enriquez is also indebted to MINECO for a “Torres Quevedo” contract (ref: PTQ- 14-07289), which is co-financed with European Social Funds. The corresponding author, V. Fuertes, is assigned to the ‘’ Doctorado en Física” program of Complutense University.

Appendix A. Supplementary data

Supplementary material related to this article can be found, in the online version, at doi: https://doi.org/10.1016/j.jeurceramsoc.2018.08.044.

References

[1] A. Roula, K. Boudeghdegh, N. Boufafa, O. Aissa, Improving usual and dielectric properties of ceramic high voltage insulators, CerâMica 55 (2009) 206–208, https://doi.org/10.1590/S0366-69132009000200014.
[2] M.U. Ismail, H. Tsunatori, Z. Nakai, Preparation of mullite cordierite composite powders by the sol-gel method: its characteristics and sintering, J. Am. Ceram. Soc. 73 (1990) 537–543, https://doi.org/10.1111/j.1151-2916.1990.tb06550.x.
[3] J.E. Contreras, E.A. Rodríguez, Nanostructured insulators – a review of nanotechnology concepts for outdoor ceramic insulators, Ceram. Int. 43 (2017) 8545–8550, https://doi.org/10.1016/j.ceramint.2017.04.105.
[4] M. Bengisu, Engineering Ceramics, (2001), https://doi.org/10.1007/978-3-662-04350-9.
[5] I.O. Owate, R. Freer, The electrical properties of some cordierite glass ceramics in

the system MgO-Al2O3-SiO2-TiO2, J. Mater. Sci. 25 (1990) 5291–5297, https://doi.org/10.1007/BF00580163.
[6] S. Xue, J. Zhai, S. Xiao, S. Xiu, B. Shen, Improved dielectric breakdown strength and suppressed energy loss in niobate glass-ceramics crystallized by microwave process, Mater. Lett. 190 (2017) 154–156, https://doi.org/10.1016/j.matlet.2017.01.002.
[7] H. Wang, J. Liu, J. Zhai, B. Shen, Ultra high energy-storage density in the barium potassium niobate-based glass-ceramics for energy-storage applications, J. Am. Ceram. Soc. 99 (2016) 2909–2912, https://doi.org/10.1111/jace.14446.
[8] P.W. McMillan, G. Partridge, F.R. Ward, Glass-ceramics for use in silicon semiconductor applications, J. Mater. Sci. 4 (1969) 634–640, https://doi.org/10.1007/BF00550119.
[9] J. Liu, K. Yang, J. Zhai, B. Shen, Effects of crystallization temperature on phase evolution and energy storage properties of BaO-Na2O-Nb2O5-SiO2-Al2O3 glass-ceramics, J. Eur. Ceram. Soc. 38 (2018) 2312–2317, https://doi.org/10.1016/j.jeurceramsoc.2018.01.003.
[10] Z.H. Khan, K. Zanganeh, C. Salvador, Experimental study of dielectric break-down of refractory board materials for application in high-temperature sieving electrostatic precipitator, Proc. Jt. Electrost. Conf. (2012) 1–9.
[11] H. Frohlich, On the theory of dielectric breakdown in solids, Proc. R. Soc. A Math. Phys. Eng. Sci. 188 (1947) 521–532, https://doi.org/10.1098/rspa.1947.0023.
[12] M. Touzin, D. Goeuriot, C. Guerret-piécourt, D. Juvé, H. Fitting, Alumina based ceramics for high-voltage insulation, J. Eur. Ceram. Soc. 30 (2010) 805–817, https://doi.org/10.1016/j.jeurceramsoc.2009.09.025.
[13] M. Yoshimura, H.K. Bowen, Electrical breakdown strength of alumina at high temperatures, J. Am. Ceram. Soc. 64 (1981) 404–410, https://doi.org/10.1111/j.1151-2916.1981.tb09879.x.
[14] J.J. O'Dwyer, The Theory of Dielectric Breakdown in Solids, (1964), https://doi.org/10.1149/1.2411805.
[15] H. Eyring, Dielectric breakdown of solids, J. Chem. Educ. 29 (1952) 108, https://doi.org/10.1021/ed029p108.2.
[16] J.J. O'Dwyer, The theory of avalanche breakdown in solid dielectrics, J. Phys. Chem. Solids 28 (1967) 1137–1144, https://doi.org/10.1016/0022-3697(67)90057-1.
[17] V. Fuertes, M.J. Cabrera, J. Seores, D. Muñoz, J.F. Fernández, E. Enríquez, Hierarchical micro-nanostructured albite-based glass-ceramic for high dielectric strength insulators, J. Eur. Ceram. Soc. (2018) 0–1, https://doi.org/10.1016/j.jeurceramsoc.2018.02.009.
[18] E. Enríquez, V. Fuertes, M.J. Cabrera, J. Seores, D. Muñoz, J.F. Fernández, New strategy to mitigate urban heat island effect: energy saving by combining high albedo and low thermal diffusivity in glass ceramic materials, Sol. Energy 149 (2017), https://doi.org/10.1016/j.solener.2017.04.011.
[19] H. Hu, L. Dai, H. Li, K. Hui, J. Li, Temperature and pressure dependence of electrical conductivity in synthetic anorthite, Solid State Ion. 276 (2015) 136–141, https://doi.org/10.1016/j.ssi.2015.04.008.
[20] M.S. Islam, M. Mortimer, A. Jones, D. Palmer, Alkali ion migration in albite and K-feldspar, Phys. Chem. Miner. 31 (2004) 313–320, https://doi.org/10.1007/s00269-004-0389-8.
[21] J. Liebault, J. Vallayer, D. Goeuriot, D. Treheux, F. Thevenot, How the trapping of charges can explain the dielectric breakdown performance of alumina ceramics, J. Eur. Ceram. Soc. 21 (2001) 389–397, https://doi.org/10.1016/S0955-2219(00)00186-2.
[22] J. Reinosa, F. Rubio-marcos, E. Solera, F. Ferna, M.A. Bengochea, Sintering behaviour of nanostructured glass-ceramic glazes, Ceram. Int. 36 (2010) 1845–1850, https://doi.org/10.1016/j.ceramint.2010.03.029.
[23] J.J. Reinosa, D.M.Y. Marero, A. Del Campo, M.Á. De La Rubia, J.F. Fernández, Chemical analysis with high spatial resolution by rutherford backscattering and Raman Confocal spectroscopies: surface hierarchically structured glasses, J. Am. Ceram. Soc. 96 (2013) 1783–1788, https://doi.org/10.1111/jace.12397.
[24] E. Enríquez, J.F. Fernández, M.Á. García, M.J. Cabrera, J. Seores, F.J. Villar, et al., Glass-ceramic Material of Albite And/or Anorthite Exhibing Warmth, Centro tecnológico Vidres-ICV (CSIC), 2016 PCT3261.1b.
[25] M. Niittymäki, T. Suhonen, J. Metsäjoki, K. Lahti, DC dielectric breakdown behavior of thermally sprayed ceramic coatings, Proc. 24th Nord. Insul. Symp. (2015) 80–85, https://doi.org/10.5324/nordis.v0i24.2289.
[26] L. Carbajal, F. Rubio-Marcos, Ma. Bengochea, J.F. Fernandez, Properties related phase evolution in porcelain ceramics, J. Eur. Ceram. Soc. 27 (2007) 4065–4069, https://doi.org/10.1016/j.jeurceramsoc.2007.02.096.
[27] X. Wang, P. Xiao, Characterisation of clay sintering process using impedance spectroscopy, J. Eur. Ceram. Soc. 22 (2002) 471–478, https://doi.org/10.1016/S0955-2219(01)00335-1.
[28] D.A. McKeown, Raman spectroscopy and vibrational analyses of albite: from 25°C through the melting temperature, Am. Mineral. 90 (2005) 1506–1517, https://doi.org/10.2138/am.2005.1726.
[29] M.J. Ayora Cañada, A. Dominguez-vidal, A. Dominguez-Arranz, Raman Microspectroscopic study of Iberian pottery from the La Vispesa archaeological site, Spain, J. Raman Spectrosc. 43 (2012) 317–322, https://doi.org/10.1002/jrs.3030.
[30] A.K. Yadav, P. Singh, A review of the structures of oxide glasses by Raman spectroscopy, RSC Adv. 5 (2015) 67583–67609, https://doi.org/10.1039/C5RA13043C.
[31] D.W. Matson, S.K. Sharma, J.A. Philpotts, Raman spectra of some tectosilicates and of glasses along the orthoclase-anorthite and nepheline-anorthite joins, Am. Mineral. 71 (1986) 694–704.
[32] P.F. McMillan, B. Piriou, A. Navrotsky, A Raman spectroscopic study of glasses along the join silica-calcium aluminate, silica-sodium aluminate, and silica-potassium aluminate, Geochim. Cosmochim. Acta 46 (1982) 2021–2037, https://doi.org/10.1016/0016-7037(82)90183-1.
[33] T. Deschamps, C. Martinet, J.L. Bruneel, B. Champagnon, Soda-lime silicate glass under hydrostatic pressure and indentation: a micro-Raman study, J. Phys. Condens. Matter 23 (2011), https://doi.org/10.1088/0953-8984/23/3/035402.
[34] A.G. Kalampounias, IR and Raman spectroscopic studies of sol–gel derived alkaline-earth silicate glasses, Bull. Mater. Sci. Indian Acad. Sci. 34 (2011) 299–303, https://doi.org/10.1007/s12034-011-0064-x.
[35] R. Le Parc, B. Champagnon, J. Dianoux, P. Jarry, V. Martinez, Anorthite and CaAl2Si2O8 glass: low frequency Raman spectroscopy and neutron scattering, J. Non Cryst. Solids 323 (2003) 155–161, https://doi.org/10.1016/S0022-3093(03)00302-8.
[36] P. Wu, G. Eriksson, A.D. Pelton, Optimization of the thermodynamic properties and phase diagrams of the Na2O-SiO2 and K2O-SiO2 systems, J. Am. Soc. 76 (1993) 2059–2064, https://doi.org/10.1111/j.1151-2916.1993.tb08333.x.
[37] H. Dupont, A. Donzel, J. Ernest, On laser-induced breakdown and fracture in glasses, Appl. Phys. Lett. 11 (1967) 271–272, https://doi.org/10.1063/1.1755130.
[38] I. Parsons, Feldspars and Their Reactions, (1994), https://doi.org/10.1180/minmag.1995.059.397.23.
[39] H. Lee, N.J. Smith, C.G. Pantano, E. Furman, M.T. Lanagan, Dielectric Breakdown of Thinned BaO-Al2O3-B2O3-SiO2 Glass, J. Am. Ceram. Soc. 93 (2010) 2346–2351, https://doi.org/10.1111/j.1551-2916.2010.03749.x.

ARTÍCULO 7. New strategy to mitigate urban heat island effect: Energy saving by combining high albedo and low thermal diffusivity in glass ceramic materials

E. Enríquez, V. Fuertes, M.J. Cabrera, J. Seores, D. Muñoz, J. F. Fernández.

Solar Energy, 149, 2017, 114-124.

Factor de impacto: 4,374 (según JCR Edition Science 2017).

Solar Energy 149 (2017) 114–124

Contents lists available at ScienceDirect

Solar Energy

journal homepage: www.elsevier.com/locate/solener

New strategy to mitigate urban heat island effect: Energy saving by combining high albedo and low thermal diffusivity in glass ceramic materials

E. Enríquez [a,*], V. Fuertes [b], M.J. Cabrera [a], J. Seores [a], D. Muñoz [a], J.F. Fernández [b]

[a] Centro tecnológico Vidres, S.L., Ctra. Onda, km 3.4, 12540 Villareal, Castellón, Spain
[b] Electroceramics Department, Instituto de Cerámica y Vidrio, CSIC, Kelsen 5, 28049 Madrid, Spain

ARTICLE INFO

Article history:
Received 13 January 2017
Received in revised form 4 April 2017
Accepted 5 April 2017
Available online 12 April 2017

Keywords:
High albedo
Energy saving
Glass ceramic
Thermal diffusivity

ABSTRACT

The Global warming is a real problem that attracts great amount of investigations in order to reduce its adverse impact over the planet. The reduction of the heat island effect and the energy consumption into the building areas is an urgent goal. An interesting solution consists in the use of cool roofs, based on high reflective and high emissivity coatings. However, today, some cool roof materials possess some major drawbacks as high solar degradation, decrease of NIR reflection in comparison with the visible reflection and aesthetic restrictions. In order to overcome such limitations, in this work, a tile coated with a new glass ceramic material has been developed in order to improve the solar reflective properties and to reduce its thermal conductivity and increase the specific heat. These three parameters are key to obtain low thermal diffusivity materials to serve as efficient cool roof applications. The increase in solar reflectivity is complimented also by a high reflectivity in the NIR range that results highly convenient for colored materials. These combined properties in addition of increasing the albedo also contributed to improve the thermal comfort sensation inside the buildings. Therefore a great energy saving over 20% is determined in comparison with conventional ceramic tiles. In addition, these materials also offer a structural solution for durable facades and allow a great decorative variability.

1. Introduction

Nowadays, the Global warming is an urgent problem that attracts great amount of investigations in order to reduce its impact over the planet. The energy consumption in great cities contributes significantly to this effect, due to the creation of the urban heat island (UHI) and the CO_2 contamination (Chung et al., 2015; Cozza et al., 2015). Some solutions to reduce these phenomena are to increase green zones in the cities and to substitute hot pavements, such as asphalt or dark floor, for reflective materials. In addition, regarding to buildings sustainability, a priority challenge faces for solutions to reduce the energy consumption, both in winter and in summer. An interesting solution consists in the use of green roofs, which are composed of different kind of plants, such as grass, shrubs...and which heat absorption depends on the water evaporation and type of vegetation. The major associated problem is the maintenance issue. Another approach is the use of cool roofs, based on high reflective, that is, high albedo (reduction of solar radiation absorption), and high emissivity coatings, that contribute to decrease the ambient and inner temperatures. Some studies reveal that an increase of albedo by 25% and 15% in roofs and pavements, respectively, can reduce the radiative forcing by 0.15 W/m^2 over the global land area, which corresponds to a reduction of 44 Gt of emitted CO_2 (Santamouris, 2014). Therefore, moderated increase of the albedo produces great mitigation of heat island effects, which reduces the ambient temperatures. The mitigation efficiency has been proved to be higher in cool roofs than in green roofs.

Conventional roofs are made of asphaltic fabric, metal covering, rubber materials or typical clay tiles, which greatly increase the surface temperature and easily transfer heat to the inner of the building. Cool roofs are composed of a reflective covering, usually a white paint based on TiO_2 (also used as opacifier), aluminium trihydroxide (ATH) or organic compounds (Elton and Legrix, 2014; Ferrari et al., 2013; Karlessi et al., 2009; Kinoshita and Yoshida, 2016; Meyer et al., 2002). However, these kinds of materials are easily damaged due to the effect of soiling (Levinson et al., 2005) and the photodegradation of organic components under UV in TiO_2, which produces the white paint turns to yellowish. Therefore,

* Corresponding author.
E-mail address: esther@icv.csic.es (E. Enríquez).

http://dx.doi.org/10.1016/j.solener.2017.04.011
0038-092X/

the cool roof coating should be frequently restored. The cool paints base their high albedo on the high whiteness surfaces, which reflects almost the entire visible range of the solar spectrum. Additionally, these paints do not especially reflect the NIR radiation (having lower reflection than in the visible range) so the ambient temperature is thus transmitted. Recent works are focused on NIR reflection increase in order to achieve cool roofs with colored paints, with an alumina base, for example (Álvarez-Docio et al., 2017). However, good results are only achieved with light and pastel colors (Antonaia et al., 2016; Cozza et al., 2015; Zinzi, 2015).

Another solution for cool roofs consists of using ceramic tiles coated with reflective and NIR transparent coatings. These ceramic roofs have good technical characteristics such as mechanical properties, chemical inertia and fireproof, and the NIR radiation that penetrates into the transparent coating is reflected by the reflective coating (Ferrari et al., 2013; Levinson et al., 2007; Pisello et al., 2013). However, the coated tiles require at least three different layers and typically dissimilar materials. As consequence, a process with different sintering steps is required in these cases, which is not desirable for industry applications. Another tile solution consists of adding a thermal insulation layer below the glaze (Marangoni et al., 2016), typically by increasing the porosity that reduces the thermal conductivity but also reduces the mechanical properties. The introduction of an opacifier pigment (such as $ZrSiO_4$ and TiO_2) into the engobe layer also provides higher reflectance in the visible range due to their higher whiteness (Ferrari et al., 2013), however, these pigments increase considerably the tile cost.

The main use of cool materials is focused on roof coverings where the solar radiation has the highest incidence. Currently, these cool materials have also been proposed to be used in building facades since the new architectonic designs produce larger solar exposition (Ihara et al., 2015), which can further increase the impact of heat islands. For this purpose, ceramics are very effective materials because of its mechanical and chemical resistance, cleanliest, durability and decorative versatility.

Following the current state of the art, in this work, we propose an approach based on nanostructured glass ceramics that combines high albedo and low thermal diffusivity using the traditional single firing ceramics process. The unique characteristics of the nanostructured materials are based on greatly improving its reflectance, especially in the NIR range, reducing its thermal conductivity and increasing its specific heat (Hodgman et al., 1920). These three parameters are key to obtain a low thermal diffusivity material that is an essential factor to improve the heat island mitigation and also the thermal comfort sensation inside the buildings. Low thermal diffusivity may avoid the heat transmission both outward and inward, which provides great energy saving. The thermal diffusivity is related to the thermal conductivity and specific heat according to the Eq. (1).

$$\alpha = \frac{\kappa}{\rho C_p} \tag{1}$$

where α is the thermal diffusivity, κ is the thermal conductivity, ρ is the density and C_p the specific heat.

Moreover, the great mechanical, chemical and physical properties of the ceramic materials would allow their use in different building surfaces and would increase its lifetime, due to its resistance to the solar radiation and weather events. In addition, they provide surfaces with great stain resistance. The increase of the thermal inertia produced for the low thermal diffusivity, would reduce the heat transfer, preserving the inner temperature of buildings, which could also avoid the heat loss in winter, and therefore, it could produce larger energy saving and heat island mitigation.

2. Experimental procedure

2.1. Sample preparation

The glass ceramic material was prepared following the standard ceramic processing for the tile industry. Firstly, a frit previously melted at 1500 °C (previously warmed at 900 °C and then directly brought under the dwell temperature) and water quenched, was homogenized with kaolin in a weight proportion 90/10, in an alumina ball miller during 20 min with 37 wt% of water (Andrews, 1961; Reinosa et al., 2013, 2010). The frit composition expressed in term of equivalent oxides is shown in Table 1. Then, the material prepared was dried in powder to obtain a pressed pellet sample (pellets of ~10 mm in thickness, pressed at 39 MPa of pressure), or was deposited by the waterfall method (Norsker and Danisch, 1993) as a 300–900 μm in thickness coating on porcelain stoneware supports (SiO_2 65.60%, Al_2O_3 18.14%, Fe_2O_3 0.387%, TiO_2 0.428%, Na_2O 5.010%, K_2O 1.000%, CaO 0.472%, MgO 0.158%, P_2O_5 0.078% (Carbajal et al., 2007; Cavalcante et al., 2004)). Therefore, the layer structure of tiles consists in a porcelain support of 1 cm and the enamel coating. The particle size of this material after the milling and drying has a bimodal distribution with 12.95 μm and 225.33 μm. Finally, both pressed powder and compacted coating (tiles), for comparison purposed, were thermally treated in an industrial furnace at 1220 °C during 6 min with a 30 °C min^{-1} heating rate. Additionally, colored tiles were processed by inkjet deposition of a saturated surface of black type ceramic nanopigment based on Fe-Cr-Mn oxide spinel, in order to check the validity of results in colored surfaces. This information is presented as supporting information.

The final composition of the glass ceramics expressed in term of equivalent oxides as SiO_2, CaO, ZrO_2, Al_2O_3, Na_2O, K_2O and ZnO is shown in Table 1. Table 1 also shows the composition of a conventional commercial matt glaze for comparison purposes, that hereafter it is denoted as glaze. This conventional glaze was chosen due to its similar feldspars composition, anorthite based, although with more glass phase.

The main parameters of the pressed powder samples and ceramic tiles prepared in this work are described in Table 2 (Table SI for colored ceramic tiles) that includes prepared samples and the commercial products. As explained, in order to be able to compare with raw TiO_2 and ATH powder (main commercial materials used as additives in reflective paints), samples were prepared as pressed powder in addition of as ceramic tiles (coating of porcelain substrates). In addition, a sample of reflective paint (Imperlux termic Outdoor, Arelux®) was prepared by depositing three layers (manufacturer recommendation to obtain high efficiency reflective effect) of paint on the same porcelain substrate.

The main physical parameters of reflective materials, TiO_2 (Feng et al., 2012; Jiménez-Pérez et al., 2015), ATH (Meyer et al., 2002; Shi et al., 2012; Wefers and Misra, 1987) and a standard reflective paint based on polyethylene composition, are provided for comparison purposed, Table 3.

2.2. Characterization

Microstructural characterization was studied by means of Field Emission Scanning Electron Microscopy (FESEM) using a Hitachi S-4700. Metalographically polished samples were chemically etched with 5 vol% of HF with the aim of removing the glass phase to reveal the microstructure. In addition, the crystalline phases formed were identified by using X ray diffraction (XRD) technique in a diffractometer Bruker D8 Advance with Cu Kα radiation, 40 kV and 40 mA, in sintered samples. The identification of the crystalline phases was realized by the comparison with the JCPDS patterns,

Table 1
Composition of the frit, studied glass ceramic and glaze expressed as equivalent oxides. The minority components are all included in others.

Oxides wt%	SiO_2	B_2O	P_2O_5	ZrO_2	Al_2O_3	CaO	BaO	MgO	Na_2O	SrO	K_2O	ZnO	Others
Frit	54.54	–	–	1.43	19.56	8.90	–	–	2.47	–	1.46	–	3.32
Glass ceramic	47.99	–	–	7.31	21.42	11.82	–	–	4.58	–	1.65	4.30	0.94
Glaze	43.70	3.50	2.88	–	32.20	2.98	3.12	2.63	1.50	3.28	1.59	2.14	0.21

Table 2
Description and properties of the prepared samples: Materials densities were measured for sintered samples in coatings. For pressed powders the apparent density was measured, that is, this density does not correspond with the real sintered material density. The roughness values are given relative to the shape of the samples studied.

Nomenclature	Density ($g\,cm^{-3}$)	Thickness (mm)	Average roughness (μm)
Coated samples			
Glass ceramic	2.63	0.77	9.32
Glaze	2.70	0.72	7.35
Reflective paint	–	0.18	17.75
Pressed powder samples			
Glass ceramic	1.71	2.61	5.06
Glaze	1.76	2.90	10.58
TiO_2	1.65	3.23	4.48
ATH	2.16	2.42	5.98

and the glass phase content was obtained through the integration of the areas corresponding to the glassy and crystalline phases.

The optical measurements were carried out by a Perkin Elmer Lambda 950 spectrophotometer with an integration sphere to obtain the total reflectance (diffuse and direct reflectance). The reflectance spectra were obtained in the solar spectrum range (300–2500) nm with a step of 3 nm. In the reflectance measurement with integration sphere, a Spectralon® material was used as pattern, which is considered as 100% of reflectance in these measurements. From these spectra it is possible to obtain the proportion of the solar radiation reflected by the studied material following the Standard Test Method for Solar Absorptance, Reflectance, and Transmittance of Materials Using Integrating Spheres (ASTM E903-96) (Akbari et al., n.d.; International, 1996). This concept is expressed with the solar reflectance (SR) (Levinson et al., 2010a, 2010b), which can be calculated with the formula shown in Eq. (2) in the whole solar spectrum (300–2500 nm).

$$SR = \frac{\int_{300}^{2500} RI_\lambda d\lambda}{\int_{300}^{2500} I_\lambda d\lambda} \quad (2)$$

where R is the measured spectral reflectivity and I_λ the spectral irradiance of the sun at the earth surface ($W/(m^2\,nm)$), according to the ASTM Standard G-173-03 which is the most commonly standard used for edification applications (Ferrari et al., 2013; Libbra et al., 2011).

In addition, a LCS-100 solar simulator (Lasing S.A.) with an AM1.5G (applied to the same Standard G-173-03 with 1.5 air mass) filter was used to measure the reflective effect of the solar radiation on the samples. The solar filter is 81011-LCS with 2″ square AM0 filter mounted in frame. In addition, the solar simulation includes an AM1,5G spectral correction filter which shapes the light output to closely match the total (direct and diffuse) solar spectrum on the Earth's surface, at a zenith angle of 48.23 (ASTM 892). This provides a Class A irradiance spectrum suitable for photovoltaic testing. The solar simulation measurements consist in irradiating the surface sample with a xenon lamp (100 W) with the filter that reproduces the solar spectrum with one sun equivalent power. Hence, it is possible to obtain the thermal behavior of samples in the entire solar spectrum with the corresponding intensity in each wavelength. Samples surfaces were irradiating during 5 min. Achieved temperature on surface was simultaneously measured by means of a thermal infrared camera FLIR E30 with an image resolution of 160 × 120 pixels and a temperature range of −20 to 350 °C with 0.1 °C of thermal resolution. At the same time, temperature transmitted through the sample at the rear part was measured by means a PT100 thermocouple placed in the opposite size of the tile and connected to a multimeter Keithley 2410–1100 V, in voltage and current ranges of 0–100 V and 0–21 mA, respectively. The thermocouple system was calibrated using the cold focus method (using ice water at 0 °C to check a possible temperature deviation) to avoid the temperature drop due to the contacts resistant. Moreover, the well-contact between the thermocouple and rear tile surfaces is ensured using a conductive paste (commonly used in thermal conductivity measurements to ensure the well-contact). Therefore, heating curves can be obtained in both sides with rather high resolution, which allows not only knowing the reflective capacity, but also the in situ heat transfer through the sample, related with the thermal diffusivity. The experimental setup can be schematically seen in Fig. 1.

The infrared radiation emitted and reflected was registered by a thermal infrared camera. The whiteness and CIE L*a*b* coordinates, the most common uniform color space, were measured by a colorimeter Konica Minolta, Spectra Magic NX, with Color Data Software CM-S100w. L* measures from white to black (0–100), a* measures from green to red and b* from blue to yellow.

Thermal conductivity was obtained by means of DTC-25 Conductivity meter of TA Instrument using the guarded heat flow method. Thermal conductivity was measured at room temperature. Heat capacity measurements were carried out with a Discovery DSC Calorimetry of TA Instruments, which perform direct measurements of heat capacity and it works in the temperature range of −90 °C and 500 °C.

3. Results and discussion

3.1. Microstructural characterization

Fig. 2a shows the XRD pattern of samples prepared: glass ceramic and glaze, with the proportions shown in Table 1. As seen, the main phase of the glass ceramic is Ca-feldspar (anorthite: JCPDS

Table 3
Thermal properties of typical reflective materials: thermal conductivity, density, heat capacity and thermal diffusivity.

Material	K ($W\,m^{-1}\,K^{-1}$)	ρ ($g\,m^{-3}$) ($\cdot 10^6$)	C_p ($J\,g^{-1}\,°C^{-1}$)	α ($m^2\,s^{-1}$) ($\cdot 10^{-6}$)
TiO_2	2.5–5	4.25	0.686	0.90–1.70
ATH	10–30	2.42	1.176	3.50–45.7
Reflective paint	0.056	0.95–1.05	1.800–2.300	0.25–0.40

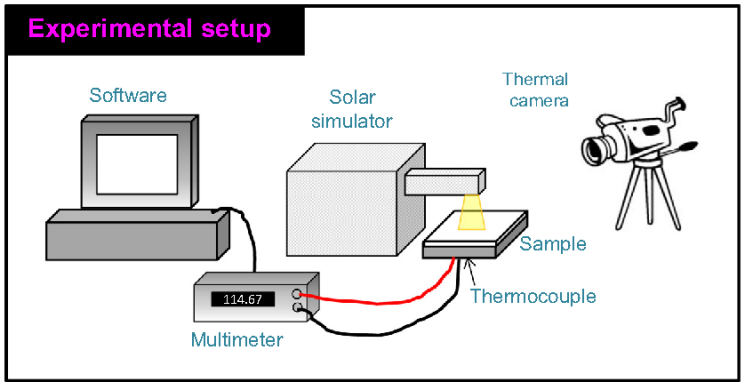

Fig. 1. Experimental setup of solar simulator measurements. The setup includes a thermal infrared camera, a solar simulator, a PT100 thermocouple, a multimeter and software to collect data.

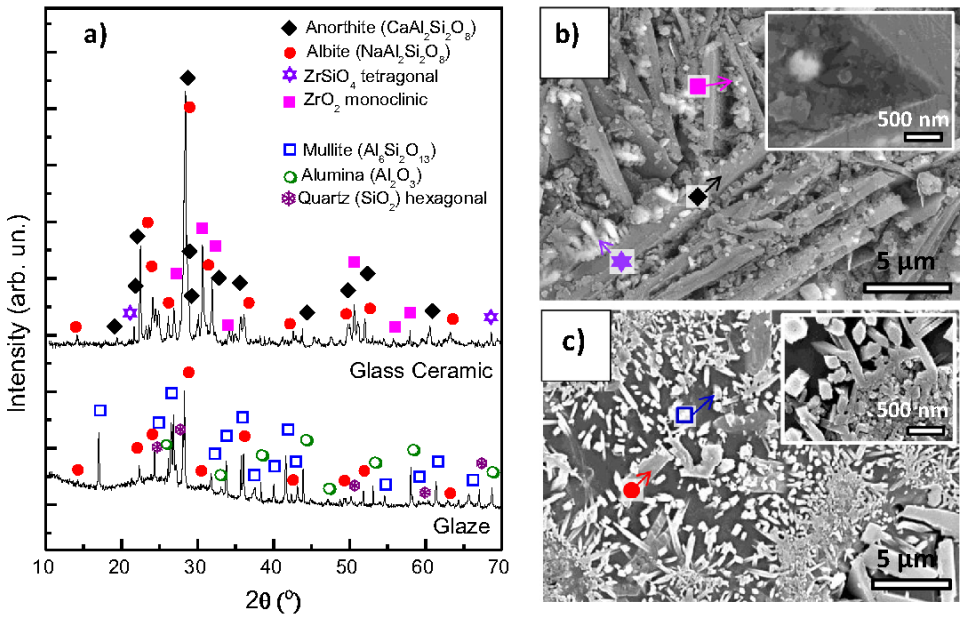

Fig. 2. (a) X ray diffractograms of the sintered glass ceramic and glaze. FESEM micrographs of the chemically etched (b) glass ceramic and (c) glaze materials. The inset of the micrographs shows high magnification where it is possible to observe in detail the formed nanostructure in case of glass ceramic. The colored symbols on the micrograph corresponds with the main crystalline phases identified in a. (For interpretation of the references to color in this figure legend, the reader is referred to the web version of this article.)

01-086-1705) with lower concentrations of Na-feldspar (albite: JCPDS 00-009-0466). Both phases are hardly isolated in nature (Shmulovich and Graham, 2008) and therefore, often they also appear combined in the feldspar materials. In addition, zircon ($ZrSiO_4$: 00-006-0266) and different phases of zirconia (ZrO_2: JCPDS 00-050-1089; JCPDS 00-037-1484; JCPDS 00-034-1084) crystals appear in low concentrations. The ZrO_2 formation is more favorable than $ZrSiO_4$ due to its lower enthalpy of formation ($\Delta H_f(ZrO_2) = -1080$ kJ/mol and $\Delta H_f(ZrSiO_4) = -2034.2$ kJ/mol (Ellison and Navrotsky, 1992)). $ZrSiO_4$ remains from the glass melting process which indicates that the saturation of Zr^{4+} in the melt was exceeded for this composition. The narrow peaks of the patterns point out high crystallinity of the glass ceramics and therefore low glass phase content. In case of glaze, the XRD pattern shows a main crystalline phase of mullite ($Al_6Si_2O_{13}$, aluminosilicate nesosilicate: JCPDS 01-079-1275) with lower concentrations of albite, alumina (JCPDS 00-010-0173) and quartz (JCPDS 00-046-1045). The XRD peaks are less intense and wider that indicates less crystallization. As seen, the broad band at 15–35° indicates higher glass phase content than the glass ceramic. The glass phase content is 9% and 35% for glass ceramic and glaze, respectively. Therefore, the percentage of glass phase in the glass ceramic is much lower than in glaze due to the higher crystallization attained by the compositional design.

Fig. 2b and c show FESEM micrographs of the sintered glass ceramic material and the glaze, respectively. Fig. 2b shows the presence of elongated anorthite crystals with high aspect ratio and 5–10 µm in length (indicated in the figure by black diamond). The ZrO_2 grains consist in spherical morphologies having 100–300 nm in diameter (pink square) and tends to be placed at the feldspar crystal edges. Zircon crystals are irregular in shape with grains in the range of 0.5–2 µm (purple star), and appear forming aggregates located also at the feldspars crystal edges. However, the unique feature of the microstructure is the appearance of

nanostructure grains between the large feldspar microcrystals. The inset of the micrograph shows a FESEM magnification where it is possible to observe in detail the nanostructure. This nanostructure is composed mainly by anorthite nanoparticles and ZrO_2. The nanostructure is possibly formed by a larger devitrification of the glassy phase owing to the increase of the nuclei creation that favors the nucleation of nanocrystals with the same composition than the crystalline phase already formed. This increase in the number of nuclei can be in part attributed to a greater amount of Zr^{4+} cations in the composition and a faster sintering profile that limits the growth of the crystals (Brown and Mackenzie, 1982) The glassy phase that does not undergo devitrification (removed from the sample in the FESEM micrographs by chemical etching to reveal the microstructure) is surrounding the spaces between microcrystals and nanoparticles.

In Fig. 2c it is observed the characteristic microstructure of the glaze materials where mullite (blue square) and albite (red circle) large grains appears in a glass matrix (dark continuous phase). The inset of Fig. 2c shows in detail the faceted morphology of crystalline grains with 0.5–1 μm in cross section.

3.2. Thermal properties

As explained above, in addition to reflectivity, thermal diffusivity constitutes an essential parameter to ensure better thermal comfort and energy saving in the inner buildings and therefore, reduce urban heating. Consequently, several parameters were measured to obtain the thermal diffusivity of glass ceramic and glaze materials, in order to compare them with typical reflective materials, TiO_2 and ATH. Thereafter, thermal diffusivity was calculated by means of the Eq. (1). Table 4 shows the values of the different parameters that contribute to the thermal diffusivity of glass ceramic and glaze materials.

As result of lower thermal conductivity and slightly higher heat capacity, the thermal diffusivity reduces greatly ~60% for glass ceramic material in comparison with glaze material. While the densities of both materials are quite similar and the heat capacity slightly increases for glass ceramic (enough to produce a significant change in the thermal diffusivity combined with the other parameters), the reduction in thermal diffusivity of the glass ceramic is mainly owing to the decrease of the thermal conductivity. The thermal conductivity is hardly influenced by the phonon scattering, since the phonon propagation is the thermal conductivity basis. Therefore, larger phonons scattering would reduce the thermal conductivity. The phonon scattering may be produced by different effect, among them, a disordered structure, defects, phonons coupling or a great number of grain boundaries (Zhao et al., 2017). As seen, the glass ceramic micro-nanostructure possesses large amount of boundaries between the different crystal morphologies and phases (feldspars microcrystals and nanocrystals, and zircon and zircona phases and low amount of amorphous glassy phase at the interphases), which favors the phonon scattering through the material, and difficult the phonon propagation to decrease the thermal conductivity.

In comparison with the thermal diffusivity values of TiO_2, ATH and reflective paint, presented in Table 3, glass ceramic values are nearly more than one order of magnitude lower than the reflective raw materials and have diffusivity values less than half of the reflective paint value, even though its thermal conductivity is much lower. Therefore, it is important to achieve an adequate combination of the three parameters to contribute for thermal diffusivity in order to design materials that effectively avoid the heat transfer.

3.3. Optical characterization

The chromatic coordinates and whiteness of all samples were measured in order to compare the color differences that influence in the radiation absorption. The results are presented in Table 5. Glass ceramic in powder form achieves large whiteness values as high as the one measured for reflective paints. Glass ceramic tiles whiteness is lower than the value obtained for powders because of the large light scattering of powder particles. In comparison with conventional tiles based on glaze materials, the glass ceramic materials present superior whiteness. In terms of absolute value for whiteness, the value of $L^* > 94$ is very high and combined with very low values of a^* and b^* coordinates. The glass ceramic shows one of the largest white chromatic coordinates in the today market of ceramic tiles. The CIE $L^*a^*b^*$ coordinates of colored materials are presented in Table SII of supporting information, where is seen that L^* in glass ceramic tile is >7% respect to the glaze tile. Therefore, in these Glass Ceramic materials, it is possible to obtain higher whiteness values than conventional ceramic tiles and similar values than paints based on TiO_2, which will favor the reflective effects.

3.3.1. Reflectance measurements and solar reflectance (SR)

Reflectance measurements were carried out within the range of the solar radiation in order to obtain the solar reflectance (SR) by means of Eq. (2). The pattern used to calibrate the 100% of reflectance in the equipment was Spectralon®, which is a much known material with reflectance near to 100%. Fig. 3a shows the reflectance spectra of samples in pressed pellets: TiO_2, ATH, glass ceramic and glaze powders. As seen, glass ceramic powders present high reflectance in the visible range and especially in the near infrared range (NIR), achieving values over 100% of reflectance (similar reflectance behavior than polished metals). This result means that the reflectance of this material in the NIR range overcomes the reflectance of the material used as pattern, Spectralon®. This is the reason of the reflectance values over 100%. Moreover, glass ceramic presents high reflectance of the UV spectrum, which is the highest energetic radiation. On the other hand, glaze powders present lower reflection spectra than glass ceramic powders in the entire spectral range, especially in the UV and NIR ranges (UV: 60% lower reflectivity than glass ceramic; and visible and NIR: 10% lower reflectivity than glass ceramics). These results produce a total improvement of 10% in the albedo for glass ceramic powders respect to the glaze powder. This large reflectance of glass ceramics is attributed to its unique nano-microstructure that combined micrograins surrounded by nanograins, according to the FESEM micrographs, which is responsible of a higher light scattering and therefore, higher UV–Vis-NIR spectral reflection.

The conventional materials used in reflective paints offer slightly high reflectance in the visible range than the glass ceramic powders, but are clearly inferior in reflectance performance for the infrared range, from 1200 to 2500 nm, where TiO_2 achieves reflectance values only 75% and ATH below 40%. In addition, TiO_2

Table 4
Thermal properties of the studied materials: thermal conductivity, density, heat capacity and thermal diffusivity.

Material	κ (W/mK)	ρ (g/m^3) (·10^6)	C_p (J/g °C)	α (m^2/s) (·10^{-6})
Glass ceramic	0.35	2.63	0.765	0.17
Glaze	0.80	2.70	0.742	0.40

Table 5
Chromatic coordinates in the CIE $L^*a^*b^*$ system of the samples measured.

Sample	L^*	a^*	b^*
Glass ceramic	94.59	−0.85	0.85
Glaze	90.00	−0.37	1.01
Reflective paint	95,73	−0,57	1,12
Glass ceramic powder	98.14	−0.2	0.59
Glaze powder	92.69	−0.75	3.12
TiO_2	98.54	−0.09	1.22
ATH	99.07	0.10	0.58

absorbs much ultraviolet radiation getting very low reflection values in this region, meanwhile ATH has similar reflection values than glass ceramic at the UV region. Therefore, the higher absorption of these conventional materials, especially in the NIR range which corresponds with heat radiation, provides lower albedo than in glass Ceramics.

Table 6 shows the average reflectance values in each range (UV, Visible and NIR) and in the entire solar radiation range for all materials, showing the differences in the reflectance properties.

Fig. 3b shows the reflectance spectra of glass ceramic and glaze sintered as coating on porcelain substrate. Moreover, commercial reflective paint deposited on the porcelain substrate (3 layers at least) was measured in order to compare performance with glass ceramic tiles.

As seen, reflectance values of coating samples are lower than the values obtained for pressed powder, since the pellets are lower compacted than films, according to density presented in Table 2, and consequently, they produce higher light scattering. Glaze tile presents reflectance values up to 79% in the visible range meanwhile glass ceramic tile achieves values of ~87%. In the UV range, reflection is similar for both samples. In comparison with the reflective paint, higher reflectance in the visible spectrum is correlated partially to its larger surface roughness that enhanced light scattering. However, reflective paint undergoes a strong UV absorption with only 9.5% of reflectance (and partially in the visible range, until 440 nm) and lower reflective efficiency in the NIR while glass ceramic tile achieves values over 100%, regarding to the Spectralon®. This fact globally reduces the average reflection in the whole spectrum (Table 6), being 10% lower than the value of glass ceramic. Colored ceramic tiles also present significantly reflectance differences between glaze and glass ceramic materials, with an increase up to 8%. The study of colored ceramic tiles is explained in supporting information (Fig. S1 and Table SIII).

The solar radiation has different intensities along the spectrum, so the reflectance of these materials is more efficient in regions where higher intensities are reflected. Therefore, it is necessary

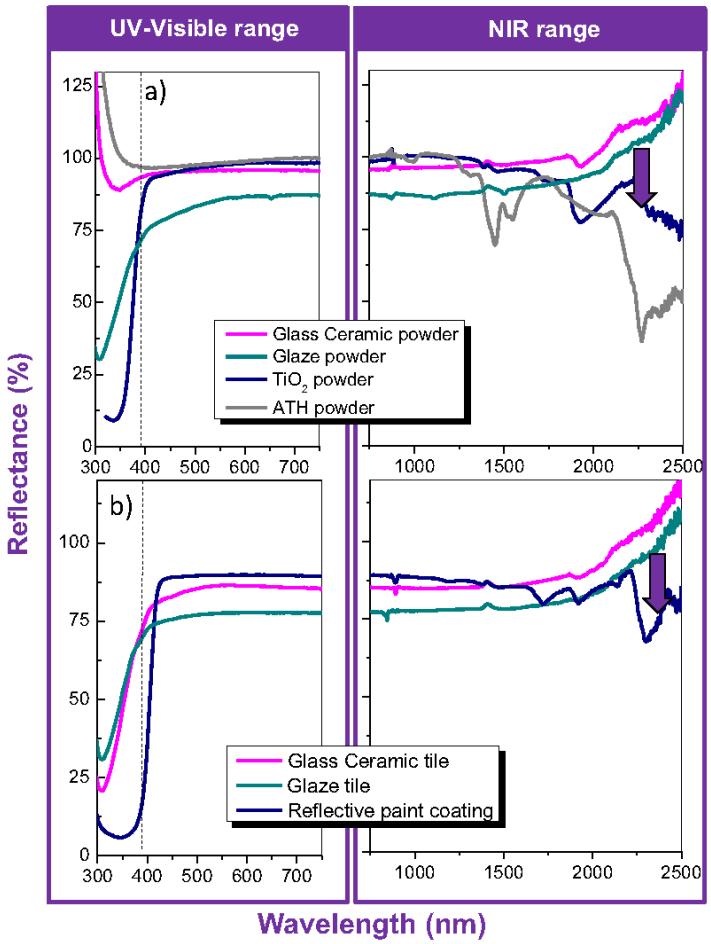

Fig. 3. Reflectance spectra of (a) pressed powder materials (glass ceramic, glaze, TiO_2 and ATH in powder) and (b) glass ceramic and glaze tiles, and reflective paint coating (all deposited on porcelain substrate), in the solar range (300–2500) nm.

Table 6
Average reflectance values and solar reflectivity (SR) of studied materials.

Sample	$R_{average}$ (%)				SR
	UV	Vis	NIR	Total	
Glass ceramic	46.5	85.0	82.2	87.6	84.4
Glaze	50.4	76.9	75.5	81.4	77.3
Reflective paint	9.5	88.0	78.8	82.7	85.5
Glass ceramic powder	95.9	95.7	93.5	102.0	96.2
Glaze powder	54.8	84.3	88.0	89.9	84.9
TiO_2	35.0	96.9	92.3	90.7	95.3
ATH	114.7	98.4	74.2	86.0	96.8

to calculate the solar reflectivity (Eq. (2)) in order to compare the data among the different materials.

Solar reflectivity of powder and tile samples is represented in Fig. 4 in comparison with the solar spectrum. Glass ceramic powders (Fig. 4a), TiO_2 (Fig. 4c) and ATH (Fig. 4d) hardly present differences in the visible range, and reflect more than 95% of the solar radiation. The main differences between glass ceramic powders and TiO_2 materials are located both in the UV and in the NIR ranges. These slight differences result in a very similar solar reflectivity, as seen in Table 6, in spite of a larger difference in the average reflectance. It is important to note that, herein, inorganic reflective raw materials (TiO_2 and ATH) are measured to compare materials in powder form. However, the paint commercial products include only a small fraction (typically 10–30 wt%) of these inorganic powders in an epoxy type matrix. The presence of an organic matrix decreases the SR because of the high NIR absorption of the organic compounds, as occurs in the reflective paint measured below. Moreover, several layers of reflectivity paint are needed to obtain an efficiency reflective coating in the visible region. In comparison with the glaze SR (Fig. 4b), glass ceramic powder enhances 12% the reflectivity of the solar spectrum.

Fig. 4 also shows the solar reflectance spectra of glass ceramic (Fig. 4e), glaze (Fig. 4f) and reflective paint (three layers) (Fig. 4g) coating porcelain substrate, in comparison with solar spectrum. For all these samples, the solar reflection decreases in comparison with powders because of the lower reflectance and the thickness of the coating is quite lower than the one of the pellet used for the powders.

As seen, glass ceramic tile SR is as larger as the one observed for paints and shows an increase of 7% when compared with the glaze tile. The slightly higher reflectivity of the reflective paint is favored by the larger roughness surface (Table 3) that produces higher light scattering, as explained above.

Therefore, the glass ceramic materials present higher reflective properties than currently glaze and similar reflective behavior than commercial reflective paints. This response is also attributed to the unique micro-nanostructure of the glass ceramic that produces larger light scattering. The combination of large presence of grain boundaries and the different phases modifies the light propagation because of the different refractive index and different crystal sizes. In addition, this fact has been also checked measuring the direct reflection of these samples which does not overcome 12%. Therefore, the main reflection corresponds to the diffuse component. In spite of having similar SR than commercial paints, glass ceramic has the advantage to possess higher reflection in the NIR range. Hence, totally, this material provides to the buildings an efficient thermal isolation from the heat generated into the cities as consequence of other heat sources. This effect is also observed in colored ceramic tiles (Fig. S2).

In order to compare the samples with a pattern which reflects more in the NIR range than the studied samples, new measurements were carried out by using Spectralon® material as pattern from UV to visible range and changing the pattern to a film of sputtered gold on a glass substrate in the near infrared range (NIR), since metals present the highest reflectance, so, they can be a useful reference of 100% reflectance spectrum in NIR. The results obtained with this method are similar than the obtained with the Spectralon® pattern. This information is included in supplementary information (S6 section).

3.3.2. Solar simulation measurements

Fig. 5 shows the results of the solar simulation experiment. Fig. 5a shows a photograph of sample during the solar irradiation. Heating curves of tile materials compared to the coated tile with TiO_2 based reflective paint are shown in Fig. 5b (measured in the surface by the IR camera) and 5c (measured in the rear part by the thermocouple). Temperature values were normalized to room temperature (RT) for comparative purposes, in order to avoid mistakes when different samples were compared. Therefore, temperature gradients are given. Thermal photographs obtained by IR thermography after 10 s and 5 min under solar irradiance were compared in Fig. 5d.

As seen, glaze tile achieves higher temperatures than glass ceramic tile, >1 °C from RT, according with the solar reflectivity results obtain before. Moreover, the rear side heating indicates that glaze transfers heat faster than glass ceramic. The lower thermal diffusivity of glass ceramic material allows reducing both the temperature increase caused by the radiation absorption at the surface and the heat transfer to the rear of the tile. This effect is due to 3 phenomena: (a) the first one is the superior reflectivity of glass ceramics; (b) the light absorbed onto the tile surface requires larger energy to heat the material due to the larger specific heat value, Cp, in glass ceramic; and (c) thereafter the low thermal conductivity limits the heat flow through the material. On the other hand, reflective paint presents larger heating than glass ceramic at the surface, >1 °C after 5 min, with a similar value than the obtained for the glaze material. In the case of the rear side, reflective paint heats even more than glaze material, due to the higher thermal diffusivity of the paint component, in spite of its larger radiation reflection. Temperature differences at the rear part between reflective painted and glass ceramic tiles, increases up to 1.1 °C. These differences does not correlate with the similarities in SR, proving that the solar radiation it is not the only parameter to be controlled in reflective materials to effectively serve as heating insulators. In addition of the SR, thermal inertia (thermal diffusivity) of materials are required for practical applications. Glass ceramic materials provide a unique combination of high SR and low thermal diffusivity to both avoid the radiation absorbance, increase the energy required to heat the material and the resistance for heat flow.

Fig. 5d shows the thermal images extracted from the IR thermal videos at the beginning (10 s) and after 5 min of solar irradiance, for the three samples. The images at 10 s indicate that all samples are at similar temperatures at the beginning of the experiment. After 5 min, the glaze surface is heated up to 27.9 °C, >1 °C more than glass ceramic surface and only ~0.2 °C more than reflective paint.

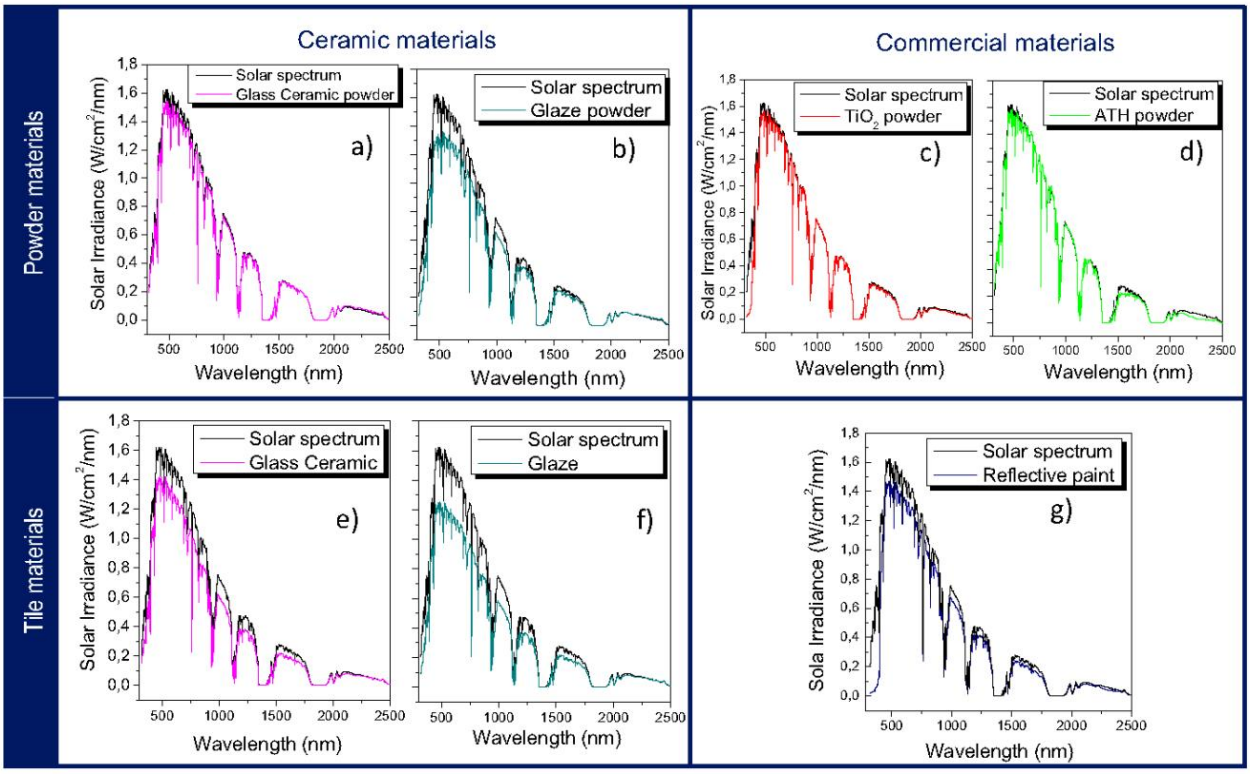

Fig. 4. Spectral reflectivity of powder samples in comparison with the solar spectrum: (a) glass ceramic powder, (b) glaze powder, (c) TiO_2 and (d) ATH; and in tile materials (coating porcelain substrate) in comparison with the solar spectrum: (e) glass ceramic, (f) glaze and (g) reflective paint.

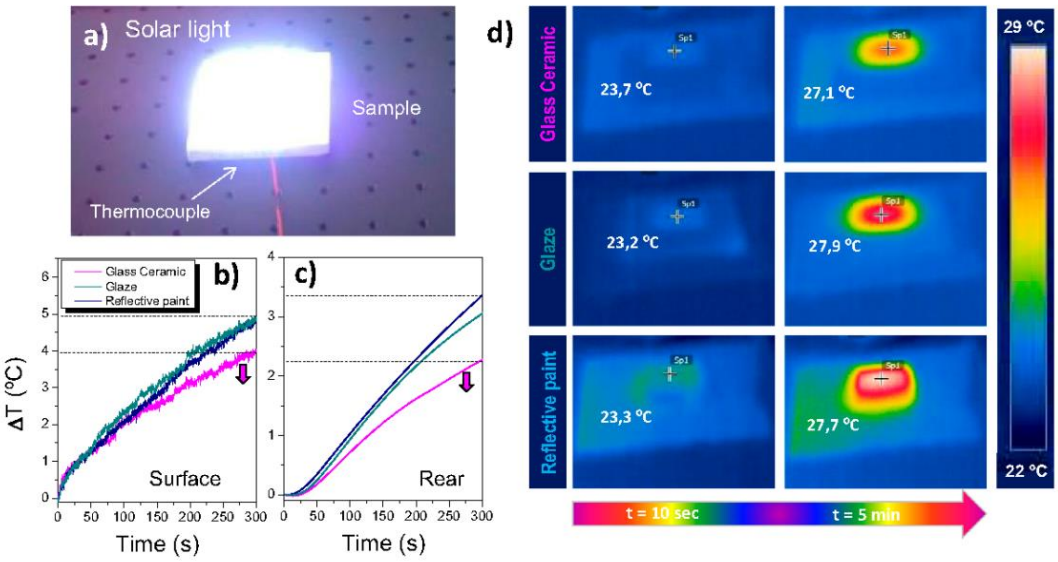

Fig. 5. (a) Photograph taken during the experiment when the solar simulator is irradiating the sample surface showing the high reflectivity. Heating curves of glass ceramic, glaze and reflective paint on porcelain substrate (b) at the surface (measured with the IR camera) and (c) at the rear part (measured with the thermocouple). (d) Thermal images extracted from the IR thermal videos at the beginning (10 s) and at the end (5 min) of the measurement, for glass ceramic, glaze and reflective paint tiles.

That is, glass ceramic undergoes lower heating at the surfaces because of higher reflection and the low heat transfer due to a lower thermal diffusivity, as explained above. These graphical results clearly illustrate the different thermal properties of both materials under solar irradiance.

The same experiment was performance for colored ceramic tiles, obtaining similar results than for white ceramic tiles, difference of ~1 °C between glaze and glass ceramic both in the surface and rear part (supporting information, Fig. S3).

3.4. Experiment with a scaled demonstrator

According to previous results, two boxes formed by binded tiles of 15 cm × 15 cm × 15 cm were fabricated with white glass ceramic and glaze tiles. Boxes were situated on a building roof during two day-night cycles (Chung et al., 2015; Levinson et al., 2010a, 2010b; Zinzi, 2015) in May at the industrial area of Villarreal (located in Castellon, Spain). Temperature measurements were registered inside each box through a PT100 thermocouple disposed in the center of the box held by the contact wires, as schematically is represented in Fig. 6. The curves obtained from the thermocouples are shown in Fig. 7a and the temperature difference between both boxes is plotted in Fig. 7b. These curves show larger differences, up to 1.5 °C, between glass ceramic and glaze boxes, in the midday hours, confirming a larger albedo of the solar spectrum and lower thermal diffusivity toward the inner for the glass ceramic material. During the night, the temperature difference between both boxes reduces and ranged between 0 and 0.5 °C, since the solar reflection does not continue to produce heat. These results clearly agree with the data obtained above, checking the higher efficiency of this glass ceramic material in the energy saving purposes.

The same test was performed with enamels decorated by inkjet in dark colors to check the effect of the solar radiation absorption. Results are included in supporting information (Fig. S4), obtaining that the inside temperature difference between the two colored boxes achieves 1.6 °C in the midday hours.

3.4.1. Energy saving estimation

Considering the data obtained from the above temperature curves, an estimation of the energy savings that will occur by replacing glaze by glass ceramic tile in a building facade was calculated. In other works, energy saving is estimated by means of statistic simulation software (Chung et al., 2015; Huang et al., 2015; Ihara et al., 2015; Pisello, 2015) or by extrapolation of experimental results (Zinzi, 2015). Herein, the calculations are carried out according to the thermodynamic principles that relate the heat required to warm a material from an initial temperature to a final temperature, according to the Eq. (3).

$$Q = m \cdot C_p \cdot (T_i - T_f) \quad (3)$$

where Q is the heat required, m the material mass, C_p the specific heat, T_i and T_f the initial and final temperature, respectively.

Therefore, from the experimental temperature differences recorded between both material boxes, ~1.5 °C, in the midday hours, when acclimatization systems are highly required, and considering the same mass for both materials, it is possible to calculate

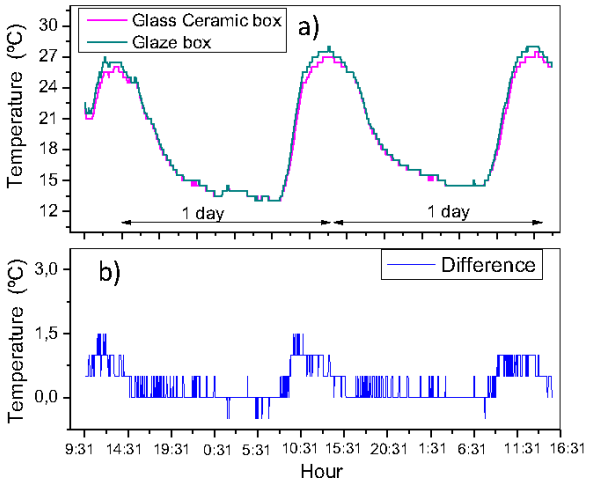

Fig. 7. (a) Temperature curves registered by the thermocouples inside the boxes of glass ceramic and glaze materials and (b) the difference between them, along two day-night cycles.

the necessary energy to bring both materials to a comfortable temperature, 25 °C in summer. As an example, considering glass ceramic tiles at 30 °C and the conventional ones at 30 °C plus temperature difference (that is 31.5 °C), the energy required to reduce both of them to 25 °C is calculated (Table 7). However, depending on the required temperature reduction, the energy saving of the glass ceramic material may vary, since the lower the temperature to be reduced, the greater the efficiency of the material.

As seen in Table 7, it is possible to obtain an energy saving of ~**21%** over the midday hours if glaze coating is substituted by glass ceramic coating in porcelain tiles used in the buildings facades. Moreover, in case of colored tiles, the energy saving increases to ~**22%** as explained in supporting information (Table SIV).

Therefore, glass ceramic materials provide significant energy savings when they are used as lining. These linings can be used in outside facades and roofs, as they reflect more solar radiation than the current available materials and have lower thermal diffusivity which avoids the heat flow. In addition, the reflective paints used today required several layers to achieve the same albedo values. Moreover, paints undergo high degradation along short time and need constant arrangements unlike ceramic tiles that have high coefficients of resistance and durability, and avoid surface

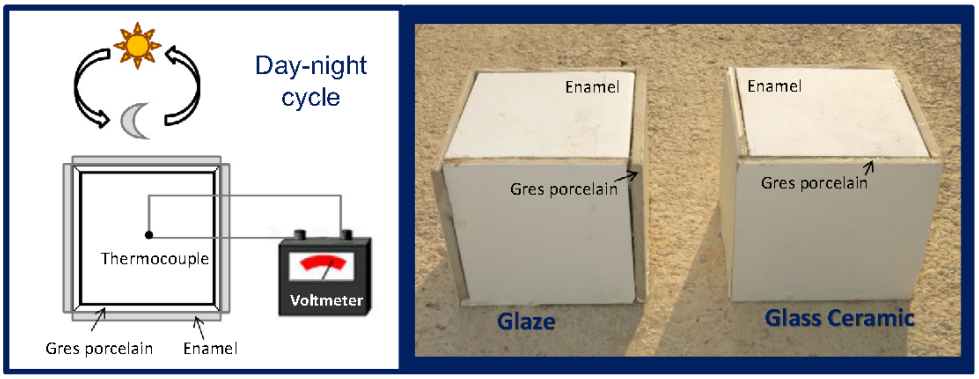

Fig. 6. In the left: Setup of the scaled demonstrator consisting on a tile box of 15 cm × 15 cm × 15 cm with a thermocouple located inside to measure the temperature with a voltmeter; In the right: a picture of the measured tile boxes.

Table 7
Calculated energy requirements for cooling Glass ceramic and Glaze tiles and energy saving that would be obtained by replacing Glaze by Glass ceramic tiles.

Tile	Q/m (J/kg)	Energy saving (%)
Glass ceramic	3825.5	**20.7**
Glaze	4821.7	

staining. Tiles will serve also as transit areas and habitable spaces that will allow using zones like terraces and sidewalks that at present are not able to be covered with reflective materials. Likewise, these ceramic tiles could be used inside of buildings providing a great heating savings, as they have high reflectance in the infrared, which would produce that heat is not absorbed by the floor or walls rooms. Thus a new opportunity is opened to keep warm the living spaces in the cities with this new material, in this way a reduction of the energy required to heat the cities in the winter time will be also possible attained.

4. Conclusions

Development of new kind of glass ceramic based on feldspars has been successfully prepared by conventional one step ceramic process. This material possesses high proportion of crystalline phase which provides unique thermal and optical properties. The high albedo, both in white and colored surfaces, makes them a great candidate to be used as reflective material, both for pavements and cool roofs, achieving higher yields than current reflective methods, such as TiO_2 based paints. Moreover, its low thermal diffusivity added an advantage to this material since avoids the heat flow inside the building in summer. Furthermore, the designed material preserves the mechanical properties of ceramics, making them more resistant for outdoor uses and avoiding the surface staining, unlike the reflective paints.

The simulation and the scaled demonstrator tests reveal energy saving attained by replacing glaze by glass ceramic coated tiles in buildings as large as >20%, overcoming the current methods and techniques, both in efficiency and in using and resistance. Therefore, glass ceramic coated tiles offer an exceptional solution for reducing the urban heating both by increasing the albedo and by reducing the thermal inertia, that provide energy saving of buildings, which also provides great thermal comfort sensation inside the buildings. In this sense, the concept of combined high albedo materials with low thermal diffusivity properties opens new possibilities for efficient reduction of energy consumption in comfortability for buildings.

Acknowledgments

The authors express their thanks to the MINECO (Spain) project MAT2013-480089-C04-1-P, and projects CDTI (IDI-20130894 and IDI-20161120) for their financial support. Dra. E. Enriquez is also indebted to MINECO for a "Torres Quevedo" contract (ref: PTQ-14-07289), which is co-financed with European Social Funds.

Appendix A. Supplementary material

Supplementary data associated with this article can be found, in the online version, at http://dx.doi.org/10.1016/j.solener.2017.04.011.

References

Akbari, H., Levinson, R., Berdahl, P., n.d. ASTM Standards for Measuring Solar Reflectance and Infrared Emittance of Construction Materials and Comparing their Steady-State Surface Temperatures.

Álvarez-Docio, C.M., Reinosa, J.J., del Campo, A., Fernández, J.F., 2017. 2D particles forming a nanostructured shell: a step forward cool NIR reflectivity for $CoAl_2O_4$ pigments. Dye. Pigment. 137, 1–11. http://dx.doi.org/10.1016/j.dyepig.2016.09.061.

Andrews, A.I., 1961. Porcelain Enamels: The Preparation, Application, and Properties of Enamels. The Garrard Press, Champaign, IL.

Antonaia, A., Ascione, F., Castaldo, A., D'Angelo, A., De Masi, R.F., Ferrara, M., Vanoli, G.P., Vitiello, G., 2016. Cool materials for reducing summer energy consumptions in Mediterranean climate: in-lab experiments and numerical analysis of a new coating based on acrylic paint. Appl. Therm. Eng. 102, 91–107. http://dx.doi.org/10.1016/j.applthermaleng.2016.03.111.

Carbajal, L., Rubio-Marcos, F., Bengochea, M.A., Fernandez, J.F., 2007. Properties related phase evolution in porcelain ceramics. J. Euro. Ceram. Soc. 27, 4065–4069. http://dx.doi.org/10.1016/j.jeurceramsoc.2007.02.096.

Cavalcante, P.M.T., Dondi, M., Ercolani, G., Guarini, G., Melandri, C., Raimondo, M., Rocha, E., Almendra, E., 2004. The influence of microstructure on the performance of white porcelain stoneware. Ceram. Int. 30, 953–963. http://dx.doi.org/10.1016/j.ceramint.2003.11.002.

Chung, M.H., Park, J.C., Ko, M.J., 2015. Effect of the solar radiative properties of existing building roof materials on the energy use in humid continental climates. Energy Build. 102, 172–180. http://dx.doi.org/10.1016/j.enbuild.2015.05.022.

Cozza, E.S., Alloisio, M., Comite, A., Di Tanna, G., Vicini, S., 2015. NIR-reflecting properties of new paints for energy-efficient buildings. Sol. Energy 116, 108–116. http://dx.doi.org/10.1016/j.solener.2015.04.004.

Brown, I.W.M., Mackenzie, K.J.D., 1982. Process design for the production of a ceramic-like body from recycled waste glass. Part 3: The influence of microstructure and devitrification behaviour on the physical properties. J. Mater. Sci. 17, 2184–2193.

Ellison, A.J.G., Navrotsky, A., 1992. Enthalpy of formation of Zircon. J. Am. Ceram. Soc. 75, 1430–1433.

Elton, N.J., Legrix, A., 2014. Wavelength dependence of Kubelka-Munk scattering spectra for studies of TiO_2 microstructure and aggregation in paints. J. Coat. Technol. Res. 11, 555–566. http://dx.doi.org/10.1007/s11998-014-9567-x.

Feng, X., Huang, X., Wang, X., 2012. Thermal conductivity and secondary porosity of single anatase TiO_2 nanowire. Nanotechnology 23, 185701. http://dx.doi.org/10.1088/0957-4484/23/18/185701. 12pp.

Ferrari, C., Libbra, A., Muscio, A., Siligardi, C., 2013. Design of ceramic tiles with high solar reflectance through the development of a functional engobe. Ceram. Int. 39, 9583–9590. http://dx.doi.org/10.1016/j.ceramint.2013.05.077.

Hodgman, C.D., Coolbaugh, M.F., Senseman, C.E., 1920. Handbook of Chemistry and Physics: A Ready-Reference Pocket Book of Chemical and Physical Data. The Chemical Rubber Company, Cleveland, Ohio.

Huang, T.Y., Hocheng, H., Chou, T.H., Yang, W.H., Ting, C.J., Cheng, K.Y., Hsieh, C.W., 2015. Design and fabrication of sunlight-redirecting and infrared-insulating microstructure. Energy Build. 90, 114–126. http://dx.doi.org/10.1016/j.enbuild.2014.12.051.

Ihara, T., Gustavsen, A., Jelle, B.P., 2015. Effect of facade components on energy efficiency in office buildings. Appl. Energy 158, 422–432. http://dx.doi.org/10.1016/j.apenergy.2015.08.074.

International, A., 1996. Standard Test Method for Solar Absorptance, Reflectance, and Transmittance of Materials Using Integrating Spheres. West Conshohocken, USA. doi:http://dx.doi.org/10.1520/E0903-12.2.

Jiménez-Pérez, J.L., Gutiérrez Fuentes, R., Sánchez-Sosa, R., Zapata Torres, M.G., Correa-Pacheco, Z.N., Sánchez Ramírez, J.F., 2015. Thermal diffusivity study of nanoparticles and nanorods of titanium dioxide (TiO_2) and titanium dioxide coated with cadmium sulfide (TiO_2CdS). Mater. Sci. Semicond. Process. 37, 62–67. http://dx.doi.org/10.1016/j.mssp.2015.01.036.

Karlessi, T., Santamouris, M., Apostolakis, K., Synnefa, A., Livada, I., 2009. Development and testing of thermochromic coatings for buildings and urban structures. Sol. Energy 83, 538–551. http://dx.doi.org/10.1016/j.solener.2008.10.005.

Kinoshita, S., Yoshida, A., 2016. Investigating performance prediction and optimization of spectral solar reflectance of cool painted layers. Energy Build. 114, 214–220. http://dx.doi.org/10.1016/j.enbuild.2015.06.072.

Levinson, R., Akbari, H., Berdahl, P., 2010a. Measuring solar reflectance-Part I: Defining a metric that accurately predicts solar heat gain. Sol. Energy 84, 1717–1744. http://dx.doi.org/10.1016/j.solener.2010.04.018.

Levinson, R., Akbari, H., Berdahl, P., 2010b. Measuring solar reflectance – Part II: Review of practical methods. Sol. Energy 84, 1745–1759. http://dx.doi.org/10.1016/j.solener.2010.04.017.

Levinson, R., Berdahl, P., Akbari, H., Miller, W., Joedicke, I., Reilly, J., Suzuki, Y., Vondran, M., 2007. Methods of creating solar-reflective nonwhite surfaces and their application to residential roofing materials. Sol. Energy Mater. Sol. Cells 91, 304–314. http://dx.doi.org/10.1016/j.solmat.2006.06.062.

Levinson, R., Berdahl, P., Asefaw Berhe, A., Akbari, H., 2005. Effects of soiling and cleaning on the reflectance and solar heat gain of a light-colored roofing membrane. Atmos. Environ. 39, 7807–7824. http://dx.doi.org/10.1016/j.atmosenv.2005.08.037.

Libbra, A., Tarozzi, L., Muscio, A., Corticelli, M.A., 2011. Spectral response data for development of cool coloured tile coverings. Opt. Laser Technol. 43, 394–400. http://dx.doi.org/10.1016/j.optlastec.2009.07.001.

Marangoni, M., Nait-Ali, B., Smith, D.S., Binhussain, M., Colombo, P., Bernardo, E., 2016. White sintered glass-ceramic tiles with improved thermal insulation properties for building applications. J. Euro. Ceram. Soc. 37, 1117–1125. http://dx.doi.org/10.1016/j.jeurceramsoc.2016.10.019.

Meyer, L., Grishko, V., Jayaram, S., Cherney, E., Duley, W.W., 2002. Thermal characteristics of silicone rubber filled with ATH and silica under laser heating. In: Annu. Rep. Conf. Electr. Insul. Dielectr. Phenom., pp. 848–852. http://dx.doi.org/10.1109/CEIDP.2002.1048928.

Norsker, H., Danisch, J., 1993. Glazes-for the Self-Reliant Potter. Wiegeg, Eschborn, GMBh.

Pisello, A.L., 2015. Experimental analysis of cool traditional solar shading systems for residential buildings. Energies 8, 2197–2210. http://dx.doi.org/10.3390/en8032197.

Pisello, A.L., Cotana, F., Nicolini, A., Brinchi, L., 2013. Development of clay tile coatings for steep-sloped cool roofs. Energies 6, 3637–3653. http://dx.doi.org/10.3390/en6083637.

Reinosa, J.J., Marero, D.M.Y., Del Campo, A., De La Rubia, M.Á., Fernández, J.F., 2013. Chemical analysis with high spatial resolution by rutherford backscattering and Raman Confocal spectroscopies: surface hierarchically structured glasses. J. Am. Ceram. Soc. 96, 1783–1788. http://dx.doi.org/10.1111/jace.12397.

Reinosa, J.J., Rubio-Marcos, F., Solera, E., Bengochea, M.A., Fernández, J.F., 2010. Sintering behaviour of nanostructured glass-ceramic glazes. Ceram. Int. 36, 1845–1850. http://dx.doi.org/10.1016/j.ceramint.2010.03.029.

Santamouris, M., 2014. Cooling the cities - a review of reflective and green roof mitigation technologies to fight heat island and improve comfort in urban environments. Sol. Energy 103, 682–703. http://dx.doi.org/10.1016/j.solener.2012.07.003.

Shi, Z., Fu, R., Agathopoulos, S., Gu, X., Zhao, W., 2012. Thermal conductivity and fire resistance of epoxy molding compounds filled with Si_3N_4 and $Al(OH)_3$. Mater. Des. 34, 820–824. http://dx.doi.org/10.1016/j.matdes.2011.07.012.

Shmulovich, K.I., Graham, C., 2008. Plagioclase - aqueous solution equilibrium: concentration dependence. Petrology 16, 177–192. http://dx.doi.org/10.1134/S0869591108020045.

Wefers, K., Misra, C., 1987. Oxides and Hydroxides of Aluminum. Alcoa Tech. Pap. 19, pp. 1–100.

Zhao, M., Pan, W., Wan, C., Qu, Z., Li, Z., Yang, J., 2017. Defect engineering in development of low thermal conductivity materials: a review. J. Euro. Ceram. Soc. 37, 1–13. http://dx.doi.org/10.1016/j.jeurceramsoc.2016.07.036.

Zinzi, M., 2015. Characterisation and assessment of near infrared reflective paintings for building facade applications. Energy Build. 114, 206–213. http://dx.doi.org/10.1016/j.enbuild.2015.05.048.

Electronic Supporting Information (ESI)

New strategy to mitigate urban heat island effect: energy saving by combining high albedo and low thermal diffusivity in glass ceramic materials

E. Enríquez*[1], V. Fuertes[2], M.J. Cabrera[1], J. Seores[1], D. Muñoz[1], J. F. Fernández[2]

1 Centro tecnológico Vidres, S.L., Ctra. Onda, Km 3.4, 12540 Villareal, Castellón, Spain

2 Electroceramics Department, Instituto de Cerámica y Vidrio, CSIC, Kelsen 5, 28049, Madrid, Spain.

S1. Preparation of the colored tiles

Colored ceramic tiles were prepared following the same procedure explained in the *2.1 sample section* of the manuscript. Colored tiles were processed by inkjet deposition of a saturated surface of black type ceramic nanopigment based on Fe-Cr-Mn oxide spinel, in order to check the validity of results in colored surfaces. The properties of these samples are described in table ST1. Density of colored samples is the same as the white enamels. However, thicker coating than the one used for white tiles is attained and average roughness also changes. The same thermal properties have been assumed in colored enamels, since the colored inkjet thin film supposes a negligible contribution.

Table ST1
Description and properties of the colored ceramic tiles. Densities and roughness values are measured on sintered tiles.

Sample	Shape	Color	Density (g/cm^3)	Thickness	Average Roughness (µm)
Colored Glass ceramic	Film	Yes	2.63	990 µm	6.34
Colored Glaze	Film	Yes	2.70	970 µm	9.46

S2. Optical characterization of the colored tiles

The CIEL*a*b* coordinates of colored materials are presented in table ST2, where is seen that the L* greatly decreases regarding the white enamels due to the darkness tone, and b* parameter significantly increases. However, it is relevant that in spite of the dark color, the L* parameter, in glass ceramic tile is > 7% respect to the glaze tile.

Table ST2
Chromatic coordinates in the CIEL*a*b* system of the colored samples measured.

Sample	L*	a*	b*
Colored Glass ceramic	47,45	-0,96	7,3
Colored Glaze	40,98	-1,58	6,78

S3. Reflectivity response of the colored tiles

Figure S1 shows the reflectance curves of colored tiles in the entire solar spectrum range (280-2500 nm). As seen, glaze presents lower reflectance than glass ceramic in all the solar range (NIR, visible and UV). Both curves show more absorption than the white samples due to the dark colored surfaces, especially in the visible range. However, under these conditions, glass ceramic material also reflects more radiation than glaze (8 %, table ST3) due to its singular microstructural properties already mentioned in the manuscript.

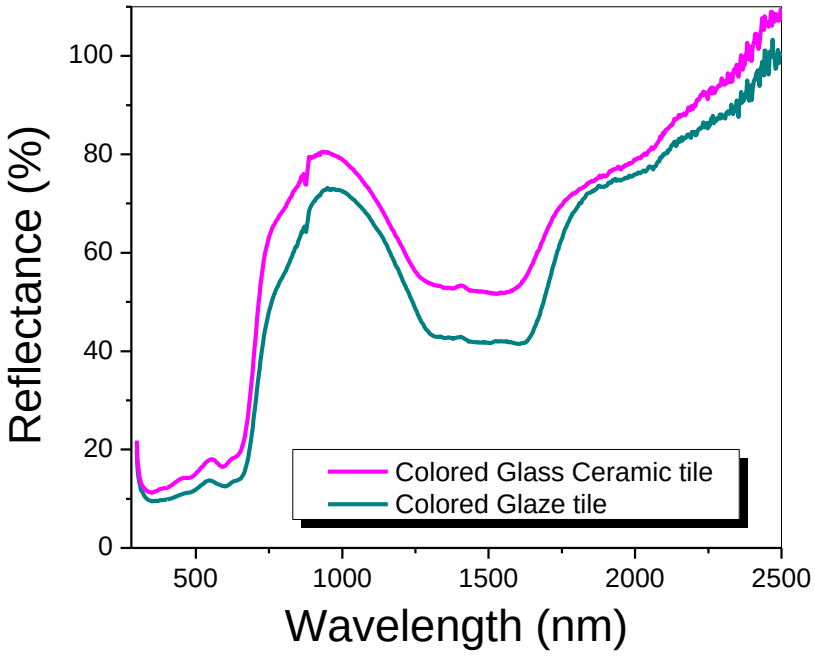

Figure S1: Reflectance spectra of colored glass ceramic and glaze tiles in the solar range (280-2500) nm. Spectra were measured using Spectralon® material as pattern in the whole range.

Consequently, in case of colored ceramics the SR is also reduced drastically, but the glass ceramic shown a SR 10% higher than the glaze samples (table ST3). Figure S2 presents the solar spectral reflectivity of colored ceramic tiles in comparison with the solar spectrum, where it is possible to observe larger reflection of glass ceramic material, especially in the visible and NIR ranges.

Table ST3
Average reflectance values and solar reflectivity (SR) of colored ceramic materials.

Sample	$R_{average}$ (%)	SR
Colored Glass ceramic	62.7	42.1
Colored Glaze	55.7	35.9

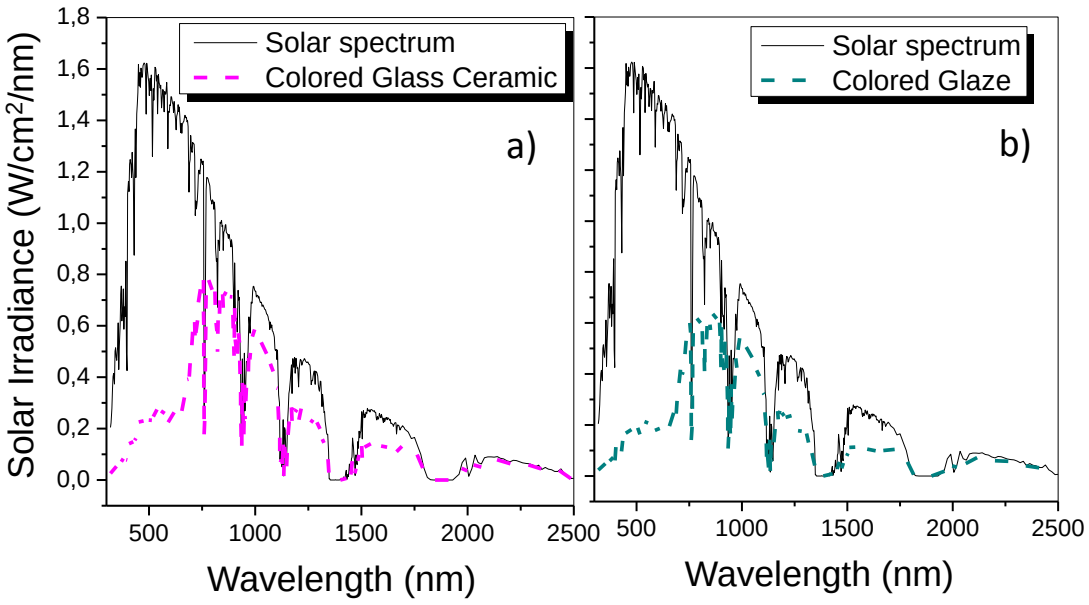

Figure S2: Spectral reflectivity of colored ceramic tiles in comparison with the solar spectrum: a) Glass ceramic and b) Glaze.

S4. Solar simulation response of the colored tiles

The solar simulation experiment was also carried out for colored tiles, obtaining the results observed in figure S3. In tiles with colored surfaces a higher absorption of the solar spectrum according with the low visible reflective produce a larger increase of temperature. However, glass ceramic presents also lower heating than glaze (~ 1 ºC), in both the surface and the rear part (figure S3a), which indicates better insulating properties in Glass ceramic materials despite lack of whiteness. Figure S3b shows the infrared images of colored surfaces where it can be observed larger heating for the glaze tile after 5 minutes of irradiating with the lamp.

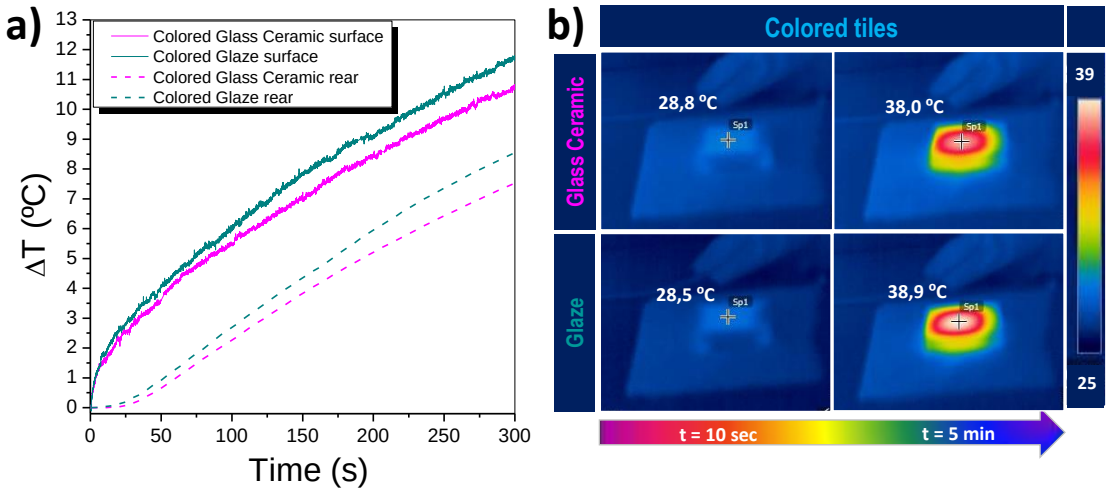

Figure S3: a) Heating curves of colored tile samples (glass ceramic and glaze) at the surface (measured with the IR camera) and at the rear part (measured with the thermocouple); **b)** Thermal images extracted from the IR thermal videos at the beginning (10 seconds) and at the end (5 minutes) of the measurement, for glass ceramic and glaze.

S5. Experiment with a scaled demonstrator of colored tiles

A scale demonstrator was also performed with enamels decorated by inkjet in dark colors to check the effect of the solar radiation absorption. In this case, in addition of the thermocouples located inside the boxes, two more thermocouples were used, positioned close to the external surface of each box, to check that both boxes receive the same radiation energy. The results are observed in figure S4. In case of the external temperatures measured close to both boxes (figure S4b), the difference is minimal, ≈0.5 ºC. Therefore, the solar energy received in both boxes is practically the same. In addition, the dark surface produces higher absorption of radiation. Regarding to the temperature inside the boxes (figure S4a), glass ceramic materials are more efficient to limit the heat flow due mainly to its lower thermal diffusivity. The inside temperature difference between the two boxes achieves 1.6 ºC in the midday hours.

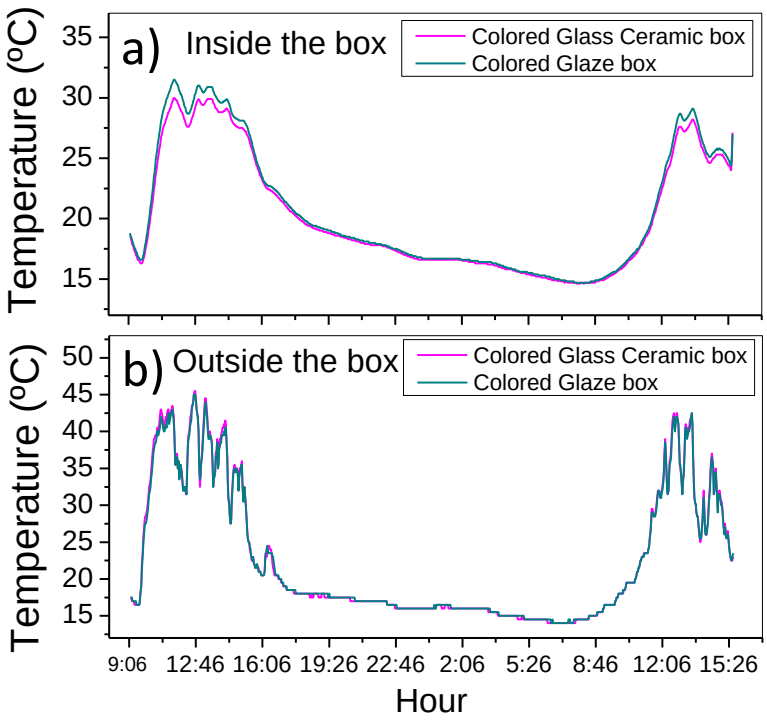

Figure S4: Temperature curves registered by the thermocouples **a)** inside and **b)** outside, close to the boxes of glass ceramic and glaze materials, decorated by inkjet in dark colors. Note that differences between temperatures close to glass ceramic and glaze outside are negligible.

With the data obtained in the scale demonstrators, an estimation of the energy saving obtained by replacing colored glaze by colored glass ceramic tile in a building façade was calculated following the same procedure explained in the manuscript. The results obtained are presented in table ST4. In this case, an energy saving of **~22%** is obtained when colored glaze is substituted by colored glass ceramic material.

Table ST4
Calculated energy requirements for cooling colored glass ceramic and glaze tiles and energy saving that would be obtained by replacing glaze by glass ceramic tiles.

Tile	Q/m (J/kg)	Energy saving (%)
Colored glass ceramic	3825.5	21.9
Colored glaze	4895.9	

S6. Reflectance measurements carried out with two different patterns: Spectralon and gold substrate.

In order to correct the spectra obtained with a single pattern, Spectralon®, which overcome 100% of reflectance in the NIR range, two different patterns were used. From UV to visible range, spectra were measured using Spectralon® material as pattern, which represents the 100% of reflectance. In the near infrared range (NIR), metals present the highest reflectance, so, a film of sputtered gold on a glass substrate was used as reference of 100% reflectance spectrum. The obtained reflectance spectra are observed in figure S5.

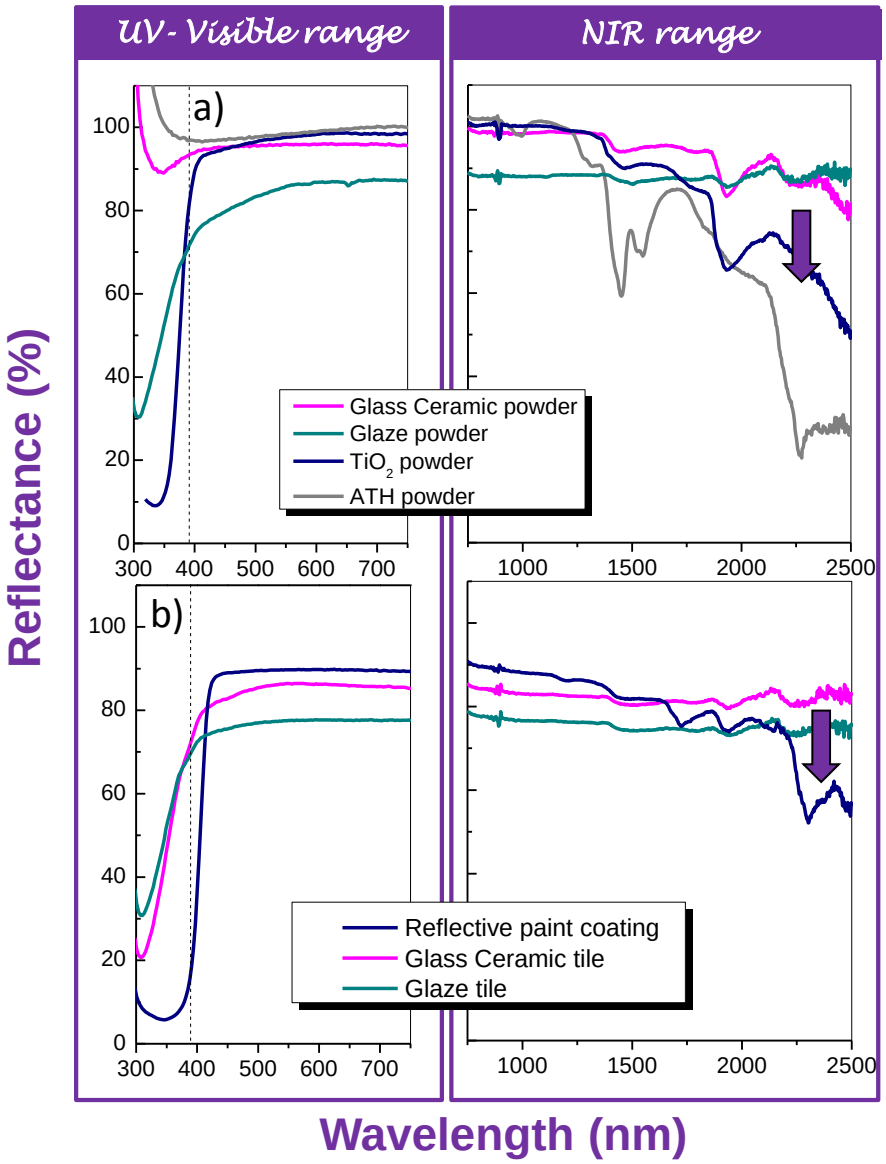

Figure S5: Reflectance spectra of **a)** pressed powder materials (glass ceramic, glaze, TiO_2 and ATH in powder) and **b)** glass ceramic and glaze tiles, and reflective paint coating (all deposited

on porcelain substrate), in the solar range (300-2500) nm. From UV to visible range, spectra were measured using Spectralon® material as reference, and in the NIR range, a gold covered substrate was used as reference.

Figure S6 shows the solar reflective spectra measured with this method (two patterns), and table ST5 presents the average reflectance and solar reflectivity obtained with this method for white samples.

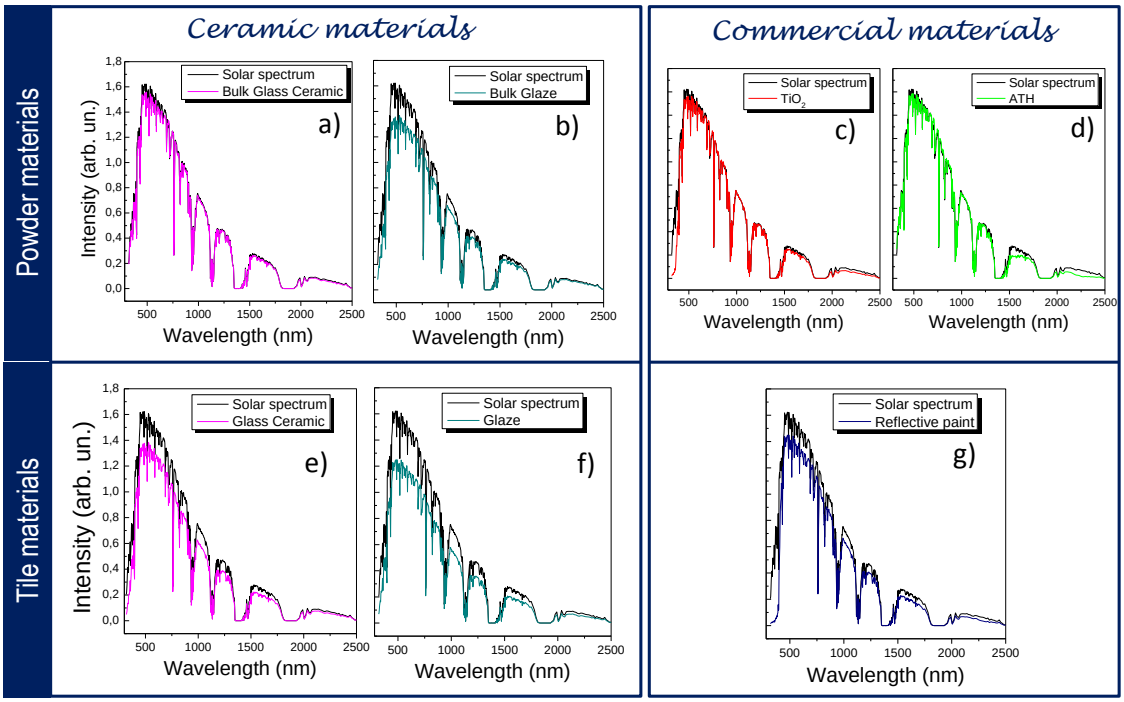

Figure S6: Spectral reflectivity of powder samples in comparison with the solar spectrum: **a)** Glass ceramic powder, **b)** Glaze powder **c)** TiO_2 and **d)** ATH; and in tile materials (coating porcelain substrate) in comparison with the solar spectrum: **e)** Glass ceramic, **f)** Glaze and **g)** reflective paint.

As seen, the values obtained by this method are slightly lower than those measured using only the Spectralon® pattern. However, the relative differences between samples are the same. Therefore, this method may be useful for avoid measurement errors since it do not alter the qualitative results, although these values may not be compared with other works.

Table ST5

Average reflectance values and solar reflectivity (SR) obtained using two different patterns.

Sample	$R_{average}$ (%)	SR (%)
Glass ceramic	80.6	82.9
Glaze	74.5	76.2
Reflective paint	77.0	83.8
Glass ceramic powder	95.6	96.7
Glaze powder	85.9	85.3
TiO_2	84.8	94.4
ATH	79.4	96.2

ARTÍCULO 8. Enhanced Luminescence in Rare-earth free Fast Sintering Glass-ceramic

V. Fuertes, J. F. Fernández, E. Enríquez. Solar Energy, 149, 2017, 114-124

Optica, 6 (5), 2019, 668-679.

Factor de impacto: 7,536 (según JCR Edition Science 2017).

Research Article Vol. 6, No. 5 / May 2019 / Optica 668

Enhanced luminescence in rare-earth-free fast-sintering glass-ceramic

V. Fuertes,[1,*] J. F. Fernández,[1] and E. Enríquez[2]

[1]Department Electrocerámica, Instituto de Cerámica y Vidrio, CSIC, Kelsen 5, 28049, Madrid, Spain
[2]Centro Tecnológico Vidres, S.L., Ctra. Onda, Km 3.4, 12540 Villareal, Castellón, Spain
*Corresponding author: vfuertes@icv.csic.es

Received 5 February 2019; revised 18 March 2019; accepted 1 April 2019 (Doc. ID 359612); published 16 May 2019

One of the major challenges pursued in the luminescent materials community is to develop rare-earth-free phosphors in order to reduce the use of rare-earth elements, because of the lack of their availability and the environmental problems derived from their mining and processing. In this work, a rare-earth-free glass-ceramic-based phosphor with high photoluminescence has been designed. This novel phosphor rich in Na-rich plagioclase feldspar crystallizations presents high crystallinity, ∼94%, and a dual micro-nanostructure provided by a fast-sintering processing route. Structural disorder in Si–Al distribution favors formation of luminescent centers in the glass-ceramic material, which results in an enhancement of both the UV–blue and the red luminescence regarding natural feldspars, 1 order of magnitude and 6 times, respectively. A microstructural and structural study by means of x-ray diffraction, Raman spectroscopy, scanning electron microscopy, transmission electron microscopy (TEM), high-resolution TEM, cathodoluminescence, and nuclear magnetic resonance evidence the important role of composition in the alteration of Si–Al ordering schemes. A strong correlation between Si–Al disorder and the presence of active luminescent centers is corroborated. Our research shows a sustainable, cost-effective, innovative, and scalable material that may be considered as an alternative to rare-earth phosphors for applications such as security markers or light-emitting glasses. This novel family of rare-earth-free glass-ceramics opens a new gate through structural tailoring to enhance and tune the intrinsic luminescent emissions displayed for relevant future optical applications.

https://doi.org/10.1364/OPTICA.6.000668

1. INTRODUCTION

The development of luminescent inorganic materials has been subject of extensive research in past years because these materials present interesting properties, a good stability, and may be industrially produced in large quantities, which make them suitable for applications in devices involving the artificial production of light [1]. Luminescence is a property strongly affected by several factors such as crystallinity, active centers, the host composition, and the interactions between each other [2]. A wide variety of luminescent centers has been considered in semiconductors and insulating materials, such as rare-earth and transition-metal ions, excitons or donor–acceptor pairs among others. Despite that most inorganic phosphors are doped with rare-earth elements and have importance in modern electronic technology, the negative environmental impact of rare-earth mining and processing, the scarcity of these elements, and the control by China of the world's rare-earth element market lead to the need for finding alternative novel rare-earth-free-doped phosphors [3].

Silicate host lattices have been considered in last years to obtain efficient luminescent emissions, which is mainly motivated because of their stiff nature [4]. Other host lattices considered have been fluoride, oxyfluorides, garnets, nitrides, and oxynitrides [5,6]. In this context, glass and glass-ceramic materials are suitable to synthetize these luminescent matrices [7], since they have a large potential for many applications in the field of photonics. Glass and glass-ceramics are highlighted by their low-cost, large-volume production, and easy shapeability. However, one of the main drawbacks of glass regarding its luminescence behavior is the presence of many point defects that generate trapping sites responsible for nonradiative recombinations, causing the light yield to be usually lower regarding crystals [8,9]. In contrast, glass-ceramics may be synthetized with higher crystallinity, reducing such a problem. Glass-ceramics for optical applications are easy and flexible to manufacture, and are more cost efficient than corresponding single crystals. In glass-ceramics, higher optical quality, higher doping concentrations, and materials larger in size and with more complex shapes can be achieved [10].

In nature, there are materials that also exhibit luminescence, as the case of feldspars, a group of rock-forming tectosilicate minerals that constitute as much as 60% of the Earth's crust. Luminescence in feldspars has been used in mineralogy for different purposes, such as quantitative separation of different mineral species, for the evidence of different mineral generations, zonation of crystals, or to establish textural relationships between minerals, among others [11]. The most common luminescence phenomena

2334-2536/19/050668-12 Journal © 2019 Optical Society of America

used to study minerals have been thermoluminescence (TL), photoluminescence (PL), and cathodoluminescence (CL). The emission bands in feldspars are mainly related to structural defects (mainly Al-O$^-$-Al, Si-O$^-$-Si) as well as activator elements incorporated in the feldspar structure like Ti^{3+}, Fe^{3+}, Eu^{2+}, Eu^{3+}, Ce^{3+}, or Sm^{3+}, among others [12]. Nevertheless, although natural feldspars exhibit noticeable luminescence and are well-known, synthetic feldspar matrices have scarcely been studied in the literature for such purposes because of the difficulties to synthesize such structures without secondary phases [4].

Within feldspar minerals, one of the most abundant groups is plagioclase feldspars, solid solutions between albite ($NaAlSi_3O_8$) and anorthite ($CaAl_2Si_2O_8$) feldspars. The framework of albite consists of rings of four tetrahedra, where each tetrahedron is centered by a Si^{4+} or an Al^{3+}, cation with a Si^{4+}/Al^{3+} ratio of 3:1. Each oxygen atom is located at the corners of each tetrahedron and links two tetrahedra. In contrast, anorthite has also rings of four tetrahedra having a Si^{4+}/Al^{3+} ratio of 1:1. Albite has four symmetrically nonequivalent sites, designated as $T_1(0)$, $T_1(m)$, $T_2(0)$, and $T_2(m)$. In the most ordered state, known as low albite, Al^{3+} cations are placed in $T_1(0)$ positions, but as disorder increases, Al^{3+} cations migrate to the other three positions. In intermediate plagioclases, as anorthite content increases, replacement of Na^+ and Si^{4+} by Ca^{2+} and Al^{3+} increases regarding a pure albite, in order to obtain the local charge balance. This replacement modifies the Si–Al ordering and favors the formation of defects such as Al–O–Al bonds [13], one of the main luminescent centers in feldspars [11].

Due to problems related to use of rare-earth elements, it is an appealing challenge in our society to obtain materials that may be able to act as phosphors without activation of rare-earth elements. All of this motivates the first-time study, to the best of authors' knowledge, of a synthetic material that may have a wide spectral luminescence because of the presence of structural defects and possible modulation by the incorporation of different nonrare-earth activator elements in the plagioclase structure.

In recent years, development of nanotechnology and nanoscience has allowed the improvement and creation of new materials with unique properties [14]. In nanosized particles, unique luminescence properties have been revealed, which might be quite different from their bulk counterparts [15]. Glass-ceramics having uniformly dispersed crystals <100 nm in size provide unique attributes for current products and are promising for new applications [16]. Luminescent properties are strongly influenced by microstructure, crystallite, and particle size of the material under study [17]. Thus, luminescence seems to be an interesting property to study in a novel glass-ceramic with dual micro-nanostructural characteristics, and relevant insulator, optical, and thermal behavior [18,19].

In this context, the aim of this work is to evaluate the luminescent behavior, mainly intrinsic luminescence produced by structural defects, of a novel rare-earth-free glass-ceramic obtained by the fast-sintering process, which was carried out by PL and CL techniques. A thorough analysis of the structural defects involved in such emissions by deconvolution of emission curves will allow establishing the relevance of the synthetized feldspar structure. Luminescence emissions were compared with a natural sodium aluminosilicate. For this purpose, x-ray diffraction (XRD) patterns, Raman spectroscopy measurements, and scanning electron microscopy (SEM) micrographs are presented. Moreover, transmission electron microscopy (TEM) and high-resolution TEM (HRTEM) images are presented in order to analyze in detail the micro-nanostructure of the glass-ceramic host. Finally, nuclear magnetic resonance (NMR) measurements are presented to evince the important role of composition in the alteration of Si–Al ordering schemes and the generation of Si–Al disordered distribution.

2. EXPERIMENTAL PROCEDURE

A. Sample Preparation

The glass-ceramic was prepared by a conventional ceramic process as described in previous works [18]. The precursors used were kaolin with a particle size $d_{50} = 5.34$ μm, and frit in a weight proportion of 10/90, respectively. The frit and kaolin compositions expressed in term of equivalent oxides are shown in Table 1. Precursors were mixed by milling in an alumina ball mill for 20 min with 37 wt. % of water. Then, the mixture was dried at 60°C for 24 h and sieved using a mesh of 100 μm. The dried and sieved mixture possesses monomodal particle size distributions with $d_{50} = 6.72$ μm. Disk samples 2 cm in diameter of mixture powder were pressed at 39.2 MPa. Pressed samples were thermally treated in an industrial furnace at 1220°C for 6 min with a 30° C min^{-1} heating rate, in a fast-sintering cycle that comprises a total time of 55 min. The key component to obtain a Na-rich plagioclase structure is Sr^{2+}, which is a lattice disruptor that favors the formation of the sodium-rich (Na-rich) aluminosilicate after devitrification process, even though the frit just presents a 2.68% of Na_2O. Moreover, a Na-rich mineral sample (commercial product, Feldspar ASM-100 with ref. AM601.797) was selected for having a similar structural composition, in order to compare their luminescence properties. For optical applications, materials need to be shaped, which usually requires a thermal treatment. Thus, a Na-rich mineral sample was thermally treated at 1220°C for 6 min with a 30° C min^{-1} heating rate, in order to compare its luminescence with the glass-ceramic developed in this work.

B. Characterization

Structural characterization was carried out at long and short range by XRD and solid-state magic-angle spinning (MAS) NMR, respectively, on the powders obtained by milling the sintered samples at room temperature. XRD patterns were recorded over the angular range 10–70° 2θ by using an x-ray diffractometer Bruker

Table 1. Chemical Composition of the Glass-Ceramic and the Natural Na-Rich Feldspar, Expressed as wt. % of Equivalent Oxides

Oxides wt. %	Frit	Kaolin	Natural Na-Rich Feldspar
SiO_2	51.63	55.49	69.25
ZrO_2	–	–	–
SrO	8.05	–	0.02
Na_2O	2.68	–	10.44
K_2O	1.46	1.21	0.20
Al_2O_3	21.14	42.48	19.27
ZnO	1.10	–	–
CaO	10.47	0.18	0.51
B_2O_3	1.40	–	–
P_2O_5	0.84	0.04	0.02
MgO	1.04	0.10	0.05
BaO	–	–	0.07
Fe_2O_3	0.12	0.43	0.14
TiO_2	0.09	0.07	0.03

Research Article Vol. 6, No. 5 / May 2019 / Optica 670

D8 Advance with Cu Kα radiation, 40 kV, and 40 mA in order to identify the crystalline phases formed. The identification of the crystalline phases was carried out by comparison with the corresponding JCPDS cards. The crystalline phases and the glassy phase content were calculated by the diffraction software Bruker's Diffrac. Eva, through the integration of the areas corresponding to the amorphous and crystalline contribution.

^{29}Si MAS NMR spectra were recorded on a Bruker AV-400-WB spectrometer equipped with 4 mm MAS probe and operating at 79.49 MHz by a simple pulse of $\pi/2$ at 50 KHz. A relaxation time of 60 s, spectral width of 40 kHz, and 2 h of accumulation time with a spinning rate of 10 kHz were taken. Kaolin (−91.2 ppm) was used as secondary reference with respect to tetramethylsilane (TMS) as primary reference.

Microstructural characterization was studied by means of field emission SEM (FESEM), using a Hitachi S-4700. Polished samples were chemically etched with 5 vol. % of hydrofluoric acid (HF) with the aim of removing the glassy phase and revealing the microstructure.

TEM was performed at 200 keV on Philips Tecnai F20. HRTEM images were also acquired to study the local crystalline quality. Electron diffraction pattern and diffraction pattern simulations after fast Fourier transform (FFT) of HRTEM images were also used. For TEM measurements, samples were prepared in the cross section by standard sample preparation methods, carrying out a mechanical thinning and argon ion milling to attain the required electron transparency.

The PL measurements were carried out at room temperature with a spectrofluorometer (Fluorolog-3, HORIBA Jobin Yvon). The luminescence intensity was measured over the wavelength range 330–700 nm using a xenon arc lamp as an excitation source (λexc ¼ 380 nm). Samples were measured in front-face mode, with an integration time of 0.1 s. Density of the grating used was 1200 (blaze, 500), the side entrance/exit bandpass was 2.00 nm, and the spot of the source was 1 cm × 0.3 cm. The CL images were acquired with a CL spectrometer (Gatan Mono CL3) attached to a SEM (Fei Inspect) with a cooling system with liquid N_2 and spectral expansion up to the infrared. The excitation for CL measurements was provided at 30 kV electron beam in low-vacuum mode. CL spectra were accumulated in a single-shot mode within an exposure rate of 2 nm s^{-1}. All the CL spectra were taken at room temperature. The whiteness and CIE L*a*b* coordinates, the most common uniform color space, were measured by a colorimeter Konica Minolta, Spectra Magic NX, with Color Data Software CM-S100w. L* measures from white to black (0–100), a* measures from green to red, and b* measures from blue to yellow.

3. RESULTS AND DISCUSSION

A. Luminescent Response Associated with the Micro-Nanostructure: a Correlation for Glass-Ceramic

Figure 1 depicts the PL behavior at room temperature of fast-sintered glass-ceramic in comparison with the PL of the thermally treated Na-rich feldspar mineral. The raw Na-rich feldspar mineral was also evaluated, but it does not present luminescence due to structural defects (further analysis in Fig. S1 in Supplement 1), as occurs in the thermally treated samples. This fact might be probably due to high Si–Al order in tetrahedral sites, as will be discussed later. The excitation spectra [Figs. 1(a) and 1(c)] of both samples register two bands: a broad band centered at 322 nm for both materials and a sharp one at 355 nm for the

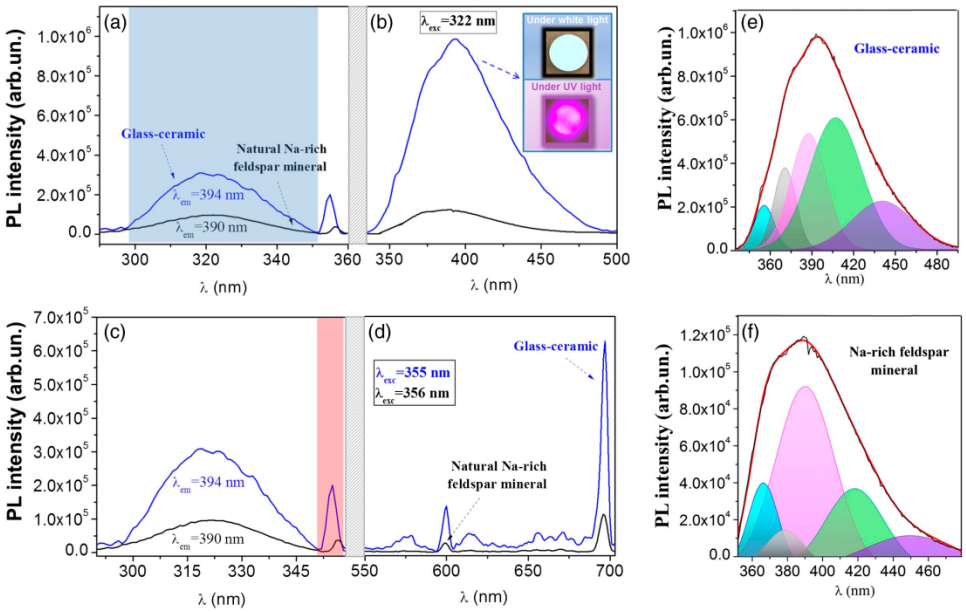

Fig. 1. Enhancement of photoluminescence in glass-ceramic in comparison with thermally treated (TT) Na-rich feldspar mineral. Room-temperature photoluminescence spectra in 1220 °C, 6 min thermal-treated glass-ceramic (blue) and in a Na-rich feldspar mineral TT (black): (a), (c) excitation spectra under λ_{em} = 394 nm for glass-ceramic material and λ_{em} = 390 nm for the Na-rich feldspar mineral TT; (b) UV–blue emission spectra for λ_{exc} = 322 nm [blue highlighted band in (a)]; (d) emission spectra in the range 550–700 nm [red highlighted band in (c)] under λ_{exc} = 355 nm and 356 nm for glass-ceramic and Na-rich feldspar mineral TT, respectively; and (e), (f) deconvolution of UV–blue emission for glass-ceramic and Na-rich feldspar mineral TT, respectively. Each defect-related emission is associated with the same color in order to make easier the comparison between each.

glass-ceramic and at 356 nm for the Na-rich feldspar mineral. The band at 322 nm is the most intense for both materials, and it corresponds to intrinsic luminescence, related to defects of feldspar structure, while the second one is mainly related to transitions undergone by iron impurities. Therefore, thermal treatment favors the structural-reorganization-inducing defects responsible for the observed luminescence. Exciting the first band at an absorption wavelength of 322 nm, the UV–blue emission was measured and plotted for both materials in Fig. 1(b). This emission is the typical UV–blue emission [20] characteristic of feldspar minerals, and it shows a PL intensity measured of 1 magnitude order higher in the glass-ceramic regarding the thermally treated Na-rich feldspar mineral used as reference. As well, a redshift from 390 nm to 394 nm was noticed for the novel rare-earth-free glass-ceramic of this work. In the inset of Fig. 1(b), two photographs of a glass-ceramic sample are shown. The upper image shows the glass-ceramic under white light excitation, which evinces their whiteness, making it suitable for being used as glaze in ceramic tile or as a white pigment in polymer-based applications. The bottom image under UV light excitation reveals the great luminescence emission of this synthetic rare-earth-free phosphor. The color observed is slightly pinkish ($L^*(C) = 65.71$, $a^*(C) = 37.28$, and $b^*(C) = -16.36$) because of the combination of UV–blue and red emission, since excitation was carried out with a UV source with some spectral width.

Under $\lambda_{exc} = 355$ nm for the glass-ceramic and $\lambda_{exc} = 356$ nm for the thermally treated mineral, the second band of Fig. 1(c) was excited, and the correspondent emission was plotted in Fig. 1(d). In this case, emission spectra are dominated by red emission, centered at 697 nm and 696 nm for the glass-ceramic and the thermally threated mineral, respectively, and this is attributed to Fe^{3+} emissions. The red luminescence in alkali feldspars occurs when a Fe^{3+} ion occupies Al^{3+} tetrahedral sites in the feldspar structure [11], and a ${}^4T1 \rightarrow {}^6A1$ transition of Fe^{3+} takes place. For ordered alkali feldspar, Fe^{3+} should substitute Al^{3+} in T_{10} positions. In the case of disordered feldspars, T_{1m}, T_{20}, and T_{2m} position would also be substituted, but in lesser extent than that of T_{10} sites, if a total disorder does not exist. After signal deconvolution of all lluminescence emissions, Figs. 1(e) and 1(f), their assignments, and the relative intensity of emission bands between glass-ceramic and mineral feldspar are summarized in Table 2. Regarding PL intensity, the most intense red emission, at about 696–697 nm, is 6 times higher in the glass-ceramic and it may correspond to Fe^{3+} on tetrahedral sites [21,22], as it has been discussed. Besides, some small emissions are found in the glass-ceramic in the range 656–685, which are probably caused by Fe^{3+} ions located at $T_1(m)$, $T_2(0)$, and $T_2(m)$ tetrahedral positions [23], which suggest that some degree of disorder in Si–Al distribution might occur. The differences in Fe^{3+} site occupancy together with alteration in the local crystalline field due to variations in chemical composition strongly influence the position and intensity of this peak [11,24]. These Fe^{3+}-related emissions have their origin in the presence of Fe_2O_3 in the precursors, both frit and kaolin, as it can be seen in Table 1. In order to check that iron oxide is presented in the glass-ceramic after sintering, an energy dispersive x-ray (EDX) analysis and x-ray fluorescence (XRF) are carried out (see Fig. S2, Tables S1 and S2 in Supplement 1). In addition, quartz emissions are found in the range 578–656 nm.

In the 335–500 nm range, feldspar emissions can be deconvoluted in five emission bands, which may be mainly attributed to $[AlO_4/alkali^+]$ or $[AlO_4]^0$ defects, and Al-O^--Al centers, according to Table 2. The first two types of defects are caused when Al^{3+} ion substitutes Si^{4+}, and then a positive charge is necessary to maintain local charge balance. If the positive charge is an alkali cation placed in adjacent positions to Al^{3+} cations, the center formed will be $[AlO_4/alkali^+]$, while if a hole is trapped, the resulting center will be an $[AlO_4]^0$ [20,22]. In the case of Al-O^--Al centers, also known as Löwenstein bridges, they are the most common structural defect in feldspars, and they occur, typically in the range 400–480 nm, when an oxygen hole center is adjacent to two Al^{3+} cations, one of them structural and the other one an Al^{3+} impurity [22,26–29]. This emission might also be related to Ti centers, whose corresponding emissions occur when Ti^{4+} is incorporated as Ti^{3+} in Al-sites, forming Al-O^--Ti bridges [26,29]. Both emission centers have been proposed in the bibliography as the origin of the blue luminescence in feldspars. In the case of a sodic plagioclase, substitution of Na^+ and Si^{4+} by Ca^{2+} and Al^{3+} take place regarding albite structure, which generate some Si–Al disorder and the formation of Al-O^--Al linkages, $[AlO_4/alkali^+]$ and $[AlO_4]^0$ centers might be favored [13].

Table 2. PL Emission Peaks, Excitation Wavelength (First Wavelength Corresponds to the Glass-Ceramic While the Second One to the Thermally Treated Mineral), Intensity Ratios, and Peak Assignments for Glass-Ceramic and Thermally Treated Mineral Feldspar Peaks

$\lambda_{glass\text{-}ceramic}$ (nm)	$\lambda_{mineral\ TT}$ (nm)	λ_{exc} (nm)	$I_{glass\text{-}ceramic}/I_{mineral\ TT}$	Assignment
356	366	322	4.5	quartz emission [25]
371	379	322	18.1	$[AlO_4/alkali^+]$ or $[AlO_4]^0$ [20,22]
388	390	322	5.4	$[AlO_4/alkali^+]$ or $[AlO_4]^0$ [20,22]
410	418	322	14.1	Al-O^--Al center [2627–28]
440	450	322	12.7	Al-O^--Al center [29,26]
578	–	355–356	–	oxygen vacancies in quartz [30]
600	599	355–356	4.9	quartz emission [25,31]
614	615	355–356	9.5	nonbridging oxygen hole center in quartz [32]
615	609	322	11.6	nonbridging oxygen hole center in quartz [32]
656	–	355–356	–	nonbridging oxygen hole center in quartz [32]
663	–	355–356	–	Fe^{3+} impurities on tetrahedral sites [23]
671	670	355–356	6.9	Fe^{3+} impurities on tetrahedral sites [23]
676	–	355–356	–	Fe^{3+} impurities on tetrahedral sites [23]
685	–	355–356	–	Fe^{3+} impurities on tetrahedral sites [21,22]
697	696	355–356	6.3	Fe^{3+} impurities on tetrahedral sites [21,22]

Research Article Vol. 6, No. 5 / May 2019 / Optica 672

Taking into account that the low content of Ti cations in the starting composition and that impurity centers such as transition metal elements (like Ti^{4+}) and rare-earth elements have narrower bandwidths than those created by defect centers, it can be concluded that the broad blue emissions observed in the glass-ceramic are mainly attributed to Al-O^--Al centers.

Emissions undergo shifts between both matrices, which might be due to the different crystal fields because of differences in crystallinity, which strongly affects luminescence [33]. It is observed that all emissions are much more intense in the glass-ceramic material, up to 18 times for emissions related to [AlO_4/alkali$^+$] or [AlO_4]^0 and up to 14 times for Al-O^--Al linkages, than in the thermally treated mineral. Differences in structure, microstructure, and crystallinity between the rare-earth-free glass-ceramic and the thermally treated mineral might be responsible for the enhancement of luminescence behavior displayed in Fig. 1. For this reason, a structural analysis is carried out hereafter.

B. Structural and Microstructural Study: XRD, FESEM, and TEM Study

Figure 2(a) shows the XRD pattern for the glass-ceramic, which indicates the major phase formation of a plagioclase in the glass-ceramic. XRD pattern may correspond to a Na-rich plagioclase (JCPDS Card no. 00-041-1480) or a calcium-rich (Ca-rich) plagioclase (JCPDS Card no. 00-041-1481). On account of the similarity of both XRD patterns and the overlapping of XRD peaks, it cannot be precisely identified by this technique if the major phase is sodium (albite) or CA-rich (anorthite) feldspar. However, Raman spectroscopy is a suitable tool for such purpose, since it does allow discriminating between phases in alkali feldspars [34]. The Raman spectrum of the micro-nanostructured glass-ceramic, taken on a microcrystal, is illustrated in Fig. 2(b). The two main Raman modes, typical of Raman spectra for feldspars, are those labelled as ν_a and ν_b in Fig. 2(b). Bersani *et al.* [35] have recently reported that the difference between peak position of ν_a and ν_b ($\Delta\nu_{ab} = \nu_a - \nu_b$) delimit the content of anorthite present in the samples. Samples with $\Delta_{ab} > 27$ cm^{-1} have an anorthite content <60 mol.%. In our case, $\Delta_{ab} = 32$ cm^{-1}, and therefore anorthite content is <60 mol.%. By comparison with spectral features of other plagioclases reported in literature [34,35], it is confirmed that the major phase of the micro-nanostructured glass-ceramic is a Na-rich plagioclase phase, and henceforth, it will be referred as Na-rich plagioclase-based glass-ceramic. The presence of SrO in the precursor frit (Table 1) permits the formation of the Na-rich plagioclase phase during the fast-sintering process by the devitrification process, although the frit only has a 2% of Na_2O [18]. In Fig. 2(a), it is also included the diffraction pattern of the raw and the thermally

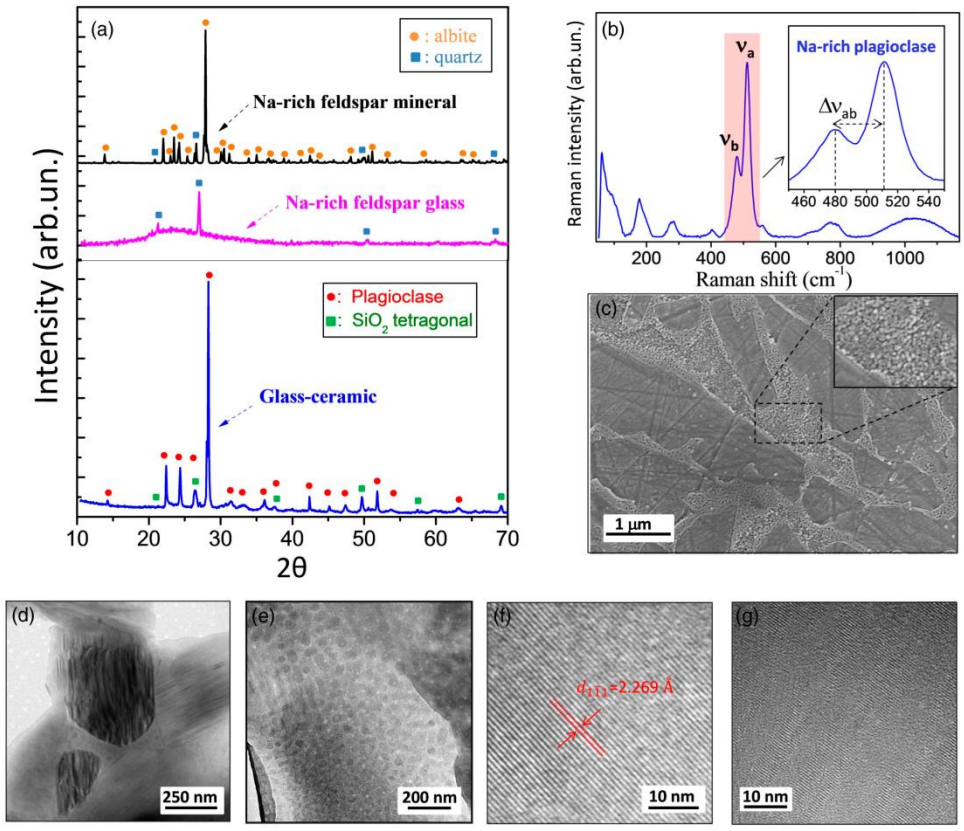

Fig. 2. Structural, microstructural, and morphological characterization of glass-ceramic and mineral Na-rich feldspar: (a) XRD pattern for Na-rich feldspar mineral (in black), Na-rich feldspar glass (in pink), and the glass-ceramic (in blue); (b) Raman spectrum of the glass-ceramic showing that Na-rich plagioclase is the major phase; (c) FESEM micrograph for glass-ceramic showing the presence of large microcrystals almost isolated by nanostructured regions; (d) TEM micrograph showing stripped patterns of microcrystals in addition of the appearance on nanocrystals in the nanostructured regions; (e) detailed presence of nanocrystals embedded in a glass matrix in the nanostructured regions; (f) HRTEM micrograph of a selected region in microcrystal with high crystallinity; and (g) HRTEM micrographs of microcrystals showing crystalline modulation of the interplanar spacing.

treated Na-rich feldspar mineral. The XRD pattern of the raw Na-rich feldspar mineral has a crystalline structure, which agrees with reflections of JCPDS Card no. 01-074-0603 that correspond to a low albite sample, although reflections appear slightly shifted to lower 2θ (see Fig. S3 in Supplement 1), which might be due to the presence of calcium and potassium in the structure (see Table 1), forming a ternary feldspar with albite as major phase. A shift to lower 2θ in the XRD pattern [36] is observed for the Na-rich feldspar mineral, since ionic radius of Ca^{2+} and K^{+} cations are higher than the one corresponding of Na^{+} cation. The incorporation of such cations in albite structure produces a crystal cell expansion. This fact justified the lack of luminescence in the raw mineral. However, when the raw mineral is thermally treated, a Na-rich feldspar glass is formed (and named as Na-rich feldspar glass henceforth), presenting a broad halo at low angles, characteristic of vitreous materials and some crystalline peaks corresponding to quartz phase, as can be seen in Fig. 2(a).

Both thermally treated materials are based on sodium aluminosilicate having quite a different crystallinity degree. Up to 1 magnitude order enhancement in luminescence emission may be originated by different factors: crystallinity, structure, and microstructure [17]. From the XRD pattern of glass-ceramic [Fig. 2(a)], the average crystallite size and the glassy phase content are determined, being 52 nm and only 6 vol. %, respectively [18], Crystallinity plays a very important role because, in glassy phase, there are many point defects that generate trapping sites and nonradiative recombinations as consequence, which will lead to lower luminescence [8,9]. The Na-rich feldspar glass possesses much more content of glassy phase than the glass-ceramic (about 55 vol. %), which might explain why the luminescent performance exhibited in the rare-earth-free glass-ceramic is higher. Moreover, structure and/or the microstructure of the Na-rich plagioclase-based glass-ceramic can be responsible of enhancement in luminescence.

From a mineralogical point of view, the glass-ceramic may be considered as an intermediate albite with high degree of Si–Al disorder [37]. The basic cell unit of its triclinic structure consists of rings of four tetrahedra [four symmetrically nonequivalent sites, designated as $T_1(0)$, $T_1(m)$, $T_2(0)$, and $T_2(m)$] [37,38]. As calcium content increases anorthite content, migration of Al^{3+} cations from $T_1(0)$ positions to $T_1(m)$, $T_2(0)$, and $T_2(m)$ positions might increase, regarding a low albite feldspar to obtain the local charge balance. Anorthitic structures are energetically more favorable for an Si–Al ordered structure. In contrast, when in albite the formation of Al-O^{-}-Al bridges is favoured, and therefore the structure is more likely to be disordered [13,35]. Besides, the presence of different Al^{3+} tetrahedral positions favor their substitution by Fe^{3+} impurities, which causes the increase of red luminescence [Fig. 1(d)]. Thus, first, it can be established that structure might play a key role in the enhancement of luminescence.

In the case of the Na-rich feldspar glass, luminescence comes from tetrahedral ring distortion, which is also presented in the glassy phase but not in an ordered arrangement at large scale, as in the glass-ceramic.

Figure 2(c) shows a FESEM micrograph of the rare-earth-free glass-ceramic having a unique dual microstructure, with elongated Na-rich plagioclase microcrystals surrounded by nanostructured regions that isolate microcrystals. However, the Na-rich feldspar glass does not have any microstructure due to its vitreous nature. A depth TEM analysis of the glass-ceramic feldspar [Figs. 2(d) and 2(e)] showed in detail the nanostructured region between two microcrystals. In these two microcrystals, it can be observed a striped pattern of ∼175–500 nm in width, alternating clear and dark zones. The difference in contrast in such microcrystals indicates compositional differences. These modulations resemble the spinodal decomposition, which is characteristic of some in feldspar minerals [39,40]. To the best of authors' knowledge, this has never been reported for synthetic plagioclases. Spinodal decomposition is used in different materials to enhance their properties, which may open a new research line in feldspar synthetic materials in order to look for new properties derived from such modulations [41,42]. Figure 2(e) shows a nanostructured region of the glass-ceramic having nanocrystals with an average diameter between 30–40 nm. A HRTEM image of Fig. 2(f) is performed on a microcrystal, according to the microstructure depicted in Fig. 2(c). It can be observed that is totally crystalline with three crystallographic directions presented, according to the spots of the corresponding FFT pattern (see Fig. S2a in Supplement 1). The indexing process allows identifying these spots with $(1\bar{5}2)$, $(2\bar{2}0)$, and $(11\bar{2})$ planes, which correspond to interplanar distances of 0.1840 nm, 0.3150 nm, and 0.3570 nm, respectively. These values are slightly different from those tabulated for albite, i.e., 0.1844 nm for $(1\bar{5}2)$, 0.3148 nm for $(2\bar{2}0)$, and 0.3504 nm for $(11\bar{2})$ [43]. This fact is supported by the presence of calcium and strontium in the composition, which may cause the distortion of the Na-rich plagioclase structures regarding the albite structure and consequently distortion in some crystallographic directions. Apart from these regions characterized by their crystallinity and homogeneity, there are some spinodal modulation regions where some crystallinity modulations are observed, as the HRTEM image of Fig. 2(g) depicts. The FFT pattern of this HRTEM image (see Fig. S2b in Supplement 1) reveals the presence of the (202) plane, which corresponds to an interplanar distance of 0.2006 nm [43] and the $(1\bar{1}1)$ plane. The latter exhibits a widened spot, which corresponds to interplanar spacing from 0.3824 nm to 0.3940 nm, indicating a slight gradual compositional variation. An inversed image of the $(1\bar{1}1)$ spot (see Fig. S2c in Supplement 1) revealed that this compositional modulation is composed of alternate crystalline and noncrystalline regions.

This unique micro-nanostructure is originated from both the formation process and the composition. As consequence, the enhanced luminescence seems to have a strong dependence on such crystal modulations. In order to deepen this study and evaluate the influence of the micro-nanostructure in the enhancement of the luminescence of this new synthetic material, the importance of the nanostructuration in the luminescence emission is studied by means of quenching experiments. Luminescent nanoparticles present quantum confinement effects, which leads to novel optoelectronic properties. However, nanosized phosphors usually have a larger defect number because of a larger surface-to-volume ratio, which sometimes leads to a decrease of quantum efficiency [3].

In the micrographs of Figs. 3(a)–3(c) (and Figs. S5a–S5c in Supplement 1), it might be observed the evolution of the glass-ceramic microstructure for different thermal treatments. At 1100°C [Figs. 3(a) and S5a], large isolated microcrystals in a glass matrix are formed. For quenched samples at 1220°C [Figs. 3(b) and S5b], nanocrystals nucleate at the glassy phase but are agglomerated and not well formed yet. However, it is during the cooling when the nanostructure comes to settle the whole sample, isolating microcrystals between each other [Figs. 3(b)–3(c) and S5

Research Article Vol. 6, No. 5 / May 2019 / Optica 674

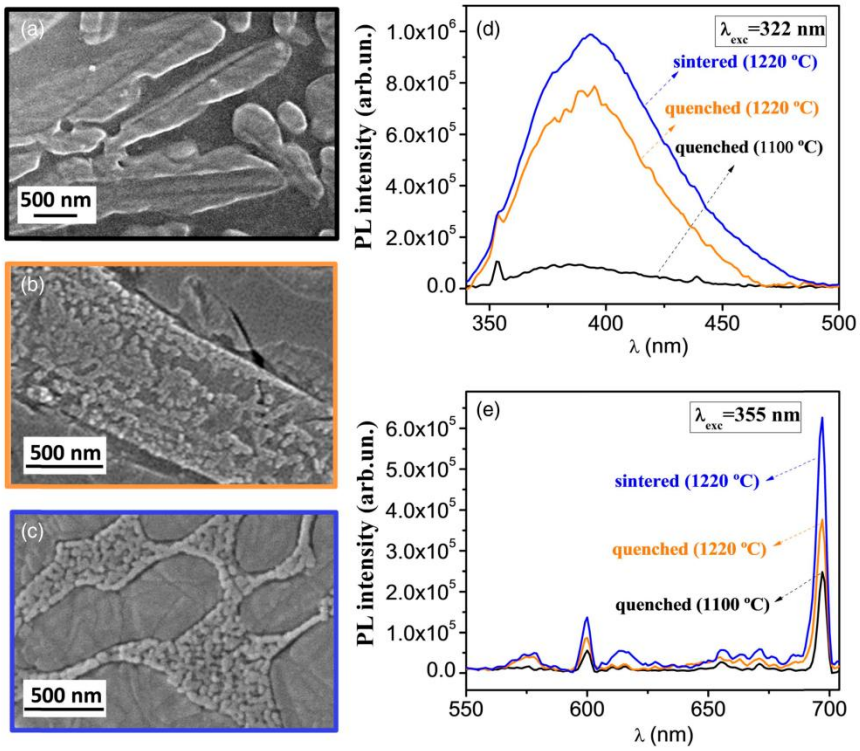

Fig. 3. Processing dependence of luminescence in glass-ceramics: FESEM micrographs for glass-ceramic for different thermal treatments: (a) 1100°C and quenched, (b) 1220°C and quenched, and (c) 1220°C and slow cooled. Emission spectra for glass-ceramic thermally treated at 1100°C and quenched (in black), at 1220°C and quenched (in orange), and at 1220°C and slow cooled (in blue) are showed for different excitation wavelengths: (d) $\lambda_{exc} = 322$ and (e) $\lambda_{exc} = 355$ nm.

b–S5c]. Figure S6 of Supplement 1 shows the XRD pattern for these three samples. At 1100°C, the plagioclase crystallization has already produced, and it is possible to observe the well-defined XRD pattern, with a very low amount of glassy phase. In addition, tetragonal SiO_2 also appears. For the quenched sample at 1220°C, the XRD pattern is very similar to the one quenched at 1100°C; however, the diffraction peak intensities increases, which indicates higher crystallinity. Finally, in the XRD pattern of the sample sintered at 1220°C for 6 min, the Na-rich plagioclase diffraction pattern with higher crystallinity can be observed.

Figures 3(d) and 3(e) depict the luminescence emission under an excitation at 322 nm and 355 nm, respectively. At 322 nm, structural defects of the glass-ceramic are the main responsibility of the emission. In this case, band emission at ~350–500 nm considerably rises as nanostructuration is formed. The luminescence intensity increases up to 1 magnitude order when the glassy region transforms in a nanostructure region in glass-ceramic feldspar sintered at 1220°C and slowly cooled. It is also illustrated as a general feature, that the enhancement of luminescent is correlated with the appearance of nanostructured regions. The development of a dual microstructure is a key factor for such micronanostructural evolution. However, it may be taking into account that the nanocrystal region occurs in the presence of microcrystal that shows compositional modulations, that is, the plagioclase structure is defective.

Fe^{3+} as well as some emissions related to quartz are excited at 355 nm. Red emission placed at 697 nm increases around 1.5 times when the nanostructure starts to appear (quenched at 1220°C) and 2.5 times when all the micro-nanostructure is developed (sintered at 1220°C) regarding when only Na-rich plagioclase microcrystals are presented in the sample (quenched at 1100°C). Red luminescence improvement with the micro-nanostructure is less noticeable than UV–blue emission, which suggests that structural defects such as Al-O^--Al linkages and alkali cations placed adjacent to Al^{3+} cations evolved during the slow cooling as consequence of almost complete devitrification of the glass-ceramic feldspars.

C. Cathodoluminescence Reveals the Appearance of Luminescence in Fast-Sintered Glass-Ceramics

CL coupled to a SEM microscope for fast-sintered glass-ceramic is presented in Fig. 4. Although the SEM resolution in Fig. 4(a) is not as high as in FESEM micrographs, Fig. 2 and 3, the main features of the elongated microcrystals almost isolated in a matrix are observed. The micrograph resolution does not resolve the nanoparticles in the matrix, but the location of such regions are well defined in previous FESEM measurements, being between microcrystals. Therefore, measurements in these two regions were carried out.

Figure 4(b) shows an average SEM-CL spectrum for both the microcrystal and the nanocrystals regions. The spectra are measured from 250 to 800 nm in order to compare both CL emissions. CL intensity for nanocrystals is slightly lower than for microcrystals, which might be associated by a larger scattering of the nanoregions because of a larger surface-to-volume ratio.

Research Article Vol. 6, No. 5 / May 2019 / Optica 675

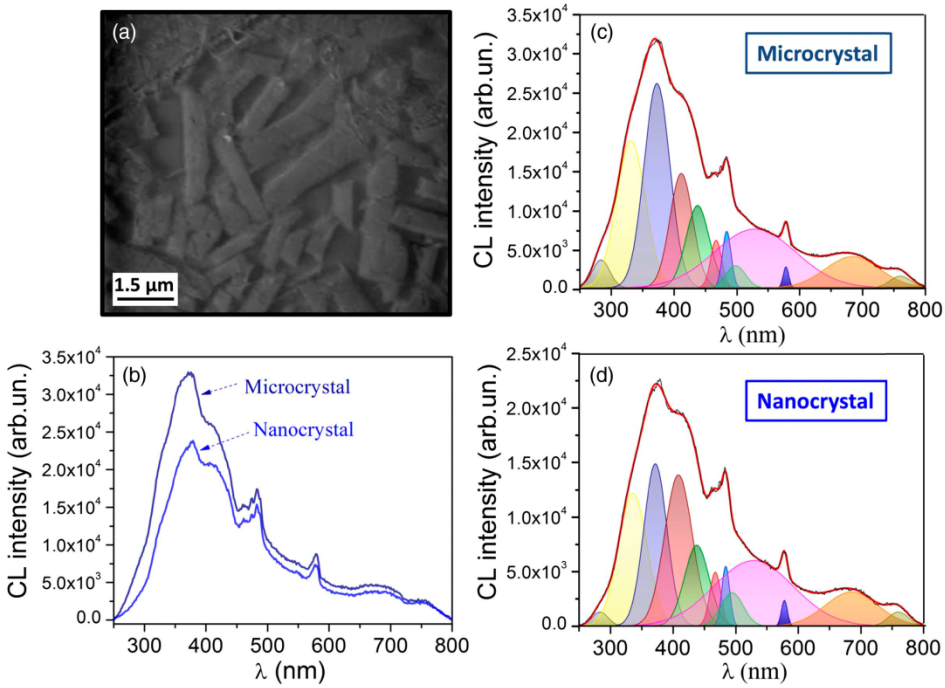

Fig. 4. Microscopic analysis of the cathodoluminescence occurrence: (a) SEM-CL micrograph of micro-nanostructured fast-sintered glass-ceramic; (b) characteristic SEM-CL spectra for microstructured and nanostructured regions; and (c), (d) the corresponding deconvolutions of CL spectra for microcrystals and nanocrystals, respectively, showing different emission bands associated with defects tabulated in Table 3.

The deconvolution of both spectra is plotted in Figs. 4(c) and 4(d). The emission peaks obtained from the deconvolution of the CL curve for nanocrystals and microcrystals are similar, and they are summarized in Table 3. However, some wavelength shifts between them are observed, as well relevant differences in the area contribution of some of the emission peaks (Table 3).

The glass-ceramic presents several emission peaks that correspond to structural defects such as Al-O^--Al bond and [AlO_4/alkali$^+$] or [AlO_4]^0 centers. The first emission peak at around 284 nm is a UV emission that has been reported for high albite plagioclases, which is probably caused by a defect site associated with a sodium feldspar lattice structure [28]. Additionally, emission peaks at ca. 331 nm and ca. 336 nm may be associated with strained Si–O bonds in feldspars [44,45]. The presence of hole trapped in nonbridging oxygen or Si–O bond defects can be responsible for these UV emissions [44,45]. The UV luminescence emissions at ca. 372 nm and ca. 373 nm are the most intense ones and are described as [AlO_4/alkali] or [AlO_4]^0 centers. Emissions in the range of 409–484 nm are mainly attributed to Al-O^--Al defect centers [22,26–29]. However, according to the low spectral contribution displayed in Figs. 4(c) and 4(d) [26,29], the emission bands at ca. 466 nm for microcrystals and ca. 465 nm for nanocrystals could be also related to Ti centers. The emissions peaks in the range of 494–529 nm are probably associated with a hole on oxygen adjacent to a divalent impurity (Si – O^-…M^{2+}), as it was suggested that this kind of center is

Table 3. Assignment of the Main Emission Peaks: CL Emission Peak Positions of Deconvoluted Spectra for Microcrystals and Nanocrystals in the Glass-Ceramic[a]

λ_{micro} (nm)	λ_{nano} (nm)	$Area_{nano}/Area_{micro}$	Assignment
284	284	0.5	defect site in a Na-feldspar lattice structure [28]
331	336	0.9	defects in Si–O strained structures [44,45]
373	372	0.7	[AlO_4/alkali$^+$] or [AlO_4]^0 [20,22]
412	409	1.6	Al-O^--Al center [2627–28]
437	438	1.0	Al-O^--Al center [29,26]
467	467	1.1	Ti or Al-O^--Al center [29,26]
484	484	1.0	Al-O^--Al center [29,26]
498	494	1.7	Si-O^-…M^{2+} with M = Mg or Zn [11]
529	529	1.1	Si-O^-…M^{2+} with M = Mg or Zn [11]
578	578	1.3	oxygen vacancies in quartz [30]
684	685	1.1	Fe^{3+} → Fe^{2+} impurities [21,22]
760	760	1.2	Fe^{3+} impurities on T_1 sites [26]

[a]The $Area_{nano}/Area_{micro}$ ratio and the emission peak assignments according to referenced defect are also summarized.

Research Article Vol. 6, No. 5 / May 2019 / Optica 676

stabilized by a divalent metal ion, M^{2+}, in a T site adjacent to the oxygen [11]. The most likely cations are Sr^{2+}, Mg^{2+}, or Zn^{2} according to the glass-ceramic chemical composition [11,19]. Emission peak at ca. 578 nm is assigned to oxygen vacancies in a quartz-type structure [30]. Emissions peaks at ca. 684 nm and ca. 685 nm, corresponding to Fe^{2+} cations, are consequence of the irradiation with a high-energy electron, accelerated at 30 keV, that reduces Fe^{3+} cations into Fe^{2+} cations. Additionally, emission peaks at ca. 684 nm and ca. 685 nm can be related to lattice defects, such as broken Si–O bonds [46]. Finally, red emissions at 760 nm are assigned to Fe^{3+} cations in Al^{3+} tetrahedral sites, probably in $T_1(0)$ positions, as is found in other albite-rich feldspars [26].

As well, main CL emissions registered are quite broad, which indicates that the electron transitions occur in energy levels, which are influenced by the local crystal field. The wavelength shifts observed in some emission peaks for the microstructure and nanostructure regarding each other revealed the strong influence of the host crystal. The fast-sintered glass-ceramic generate structural strains according with the micro-nanostructure analysis that the revealed regions have variation of alkali–alkaline earth cations, which modulated the crystal field in the material. These modulations of the crystal field are on the origin of the enhancement of luminescence emission measured [24,47]. The area ratio between nanocrystals and microcrystals for each CL peak is presented in Table 3. The most relevant contributions are related to intrinsic oxygen defects such as Löwenstein bridges or $Si\text{-}O^{-}\ldots M^{2+}$ defects, which possess a more considerable weight in the emissions of the nanocrystal regions than in the microcrystal emissions. These oxygen defects seem to be a clear distinctive between both parts, which may indicate that charge might be accumulated preferentially in nanostructured regions instead of microcrystals. Defects related to $[AlO_4/alkali^{+}]$ or $[AlO_4]^{0}$ centers (~ 372–373 nm) are also remarkable, and their contribution in microcrystals is more relevant than in nanocrystal regions, and finally, structural defects at ca. 331 nm for microcrystals and ca. 336 nm for nanocrystals are also relevant luminescent centers. The defects related to impurities as Fe cations show also a higher contribution to the luminescence. The recombinative centers created by Fe cations give a considerable red emission, being also somewhat higher for nanocrystals than for microcrystals.

To sum up, microcrystals and nanocrystal regions contribute similarly to luminescence of this rare-earth-free glass-ceramic, although they present a different density of defects. Therefore the hypothesis that nanostructured areas may responsible for the luminescence enhancement is not supported. The CL analysis revealed that both the micro and the nanoregions contributed the enhancement of the luminescence in comparison with feldspar glass.

D. NMR Study: Identification of Structural Defects Responsible for Luminescence in Fast-Sintered Glass-Ceramics

The presence of Si–Al disorder, Al-O^{-}-Al bonds, and alkali cations adjacent to Al^{3+} cation is responsible in feldspar glass-ceramics for enhancement of luminescence emissions. In order to stablish if a correlation exists between Si–Al disorder and the defects, NMR measurements are carried out. Figure 5 shows the ^{29}Si NMR spectrum for the precursor frit [Fig. 5(a)] and the micro-nanostructured glass-ceramic [Fig. 5(b)], whose analysis allows obtaining information about electronic environment around Si sites.

^{29}Si NMR spectrum of the frit [Fig. 5(a)] exhibits a broad band, from −65 to −125 ppm approximately with a maximum at ~ − 92 ppm. The different polymerization state in which silicon is found in the vitreous network of the precursor frit might be inferred from the deconvolution of it spectrum. ^{29}Si NMR peaks are tabulated in Table 4 in addition to the area contribution of each band and the corresponding Qn assignment. According to bibliography [48,49], chemical shift values from −66 ppm to −74 ppm are assigned to Q0 units in the ^{29}Si NMR spectrum. Bands in the range of −82 to −75 ppm correspond to Q1 units, and in the range of −86 to −84 ppm correspond to Q2 units. Q3 units appear in the range of −101 to −90 ppm while Q4 groups provide bands in the range from −120 to −103 ppm. Q3 species are the major contribution with around 86% of the total area, as indicated in Table 4.

The deconvoluted ^{29}Si NMR spectrum for the micro-nanostructured glass-ceramic is shown in Fig. 5(b). Chemical shift peaks tabulated at −71.0 ppm and −66.7 ppm might be associated to Q_0 units, peaks at −79.3 ppm and −75.4 ppm correspond to Q_1 units, and peaks at −109.4 ppm to Q_4 units, all of them arising from the parent glass. The small quantity of glassy phase in the highly crystalline glass-ceramic, previously discussed by XRD measurements, is also evinced by NMR, because of the small area contribution of these associated bands. The other peaks mainly correspond to Q_4 units of the Na-rich plagioclase with the exception of the peak located at ~ − 85 ppm, which is associated to Q_4(4Al), characteristic of anorthite-like sites [50,51]. The peak at ~ − 89 ppm may be associated to T_2(3Al) site of albite structure,

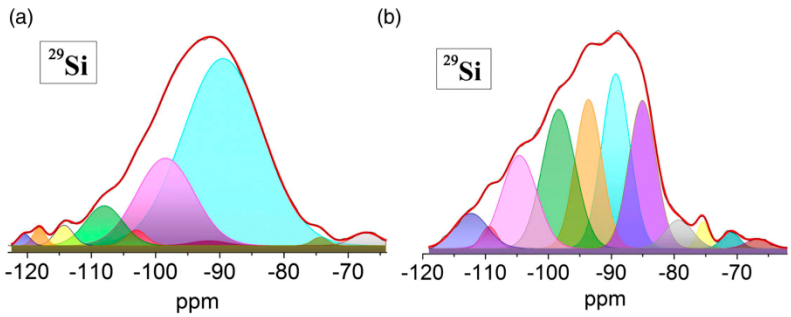

Fig. 5. Structural evolution of ^{29}Si NMR spectra with crystallization: (a) the precursor frit and (b) the micro-nanostructured glass-ceramic sintered at 1220°C and slow cooled. Deconvolution of ^{29}Si NMR spectrum in different chemical shift peaks is shown by colored peaks indicating a different polymerization state of Q_n units (assignment of chemical shift peak is summarized in Table 4).

Table 4. Assignments of Deconvoluted ^{29}Si NMR Spectrum: Chemical Shift (ppm), Area Contribution (%), and Assignment for Each Deconvoluted Band of the ^{29}Si NMR Spectrum for the Precursor Frit and the Micro-Nanostructured Glass-Ceramic Sintered at 1220°C and Slow Cooled[a]

Precursor Frit			Micro-Nanostructured Glass-Ceramic		
Chemical Shift (ppm)	Area Contribution (%)	Q_n Unit Assignment	Chemical Shift (ppm)	Area Contribution (%)	Site Assignment
−67.1	1.6	Q_0	−66.7	0.9	Q_0 unit (glass)
−73.9	0.6	Q_0	−71.0	1.2	Q_0 unit (glass)
−89.5	64.5	Q_3	−75.4	1.3	Q_1 unit (glass)
−91.7	0.7	Q_3	−79.3	3.3	Q_1 unit (glass)
−98.5	21.6	Q_3	−85.0	16.8	Q_4(4Al) (*)
−103.0	1.4	Q_4	−89.3	20.5	T_2 (3Al)
−108.0	6.4	Q_4	−93.6	16.7	T_{2m} (2Al)
−114.3	1.6	Q_4	−98.3	19.2	T_{20} (1Al)
−118.1	1.0	Q_4	−104.6	13.7	T_{1m} (1Al)
−120.5	0.6	Q_4	−109.4	1.5	Q_4 unit (glass)
–	–	–	−112.3	4.9	T_1 (0Al)

[a]Area contribution shows that Q_3 species are the major one in the precursor frit and Q_4 species are the major one in the case of glass-ceramic. (*) indicates an anorthite-like site. The rest of tabulated positions between −112.3 ppm to −89.3 ppm correspond to albite-like sites.

typically placed in the range from −91 to −87 ppm in plagioclases [51]. The rest of peaks located at −112.3, −104.6, −98.3, and −93.6 ppm match well with albite-like sites corresponding to T_1(4Si, 0Al) T_1m(3Si, 1Al), T_{20}(3Si, 1Al), and T_{2m}(2Si, 2Al) positions, respectively [50–52]. Chemical shifts registered for the synthetic glass-ceramic slightly differ from reported values in bibliography for natural minerals, as occurred with luminescence emission. This fact is due to the presence of different elements such as calcium, strontium, and in lesser extent potassium, which act as lattice disruptors in the Na-rich plagioclase structure regarding a pure albite and consequently change bond distances and resonances.

In a low albite, the most ordered kind of albite, Si is placed in $T_1(m)$, $T_2(0)$, and $T_2(m)$ sites while Al in $T_1(0)$ and the corresponding ^{29}Si NMR spectrum exhibit three bands of equal intensity [51]. However the ^{29}Si NMR spectrum of the rare-earth-free glass-ceramic [Fig. 5(b)] presents more bands, with different width and intensity and even overlapping each other, which indicates that Si neighbors have considerably changed with regard to an ordered state [53]. Moreover, the presence of T_2(3Al) and T_1(0Al) sites in albite-like domains corroborate that a Si–Al disorder distribution is presented. It can be stablished a perfect correlation between Si–Al disorder and formation of luminescent centers, such as Al-O$^-$-Al bonds and alkali adjacent to Al^{3+} tetrahedra, which has been proved to be crucial to display an enhanced luminescent behavior. In addition, the high crystallinity of the glass-ceramic regarding the Na-rich feldspar glass favors this luminescent enhancement. Therefore, structure carried out a decisive role in such improvement of luminescence while microstructure is related to the processing that modulated such structure. The occurrence of two devitrification steps, first the appearance at 1100°C of microcrystal and second the nucleation of nanocrystal at 1220°C that extend during the slow cooling process are responsible to keep such Si–Al disorder. Moreover, the presence of different alkaline and alkaline-earth cations favor both the deformation and interplanar spacing that contribute to the modulations of crystal field.

It is worth mentioning that the strong relation between luminescence and structural disorder in this novel family of rare-earth-free luminescent materials opens the topic toward the tailoring of feldspar structure by incorporating compositional variations or dopants. Further advances in rare-earth-free luminescence materials will be attempted based in inducing structural disorder at long range in feldspar structures and therefore enhancing and tuning the corresponding luminescence emissions.

4. CONCLUSION

Novel rare-earth-free glass-ceramic-based phosphor with high luminescence has been designed by a scalable approach based on a conventional ceramic process. This novel phosphor is rich in Na-plagioclase feldspar crystallizations and presents high crystallinity, ~94%, along with a unique micro-nanostructure developed by a fast-sintering process. TEM and HRTEM analyses reveal the coexistence of compositionally homogeneous microcrystals and some others, which present compositional inhomogeneities, manifested by spinodal decomposition modulations.

In this work, luminescence of a novel rare-earth-free glass-ceramic based on feldspar crystallizations has been deeply studied for the first time, to the best of our knowledge. CL, ^{29}Si NMR measurements, and quenching experiments show that structure has a key role in the luminescence behavior of this novel phosphor. Structural disorder in Si–Al distribution favors the formation of several luminescent centers, namely, Al-O$^-$-Al bonds, [AlO_4/alkali$^+$] and [AlO_4]^0, that result in an increase of 1 magnitude order in the broad UV–blue PL emission exhibited and around 6 times in the red luminescence regarding a Na-rich feldspar glass obtained from a mineral source. Moreover, the high crystallinity of the glass-ceramic also favors such luminescent enhancement.

It should be noticed that the results obtained in this work for a new class of micro-nanostructured rare-earth-free phosphors can be considered as a reference for future works in this research topic, since through a suitable compositional modification, a rise of structural disorder may be obtained. Consequently, luminescent emissions could be tuned and increased. Further advances in glass-ceramic feldspar to improve its luminescence behavior would be technologically very relevant for applications such as security markers or light-emitting glasses.

Funding. Ministerio de Economía y Competitividad (MINECO) (MAT2017-86450-C4-1-R, PTQ- 14-07289).

Acknowledgment. The authors express their thanks to B. Galiana and M. J. De la Mata for their contributions in carrying out TEM and NMR measurements, respectively.

See Supplement 1 for supporting content.

REFERENCES

1. C. Feldmann, T. Jüstel, C. R. Ronda, and P. J. Schmidt, "Inorganic luminescent materials: 100 years of research and application," Adv. Funct. Mater. **13**, 511–516 (2003).
2. D. Ehrt, "Photoluminescence in glasses and glass ceramics," IOP Conf. Ser. Mater. Sci. Eng. **2**, 012001 (2009).
3. R. E. Rojas-Hernandez, F. Rubio-Marcos, A. Serrano, A. D. Campo, and J. F. Fernandez, "Precise tuning of the nanostructured surface leading to the luminescence enhancement in $SrAl_2O_4$ based core/shell structure," Sci. Rep. **7**, 1–9 (2017).
4. P. G. G. Slaats, G. J. Dirksen, and G. Blasse, "Luminescence of some activators in synthetic potassium feldspar crystals," Mater. Chem. Phys. **30**, 19–23 (1991).
5. M. Karbowiak, A. Mech, A. Bednarkiewicz, W. Stręk, and L. Kępiński, "Comparison of different $NaGdF_4:Eu^{3+}$ synthesis routes and their influence on its structural and luminescent properties," J. Phys. Chem. Solids **66**, 1008–1019 (2005).
6. N. C. George, K. A. Denault, and R. Seshadri, "Phosphors for solid-state white lighting," Annu. Rev. Mater. Res. **43**, 481–501 (2013).
7. G. Boulon, "Luminescence in glassy and glass ceramic materials," Mater. Chem. Phys. **16**, 301–347 (1987).
8. M. Nikl, J. A. Mares, E. Mihokova, K. Nitsch, N. Solovieva, V. Babin, A. Krasnikov, S. Zazubovich, M. Martini, A. Vedda, P. Fabeni, G. P. Pazzi, and S. Baccaro, "Radio- and thermoluminescence and energy transfer processes in Ce^{3+}(Tb^{3+})-doped phosphate scintillating glasses," Radiat. Meas. **33**, 593–596 (2001).
9. G. P. Pazzi, P. Fabeni, C. Susini, M. Nikl, E. Mihokova, N. Solovieva, K. Nitsch, M. Martini, A. Vedda, S. Baccaro, A. Cecilia, and V. Babin, "Defect states induced by UV-laser irradiation in scintillating glasses," Nucl. Instrum. Methods Phys. Res. Sect. B **191**, 366–370 (2002).
10. O. Dymshits, M. Shepilov, and A. Zhilin, "Transparent glass-ceramics for optical applications," MRS Bull. **42**(3), 200–205 (2017).
11. D. Barbin, V. Pagel, M. Blanc, and P. Ohnenstetter, *Cathodoluminescence in Geosciences* (Springer, 2000).
12. A. S. Marfunin, *Spectroscopy, Luminescence and Radiation Centers in Minerals* (Springer, 1979).
13. A. Putnis, "The crystal structure of minerals II—silicates," in *An Introduction to Mineral Sciences* (Cambridge University Press, 1992), pp. 141–184.
14. J. E. Contreras and E. A. Rodríguez, "Nanostructured insulators—a review of nanotechnology concepts for outdoor ceramic insulators," Ceram. Int. **43**, 8545–8550 (2017).
15. X. Cui, Y. Cheng, H. Lin, F. Huang, Q. Wu, and Y. Wang, "Size-dependent abnormal thermo-enhanced luminescence of ytterbium-doped nanoparticles," Nanoscale **9**, 13794–13799 (2017).
16. G. H. Beall and L. R. Pinckney, "Nanophase glass-ceramics," J. Am. Ceram. Soc. **82**, 5–16 (1999).
17. N. Joffin, J. Dexpert-Ghys, M. Verelst, G. Baret, and A. Garcia, "The influence of microstructure on luminescent properties of Y_2O_3:Eu prepared by spray pyrolysis," J. Lumin. **113**, 249–257 (2005).
18. V. Fuertes, M. J. Cabrera, J. Seores, D. Muñoz, J. F. Fernández, and E. Enríquez, "Hierarchical micro-nanostructured albite-based glass-ceramic for high dielectric strength insulators," J. Eur. Ceram. Soc. **38**, 2759–2766 (2018).
19. E. Enríquez, V. Fuertes, M. J. Cabrera, J. Seores, D. Muñoz, and J. F. Fernández, "New strategy to mitigate urban heat island effect: energy saving by combining high albedo and low thermal diffusivity in glass ceramic materials," Sol. Energy **149**, 114–124 (2017).
20. J. Garcia-Guinea, P. D. Townsend, L. Sanchez-Munoz, and J. M. Rojo, "Ultraviolet-blue ionic luminescence of alkali feldspars from bulk and interfaces," Phys. Chem. Miner. **26**, 658–667 (1999).
21. Y. Kirsh and P. D. Townsend, "Speculations on the blue and red bands in the TL emission spectrum of albite and microcline," Int. J. Radiat. Appl. Instrum. Part D **14**, 43–49 (1988).
22. V. Correcher, J. Garcia-Guinea, L. Sanchez-Muñoz, and T. Rivera, "Luminescence characterization of a sodium-rich feldspar," Radiat. Eff. Defects Solids **162**, 709–714 (2007).
23. M. Ostrooumov, *Amazonite : Mineralogy, Crystal Chemistry, and Typomorphism* (Elsevier, 2016).
24. M. R. Krbetschek, J. Götze, G. Irmer, U. Rieser, and T. Trautmann, "The red luminescence emission of feldspar and its wavelength dependence on K, Na, Ca—composition," Mineral. Petrol. **76**, 167–177 (2002).
25. W. J. Rink, H. Rendell, E. A. Marseglia, B. J. Luff, and P. D. Townsend, "Thermoluminescence spectra of igneous quartz and hydrothermal vein quartz," Phys. Chem. Miner. **20**, 353–361 (1993).
26. M. Kayama, S. Nakano, and H. Nishido, "Characteristics of emission centers in alkali feldspar: a new approach by using cathodoluminescence spectral deconvolution," Am. Mineral. **95**, 1783–1795 (2010).
27. D. J. Huntley, D. I. Godfrey-Smith, and E. H. Haskell, "Light-induced emission spectra from some quartz and feldspars," Int. J. Radiat. Appl. Instrum. Part D **18**, 127–134 (1991).
28. M. L. Clarke and H. M. Rendell, "Infra-red stimulated luminescence spectra of alkali feldspars," Radiat. Meas. **27**, 221–236 (1997).
29. S. Maki, S. Ohgo, and H. Nishido, "Cathodoluminescence characterization of feldspar minerals from granite-syenite rocks in Iwagijima Island, Ehime Prefecture, Japan," Naturalistae **538**, S13–S16 (2016).
30. J. Götze, "Defect structure and luminescence behaviour of agate—results of electron paramagnetic resonance (EPR) and cathodoluminescence (CL) studies," Mineral. Mag. **63**(2), 149–163 (1999).
31. M. A. Kasymdzhanov and P. K. Khabibullaev, "Nanosecond duration broadband luminescence of quartz glasses," Turkish J. Phys. **22**, 475–480 (1998).
32. J. Götze, M. Plötze, and D. Habermann, "Origin, spectral characteristics and practical applications of the cathodoluminescence (CL) of quartz—a review," Mineral. Petrol. **71**, 225–250 (2001).
33. L. Wondraczek, S. Krolikowski, and P. Nass, "Europium partitioning, luminescence re-absorption and quantum efficiency in (Sr, Ca) åkermanite–feldspar bi-phasic glass ceramics," J. Mater. Chem. C **1**, 4078–4086 (2013).
34. J. Freeman, E. Kuebler, L. Jolliff, and A. Haskin, "Characterization of natural feldspars by Raman spectroscopy for future planetary exploration," Canad. Mineral. **46**, 1477–1500 (2008).
35. D. Bersani, I. Aliatis, M. Tribaudino, L. Mantovani, A. Benisek, M. A. Carpenter, G. D. Gatta, and P. P. Lottici, "Plagioclase composition by Raman spectroscopy," J. Raman Spectrosc. **49**, 684–698 (2018).
36. V. Fuertes, A. Mariscal, R. Serna, F. J. Mompeán, M. García-Hernández, J. F. Fernández, and E. Enríquez, "Multifunctional ZnO/Fe-O and graphene oxide nanocomposites: enhancement of optical and magnetic properties," J. Eur. Ceram. Soc. **37**, 3747–3758 (2017).
37. V. F. de la Llave, A. del Campo, J. F. Fernández, and E. Enríquez, "Structural insights of hierarchically engineered feldspars by confocal Raman microscopy," J. Raman Spectrosc. (2019) https://doi.org/10.1002/jrs.5556 (early view).
38. I. Aliatis, E. Lambruschi, L. Mantovani, D. Bersani, S. Andó, G. Diego Gatta, P. Gentile, E. Salvioli-Mariani, M. Prencipe, M. Tribaudino, and P. P. Lottici, "A comparison between ab initio calculated and measured Raman spectrum of triclinic albite ($NaAlSi_3O_8$)," J. Raman Spectrosc. **46**, 501–508 (2015).
39. A. Putnis, "Transformation processes in minerals I: exsolution," in *An Introduction to Mineral Sciences* (Cambridge University Press, 1992), pp. 333–384.
40. L. Sánchez-Munõz, A. Del Campo, and J. F. Fernández, "Symmetry constraints during the development of anisotropic spinodal patterns," Sci. Rep. **6**, 1–10 (2016).
41. M. U. Kim, J. P. Ahn, H. K. Seok, E. Fleury, H. J. Chang, D. H. Kim, P. R. Cha, and Y. C. Kim, "Application of spinodal decomposition to produce metallic glass matrix composite with simultaneous improvement of strength and plasticity," Met. Mater. Int. **15**, 193–196 (2009).
42. S. U. Rehman, Q. Jiang, W. Lei, L. He, Q. Tan, Q. Quan, L. Wang, M. Zhong, S. Ma, A. Ul Haq, and Z. Zhong, "Improved microstructure and magnetic properties of Alnico 8 Alloys by B-doping," IEEE Trans. Magn. **54**, 1–6 (2018).
43. L. Van Der Plas, "The x-ray powder patterns of feldspars," in *Developments in Sedimentology* (Elsevier, 1966), Vol. **6**, pp. 211–212.
44. J. Garcia-Guinea, V. Correcher, L. Sanchez-Muñoz, A. A. Finch, D. E. Hole, and P. D. Townsend, "On the luminescence emission band at 340 nm of stressed tectosilicate lattices," Nucl. Instrum. Methods Phys. Res. Sect. A **580**, 648–651 (2007).

45. A. Aparicio and M. Á. Bustillo, "Cathodoluminescence spectral characteristics of quartz and feldspars in unaltered and hydrothermally altered volcanic rocks (Almeria, Spain)," Spectrosc. Lett. **45**, 104–108 (2012).
46. D. K. Richter, T. Götte, and D. Habermann, "Cathodoluminescence of authigenic albite," Sediment. Geol. **150**, 367–374 (2002).
47. J. Götze, "Potential of cathodoluminescence (CL) microscopy and spectroscopy for the analysis of minerals and materials," Anal. Bioanal. Chem. **374**, 703–708 (2002).
48. O. V. Filonenko, V. S. Kuts, M. I. Terebinska, and V. V. Lobanov, "Quantum chemical calculation of ^{29}Si NMR spectrum of silicone dioxide fullerene-like molecules," Chem. Phys. Technol. Surf. **6**, 263–268 (2015).
49. K. J. D. MacKenzie and E. S. Mark, *Multinuclear Solid-State NMR of Inorganic Materials* (Pergamon, 2002).
50. R. J. Kirkpatrick, R. A. Kinsey, K. A. Smith, D. M. Henderson, and E. Oldfields, "High resolution solid-state sodium-23, aluminum-27, and silicon-29 nuclear magnetic resonance spectroscopic reconnaissance of alkali and plagioclase feldspars," Am. Mineral. **70**, 106–123 (1985).
51. R. J. Kirkpatrick, M. A. Carpenter, W. H. Yang, and B. Montez, "^{29}Si magic-angle NMR spectroscopy of low-temperature ordered plagioclase feldspars," Nature **325**, 236–238 (1987).
52. W. H. Yang, R. J. Kirkpatrick, and D. M. Henderson, "High-resolution ^{29}Si, ^{27}Al and ^{23}Na NMR spectroscopic study of Al-Si disordering in annealed albite and oligoclase," Am. Mineral. **71**, 712–726 (1986).
53. L. Sanchez-Muñoz, L. Nistor, G. Van Tendeloo, and J. Sanz, "Modulated structures in $KAlSi_3O_8$: a study by high resolution electron microscopy and ^{29}Si MAS-NMR spectroscopy," J. Electron Microsc. **47**, 17–28 (1998).

Supplementary Material 1

optica

Enhanced luminescence in rare-earth-free fast-sintering glass-ceramic: supplementary material

V. FUERTES*[1], J. F. FERNÁNDEZ[1], E. ENRÍQUEZ[2]

[1] Electroceramics Department, Instituto de Cerámica y Vidrio, CSIC, Kelsen 5, 28049, Madrid, Spain
[2]Centro Tecnológico Vidres, S.L., Ctra. Onda, Km 3.4, 12540 Villareal, Castellón, Spain
*Corresponding author: vfuertes@icv.csic.es

Published 16 May 2019

This document provides supplementary information to "Enhanced luminescence in rare-earth-free fast-sintering glass-ceramic," https://doi.org/10.1364/OPTICA.6.000668.

I. Room temperature photoluminescence spectra in Na-rich feldspar mineral

Figure S1 depicts the photoluminescence behavior of the Na-rich feldspar mineral at room temperature. Figure S1a shows the excitation spectrum, which registers three main bands: two narrow bands centered at 268 nm and at 323 nm and a broad band centered at 284 nm. The corresponding photoluminescence emission is measured exciting at these wavelengths, and it is depicted in figures S1b-d, respectively. In all of the cases, the broad band presented in the glass-ceramic and the thermally treated Na-rich feldspar mineral, between 330 nm and 500 nm, is not observed. This fact indicates that the Na-rich feldspar mineral does not have structural defects such as Al-O⁻-Al centers, $[AlO_4/alkali^+]$ and $[AlO_4]^0$, which is due to its Si/Al ordered

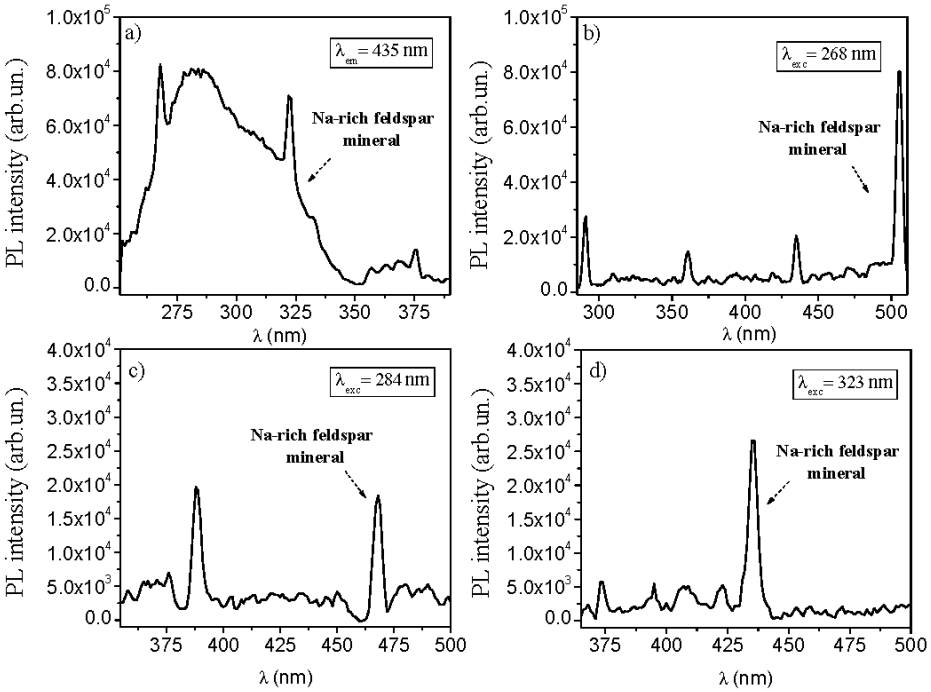

Figure S1. Room temperature photoluminescence spectra in Na-rich feldspar mineral: a) excitation spectra under λ_{em}=435 nm. Emission spectra for: b) λ_{exc}=268 nm; c) λ_{exc}=284 nm and d) λ_{exc}=323 nm.

structure, corresponding to a low albite structure, as it is discussed by XRD in the section 3.2 of the manuscript. Moreover, the PL intensity is around two orders of magnitude lower than in the fast-sintered glass-ceramic.

Band emissions of figure S1b (excited at λ_{exc}=268 nm) correspond to quartz defects [1], except the emission at 435 nm, which can be due to Al-O$^-$-Ti bridges, because of the presence of some amount of Ti in the starting composition [2]. This emission occurs when Ti^{4+} is incorporated as Ti^{3+} in Al-sites, forming Al-O$^-$-Ti bridges. These impurity centers cause narrow emission, as occurs in this case. The two band emissions of figure S1c (excited at λ_{exc} =284 nm) are also caused by quartz defects and Al-O$^-$-Ti bridges, respectively [1,2]. Finally, emission at 435 nm of figure S1c, it is associated to Al-O$^-$-Ti bridges.

II. FE-SEM micrograph and EDS analysis of glass-ceramic.

Figure S2 shows a FE-SEM micrograph for the glass-ceramic. An EDX analysis was carried out in the two points marked.

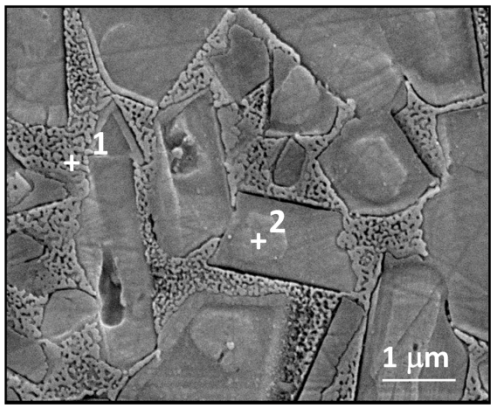

Figure S2. FE-SEM micrograph for glass-ceramic. An EDX analysis was carried out in the two marked points. Chemical composition expressed as oxides is included in table S1.

Either the point 1 (nanostructured region) and the point 2 (microstructured region) shows the presence of Fe_2O_3, according to oxide composition included in table S1.

	Na_2O	Al_2O_3	SiO_2	K_2O	CaO	Fe_2O_3	SrO
Point 1	1.56	21.59	54.33	1.28	9.68	0.69	10.88
Point 2	1.69	21.62	55.77	1.47	11.29	0.53	7.63
XRF	2.29	22.3	53.6	1.26	7.80	0.19	7.10

Table S1. Oxide composition obtained by EDX in points 1–2 marked in Fig. S2 for glass-ceramic.

The presence of Fe_2O_3 is low, < 1 % wt., which is under the resolution limit of the equipment. Therefore, with this measurement we can detect the presence of Fe_2O_3, but not the content. For this purpose, X-Ray fluorescence (XRF) has been carried out obtaining the composition presented in table S2. The presence of iron oxide come from the precursors (both frit and kaolin). Since the work is carried out in an air atmosphere, thus an oxidizing atmosphere, iron is expected to be found as Fe^{3+}, substituting Al^{3+} in some tetrahedra and therefore being responsible for red emissions detected, as it is explained in the section 3.1 of the manuscript.

Oxides % wt	**XRF**
SiO_2	54.85
SrO	7.27
Na_2O	2.34
K_2O	1.29
Al_2O_3	22.82
ZnO	1.26
CaO	7.98
B_2O_3	0.54
P_2O_5	0.54
MgO	0.82
Fe_2O_3	0.19
TiO_2	0.09

Table S2. Oxide composition obtained by XRF for glass-ceramic.

III. XRD pattern of Na-rich feldspar mineral.

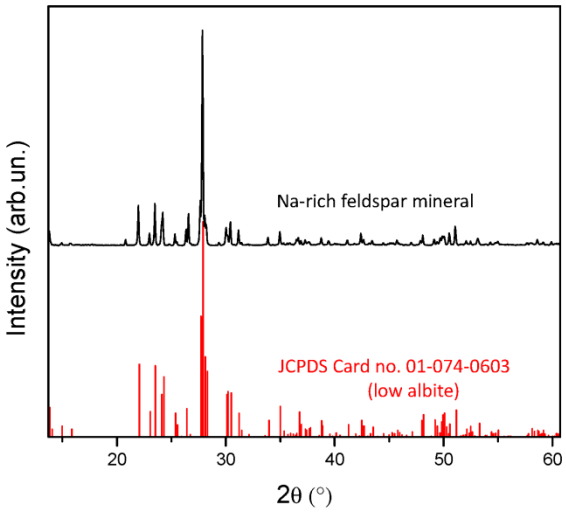

Figure S3. XRD pattern for the Na-rich feldspar mineral, compared with JCPDS Card no. 01-074-0603 (low albite), whose reflections appear slightly shifted to lower 2θ.

IV. FFT simulated diffraction patterns of glass-ceramic.

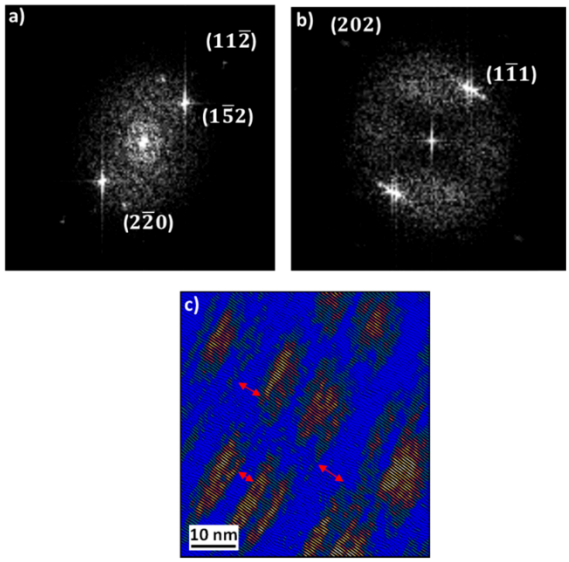

Figure S4. FFT simulated diffraction pattern of the HRTEM image showed in a) figure 2f and b) figure 2g in the manuscript. Its indexing reveals the presence of $(1\bar{5}2)$, $(2\bar{2}0)$ and $(11\bar{2})$ crystalline planes in a) and (202), $(1\bar{1}1)$ planes in b) $(1\bar{1}1)$ direction presents a widened spot which indicates a gradual compositional variation. c) Inversed image of $(1\bar{1}1)$ spot from figure 2g. Yellow color represents crystalline zones while blue ones correspond to non-crystallized areas. In such crystalline regions, compositional variations are presented.

V. FE-SEM micrographs and XRD patterns for glass-ceramic with different thermal treatments.

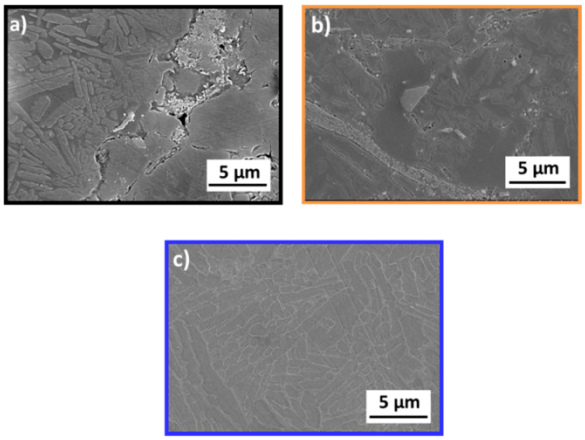

Figure S5. FE-SEM micrographs at low magnification for glass-ceramic for different thermal treatments: a) 1100 ºC and quenched; b) 1220 ºC and quenched c) 1220 ºC and slow cooled.

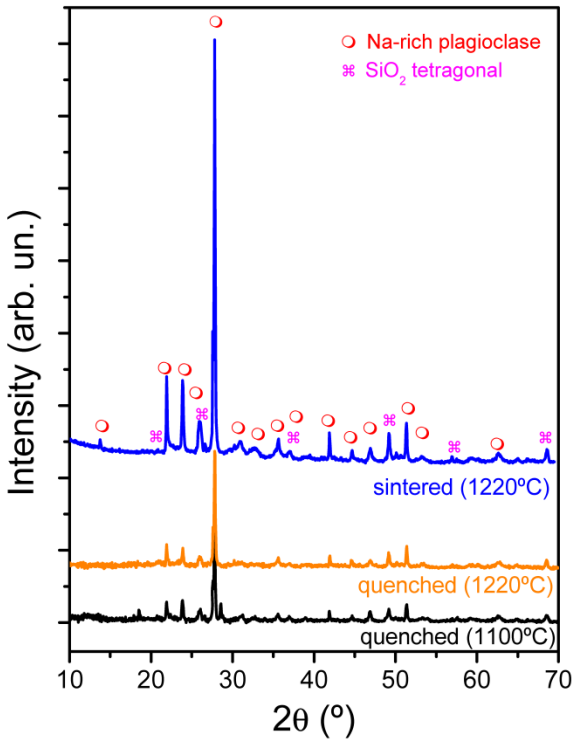

Figure S6. XRD pattern of the quenched samples at 1100ºC and 1220ºC in comparison with the sample sintered at 1220ºC with a dwell time of 6 minutes.

References:

1. J. Götze, M. Plötze, and D. Habermann, "Origin, spectral characteristics and practical applications of the cathodoluminescence (CL) of quartz - A review," Mineral. Petrol. **71**, 225–250 (2001).
2. M. Kayama, S. Nakano, and H. Nishido, "Characteristics of emission centers in alkali feldspar: A new approach by using cathodoluminescence spectral deconvolution," Am. Mineral. **95**, 1783–1795 (2010).

ARTÍCULO 9. Tunable UV/blue Luminescence in Rare-earth Free Glass-ceramic Phosphor

V. Fuertes, J. F. Fernández, E. Enríquez.

Journal of the European Ceramic Society, 39 (10), 2019, 3221-3228

Factor de impacto: 3,794 (según JCR Edition Science 2017).

Journal of the European Ceramic Society 39 (2019) 3221–3228

Contents lists available at ScienceDirect

Journal of the European Ceramic Society

journal homepage: www.elsevier.com/locate/jeurceramsoc

Original Article

Tunable UV/blue luminescence in rare-earth free glass-ceramic phosphor

V. Fuertes[a,*], J.F. Fernández[a], E. Enríquez[b]

[a] Dept. Electrocerámica, Instituto de Cerámica y Vidrio, CSIC, Kelsen 5, 28049, Madrid, Spain
[b] Centro tecnológico Vidres, S.L., Ctra. Onda, Km 3.4, 12540, Villareal, Castellón, Spain

ARTICLE INFO

Keywords:
Tunable luminescence
Glass-ceramic phosphor
Rare-earth free phosphor
Engineered feldspar
Micro-nanostructured

ABSTRACT

A novel rare-earth (RE) free feldspar glass-ceramic phosphor has been designed by a fast sintering route, following a conventional ceramic process. In this work, it is studied how subtle chemical modifications of structural elements may affect luminescence behaviour in this novel matrix. These cation additions acting as glass network former and as modifiers, 1 wt % of SiO_2 and $CaCO_3$ or Na_2CO_3, respectively, produce a photoluminescence enhancement up to 200%. Whereas, addition of Al_2O_3, a glass network former, decreases the photoluminescence emission. Raman spectroscopy evinces a correlation between photoluminescence emission and the Al,Si disorder at microscopic scale. These findings open a new challenge in order to obtain larger structural disorder to make this RE free glass-ceramic much more powerful for future optical applications, highlighting for security markers or light emitting glasses. This new phosphor might be considered as a more sustainable and low-cost alternative to RE phosphors.

1. Introduction

In the last decades, the research and development of new materials for optical applications have been much focused on artificial production of light, being luminescent materials, also called phosphors, subject of a deep study. The unique electronic properties that present rare-earth (RE) ions and the widely tuned emission colour that can be obtained by using different emission centers, namely europium, terbium, yttrium, cerium, lanthanum and gadolinium, explain the great number of rare-earth (RE) based phosphors considered in literature [1–3]. However, China produces more than 95% of all RE elements and has reduced exports by roughly 40% over last ten years [4]. Environmental problems derived from the mining and processing of RE elements, their limited supply along with the rising prices of them lead to find alternative novel RE free based phosphors that eliminate such reliance on the RE materials [4–7].

In order to preserve natural resources, glass-ceramics based phosphors might be a good alternative to RE based phosphors, since they allow developing light-emitting technologies that are much more sustainable and low-cost together with high efficiency [8]. Moreover, glass-ceramics are suitable for many applications because their structure and microstructure might be easily tailored by modifying chemical composition of the precursors and through the control of nucleation and crystal growth during the crystallization step [9,10]. In addition, glass-ceramics for optical applications are easy and flexible to manufacture and the emission colour can be widely tuned since various kinds of emission centres can be incorporated, even at high concentrations [11]. Due to these appealing features, they have been obtained widespread attention in a wide range of applications in the field of photonics [8,11,12].

Feldspars are minerals that constitute around 60% of the Earth's crust and have intrinsic luminescence, which has been widely used for many applications, as dating purposes [13]. The main emission band in minerals feldspars is the ultraviolet-blue one, related to structural defects (mainly Al-O^--Al and alkali cations adjacent to tetrahedral positions) [13–15]. Despite the great knowledge about luminescence in natural feldspars and it usefulness for several applications, the synthetic counterpart has scarcely been studied.

Plagioclase feldspars are one type of feldspars that constitute a solid solution between albite ($NaAlSi_3O_8$) and anorthite ($CaAl_2Si_2O_8$) end-members. In albite, the basic building unit of the framework consists of rings of four tetrahedra, where each one is centred by a Si^{4+} or an Al^{3+}, with a ratio Si^{4+}:Al^{3+} of 3:1. Each oxygen atom is located at the corners of each tetrahedron and links two tetrahedra. Albite can have a triclinic and a monoclinic structure. In triclinic albite, there are four symmetrically non-equivalent sites, designated as $T_1(0)$, $T_1(m)$, $T_2(0)$ and $T_2(m)$ [16,17]. In the most ordered structure, known as low albite, Al-cations are placed in $T_1(0)$ positions, but as disorder increases, cations migrate to the other three positions. In the most disordered polymorph, known as *high albite*, 25% of Al^{3+} is placed in $T_1(0)$

* Corresponding author.
E-mail address: vfuertes@icv.csic.es (V. Fuertes).

https://doi.org/10.1016/j.jeurceramsoc.2019.04.027
Received 21 February 2019; Received in revised form 29 March 2019; Accepted 11 April 2019
Available online 12 April 2019

positions and the other 75% is equally distributed between $T_1(m)$, $T_2(0)$ and $T_2(m)$ sites [18]. In contrast anorthite has a Si^{4+}:Al^{3+} ratio of 1:1 and an essential Al,Si ordered structure [19]. In plagioclase feldspar, depending on the albite and anorthite content, structural properties are modified as well as population of Al in all of these positions and therefore Al,Si arrangement, since Ca^{2+}, Al^{3+}, Na^{1+} and Si^{4+} have to maintain a local charge balance and simultaneously, being compatible with Al,Si ordering scheme [19]. This ordering/disordering process generate Al-O-Al linkages, also known as Löwenstein bridges [19], and changes in the position of alkali and alkaline earth cations in the structure. As consequence, emissions from these kind of centres can occur, being one of the main luminescent centres in feldspars [13,14,20].

Taking into consideration that structure and composition strongly affect to order/disorder processes in feldspars and to the creation of such kind of defects, it is interesting to find out whether emission of engineered feldspar-based glass-ceramics might be controlled, optimized and tuned, based on the foregoing. Being able of modulating luminescence emission of a material, without using RE activator ions, is a challenge pursue in this field at present. Therefore, to widen the range of applications, in this work it is studied if spectral luminescence might be chemically modulated by tailoring the composition in order to modify structural features. To evaluate excitation and emission spectra variations in modified glass-ceramic concerning the plain glass-ceramic, PL measurements are carried out. Structural defects involved in such emissions are thorough analysed by deconvolution of emission curves, in order to show changes in defect population and therefore luminescent emission centres.

2. Experimental procedure

2.1. Material and method

The Na-rich glass-ceramic material was prepared by a conventional ceramic process described in previous works [21], by mixing the frit with Kaolin in a 90/10 proportion. Composition of Kaolin (Molcasa) and frit used as precursors is expressed in term of equivalent oxides in Table 1. This novel RE free glass-ceramic is based on aluminosilicate crystallizations, with a large content of sodium and also some calcium. For that reason, chemical modification was carried out by addition of 1 wt % of SiO_2 (25 nm in diameter nanoparticles, > 995% purity, Cabosil), 1 wt% of $CaCO_3$ (d_{50} = 3 µm, 99% chemical purity, Sigma-Aldrich), 1 wt. % of Na_2CO_3 (d_{50} = 7 µm, 98% chemical purity, Merck) and 1 wt. % of α-Al_2O_3 (6 µm in diameter particles, > 995% purity, Vicar SA) to the glass-ceramic previously prepared, for modifying the crystallization process. Therefore, these additions are not included in the initial composition of the frit but in the process previous to sintering to modify the kinetic reaction. Ca^{2+} and Na^{1+} were added as carbonates since they decomposed during thermal treatment before sintering occurs. Dried mixed composition as ceramic powders were pressed by using a circular die of 2 mm of diameter at 40 MPa. Disk samples were thermally treated in an industrial furnace at 1220 °C for 6 min with a 30 °C.min^{-1} heating rate, in a rapid cycle of ~55 min.

Table 1
Composition of the glass-ceramic precursors expressed as equivalent oxides.

Oxides % wt	Frit	Kaolin
SiO_2	51.63	55.49
SrO	8.05	–
Na_2O	2.68	–
K_2O	1.46	1.21
Al_2O_3	21.14	42.48
ZnO	1.10	–
CaO	10.47	0.18
B_2O_3	1.40	–
P_2O_5	0.84	0.04
MgO	1.04	0.10
Fe_2O_3	0.12	0.43
TiO_2	0.09	0.07

2.2. Characterization

The photoluminescence behaviour was investigated by a spectrofluorometer (Fluorolog®-3, HORIBA Jobin Yvon) at room temperature. Emission spectrum was measured over the wavelength 340–520 nm and excitation spectra in the range 290–365 nm, using a Xenon arc lamp as excitation source. X-ray diffraction (XRD) measurements were carried out in a diffractometer Bruker D8 Advance with Cu Kα radiation, 40 kV and 40 mA. Diffraction patterns were carried out from 20° to 35° 2θ with a scan step size of 0.017° 2θ and an accumulation time of 6 s in order to have good resolution to discriminate between (1–31) and (131) reflections.

Microstructural characterization was studied by means of Field Emission Scanning Electron Microscopy (FESEM) using a Hitachi S-4700 with a resolution of 1.5 nm at 15 kV, and by Raman spectroscopy using a Confocal Raman Microscope (Witec ALPHA 300RA) with a Nd:YAG laser light source (532 nm) in p-polarization. Optical resolution of the Confocal Raman Microscope is 250 nm and 700 nm in the longitudinal and transversal directions, respectively. Raman spectra were recorded at room temperature in the spectral range of 70 − 1175 cm^{-1}, by using a grating of 1800 lines per millimetre resulting in a spectral resolution of the system below 0.02 cm^{-1}. Raman images were attained with a size 30 µm × 30 µm and 130,048 spectra for each image. Samples were mounted on a piezo-driven scan platform with a positioning accuracy of 3 nm in lateral and 1 nm in vertical directions. The reflected laser light at each point was collected using a multimode optical fibre of 25 µm in diameter by a very sensitive CCD detector. Measurements were performed using objectives of 100x with a numerical aperture (NA) of 0.95. The acquired spectra were analysed by using Witec Project 2.02 program and Witec Control Plus Software.

3. Results and discussion

3.1. Modulation of photoluminescence (PL)

Excitation and emission spectra for the RE free glass-ceramic (blue line), designated as plain glass-ceramic along the manuscript, and samples modified with 1 wt % of SiO_2 (green line), 1 wt % of $CaCO_3$ (pink line), 1 wt % of Na_2CO_3 (orange line) and 1 wt % of Al_2O_3 (violet line) are depicted in Fig. 1a and b, respectively. All the samples chemically modified undergoes a wavelength shift and a full width at half maximum, FWMH, change in both excitation and emission curves regarding plain glass-ceramic, indicating that energy levels and population of defects are altered. In the case of excitation spectra (Fig. 1a) a higher intensity and a red shift is observed in modified samples regarding the plain glass-ceramic. A excitation maximum at 322 nm for the plain glass-ceramic red shifts up to 333 nm for the chemical modification with 1 wt % of Na_2CO_3 (Table 1). Another less intense peak in the range 355–360 nm is observed and it is attributed to Fe^{3+} emissions. Each material is, therefore, excited at its corresponding excitation maximum wavelengths and the emission spectra recorded and depict in Fig. 1b and emission maximum wavelengths are tabulated in Table 2. A considerable change in the UV/blue band emission characteristic of this RE free glass-ceramic is observed, undergoing a red shift up to 10 nm when Na_2CO_3 is added to the plain glass-ceramic, introducing the luminescence in the visible range. Tuning emission spectra in 10 nm is a strong shift taking into account that glass-ceramic was chemically modified just by 1 wt % of glass network modifiers that are present in the formulation of the plain sample. All of these red shifts carried out confirm that the chemical modifications interact and react with the matrix during the thermal treatment process. Besides, photoluminescence intensity of emission increases ~150% (Table 2) by excess

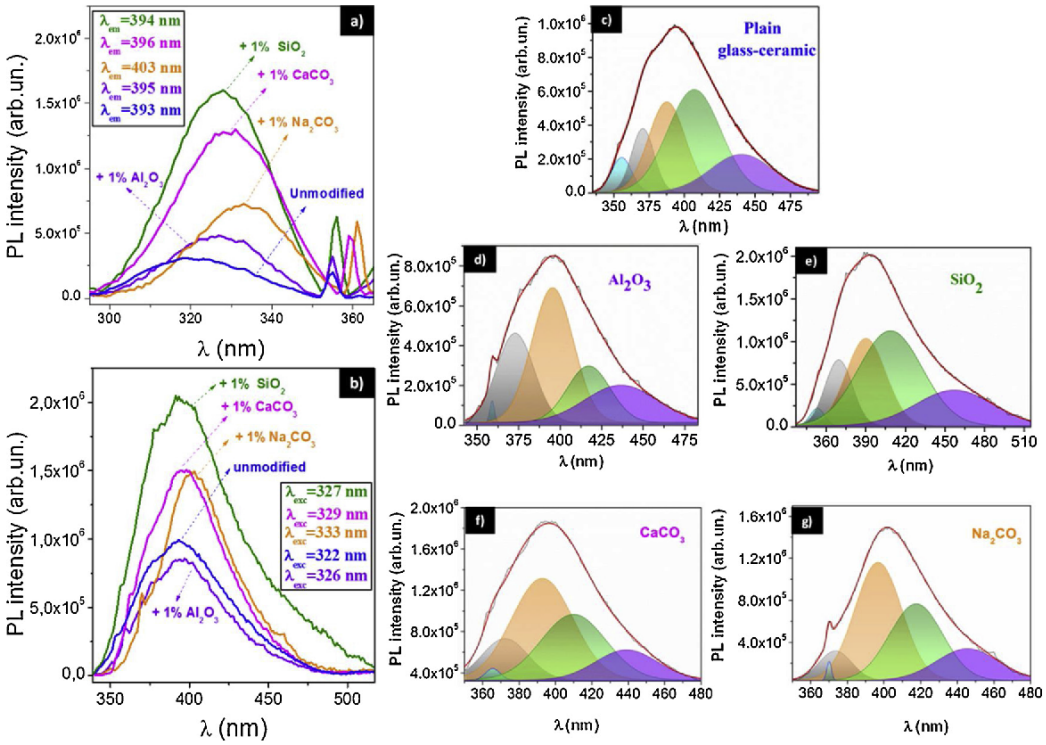

Fig. 1. a) Excitation and **b)** emission spectra measured at room temperature in UV/blue range for plain glass-ceramic (blue line) and chemically modified glass-ceramic with an excess of 1 wt % of SiO_2 (green line), $CaCO_3$ (pink line), Na_2CO_3 (orange line) and Al_2O_3 (violet line). Wavelengths at which emission and excitation are measured for each sample are included in the inset of 1a and 1b, respectively. Red shift is observed for chemically modified glass-ceramics in both excitation and emission wavelengths regarding plain material; **c–g)** Deconvolution of emission band plotted in **b)**. Each deconvolution curve is labelled with the sample that corresponds. Each kind of defect-related band is coloured in the same way for all chemical modified samples spectra (c–g), to facilitate its comparison.

Table 2
Excitation and emission wavelengths tabulated for UV/blue transitions in plain glass-ceramic and chemically modified glass-ceramics with 1 wt % of Al_2O_3, SiO_2, Na_2CO_3 and $CaCO_3$. Besides, it is included the intensity ratio, $I_{c.m.}/I_{plain}$, of the maximum emission band between the chemically modified ($I_{c.m.}$) and the plain glass-ceramics (I_{plain}).

Glass-ceramic	λ_{exc} (nm)	λ_{em} (nm)	$I_{c.m.}/I_{plain}$ (%)
Plain	322	393	100
1 wt% Al_2O_3	326	395	90
1 wt% SiO_2	327	394	200
1 wt% Na_2CO_3	333	396	150
1 wt% $CaCO_3$	329	403	150

Table 3
Assignment of deconvoluted emissions in UV/blue range and the areas ratio of each contribution of the glass-ceramic chemically modified with 1 wt. % of Al_2O_3, SiO_2, Na_2CO_3 and $CaCO_3$ regarding plain glass-ceramic ($A_{c.m}/A_{plain}$).

	Sample	Plain	1 wt % Al_2O_3	1 wt % SiO_2	1 wt % Na_2CO_3	1 wt % $CaCO_3$
Quartz	λ (nm)	356	359	353	370	365
	$A_{c.m}/A_{plain}$	–	0.1	1.3	0.1	0.3
[AlO_4/alkali$^+$] or [AlO_4]°	λ (nm)	*371*	*373*	*369*	*373*	*372*
	$A_{c.m}/A_{plain}$	–	*1.5*	*2.8*	*0.8*	*1.6*
[AlO_4/alkali$^+$] or [AlO_4]°	λ (nm)	*388*	*394*	*390*	*397*	*392*
	$A_{c.m}/A_{plain}$	–	*1.0*	*2.3*	*4.4*	*2.3*
Al-O$^-$-Al	λ (nm)	*410*	*417*	*406*	*417*	*409*
	$A_{c.m}/A_{plain}$	–	*0.3*	*2.3*	*0.9*	*1.0*
Al-O$^-$-Al	λ (nm)	*440*	*437*	*457*	*445*	*439*
	$A_{c.m}/A_{plain}$	–	*0.7*	*2.4*	*1.0*	*1.0*

addition of glass network modifiers, as alkali and alkaline earth elements, and ~200% (Table 2) by excess addition of glass former networks, as silica. In order to deepen more about how emissions evolved for the chemically modified glass-ceramics, deconvolution of the UV/blue emissions are shown in Fig. 1c–g. Assignment of deconvoluted emissions and the intensity ratio of chemically modified glass-ceramic regarding the plain ones are included in Table 3, for comparative purposes.

In the UV/blue range studied, plain glass-ceramic (Fig. 1c) exhibits five emission bands. Chemically modified glass-ceramics present changes in the deconvoluted emission band, as seen in Fig. 1d–g, and the areas ratio of each contribution of the chemically modified samples regarding the plain glass-ceramic ($A_{c.m.}/A_{plain}$) is presented in Table 3. These alterations of the emission band correspond to changes in the defect contributions. In the case of glass-ceramic modified with Al_2O_3 (Fig. 1d), the total PL intensity decreases 10% regarding plain glass-ceramic and a trend of decreasing defect density is observed (see Table 3). In the rest of chemical modifications (Fig. 1e–g) a trend of increasing defect population is noticed.

The deconvoluted band located at ca. 360 nm (signaled in blue colour) present in the plain glass-ceramic corresponds to quartz emission [22] and it is attributed to impurities contributed from the kaolin. The trend of this band is to decrease in all modified samples, except in case of SiO_2, which can be due to the fact that the additions act as network modifiers which may hinder quartz reaction.

The second deconvoluted emission band (grey band) at ca.371 nm in the plain glass-ceramic may be ascribed to emission due [AlO_4/alkali$^+$] or [AlO_4]° defects [14]. [AlO_4/alkali$^+$] occurs when Si^{4+} is substituted by Al^{3+} cation and an alkali cation is located in adjacent positions to such Al^{3+} cation in order to maintain the local charge balance [14,20]. Nevertheless, if a hole is trapped, the resulting centre

will be $[AlO_4]^\circ$ [14].The position of this emission band is also slightly modified by the chemical changes introduced, taking place a slight blue shift. Glass-ceramic modified with Na_2CO_3 (Fig. 1g) exhibits a narrower emission with a smaller relative area with regards to plain glass-ceramic. By the contrary, the addition of glass former modifiers favors the increasing of such emission band, in particular for silica, as it can be seen in the areas ratio in Table 3.

The third band (signaled in orange colour) placed at ca.388 nm in the plain glass-ceramic is strongly affected by chemical modifications, undergoing a red shift up to 397 nm with the addition of Na_2CO_3 (Fig. 1g). This UV emission band is characteristic of mineral phases containing SiO_4 tetrahedra and can be also related to $[AlO_4/alkali^+]$ or $[AlO_4]^\circ$ defects [14,20]. Attending to the glass-ceramic composition, this emission should be caused by Na^+ cations placed adjacent to Al^{3+} cations, in the case of being caused by alkali ions, since Na^+ is the major alkali cation in Na-rich feldspars. In the case of sodic plagioclases, the addition of different structural elements can cause a reorganization of Ca^{2+}, Al^{3+}, Na^+ and Si^{4+} cations in the crystal lattice regarding the former plagioclase structure. Migration to different positions in the crystal lattice results in formation of different energy defect levels, which is translated in emission wavelength shifts, as occurs in this case. These emissions have considerable relevance in all the chemically modified samples.

Likewise, the two last emissions (signaled in green and violet colours, respectively) take place in the wavelength range 409–421 nm and 437–457 nm and also undergo a red shift for the chemically modified glass-ceramics regarding plain glass-ceramic. These blue emissions are attributed to Al-O-Al linkages, also known as Löwenstein bridges, which are the most typical structural defect in feldspars and occur, typically, in the range 400–480 nm, when an oxygen hole centre is adjacent to two Al^{3+} cations, one of them structural and the other one an impurity of Al^{3+} [20,23]. Disordered feldspars show a more intense blue emission and a higher density of Al-O–-Al centres, as compared to ordered one. According to relative areas of Table 3, these results may indicate that Si-Al disorder has greatly increased in the chemically modified glass-ceramic with SiO_2 (Fig. 1e) regarding the plain glass-ceramic, and in lesser extent with $CaCO_3$ (Fig. 1f) and Na_2CO_3 (Fig. 1g). Thus, the migration of Al^{3+} from $T_1(0)$ positions to $T_1(m)$, $T_2(0)$ and $T_2(m)$ sites can be favoured and, consequently, the increase of these defect populations.

The analysis of UV/blue emission evinces that crystal field and structure might be easily modified in this novel RE free glass-ceramic, only by subtle chemical changes, probably due to the change of Si/Al ordering schemes. It has been proved that luminescence intensity may be increased by raising the population of defects that are commonly related with Si/Al disordered structures of feldspars. Further research by other techniques is necessary to corroborate this hypothesis and study structural changes, as it will be discussed hereunder.

3.2. Structural study

FE-SEM microscopy was carried out in order to study the microstructure of the different samples. Fig. 2 shows some representative micrographs for the micro-nanostructured glass-ceramic (Fig. 2a, blue box) and samples modified with 1 wt. % of Na_2CO_3 (Fig. 2b, orange box), SiO_2 (Fig. 2c, green box), Al_2O_3 (Fig. 2d, violet box) and $CaCO_3$ (Fig. 2e, pink box). Fig. 2a shows the characteristic micro-nanostructuration of the glass-ceramic where elongated microcrystals are surrounded by nanocrystal regions and glassy-phase is located in the boundary between them. The general features of this singular micro-nanostructure remain in all chemically modified samples, with a nanostructuration uniformly distributed along the sample although slight changes in microcrystals and nanocrystals are noticed. When network modifiers (Na^+ and Ca^{2+}) are added to the system, glass-ceramic is further crystallized, having more nanocrystals and less glassy-phase than the plain glass-ceramic. As consequence, in these modified samples, nanoparticles appear covering the surface in both cases due to the chemical etching carried out in order to reveal the microstructure. Nevertheless, when network formers (Si^{4+} and Al^{3+}) are added, nanocrystals structures are more resistant to the chemical etching, probably due to nanocrystals seem to be more united, forming bottlenecks in some areas. Regarding microcrystals, they appear straighter than those in the plain glass-ceramic. In conclusion, microstructural changes produced by the chemical modifications are very subtle and should not play a vital role in the modification of luminescence behaviour of this glass-ceramic phosphor. Therefore, structural aspects seem to be the responsible of the modulation of luminescence.

XRD pattern was measured in the chemically modified glass-ceramic samples to evaluate the changes in their structure in order to correlate them with their luminescence behavior. Diffraction patterns for plain sample (blue line) and chemically modified glass-ceramics with 1 wt % of SiO_2 (green line), 1 wt. % of $CaCO_3$ (pink line), 1 wt. % of Na_2CO_3 (orange line) and 1 wt % of Al_2O_3 (violet line) are illustrated in Fig. 3a. Si powder is used as internal standard, for this reason Si (111) reflection appears marked in red in Fig. 3. These XRD patterns correspond to a triclinic Na-rich plagioclase structure with a space group $C\bar{1}$. Main diffraction peaks reflect a slight enlargement of the interplanar spacing for chemically modified glass-ceramics against the plain glass-ceramic, inset of Fig. 3a. These results confirm that chemical modifiers react with the matrix during the thermal treatment and are incorporated in the structure of the Na-rich plagioclase, causing a slight expansion of the crystal lattice.

However, feldspars materials are structurally very complex and several aspects have to been considered for their complete analysis, as the case of Al/Si distribution. This issue may be studied in feldspars through the analysis of X-Ray diffraction peak position for (131) and (1–31) reflections [24–27]. Accordingly, an increase of $\Delta_{2\theta} = 2\theta_{(131)} - 2\theta_{(1-31)}$ would indicate an increase of disorder in Al/Si distribution while a decrease of $\Delta_{2\theta}$ would indicate an increase of order. In Fig. 3b is depicted an enlargement of both reflections for the different glass-ceramics studied. In all the samples (1–31) reflection is placed at 29.6°2θ, while (131) range from 30.8°2θ to 30.9°2θ, which fits well with data reported in literature for low plagioclases [28]. The difference between both reflections, $\Delta_{2\theta}$, has a constant value of 1.3°2θ for all the chemically modified glass-ceramics, in which luminescence increases regarding plain glass-ceramic, except for the Al_2O_3 addition, in which the value coincides with the plain glass-ceramic, 1.2°2θ, indicating the same Al/Si order. These results indicate that when Al/Si order increases, luminescent centres tend to be formed, and consequently luminescence intensity also increases, as it is previously shown.

As it was mentioned before, a Na-rich plagioclase might be considered as an intermediate albite from a point of view of Al/Si order-disorder. In intermediate albites, $\Delta_{2\theta}$ ranges from 1.15°2θ to 1.6°2θ whereas in high albite, the most disordered albite, this difference is between 1.6°2θ and 2.0°2θ [29]. In the chemically modified samples, $\Delta_{2\theta}$ increases up to 1.3°2θ, which indicates that slight Al/Si disordering is favoured. These findings demonstrate that Al/Si disorder may be generated in this novel RE free matrix by means of structural reorganization of Na^+, Si^{4+}, Ca^{2+} and Al^{3+}, modifying their optical properties. Future studies may allow generating high Al/Si disorder in plagioclase structures with the aim of approaching to a high albite structure, increasing the defect population in the material and consequently, photoluminescence.

3.2.1. Raman spectroscopy

XRD diffraction gives information at large scale, for these reason, the subtle changes introduced in the plain glass-ceramic structure by the addition of chemical modification, only of 1 wt %, are difficult to be observed and, therefore, it is also difficult to discriminate by XRD if samples with higher luminescence present differences in Si/Al disorder. However, Al, Si-O tetrahedral distortions due to Al/Si disorder, might be studied at microscopic scale by means of Raman spectroscopy

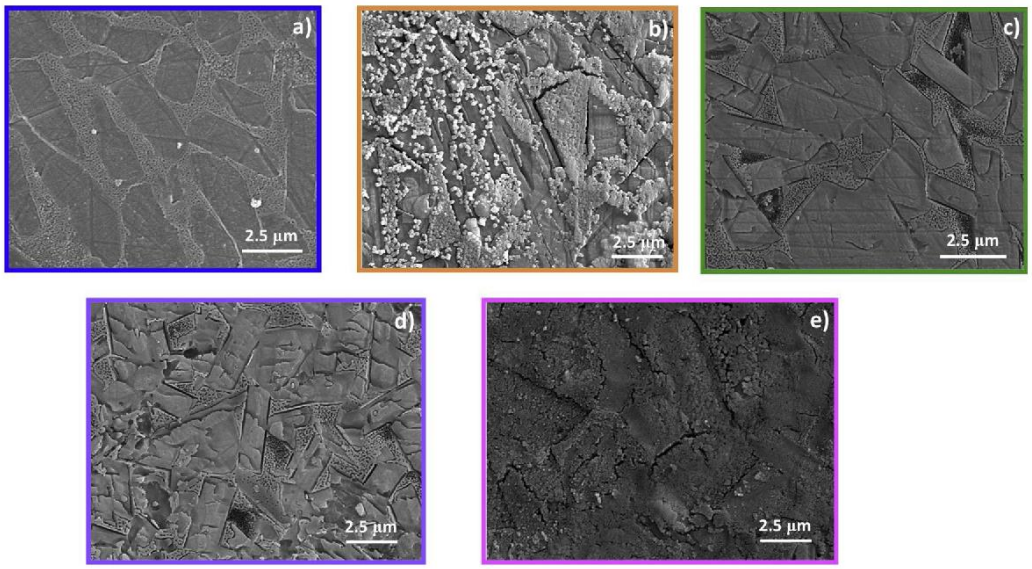

Fig. 2. FE-SEM micrographs for **a)** plain glass ceramic; and glass-ceramic chemically modified with 1 wt. % of **b)** Na_2CO_3; **c)** SiO_2; **d)** Al_2O_3 and **e)** $CaCO_3$.

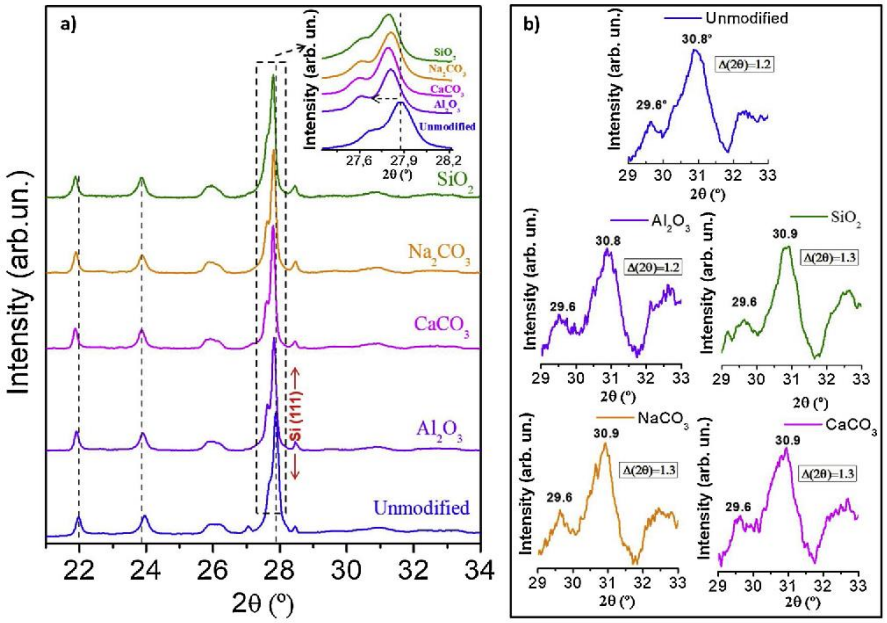

Fig. 3. a) XRD pattern in the range 21–34 ° 2θ for plain glass-ceramics (blue line) and chemically modified glass-ceramic with 1 wt % of Al_2O_3 (violet line), $CaCO_3$ (pink line), Na_2CO_3 (orange line) and SiO_2 (green line). The inset shows a shift towards lower 2θ for modified samples; **b)** enlargement of XRD pattern showing in detail the (1–31) at 29.6° 2θ and (131) at 30.8–30.9 ° 2θ reflections. An increase of $\Delta_{2\theta} = 2\theta_{(131)} - 2\theta_{(1-31)}$ indicates that Al/Si disorder increases at large scale.

[16,30,31]. Fig. 4a collects Raman spectra for the studied samples where Raman modes labelled as ν_a and ν_b are breathing modes of the four-membered tetrahedral rings [32] of feldspar structure. In the inset it might be observed the enlargement of the area marked in light blue colour in Fig. 4a, which shows in more detail ν_a and ν_b modes for all the compositions studied. The studied glass-ceramic are sodic plagioclase which might be considered as an intermediate albite from a mineralogical point of view and thus Raman modes are very similar to those of albite.

From the deconvolution of Raman spectra in the range 450-545 cm^{-1}, highlighted in blue color in Fig. 4a, four Raman modes are found (Fig. 4b) and some essential information about composition and order-disorder may be obtained from their analysis. Raman modes are tabulated in Table 4 and it is also included the Full Width at Half Maximum (FWHM) for ν_b, designated as $\Delta\Gamma_b$, as well as difference between Raman shift for modes ν_a and ν_b, defined as $\Delta_{ab} = \nu_a - \nu_b$.

Raman mode *1* (signaled in grey colour in Fig. 4b) is located at ca.467.5 cm^{-1} in the plain glass-ceramic and describes deformation of tetrahedra. Si-cations contribute to the motion, in particular in the $T_2(0)$ tetrahedra [17]. This vibration mode undergoes a considerable Raman red shift in chemically modified samples regarding the plain glass-ceramic $\approx$-3 cm^{-1} in case of Al_2O_3 modified glass-ceramics and toward larger wavenumbers, $\approx$12 cm^{-1} for the rest of chemically modified glass-ceramics. Moreover, the relative intensity of this Raman mode (Fig. 4b) also varies, being higher than in the plain glass-ceramic for Al_2O_3 modified sample, and considerably decreasing when 1 wt % of SiO_2, Na_2CO_3 or $CaCO_3$ is added. As result, compression of crystal lattice entails a luminescence decreases, meanwhile expansion of crystal lattice improves luminescence emission.

Modes ν_a and ν_b are sensitive to both the composition and the order-

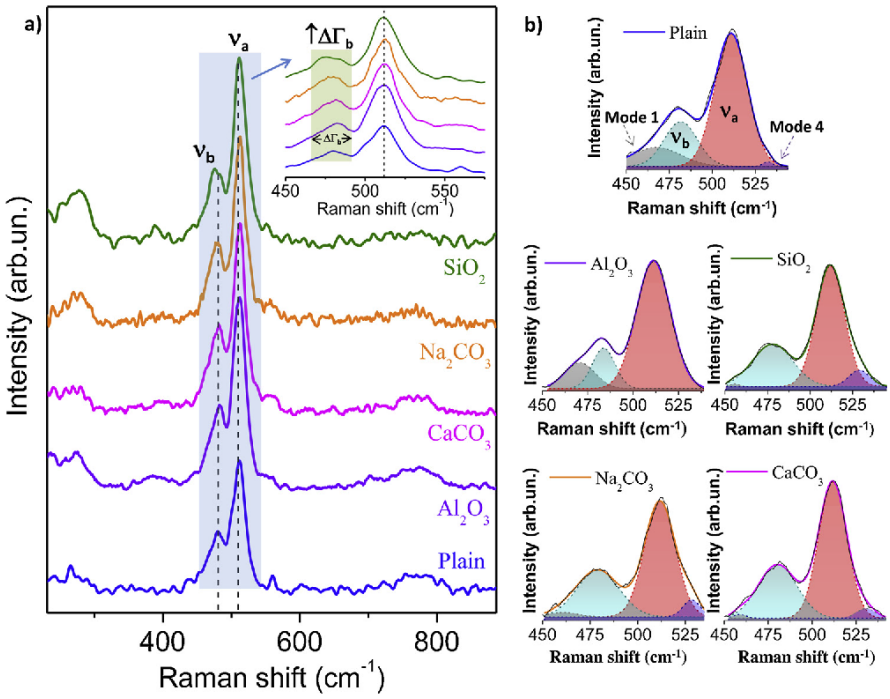

Fig. 4. a) Raman spectra at room temperature of plain glass-ceramic (blue line) and chemically modified glass-ceramic with 1 wt. % of Al_2O_3 (violet line), $CaCO_3$ (pink line), Na_2CO_3 (orange line) and SiO_2 (green line). In the inset it is shown an enlargement of the ring-breathing Raman modes, ν_a and ν_b. The width of ν_b is highlighted in green colour and it is labelled as $\Delta\Gamma_b$ that increases as Al/Si disorder increases. **b)** Deconvolution of Raman spectra in the range 450-545 cm ^{1} shows the presence of four Raman modes for all the samples studied.

disorder changes [17]. Attending to Raman peak positions tabulated in Table 4, ν_a mode remains almost unchanged for all the modified samples. However, ν_b mode shows a similar trend to Raman mode *1*. Bersani et al. [33] have studied Raman features of more than 20 plagioclases with different composition and Si/Al order. According to this study, the Raman blue shift observed when alumina is added to the system matches with formation of one more anorthitic feldspar while the effect of adding $CaCO_3$, Na_2CO_3 and SiO_2 is the formation of more albitic plagioclase. In addition, in that work, it is also established that samples with $\Delta_{ab}=\nu_a-\nu_b < 27$ cm^{-1} have an anorthite content > 60 mol% while samples with $\Delta_{ab} > 27$ cm^{-1} have an anorthite content < 60 mol%. From tabulated values of Table 4, the calculated differences between both peak positions are 29.4 cm^{-1} in plain glass-ceramic, 27.3 cm^{-1} in Al_2O_3 and 31.5 cm^{-1}, 32.5 cm^{-1} and 33.9 cm^{-1} for $CaCO_3$, Na_2CO_3 and SiO_2 modified glass-ceramics respectively. Therefore, these last additions favor the formation of closer albitic structure.

From results obtained in this section and in Section 3.1, it is evinced that higher presence of albite in the plagioclase results in higher luminescence. Anorthite tends to promote Si/Al ordering in the tetrahedra ring, which is energetically more favourable [19,33], reducing the luminescence. In contrast, when the ordering scheme is albite-like, formation of Al-O-Al bridges is favoured and therefore this structure is more prone to be disordered [19,33]. However, certain content of anorthite is needed to induce the formation of luminescent centres such as Al-O$^-$-Al linkages. Since alumina modified sample presents $\Delta_{ab} \approx 27$ cm^{-1}, which indicates an anorthite content close to 60 mol%, this composition is less favourable for the luminescent response.

In addition, through the analysis of $\Delta\Gamma_b$ values (tabulated in Table 4), Al/Si order-disorder changes may be noticed. An increase of this parameter, that means the increase of the FWHM of the band υ_b situated at ≈480 cm^{-1}, indicates a rise of Al/Si disorder in the system at microscopic scale [33], while the decrease means high ordering because more Al^{3+} cations will be placed at $T_1(0)$ positions and therefore less luminescent centres will be formed [19]. As seen, $\Delta\Gamma_b$ value is reduced for glass-ceramics chemically modified with 1 wt % Al_2O_3, and increased for the rest of chemical modifications, reaching the maximum for SiO_2. This fact correlates with the luminescence behaviour measured in Section 3.1, leading to formation of more luminescent centres (see Table 3), motivated by an increase of Al/Si disorder regarding plain glass-ceramic. These results are collected in Fig. 5a and demonstrate that the increase of disorder effectively increases the luminescence performance of the plagioclase-based glass-ceramic due to migration of Al^{3+} cations from $T_1(0)$ positions to $T_1(m)$, $T_2(0)$ and $T_2(m)$ and the resulting generations of defects in the inner structure of the RE free glass-ceramic. According to these results, it could be easy to extrapolate that an increase of SiO_2, $CaCO_3$ or Na_2CO_3 content, above 1 wt % and below the solubility limit of the matrix, should promote an increase of Si/Al disordering and, therefore, an increase of luminescence.

Table 4
Tabulated Raman modes obtained from deconvolution of Raman spectra in the range 450-545 cm ^{1}. In addition, the difference between Raman shift for modes ν_a and ν_b, defined as $\Delta_{ab}=\nu_a-\nu_b$ and the FWHM of mode ν_b, $\Delta\Gamma_b$, for plain glass-ceramic and chemically modified glass ceramics with 1 wt % of Al_2O_3, SiO_2, Na_2CO_3 and $CaCO_3$, is also included. An increase of $\Delta\Gamma_b$ regarding plain glass-ceramic indicates an growth of Si/Al disorder [33].

Glass-ceramic	Mode 1 (cm^{-1})	ν_b (cm^{-1})	ν_a (cm^{-1})	Mode 4 (cm^{-1})	Δ_{ab} (cm^{-1})	$\Delta\Gamma_b$ (cm^{-1})
plain	467.5	481.7	511.1	532.2	29.4	22.6
+ 1%wt Al_2O_3	470.6	483.8	511.1	–	27.3	14.8
+ 1%wt $CaCO_3$	458.7	480.2	511.7	530.7	31.5	26.1
+ 1%wt Na_2CO_3	460.8	479.2	511.7	528.4	32.5	26.1
+ 1%wt SiO_2	455.6	478.0	511.9	529.0	33.9	27.8

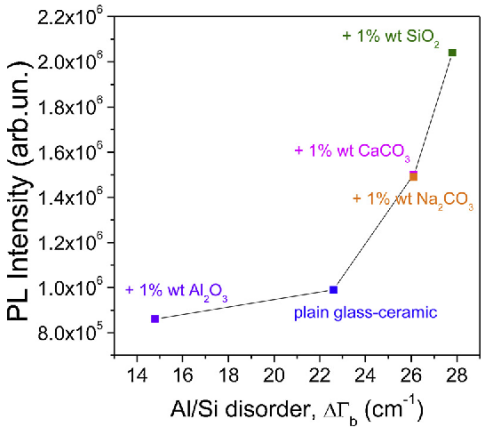

Fig. 5. Correlation between PL intensity emission and Si/Al disorder ($\Delta\Gamma_b$) for the plain glass-ceramic (blue) and chemically modified glass-ceramic with 1 wt. % of Al_2O_3 (violet), $CaCO_3$ (pink), Na_2CO_3 (orange) and SiO_2 (green).

Raman mode 4 (violet band in Fig. 4b) also describes (Si,Al) tetrahedral deformation along with Na-O stretching [34].This Raman mode is less pronounced than the other three modes previously analysed for the plain glass-ceramic, as it can be observed in Fig. 4b. In Al_2O_3 modified sample is even missing, whereas when modified by $CaCO_3$ and Na_2CO_3 a higher relative intensity in the vibrational spectrum is found. This Raman mode is even more significant in samples modified with silica, indicating that a higher tetrahedral deformation occurs along with Na-O stretching.

The rest of the Raman modes observed in Fig. 4a are described in the section S1 of supporting information.

In summary, it can be said that silica, sodium and calcium have a contrary effect than alumina both in vibrational behaviour and luminescence. In the latest case, red shift is observed in most of the Raman modes regarding Raman spectrum of plain glass-ceramic whereas a blue-shift is undergone by the others. Compositional and vibrational changes observed by Raman spectroscopy agree well with changes made in luminescent behaviour.

It is worth mentioning that, even though disorder is hardly achieved at long range, as XRD measurements showed, an increase of the disorder at local scale, as Raman spectroscopy supported, is enough to considerably improve luminescence emission. According to all these results, Fig. 6 shows a schematic model of the luminescence effect related with Al/Si order/disorder characteristic of glass-ceramic feldspar. Fig. 6a presents schematically the distortion of tetrahedral rings based on the Si/Al disorder and the appearance of structural defects: Al-O^--Al, [AlO_4/Na^+]). As a result, an increase of radiative recombinations is produced and therefore luminescence rises accordingly with the defect population. In the band diagram of Fig. 6, it is indicated the main electronic transitions. Electrons are UV excited from the valence to a higher state. From these electronic states, electrons decay to states with lower energy, corresponding to Al-O^--Al and [AlO_4/Na^+] defects, by non-radiative transitions. The holes generated in the valence band can recombine with the electrons located in these defect states, by radiative recombinations, emitting photons with energies in the UV and the visible range.

These results evince that this new family of RE free glass-ceramic phosphors possesses interesting luminescence properties that might be modulated by structural modification and open the challenge to be improved by achieving a long range disorder in Al/Si distribution for an albitic structure.

4. Conclusions

A RE free glass-ceramic phosphor based on sodic plagioclase crystallizations has been designed by fast sintering route and following a conventional ceramic process. In this work, the effect of the photoluminescence emission tuning has been studied when structural modifications are induced in the feldspar structure.

Photoluminescence measurements indicate that emission improvements are achieved by chemical modification of the RE free glass-ceramic with different glass modifiers just by adding 1 wt % during the devitrification of the glass-ceramics. An increase of 200% in the emission intensity is achieve when 1 wt % SiO_2 is added to the glass-ceramic, while using 1 wt % of $CaCO_3$ or Na_2CO_3 produce a luminescence emission enhancement of 150%. However, when Al_2O_3 is used, a decrease of structural defect population occurs, which leads to reduce photoluminescence intensity. UV/blue emissions undergo a red shift for all the chemical modifications, introducing the luminescence in the visible range when Na_2CO_3 is employed.

XRD and Raman spectroscopy allows establishing that there is a clear correlation between the increase of Al/Si disorder at microscopic scale and the increase of photoluminescence intensity, being the main luminescent centres generated by Al-O^--Al linkages and [AlO_4/alkali$^+$] or [AlO_4]$^\circ$ defects. Moreover, it is proved that Na-rich plagioclase matrices are more suitable than Ca-rich plagioclases for luminescent applications, since in the first one Al/Si disorder is favoured. It is worth pointing out that the enhanced luminescence performance exhibited for chemical modification of the plain glass-ceramic with 1 wt % SiO_2, $CaCO_3$ or Na_2CO_3, has been achieved by inducing Al/Si disorder at local scale, although such Al/Si disorder is not very noticeable at long range, as it is observed by XRD. A model of the observed effect in the luminescence related with Al/Si order/disorder has been developed, which explains the increase of radiative recombinations produced by the chemical modification of the plain glass-ceramic. This fact opens

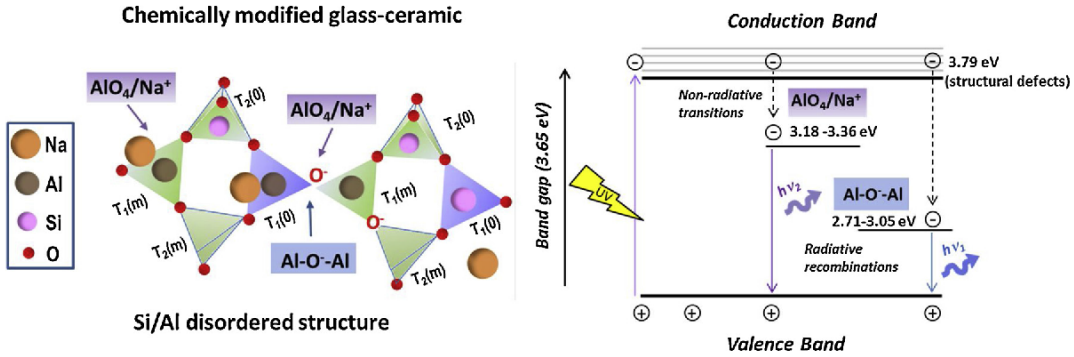

Fig. 6. Schematic model of the correlation between structural defects in glass-ceramic feldspar with the luminescence; **a)** chemically modified glass-ceramic feldspar structure; **b)** band diagram where it is shown that the radiative recombinations and luminescence origin in glass-ceramic feldspars. Energies indicated in Fig. 6 correspond to chemically modify glass-ceramic with 1 wt % SiO_2. Band gap energy is calculated Tauc's theory (supporting information S2).

a challenge towards more complex structural modifications with the aim of raising such Al/Si disorder at long range.

These findings demonstrate that luminescence can be enhanced in this novel RE free glass-ceramic by tailoring its structure which might be technologically very relevant for future optical applications.

Acknowledgments

The authors express their thanks to the MINECO (Spain) project MAT2017-86450-C4-1-R, and projects CDTI (IDI-20130894 and IDI-20161120) for their financial support. Dra. E. Enriquez is also indebted to MINECO for a "Torres Quevedo" contract (ref: PTQ- 14-07289), which is co-financed with European Social Funds.

Appendix A. Supplementary data

Supplementary material related to this article can be found, in the online version, at doi:https://doi.org/10.1016/j.jeurceramsoc.2019.04.027.

References

[1] C.R. Ronda, T. Jüstel, H. Nikol, Rare earth phosphors: fundamentals and applications, J. Alloys. Compd. 275–277 (1998) 669–676, https://doi.org/10.1016/S0925-8388(98)00416-2.
[2] X. Li, D. Chen, F. Huang, G. Chang, J. Zhao, X. Qiao, et al., Phase-selective nanocrystallization of NaLnF4in aluminosilicate glass for random laser and 940 nm LED-Excitable upconverted luminescence, Laser Photonics Rev. 12 (2018) 1–8, https://doi.org/10.1002/lpor.201800030.
[3] J. Zhong, D. Chen, Y. Peng, Y. Lu, X. Chen, X. Li, et al., A review on nanostructured glass ceramics for promising application in optical thermometry, J. Alloys. Compd. 763 (2018) 34–48, https://doi.org/10.1016/j.jallcom.2018.05.348.
[4] D. Chiriu, L. Stagi, C.M. Carbonaro, P.C. Ricci, Strength and weakness of rare earths based phosphors: strategies to replace critical raw materials, Phys. Status Solidi Curr. Top. Solid State Phys. 13 (2016) 989–997, https://doi.org/10.1002/pssc.201600116.
[5] C. Hurst, China's rare earth elements industry: what can the west learn? Inst. Anal. Glob. Secur. 43 (2010), http://www.iags.org/rareearth0310hurst.pdf.
[6] R.E. Rojas-Hernandez, F. Rubio-Marcos, A. Serrano, A. Del Campo, J.F. Fernandez, Precise tuning of the nanostructured surface leading to the luminescence enhancement in SrAl2 O4 based core/shell structure, Sci. Rep. 7 (2017) 1–9, https://doi.org/10.1038/s41598-017-00541-w.
[7] R. Boonsin, G. Chadeyron, J.P. Roblin, D. Boyer, R. Mahiou, Development of rare-earth-free phosphors for eco-energy lighting based LEDs, J. Mater. Chem. C Mater. Opt. Electron. Devices 3 (2015) 9580–9587, https://doi.org/10.1039/c5tc01516b.
[8] H. Lin, T. Hu, Y. Cheng, M. Chen, Y. Wang, Glass ceramic phosphors: towards long-lifetime high-power white light-emitting-diode applications–a review, Laser Photonics Rev. 12 (2018), https://doi.org/10.1002/lpor.201700344.
[9] R. Casasola, J.M. Rincón, M. Romero, Glass-ceramic glazes for ceramic tiles: a review, J. Mater. Sci. 47 (2012) 553–582, https://doi.org/10.1007/s10853-011-5981-y.
[10] M.G. Rasteiro, T. Gassman, R. Santos, E. Antunes, Crystalline phase characterization of glass-ceramic glazes, Ceram. Int. 33 (2007) 345–354, https://doi.org/10.1016/j.ceramint.2005.10.002.
[11] O. Dymshits, M. Shepilov, A. Zhilin, Transparent glass-ceramics for optical applications, MRS Bull. 42 (2017) 200–205, https://doi.org/10.1557/mrs.2017.29.
[12] D. Chen, W. Xiang, X. Liang, J. Zhong, H. Yu, M. Ding, et al., Advances in transparent glass-ceramic phosphors for white light-emitting diodes-a review, J. Eur. Ceram. Soc. 35 (2015) 859–869, https://doi.org/10.1016/j.jeurceramsoc.2014.10.002.
[13] D. Barbin, V. Pagel, M. Blanc, P. Ohnenstetter, Cathodoluminescence in Geosciences, (2000).
[14] J. Garcia-Guinea, P.D. Townsend, L. Sanchez-Munoz, J.M. Rojo, Ultraviolet-blue ionic luminescence of alkali feldspars from bulk and interfaces, Phys. Chem. Miner. 26 (1999) 658–667, https://doi.org/10.1007/s002690050231.
[15] A.S. Marfunin, Spectroscopy, Luminescence and Radiation Centers in Minerals, (1979), https://doi.org/10.1007/978-3-642-67112-8.
[16] I. Parsons, Feldspars and Their Reactions, (1994), https://doi.org/10.1180/minmag.1995.059.397.23.
[17] I. Aliatis, E. Lambruschi, L. Mantovani, D. Bersani, S. Andó, G. Diego Gatta, et al., A comparison between ab initio calculated and measured Raman spectrum of triclinic albite (NaAlSi3O8), J. Raman Spectrosc. 46 (2015) 501–508, https://doi.org/10.1002/jrs.4670.
[18] E. Meneghinello, A. Alberti, G. Cruciani, Order-disorder process in the tetrahedral sites of albite, Am. Mineral. 84 (1999) 1144–1151.
[19] Andrew Putnis, The crystal structure of minerals II- silicates, An Introd. to Miner. Sci. (1992), pp. 141–184, https://doi.org/10.1017/CBO9781139170383.
[20] V. Correcher, J. Garcia-Guinea, L. Sanchez-Muñoz, T. Rivera, Luminescence characterization of a sodium-rich feldspar, Radiat. Eff. Defects Solids 162 (2007) 709–714, https://doi.org/10.1080/10420150701482063.
[21] V. Fuertes, M.J. Cabrera, J. Seores, D. Muñoz, J.F. Fernández, E. Enríquez, Hierarchical micro-nanostructured albite-based glass-ceramic for high dielectric strength insulators, J. Eur. Ceram. Soc. 38 (2018) 2759–2766, https://doi.org/10.1016/j.jeurceramsoc.2018.02.009.
[22] W.J. Rink, H. Rendell, E.A. Marseglia, B.J. Luff, P.D. Townsend, Thermoluminescence spectra of igneous quartz and hydrothermal vein quartz, Phys. Chem. Miner. 20 (1993) 353–361, https://doi.org/10.1007/BF00215106.
[23] S. Maki, S. Ohgo, H. Nishido, Cathodoluminescence characterization of feldspar minerals from granite-syenite rocks in Iwagijima Island, Ehime Prefecture, Japan, Naturalistae 18 (2016) 13–18.
[24] H. Kroll, W.F. Mfiller, X-ray and electron-optical investigation of synthetic high-temperature plagioclases, Phys. Chem. Miner. 5 (1980) 255–277, https://doi.org/10.1007/BF00348574.
[25] C.T. Pnbwttt, S. Surnol, J.J. Paprrp, The crystal structures of high albite and monalbite at high temperatures, Am. Mineral. 61 (1976) 2–3 http://www.minsocam.org/ammin/AM61/AM61_1213.pdf.
[26] R.T. Downs, R.M. Hazen, L.W. Finger, The high-pressure crystal chemistry of low albite and the origin of the pressure dependency of Al-Si ordering, Am. Mineral. 79 (1994) 1042–1052.
[27] D.B. Stewart, P.H. Ribbe, Structural explanation for variations in cell parameters of alkali feldspar with aluminum/silicon ordering, Am. J. Sci. (1969) 444–462.
[28] I.Y. Borg, D.K. Smith, Calculated X-ray powder patterns for silicate minerals, Geol. Soc. Am. Mem. (1969) 639–641, https://doi.org/10.1130/MEM122-p1.
[29] L.S. Muñoz, J.G. Guinea, S.L. Andrés, Caracterización estructural simple de feldespatos alcalinos: metodología de trabajo, Boletín La Soc, Española Cerámica y Vidr. 30 (1991) 69–79.
[30] E. Salje, Raman spectroscopic investigation of the order parameter behaviour in hypersolvus alkali feldspar: Displacive phase transition and evidence for Na-K site ordering, Phys. Chem. Miner. 13 (1986) 340–346, https://doi.org/10.1007/BF00308352.
[31] V. Fuertes de la Llave, A. del Campo, J.F. Fernández, E. Enríquez, Structural insights of hierarchically engineered feldspars by confocal Raman microscopy, J. Raman Spectrosc. (2019) 1–14, https://doi.org/10.1002/jrs.5556.
[32] J.J. Freeman, John J.Alian Wang, K.E. Kuebler, L.A. Haskin, Characterization of natural feldspar by Raman spectroscopy for future planetary exploration, Can. Mineral. 46 (2008) 1477–1500, https://doi.org/10.3749/canmin.46.6.1477.
[33] D. Bersani, I. Aliatis, M. Tribaudino, L. Mantovani, A. Benisek, M.A. Carpenter, et al., Plagioclase composition by Raman spectroscopy, J. Raman Spectrosc. 49 (2018) 684–698, https://doi.org/10.1002/jrs.5340.
[34] D.A. McKeown, Raman spectroscopy and vibrational analyses of albite: from 25°C through the melting temperature, Am. Mineral. 90 (2005) 1506–1517, https://doi.org/10.2138/am.2005.1726.

Tunable UV/blue Luminescence in Rare-earth Free Glass-ceramic Phosphor

V. Fuertes*[1], J. F. Fernández[1], E. Enríquez[2]

[1]Dept. Electrocerámica, Instituto de Cerámica y Vidrio, CSIC, Kelsen 5, 28049, Madrid, Spain.

[2]Centro tecnológico Vidres, S.L., Ctra. Onda, Km 3.4, 12540 Villareal, Castellón, Spain

Supporting information

S1. Raman spectroscopy analysis

According to the Raman modes observed in figure 4a, some tetrahedral cage-shear modes, below 200 cm^{-1}, are observed and present some changes in chemically modified samples concerning plain glass-ceramic. Raman mode at ca. 65 cm^{-1} for the glass-ceramic is mainly due to translation of the Na^+ cations accompanied by rigid rotations of the SiO_4 tetrahedra [1]. As it can be seen in Raman spectra depicted in figure 4a, this Raman mode gain importance when chemical modification with SiO_2 is used and undergoes a Raman red shift down to 61 cm^{-1}. In this case, the formation of a more albitic structure favours that a larger quantity of SiO_4 tetrahedra are presented. When Al_2O_3 is used as modifier this mode slightly decreases and remains at ca. 65 cm^{-1}. For the case of Na_2CO_3 and $CaCO_3$, it shifts to 61 cm^{-1} and 64 cm^{-1}, respectively, but its contribution remains approximately equal which might be due to not enough changes in SiO_4 distribution are generated regarding the plain glass-ceramic, because of the higher ability of Na^+ and Ca^{2+} cations to promote glass as glass network modifiers. Raman mode at ca. 75 cm^{-1} only appears in the glass-ceramic chemically modified with Na_2CO_3. This finding matches with the fact that translation of the Na^+ cations parallel to ***a*** axis are involved in this mode [1], because as Na-content increases in the glass-ceramic, more Na^+ cations will be available and activate this Raman mode. Raman mode at ca. 92 cm^{-1} is similar to the Raman mode placed at 65 cm^{-1} for the glass-ceramic but involve AlO_4 tetrahedra. For that reason, this Raman mode is more noticed in samples having higher amount of anorthitic structures, which are the plain and the Al_2O_3 modified glass-ceramic, as well as the glass-ceramic modified with Na_2CO_3, since Na^+ motions also contributes to this vibrational mode.

Na-O stretching mode placed at ca. 177cm^{-1} and it gains importance in all chemically modified glass-ceramic samples [2,3]. Addition of calcium cations activates in some extent this mode, keeping the same Raman shift, while silica and especially sodium cations clearly activate it, causing also a Raman red shift of 2 cm^{-1}, as it may be observed in figure 4a. Alumina addition also modifies Na-O bonds, causing a Raman blue shift to 183 cm^{-1}, as occurred for several of Raman modes above described. Raman mode of glass-ceramic at 197 cm^{-1} corresponds to a rotation-translation mode of the four-membered rings and is hardly visible. Nevertheless, it clearly appears in silica modified glass-ceramic and in lesser extent for samples modified with Na_2CO_3 and Al_2O_3.

Raman mode placed at 267 cm^{-1} is exhibiting a more marked broadening in more albitic sample. This broadening might be possibly produced by contribution of two rotation Raman modes [4]. This Raman mode correlated with another which mainly appear in alumina modified glass-ceramic, centered at 386 cm^{-1}, but also in silica doped sample, at 389 cm^{-1}, although is less pronounced. This is a bending mode more influenced by Al-O-Si bonds in the first case and Si-O-Si bonds in the second case [1]. Moreover, two broad Raman bands are observed between 600-900 cm^{-1} and 900–1200 cm^{-1}. According to the bibliography, these Raman bands correspond to tetrahedral deformation modes and vibrational stretching modes, respectively, and do not present significant changes in the studied glass-ceramic.

S2. Calculation of Band Gap

The Energy gap has been obtained through the Tauc's theory that relates the absorption coefficient with the band gap as follows:

$$\alpha = \left(h\nu - E_g\right)^{\frac{1}{\gamma}}$$

Where h is the Planck constant, $\nu = \frac{c}{\lambda}$, E_g is the energy gap and γ is a constant that indicates the kind of transition. In this case, γ = 1/2, since is an allowed direct transition.

In this work, diffused reflectance of samples powders is measured. In bulk materials, when light passes through the layer, part is absorbed and lost, and some part of the light is scattered and changes its direction from upwards to downwards, or vice versa. Following the Kubelka Munk theory, two coefficients K and S are introduced to denote the amount of absorption and direction changing scattering, respectively. The scattering and absorption are both proportional to the intensities and to the thickness of the layer. Therefore, in order to correct the reflection measures, the Kubelka Munk approximation is used:

$$F(R) = \frac{(1-R)^2}{2R} = \frac{K}{S}$$

Where K is the absorption coefficient (α), S is the scattering factor and R the reflectance. In samples with thickness above 1μm, F(R) is independent of S.

Therefore, obtaining the Kubelka Munk function [5-7] it is possible to obtain the band gap by means of linearly extrapolating the absorption to α = 0. Figure S1 shows the Tauc's curve. Table S1 presents the bang gap value obtained.

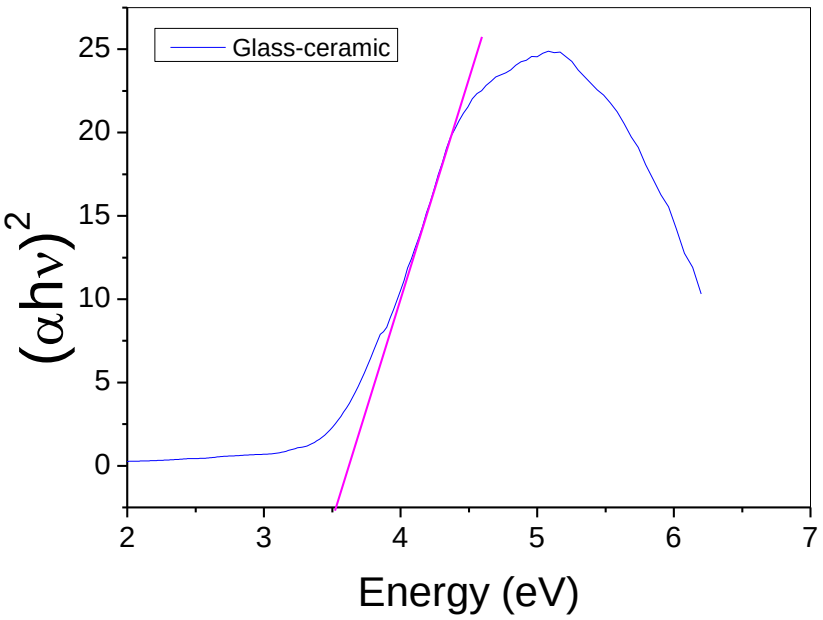

Figure S1. Tauc's theory curves of glass-ceramic obtained through the Kubelka Munk function with the band gap obtained by linearly extrapolating the absorption to α = 0.

Sample	Energy gap (E_g) (eV)
Glass-ceramic	3.65

Table S1. Glass-ceramic energy gap obtained through Kubelka Munk function.

References

[1] I. Aliatis, E. Lambruschi, L. Mantovani, D. Bersani, S. Andó, G. Diego Gatta, et al., A comparison between ab initio calculated and measured Raman spectrum of triclinic albite ($NaAlSi_3O_8$), J. Raman Spectrosc. 46 (2015) 501–508. doi:10.1002/jrs.4670.

[2] M. Zhang, B. Wruck, A. Graeme Barber, E.K.H. Salje, M.A. Carpenter, Phonon spectra of alkali feldspars: Phase transitions and solid solutions, Am. Mineral. 81 (1996) 92–104.

[3] D.A. McKeown, Raman spectroscopy and vibrational analyses of albite: From 25°C through the melting temperature, Am. Mineral. 90 (2005) 1506–1517. doi:10.2138/am.2005.1726.

[4] I. Aliatis, Vibrational dynamics and structure of natural feldspars, 2016.

[5] V. Džimbeg-malčić, Ž. Barbarić-mikočević, K. Itrić, Kubelka-Munk Theory in Describing Optical Properties of Paper (I), Tech. Gaz. 18 (2011) 117–124.

[6] C.M.C.V.R. Aragón, Evidencia óptica de semiconducción directa en γ ´ -Bi2 MoO_6, An. Afa. 17 (2005) 170–172.

[7] R. Kubrin, Nanophosphor coatings: Technology and applications, opportunities and challenges, KONA Powder Part. J. 31 (2014) 22–52. doi:10.14356/kona.2014006.

Capítulo 5.

Discusión Integradora

El trabajo de investigación desarrollado en esta memoria ha tenido como objetivo principal el desarrollo de una nueva familia de materiales vitrocerámicos micro-nanoestructurados, basados en cristalizaciones de feldespatos, con el fin de maximizar ciertas propiedades y dotarlos de nuevas funcionalidades de cara a su uso en diferentes aplicaciones. En esta sección se discuten globalmente los resultados obtenidos y presentados en los diferentes artículos de investigación que se incluyen en esta Tesis Doctoral, con el fin de integrar las conclusiones a las que se ha llegado en cada uno de los trabajos. Como se comentó anteriormente, se han desarrollado dos materiales vitrocerámicos basados en cristalizaciones de feldespatos, uno rico en albita y otro en anortita, por medio de una ruta cerámica convencional y un proceso de sinterización rápido. A la hora de estudiar sus propiedades, se ha optado por uno u otro, o ambos, en función de sus características, tal y como se justificará a continuación.

1.4. Mecanismo de cristalización de la nueva familia de materiales vitrocerámicos

En los artículos de investigación en los que se estudia la estructura y microestructura de los materiales, esto es: "***Study of the Crystallization in fast sintered Na-rich plagioclase glass-ceramic***" (artículo 1) y "***Structural insights of hierarchically engineered feldspars by confocal Raman microscopy***" (artículo 2); se analizó a fondo el mecanismo de cristalización del material vitrocerámico rico en cristalizaciones de feldespatos sódicos, debido a que presentaba una elevada complejidad estructural y, por tanto, la información extraída de dicho compuesto proporcionaría una visión más completa de la estructura y la microestructura diseñada. Se obtuvo que dicho material vitrocerámico es un material denso que presenta una elevada cantidad de fase cristalina, ~94%, y está basado en cristalizaciones de feldespatos de tipo plagioclasa rica en sodio, con un contenido de anortita estimado de 25-45 %. La microestructura diseñada está caracterizada por tener una micro-nanoestructuración jerárquica en la que microcristales, típicamente 0,8-3 μm de longitud y 0,4-0,6 μm de anchura, están aislados unos de otros por medio de regiones nanoestructuradas que presentan nanocristales de 10-20 nm de diámetro, tal y como se observa en la Figura 5.1a y b. Además, en ciertas regiones microestructuradas se producen procesos de desmezcla por descomposición espinodal, formándose dominios lamelares de ~2-3 μm, como se puede apreciar en la micrografía de TEM que se observa en la Figura 5.1c. En cuanto a la estructura de esta plagioclasa rica en Na^+, existe un cierto desorden en la distribución de Si,Al en las posiciones tetraédricas, que está favorecido por la presencia de

una cantidad considerable de cationes divalentes en la estructura, Ca^{2+} y Sr^{2+}, y de K^{+} en menor medida. Por tanto, la estructura de la plagioclasa sódica puede ser considerada como una estructura de albita con cierto desorden en la distribución de Si,Al , que da lugar a la aparición de defectos de tipo Al-O^{-}-Al o [AlO_4/alcalino^{+}], uno de los principales centros luminiscentes en feldespatos minerales. En la Figura 5.1d se representan a modo de ejemplo dos anillos tetraédricos característicos de dicha estructura.

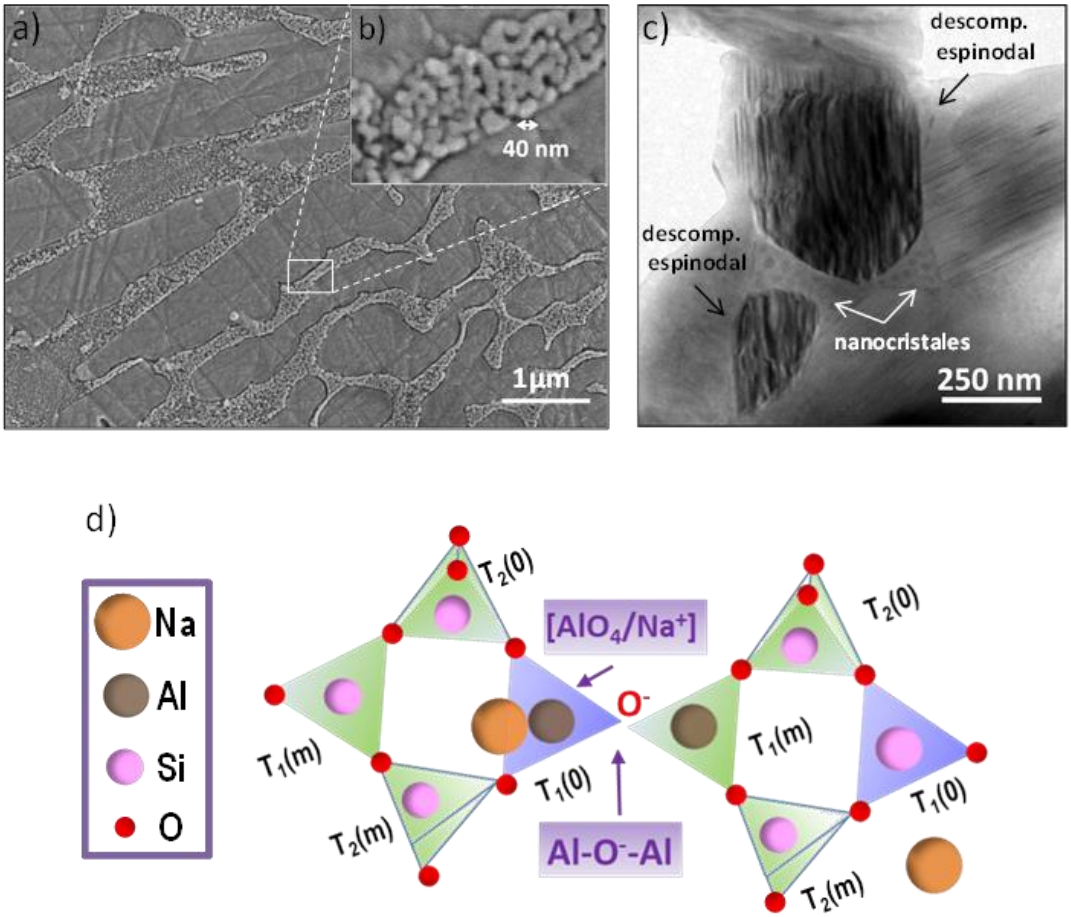

Figura 5.1. Micrografías de FESEM de albita vitrocerámica en las que se muestra: **a)** la presencia de microcristales alargados aislados por regiones nanoestructuradas y **b)** la zona nanoestructurada en mayor detalle. **c)** Micrografía de TEM que muestra un patrón a rayas en la zona microestructurada, indicando un proceso de desmezcla por descomposición espinodal. Además, se observan nanocristales situados en las zonas nanoestructuradas. **d)** Estructura de una plagioclasa sódica formada por anillos de cuatro tetraedros con átomos de silicio (representados en rosa) o aluminio (representados en marrón), con una relación Si:Al de 3:1 y donde cada oxígeno (representado en rojo) une dos tetraedros. Los átomos de sodio se presentan en naranja. En la estructura triclínica, existen cuatro sitios simétricamente no

equivalentes, etiquetados como T1 (0), T1 (m), T2 (0) y T2 (m). El Al está en los sitios T1 (0). La estructura de la plagioclasa sódica puede ser considerada como una estructura de albita con cierto desorden en la distribución de Si,Al, lo cual da lugar a la aparición de defectos de tipo Al-O--Al o [AlO_4/Na^+], principalmente.

En el caso del material vitrocerámico basado en cristalizaciones de feldespato de Ca^{2+} (anortita), también cabe destacar la presencia de una elevada cristalinidad, ~91 %. La microestructura del material presenta cristales alargados de anortita de 5-10 μm de longitud, así como cristales de $ZrSiO_4$ con formas irregulares y diámetros comprendidos entre 0,5 y 2 μm, tal y como se puede observar en la Figura 5.2a. Además, este vitrocerámico también se caracteriza por tener regiones nanoestructuradas formadas por nanocristales de anortita y partículas pseudoesféricas de ZrO_2 (con diámetros de 100–300 nm) (Figura 5.2b). Esta composición y micro-nanoestructuración proporcionan al material una elevada blancura (L*=94,59; a*=-0,85; b*=0,85), aunque posee menor transparencia que el vitrocerámico rico en albita. Por ello, el vitrocerámico rico en calcio fue el material seleccionado para el estudio de las propiedades termorreflectantes, de cara a su empleo en baldosas para aplicaciones de ahorro energético y sostenibilidad.

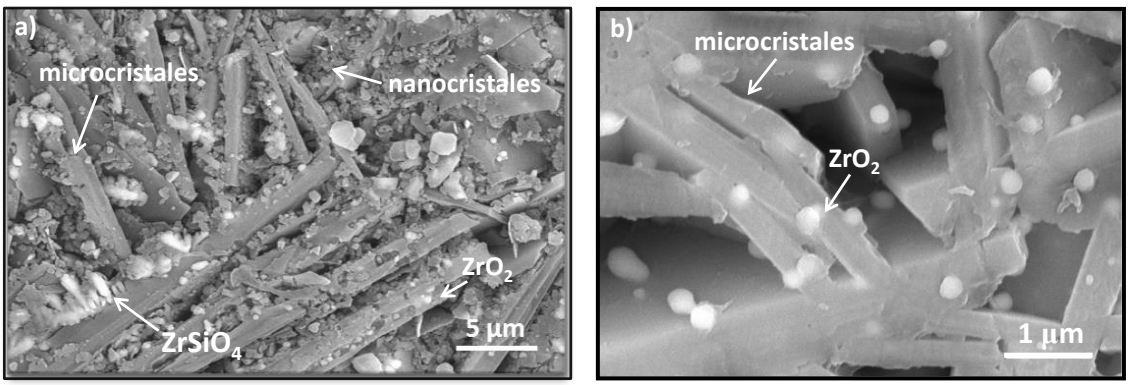

Figura 5.2. a) Micrografía de FE-SEM de anortita vitrocerámica en las que se muestra la presencia de microcristales alargados y regiones nanoestructuradas de anortita, así como granos cristalinos de ZrO_2 monoclínico y $ZrSiO_4$ tetragonal; **b)** se muestra en mayor detalle una región con microcristales de anortita y granos cristalinos de ZrO_2 monoclínico.

La estructura de la anortita, a diferencia de la de albita, es esencialmente ordenada, desde un punto de vista de la distribución de Si,Al en las posiciones tetraédricas en la red del

feldespato. Este orden estructural limita la existencia de defectos de tipo Al-O$^-$-Al o [AlO_4/alcalino$^+$] que, como se ha comentado anteriormente, es uno de los principales centros luminiscentes en feldespatos. Por ello, las propiedades luminiscentes en materiales de tipo plagioclasa cálcica o en su end-member, "anortita", no resultan de interés, sin embargo, en materiales de tipo plagioclasa sódica o en su end-member, "albita", este estudio aporta un avance relevante en materiales funcionales basados en feldespatos con capacidad luminiscente. El resto de propiedades, tanto mecánicas como dieléctricas, son, a priori, interesantes de estudiar en ambos sistemas, ya que poseen una micro-nanoestructuración singular, una baja porosidad y una elevada cristalinidad, parámetros que resultan fundamentales en estas propiedades, tal y como se discutirá a continuación.

1.5. Correlación entre la estructura y microestructura de los materiales vitrocerámicos y sus propiedades funcionales.

La Tabla 5.1 resume la correlación entre las características estructurales y microestructurales de los materiales vitrocerámicos basados en cristalizaciones de feldespatos y las propiedades estudiadas. Dicha tabla representa una ayuda para comprender cómo influyen las características físico-químicas en las propiedades funcionales, tal y como será analizado detalladamente a continuación.

		Propiedades			
		Mecánicas	**Termorreflectantes**	**Dieléctricas**	**Luminiscentes**
Microestructura	microcristales	✓✓	✓✓	✓✓	✓
	nanocristales	✓✓✓	✓✓✓	✓✓✓	✓
	cristalinidad	✓✓	-	✓✓	✓✓
	porosidad	✓	✓	✓✓	-
Estructura	defectos estructurales	-	-	-	✓✓✓
	estructura	-	-	-	✓✓✓

Tabla 5.1. Tabla resumen en la que se muestra la correlación entre las características estructurales y microestructurales de los materiales vitrocerámicos basados en cristalizaciones de feldespatos y las propiedades estudiadas. El número de símbolos verdes indican, de forma cualitativa, la influencia de cada parámetro en la propiedad correspondiente.

En los trabajos titulados ***"Enhanced Wear Resistance of Engineered Glass-ceramic by Nanostructured Self-lubrication"*** (artículo 3) y **"High impact resistance of new glass-ceramics tiles"** (artículo 4) se examinaron diferentes propiedades mecánicas. El artículo 3 se centró en la resistencia a la flexión, el módulo de Young, la dureza Vickers, la tenacidad a la fractura y las propiedades tribológicas. Como se puede observar en la Tabla 5.1 y como se ha discutido en dicho artículo, las propiedades mecánicas de ambos materiales vitrocerámicos se ven muy influenciadas por la ingeniería de la microestructura llevada a cabo. La combinación de la presencia de cristales de tamaño micrométrico y, especialmente, de tamaño nanométrico, resulta en un mayor número de fronteras de grano con respecto a materiales convencionales empleados como esmaltes con cristalizaciones en el sector cerámico, lo cual va a dificultar la propagación de grietas en la microestructura, debido a que, en las fronteras de grano se relajan las tensiones y aumenta la tortuosidad y, consecuentemente, aumentando así su resistencia a la fractura. Además, el tamaño de grano también influye en la resistencia mecánica del material, de manera que, cuanto mayor sea el tamaño, más frágil es el material. Por tanto, esta singular distribución de nano y micropartículas va a mejorar la resistencia mecánica, puesto que la aparición de nanocristales frena el crecimiento de los microcristales, tal y como se explica en el ***artículo 1***. De esta forma, se obtienen valores de resistencia a la fractura de hasta 2.1 $MPa \cdot m^{1/2}$ en ambos materiales vitrocerámicos, lo cual supone un aumento de un 40 % con respecto a un esmalte convencional y es comparable a los mejores valores obtenidos para porcelanas, cuya fase vítrea se ve reforzada estructuralmente mediante modificaciones de su composición (Figura 5.3a). [91] Este tipo de microestructura también va a influir en la mejora de la resistencia a la flexión, obteniéndose valores de 83 MPa y 111 MPa para los materiales vitrocerámicos de albita y anortita, respectivamente. Estos valores son comparables con los mejores valores obtenidos en la literatura para baldosas de gres porcelánico, donde la resistencia a la flexión alcanza valores en torno a 96 MPa, [139] y muy superiores a los típicos alcanzados en esmaltes convencionales o soportes porcelánicos, los cuales se sitúan en torno a 60 MPa.

El módulo de Young y la dureza se obtuvieron a partir de los ensayos de indentación Vickers. En el caso del módulo de Young, se obtuvieron valores de 66-78 N, comparables con los valores típicos reportados para baldosas cerámicas, por lo que en este caso la micro-nanoestructura no juega un papel fundamental. Sin embargo, la dureza sí se vio fuertemente afectada por la micro-nanoestructura, obteniéndose valores de hasta 9,5 GPa, nunca reportados hasta la fecha para un esmalte, suponiendo una mejora de un 59 % con respecto a los registrados en esmaltes convencionales empleados en la industria (Figura 5.3b). [89] Esta gran

mejora de las propiedades mecánicas está, a su vez, influenciada por el grado de cristalinidad, ya que los materiales cerámicos convencionales se caracterizan por tener una elevada cantidad de fase vítrea, sin embargo, los vitrocerámicos desarrollados poseen una cantidad inferior al 9%. Tal y como se vio en el ***artículo 1,*** en esta nueva familia de materiales vitrocerámicos, la fase vítrea procedente de la frita precursora juega un papel fundamental en la cristalización de la nanoestructura. Durante el calentamiento, esta fase vítrea, que se encuentra en estado líquido, ataca a los microcristales que han comenzado a formarse en esta etapa, logrando la nucleación de nanopartículas del mismo compuesto en los alrededores, gracias al enriquecimiento composicional procedente de los microcristales. Este proceso favorece que apenas quede fase vítrea residual en el material sinterizado, puesto que, al combinarse con el microcristal atacado, forma las nanopartículas mencionadas anteriormente.

Por último, cabe destacar la baja porosidad presente en ambos esmaltes vitrocerámicos, siendo el tamaño medio de poro inferior a 5 μm. La comparación con un esmalte convencional con valores similares de porosidad, pero con un tamaño medio de poro superior, de en torno a 18 μm, sugiere que la reducción de dicho tamaño también puede afectar a la mejora de las propiedades mecánicas, aunque en el caso del vitrocerámico, el factor dominante es la micro-nanoestructuración diseñada.

Como se ha comentado, la presencia de zonas nanoestructuradas juega un papel muy importante en la mejora de las propiedades mecánicas anteriormente mencionadas, pero en el caso de las propiedades tribológicas va a desempeñar un papel aún mayor. En el trabajo del ***artículo 3*** se demostró que los nanocristales actúan como lubricantes sólidos, favoreciendo el deslizamiento de los cuerpos sobre su superficie y reduciendo, consecuentemente, la tasa de desgaste y el daño sufrido. Todo ello se traduce en una disminución del ~36 % en el coeficiente de rozamiento y de la tasa de desgaste de más de un orden de magnitud con respecto a un esmalte convencional.

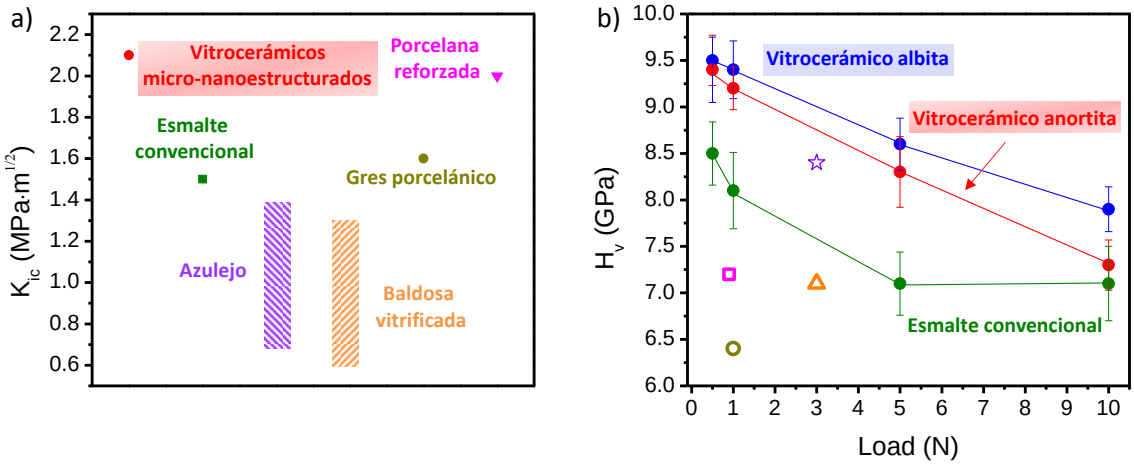

Figura 5.3. a) Resistencia a la fractura de los vitrocerámicos micro-nanoestructurados desarrollados en este trabajo, en comparación con: un esmalte convencional, un azulejo, [90] gres porcelánico, [91] una baldosa vitrificada [90] y una porcelana cuya fase vítrea es reforzada por tensiones. [91] **b)** Dureza vs carga en los vitrocerámicos micro-nanoestructurados, comparados con valores medidos para un esmalte convencional y los mejores valores reportados en la bibliografía para esmaltes vitrocerámicos basados en: cordierita (estrella violeta) y mullita (triángulo naranja), [88] el sistema CaO-MgO-SiO_2-Al_2O_3 (circulo amarillo oscuro) [93] y el sistema CaO-MgO-SiO_2-Al_2O_3-ZrO_2 (cuadrado rosa). [89] Las líneas son guías para el ojo. Los materiales diseñados en este trabajo están recuadrados en rojo y/o azul.

Todos estos factores discutidos previamente, es decir, la presencia de un mayor número de intercaras, principalmente debido a la cristalización de nanocristales, junto con una baja cantidad de fase vítrea y porosidad, favorecen una mejora considerable de la resistencia al impacto en estos materiales vitrocerámicos, eliminando el daño y el desconchamiento con respecto a un esmalte convencional, comportándose como un material elástico, a pesar de que el coeficiente de resiliencia se mantiene, tal y como se evaluó y discutió en el **artículo 4**.

Por tanto, se puede concluir que la nanoestructuración desarrollada en esta nueva familia de materiales vitrocerámicos basados en cristalizaciones de feldespatos es fundamental para obtener un rendimiento mecánico superior. El desarrollo de esmaltes nanoestructurados en la industria cerámica podría cubrir las necesidades actuales del sector e incluso mejorar las características de los productos, como se ha demostrado en este trabajo de investigación.

Las propiedades dieléctricas fueron evaluadas en los trabajos "***Hierarchical micro-nanostructured albite-based glass-ceramic for high dielectric strength insulators"*** *(artículo 5)* y "***Microstructural study of dielectric breakdown in glass-ceramics insulators"*** *(artículo 6)*. En ambos trabajos, se demostró que esta nueva familia de materiales vitrocerámicos posee un comportamiento aislante dieléctrico muy superior a otros materiales cerámicos convencionales, tales como alúmina, cordierita, esteatita o porcelanas de aluminosilicatos, como se observa en la Figura 5.4. La resistencia dieléctrica de estos materiales se sitúa por encima de 59 kV/mm a temperatura ambiente, lo cual supone una mejora de un 67-83 % con respecto a los materiales convencionales anteriormente mencionados y es comparable con la obtenida en la mica natural, la más elevada reportada para un mineral hasta la fecha. Además, estos materiales son capaces de evitar la ruptura dieléctrica hasta temperaturas de ~200 ºC, alcanzándose resistencias dieléctricas en el rango 30-44 kV/mm. De nuevo, la microestructura juega un papel fundamental en el comportamiento dieléctrico observado. Al poseer un gran número de fronteras de grano, los electrones van a sufrir una mayor dispersión con respecto a un material convencional. Sin embargo, existe el riesgo de que se produzca acumulación de carga en dichas intercaras del material. Tal y como se vio en el estudio de la cristalización de este tipo de materiales, la fase vítrea se encuentra ubicada en la frontera entre los cristales micrométricos y los nanométricos. La fase vítrea es más conductora que la cristalina en este caso, lo cual favorece el flujo de electrones a través de las fronteras de grano, evitando el atrapamiento de carga en éstas y favoreciéndose la difusión por un proceso de "hopping" acompañado de un movimiento traslacional. Además, la presencia de zonas nanoestructuradas es fundamental para la obtención del buen comportamiento resistivo con respecto a un material que sólo posea zonas microestructuradas, debido a que se favorecen, en mayor medida, eventos de dispersión en superficie. Así mismo, la mejora del comportamiento como aislador dieléctrico se ve favorecida por una baja porosidad del material, ya que los poros son sitios preferentes de atrapamiento de carga.

La elevada cristalinidad de estos materiales vitrocerámicos se manifiesta principalmente en la disminución de las pérdidas dieléctricas, $\sim 10^{-3}$, comparables a las registradas en otros materiales dieléctricos similares de la bibliografía. Sin embargo, la estructura no parece influir en las propiedades dieléctricas, puesto que, a pesar de que la albita es más desordenada que la anortita desde un punto de vista de distribución de Si,Al, aspecto que favorece la presencia de un mayor número de defectos estructurales (Al-O^--Al, [AlO_4/alcalino$^+$] etc), el vitrocerámico rico

en cristalizaciones de tipo albita posee un comportamiento aislante dieléctrico superior. Por tanto, en este caso, las características microestructurales son las que dominan, una vez más.

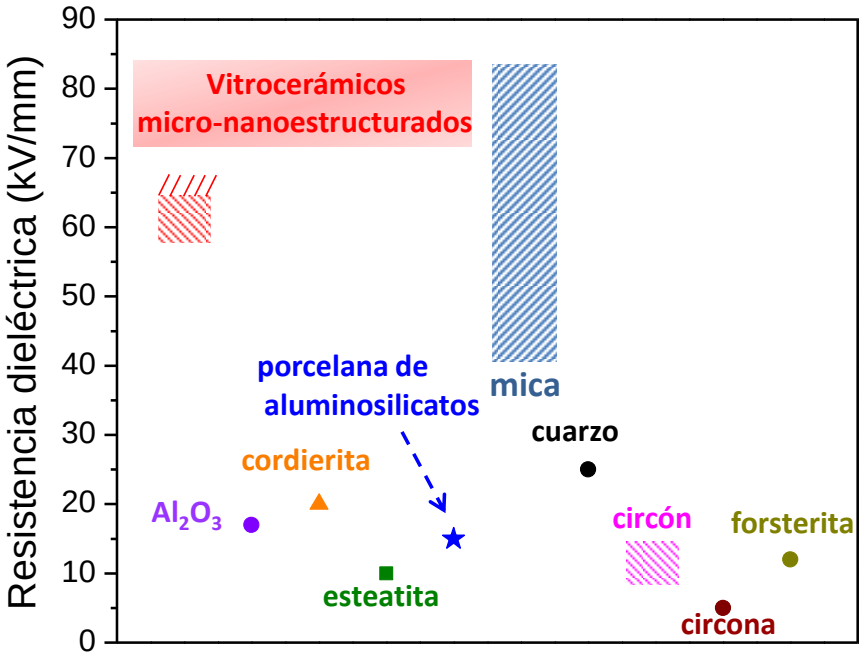

Figura 5.4. Resistencia dieléctrica para los materiales vitrocerámicos micro-nanoestructurados desarrollados en este trabajo, en comparación con materiales cerámicos dieléctricos del mercado:[78] Al_2O_3, cordierita, esteatita, porcelana de aluminosilicatos, mica, cuarzo, circón, circona y forsterita. Los materiales diseñados en este trabajo están recuadrados en rojo.

Por otro lado, las propiedades termorreflectantes fueron evaluadas en el trabajo "***New strategy to mitigate urban heat island effect: Energy saving by combining high albedo and low thermal diffusivity in glass ceramic"*** *(artículo 7)*, donde se estudia el efecto de la microestructura en las propiedades térmicas y ópticas. En el caso de las propiedades térmicas, se observa una disminución significativa de la conductividad térmica en el material vitrocerámico, alcanzándose valores tan bajos como 0,35 W/mK, que conlleva también una disminución del ~60 % en la difusividad térmica con respecto a un esmalte estándar, tal y como se puede observar en la Figura 5.5, donde también se puede comparar con la conductividad térmica para un mineral de anortita, 1,7 W/mK.[103]

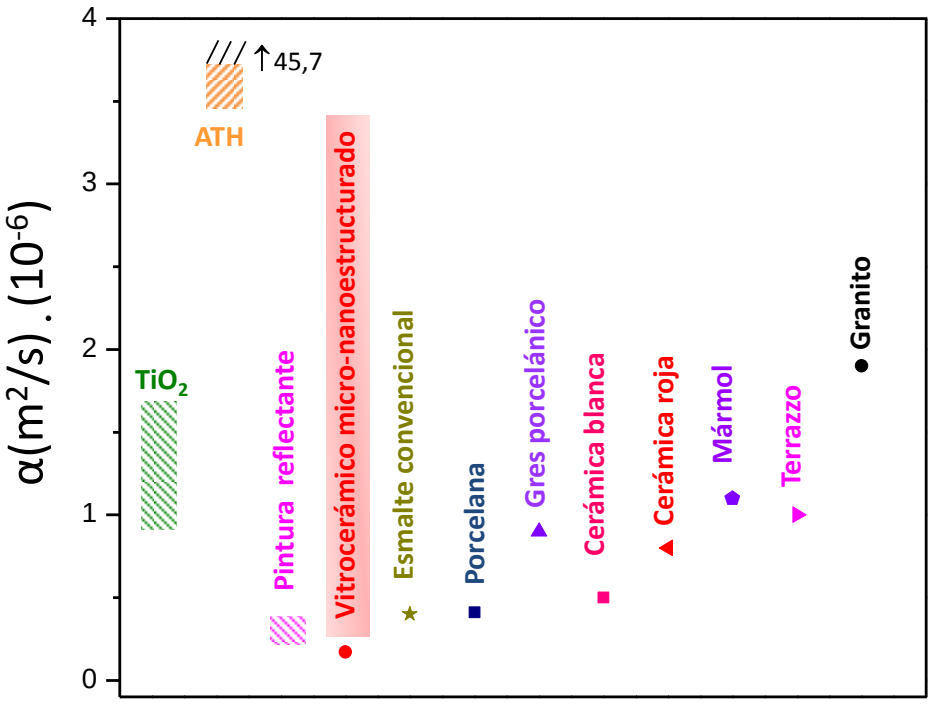

Figura 5.5. Difusividad térmica del material vitrocerámico micro-nanoestructurado desarrollado en este trabajo, en comparación con materiales empleados como aditivos en pinturas reflectantes tales como TiO_2 [131,132] y ATH;[133,134] así como un esmalte convencional evaluado[140] y otros materiales empleados en baldosas cerámicas: porcelana, [127] gres porcelánico, cerámica blanca, cerámica roja, mármol, terrazo y granito.[122] Los materiales diseñados en este trabajo están recuadrados en rojo.

Es bien sabido, que valores elevados de porosidad favorecen la disminución de la conductividad térmica del material. Sin embargo, este material posee una baja porosidad lo que debería, a priori, favorecer el transporte de fonones y, por tanto, la conducción del calor, obteniéndose valores de K superiores a los medidos. En el esmalte convencional evaluado, los cristales se encuentran embebidos en la fase vítrea, la cual forma un continuo que supone un ≈35 % del material, frente al 9 % que se encuentra en el material vitrocerámico. Está disposición de la fase vítrea favorece la propagación de los fonones a través del continuo, al contrario de lo que ocurre en el material vitrocerámico, donde la fase vítrea se encuentra en regiones aisladas, entre los bordes de grano. De esta manera, se demuestra de nuevo la gran influencia microestructural en el material vitrocerámico de nueva formulación, ya que al tratarse de un material con un mayor número de fronteras de grano que un esmalte convencional comercializado en el sector, gracias a la presencia de microcristales, nanocristales y diversas

fases secundarias, se favorecen en mayor medida los fenómenos de dispersión de fonones, dificultando su propagación y, por tanto, disminuyendo su conductividad térmica. En este caso, la fase vítrea no forma un continuo, si no que se encuentra en la frontera entre los microcristales y nanocristales, como ya se comentó, por lo que los fonones encuentran un mayor número de obstáculos en su propagación. Así mismo, como se explicó anteriormente, la anortita presenta una estructura mayormente ordenada desde un punto de vista de distribución de Si,Al en los anillos tetraédricos, por tanto, la ausencia de defectos estructurales en dicho material descarta la presencia de centros de dispersión adicionales en el material, reforzando nuevamente la idea de que la microestructura juega un papel fundamental.

El comportamiento óptico también se ve afectado por la micro-nanoestructuración, favoreciéndose la reflexión de fotones, especialmente la reflectancia difusa, y lográndose así una mayor reflectividad del espectro solar, ~12 % superior a una convencional. La baja porosidad de estos nuevos materiales vitrocerámicos también favorece el aumento de la reflectancia superficial, puesto que se evita la absorción de fotones en los poros, contribuyendo a una mayor reflexión total. La reflectividad solar (SR) media del vitrocerámico es similar a la de la pintura comercial, ~85 %, con la diferencia de que el material vitrocerámico se caracteriza por tener una mayor reflexión en la zona del infrarrojo cercano. La combinación de un mayor albedo junto con una menor difusividad térmica se traduce en un ahorro energético en climatización superior al 20 %, cuando se emplea esta nueva familia de materiales vitrocerámicos en fachadas o tejados, en lugar de baldosas convencionales. Además, si fueran empleadas como revestimientos de edificios o como baldosas para zonas de tránsito, reducirían problemas de degradación y mantenimiento, típicos en materiales con recubrimientos basados en pinturas reflectantes, gracias al alto rendimiento mecánico de estos materiales, tal y como se ha demostrado en trabajos anteriores.

Por último, se evaluaron las propiedades luminiscentes en los trabajos "***Enhanced Luminescence in Rare-earth free Fast Sintering Glass-ceramic"*** *(artículo 8)* y "**Tunable UV/blue Luminescence in Rare-earth Free Glass-ceramic Phosphor**" *(artículo 9)*. En estos trabajos, se pudo confirmar que las matrices de tipo plagioclasa rica en sodio son más adecuadas para aplicaciones luminiscentes que las ricas en calcio, ya que en las primeras se favorece en mayor grado el desorden estructural de Si,Al en las posiciones tetraédricas del feldespato, mientras que en las segundas predomina el orden estructural. Dicho desorden estructural es fundamental, ya que permite la generación de defectos estructurales que actúan como centros activos luminiscentes, principalmente enlaces de tipo Al-O^--Al, así como complejos

[AlO_4/alcalinos$^+$] y [AlO_4]^0, tal y como se observa en la Figura 5.1. Todo ello se traduce en un aumento de la intensidad de emisión luminiscente de un orden de magnitud y de seis veces en las emisiones del UV/azul y rojo, respectivamente, con respecto a un feldespato natural. A su vez, este comportamiento se ve potenciado por la elevada cristalinidad de la matriz vitrocerámica desarrollada en este trabajo de investigación. Es bien sabido que el campo cristalino ejerce una fuerte influencia en la fotoluminiscencia de un material, de manera que, en las matrices amorfas, como la de los vidrios, donde existen multitud de defectos puntuales, tienen lugar recombinaciones no radiativas. Sin embargo, en matrices cristalinas, se producen más favorablemente recombinaciones e^-- h que dan lugar a recombinaciones radiativas, bien a través de transiciones directas o por medio de defectos estructurales. Por tanto, la combinación de la elevada cristalinidad del material vitrocerámico de tipo albita, ~94%, y su estructura desordenada, proporciona una matriz idónea para este tipo de aplicaciones. Además, se ha demostrado que la emisión fotoluminiscente puede ser modulada en estos materiales, tanto en intensidad como en longitud de onda, mediante la modificación de dicho desorden Si,Al en la estructura, gracias a ligeras variaciones químicas de los elementos estructurales. Sin embargo, en este caso de las propiedades luminiscentes, la microestructura no juega un papel tan importante como ocurre en el comportamiento dieléctrico, mecánico y termorreflectante, ya que los defectos de ambas fases contribuyen aproximadamente igual en la emisión luminiscente.

1.6. Aplicaciones potenciales de la nueva familia de materiales vitrocerámicos diseñados

En base a los resultados obtenidos en esta Tesis Doctoral y la discusión llevada a cabo, se abre un amplio abanico de posibilidades de cara a las aplicaciones de esta nueva familia de materiales vitrocerámicos micro-nanoestructurados jerárquicamente en diferentes campos, tal y como se muestra a continuación y en la Figura 5.6.

- El buen comportamiento aislante dieléctrico sugiere su uso en aplicaciones de alto voltaje como aislador eléctrico, así como en aislamiento dieléctrico en electrodomésticos o en circuitos miniaturizados, entre otros.

- El buen comportamiento mecánico sugiere su aplicación en baldosas para su aplicación en pavimentos de alto tránsito o revestimientos de edificios.

- El buen comportamiento luminiscente supone una alternativa a los fósforos que emplean tierras raras, destacando en aplicaciones como vidrios emisores de luz o marcadores de seguridad. Dicho comportamiento inusual ha dado lugar a la solicitud de una primera patente de aplicación (EP19382045.3), incluida en el **anexo I.** Se trata de una nueva familia de marcadores que se evalúan mediante espectroscopia Raman. Por motivos de confidencialidad no se pueden divulgar más detalles, además de que se encuentran fuera del objeto de esta Tesis.

Las buenas propiedades termorreflectantes sugieren su aplicación en pavimentos reflectantes, revestimientos o en "cool roofs"

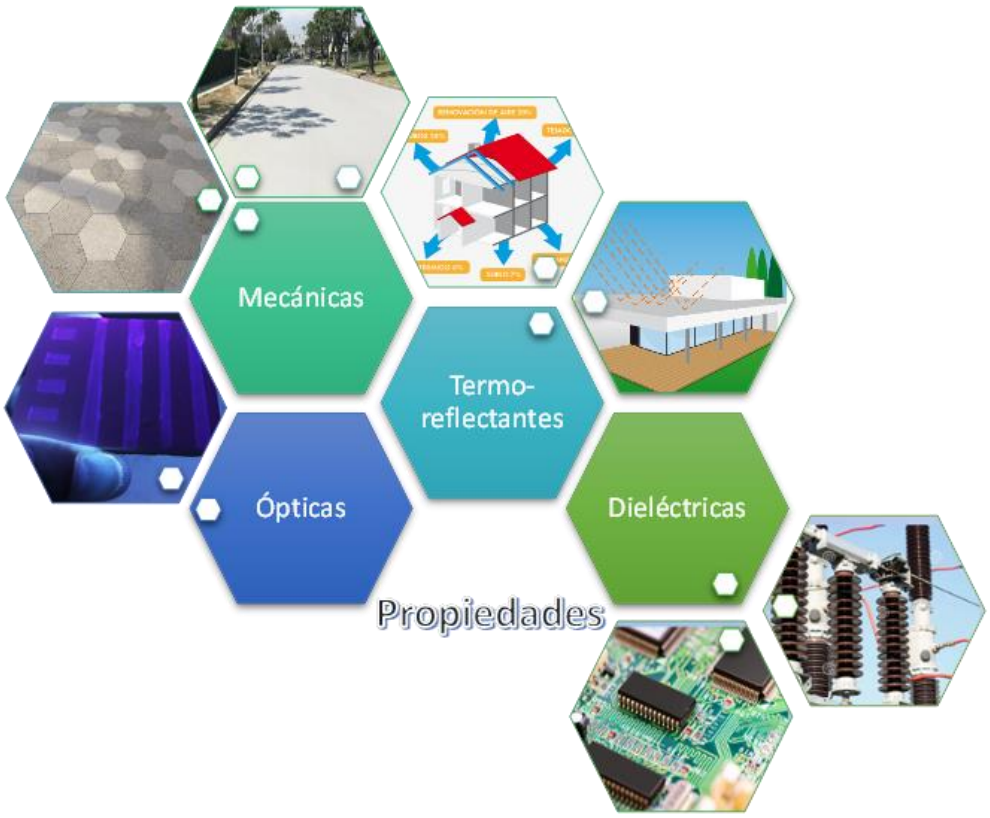

Figura 5.6. Esquema resumen de las posibles aplicaciones de los materiales vitrocerámicos micro-nanoestructurados desarrollados, gracias a las buenas propiedades dieléctricas, ópticas, mecánicas y termorreflectantes que poseen.

Capítulo 6.

Conclusiones

Tras el análisis de los resultados obtenidos en este trabajo de investigación se pueden extraer las conclusiones más relevantes que se muestran a continuación:

• Se han obtenido materiales vitrocerámicos basados en feldespatos mediante un proceso cerámico convencional y un proceso de sinterización rápido, a 1220 ºC durante 6 min con una tasa de calentamiento de 30 ºC/min. Estos materiales presentan una elevada densificación y una elevada cristalinidad (> 90 %). Además, se ha logrado diseñar una micro-nanoestructuración del material, donde se combinan cristalizaciones de diferentes tamaños distribuidas de forma jerárquica.

• Se ha demostrado que la ingeniería microestructural de los materiales vitrocerámicos basados en cristalizaciones de feldespatos es fundamental para la obtención de materiales con propiedades funcionales mejoradas con respecto a los convencionales de los esmaltes con cristalizaciones de feldespatos empleados en el sector cerámico. Dicha ingeniería está, principalmente, condicionada por dos parámetros: la composición de la frita precursora y el tratamiento térmico llevado a cabo.

• La presencia de un mayor número de fronteras de grano, consecuencia de las zonas micro y nanoestructuradas, favorece que se produzcan una mayor cantidad de fenómenos de dispersión de electrones, fonones y fotones, con respecto a un esmalte cerámico convencional. Esto da lugar a una modificación de las características del material, tales como poseer un elevado albedo, una baja difusividad térmica, elevada resistencia a la fractura y a la flexión, así como alcanzar los mejores valores de resistencia dieléctrica y dureza obtenidos para un aislador dieléctrico y un esmalte cerámico, respectivamente.

• Se ha demostrado que las zonas nanoestructuradas actúan como lubricantes sólidos, reduciendo considerablemente el coeficiente de fricción, la tasa de desgaste y el daño sufrido por la superficie del esmalte vitrocerámico, de manera que, en este caso, el proceso de desgaste se puede asemejar a un proceso de pulido.

• Se ha comprobado que las matrices de tipo plagioclasa rica en sodio con cierto desorden estructural de Si,Al en las posiciones tetraédricas del feldespato son adecuadas para aplicaciones luminiscentes. Esto es debido a que dicho desorden permite la generación de defectos estructurales que actúan como centros activos luminiscentes, principalmente enlaces de tipo Al-O^--Al y complejos [AlO_4/alcalinos$^+$]. Además, se determinó que tanto la intensidad de la emisión fotoluminiscente, como la longitud de onda de la emisión, se pueden sintonizar

controlando dicho desorden, por medio de la modificación química de los elementos estructurales.

• El comportamiento luminiscente mostrado por los materiales vitrocerámicos ricos en cristalizaciones de plagioclasa sódica los sitúa como una alternativa a los fósforos vitrocerámicos basados en tierras raras, destacando en aplicaciones como marcadores de seguridad o vidrios emisores de luz.

• La mejora simultánea de las propiedades termo-reflectantes y mecánicas permite la aplicación de esta nueva familia de materiales vitrocerámicos en baldosas cerámicas, de cara a su empleo en pavimentos en zonas de alto tránsito y en pavimentos o revestimientos reflectantes para el diseño de edificios sostenibles.

• Los altos valores de resistencia dieléctrica obtenidos en estos nuevos materiales vitrocerámicos, sumado al ahorro energético que conlleva el empleo de un ciclo rápido de sinterización con respecto a los materiales cerámicos convencionales del sector, sitúa a este tipo de materiales en una posición privilegiada de cara a su uso en aplicaciones de aislamiento eléctrico de alto voltaje.

Bibliografía

BIBLIOGRAFÍA

(1) Casasola, R.; Rincón, J. M.; Romero, M. Glass-Ceramic Glazes for Ceramic Tiles: A Review. *J. Mater. Sci.* **2012**, *47* (2), 553–582.

(2) Berto, A. M. Ceramic Tiles: Above and beyond Traditional Applications. *J. Eur. Ceram. Soc.* **2007**, *27* (2–3), 1607–1613.

(3) Reinosa, J.; Rubio-marcos, F.; Solera, E.; Ferna, F.; Bengochea, M. A. Sintering Behaviour of Nanostructured Glass-Ceramic Glazes. *Ceram. Int.* **2010**, *36* (6), 1845–1850.

(4) Moya, J. S.; Pecharromán, C.; Montero, I.; Pina-Zapardiel, R.; Esteban-Cubillo, A.; Reinosa, J. J.; Fernandez, J. F. Fabrication of Nanostructured Metallized Glazes by Conventional Fast-Firing Route. *J. Am. Ceram. Soc.* **2011**, *94* (7), 2067–2073.

(5) Falk, G.; Kraemer, L. EPD of Novel Nanostructured Silica Coatings: Processing and Applications. *ECS Trans.* **2018**, *82* (1), 7–12.

(6) Pérez-Arantegui, J.; Larrea, A.; Molera, J.; Pradell, T.; Vendrell-Saz, M. Some Aspects of the Characterization of Decorations on Ceramic Glazes. *Appl. Phys. A Mater. Sci. Process.* **2004**, *79* (2), 235–239.

(7) Roqué, J.; Molera, J.; Sciau, P.; Pantos, E.; Vendrell-Saz, M. Copper and Silver Nanocrystals in Lustre Lead Glazes: Development and Optical Properties. *J. Eur. Ceram. Soc.* **2006**, *26* (16), 3813–3824.

(8) Borgia, I.; Brunetti, B.; Mariani, I.; Sgamellotti, A.; Cariati, F.; Fermo, P.; Mellini, M.; Viti, C.; Padeletti, G. Heterogeneous Distribution of Metal Nanocrystals in Glazes of Historical Pottery. *Appl. Surf. Sci.* **2002**, *185* (3–4), 206–216.

(9) Bernardo, E.; Andreola, F.; Barbieri, L.; Lancellotti, I. Sintered Glass-Ceramics and Glass-Ceramic Matrix Composites from CRT Panel Glass. *J. Am. Ceram. Soc.* **2005**, *88* (7), 1886–1891.

(10) Bernardo, E.; Doyle, J.; Hampshire, S. Sintered Feldspar Glass-Ceramics and Glass-Ceramic Matrix Composites. *Ceram. Int.* **2008**, *34* (8), 2037–2042.

(11) Sanchez Garcia Guinea, J., L. Feldespatos: Mineralogía, Yacimientos y Aplicaciones.

Recursos Minerales de España, Textos Univ., 15, CSIC. 1992, pp 441–470.

(12) Reichl, C.; Schatz, M.; Zsak, G. World Mining Data 2018. In *World Mining Data*; 2018; Vol. 33, p 237.

(13) ASCER. Balance definitivo de 2017 del sector español fabricante de baldosas cerámicas https://www.ascer.es/prensaNoticias.aspx?cual=sector&returnURL=default.aspx?lang=es-ES&lang=es-ES&id=11579.

(14) Pan, Z.; Wang, Y.; Huang, H.; Ling, Z.; Dai, Y.; Ke, S. Recent Development on Preparation of Ceramic Inks in Ink-Jet Printing. *Ceram. Int.* **2015**, *41* (10), 12515–12528.

(15) Cain, M.; Morrell, R. Nanostructured Ceramics: A Review of Their Potential. *Appl. Organomet. Chem.* **2001**, *15* (5), 321–330.

(16) Jaquotot, P.; Campillo, A.; Reinosa, J. J.; Romero, J. J.; Bengochea, M. A.; Esteban-Cubillo, A.; Santarén, J.; Aguilar, E.; Pina, R.; Pecharroman, C.; et al. Desarrollo de Esmaltes Nanoestructurados Multifuncionales. *Boletín la Soc. Española Cerámica y Vidr.* **2009**, *48* (2), 95–98.

(17) Schasfoort, R. B.; Tudos, A. J. Introduction to Surface Plasmon Resonance. In *Handbook of Surface Plasmon Resonance*; 2017; pp 1–26.

(18) Rambaldi, E.; Tucci, A.; Esposito, L. Nano-Oxides to Improve the Surface Properties of Ceramic Tiles. *Boletín la …* **2010**, *49* (4), 253–258.

(19) Santoni, S.; Toccafondi, N.; Giorgi, R.; Baglioni, P.; Ambrosi, M.; Fratini, E. High-Performance and Anti-Stain Coating for Porcelain Stoneware Tiles Based on Nanostructured Zirconium Compounds. *J. Colloid Interface Sci.* **2014**, *432*, 117–127.

(20) Zeng, Z.; Peng, C.; Hong, Y.; Lu, Y.; Wu, J. Fabrication of a Photocatalytic Ceramic by Doping Si-, P-, and Zr-Modified TiO2nanopowders in Glaze. *J. Am. Ceram. Soc.* **2010**, *93* (10), 2948–2951.

(21) Hevia, R.; Centritto, N.; De Oliveira, P.; Bernardín, A. Materiales Vitrocerámicos: Características, Propiedades y Aplicaciones Industriales. In *Introducción a los esmaltes cerámicos*; 2002; pp 91–110.

(22) Man, H.; Hong-xia, L.; Xiu-jun, Y.; Hong-liang, X. Sintering and Crystallization Behaviour

of Nanostructured Glass-Ceramic Glazes Derived from Industrial Solid Wastes. *Glas. Technol. Eur. J. Glas. Sci. Technol. - Part A* **2011**, *52* (5), 169–174.

(23) Muñoz, L. S.; Guinea, J. G.; Andrés, S. L. Caracterización Estructural Simple de Feldespatos Alcalinos: Metodología de Trabajo. *Boletín la Soc. Española Cerámica y Vidr.* **1991**, *30* (1991, 30 (2): 69–79, 79 Ref), 69–79.

(24) Parsons, I. *Feldspars and Their Reactions*; 1994.

(25) Andrew Putnis. Transformation Processes in Minerals I : Exsolution. In *An Introduction to Mineral Sciences*; 1992; pp 333–384.

(26) Carpenter, M. A. Mechanisms of Exsolution in Sodic Pyroxenes. *Contrib. to Mineral. Petrol.* **1980**, *71* (3), 289–300.

(27) Favvas, E. P.; Mitropoulos, A. C. What Is Spinodal Decomposition? *J. Eng. Sci. Technol. Rev.* **2008**, *1*, 25–27.

(28) Andrew Putnis. The Crystal Structure of Minerals II- Silicates. In *An Introduction to Mineral Sciences*; 1992; pp 141–184.

(29) Androulakis, J.; Lin, C. H.; Kong, H. J.; Uher, C.; Wu, C. I.; Hogan, T.; Cook, B. A.; Caillat, T.; Paraskevopoulos, K. M.; Kanatzidis, M. G. Spinodal Decomposition and Nucleation and Growth as a Means to Bulk Nanostructured Thermoelectrics: Enhanced Performance in Pb1-XSnxTe-PbS. *J. Am. Chem. Soc.* **2007**, *129* (31), 9780–9788.

(30) Sato, K.; Katayama-Yoshida, H.; Dederichs, P. H. High Curie Temperature and Nano-Scale Spinodal Decomposition Phase in Dilute Magnetic Semiconductors. *Jpn. J. Appl. Phys.* **2005**, *44* (28–32).

(31) Julthongpiput, D.; Zhang, W.; Douglas, J. F.; Karim, A.; Fasolka, M. J. Pattern-Directed to Isotropic Dewetting Transition in Polymer Films on Micropatterned Surfaces with Differential Surface Energy Contrast. *Soft Matter* **2007**, *3* (5), 613.

(32) Suzuki, M.; Tanaka, T. Thermodynamic Prediction of Spinodal Decomposition in Multi-Component Silicate Glass for Design of Functional Porous Glass Materials. *High Temp. Mater. Process.* **2012**, *31* (4–5), 323–328.

(33) Goldstein, M. Light Scattering and Spinodal Decomposition in Glasses. *J. Am. Ceram.*

Soc. **1965**, *48* (3), 126–130.

(34) Freeman, J.; Kuebler, E.; Jolliff, L.; Haskin, A. Characterization of Natural Feldspars by Raman Spectroscopy for Future Planetary Exploration. *Can. Mineral.* **2008**, *46*, 1477–1500.

(35) Senderov, E. E. On the Theory of Al, Si Ordering in Albite. *Phys. Chem. Miner.* **1980**, *6* (4), 251–268.

(36) Meneghinello, E.; Alberti, A.; Cruciani, G. Order-Disorder Process in the Tetrahedral Sites of Albite. *Am. Mineral.* **1999**, *84* (7–8), 1144–1151.

(37) Aliatis, I.; Lambruschi, E.; Mantovani, L.; Bersani, D.; Andó, S.; Diego Gatta, G.; Gentile, P.; Salvioli-Mariani, E.; Prencipe, M.; Tribaudino, M.; et al. A Comparison between Ab Initio Calculated and Measured Raman Spectrum of Triclinic Albite (NaAlSi3O8). *J. Raman Spectrosc.* **2015**, *46* (5), 501–508.

(38) McKeown, D. A. Raman Spectroscopy and Vibrational Analyses of Albite: From 25°C through the Melting Temperature. *Am. Mineral.* **2005**, *90* (10), 1506–1517.

(39) Aliatis, I. Vibrational Dynamics and Structure of Natural Feldspars, 2016.

(40) Derkacheva, E. S.; Krzhizhanovskaya, M. G.; Bubnova, R. S. Thermal Behavior of Reedmergnerite NaBSi3O8 and Searlesite NaBSi2O5(OH)2. *Glas. Phys. Chem.* **2017**, *43* (5), 459–463.

(41) Krzhizhanovskaya, M. G.; Bubnova, R. S.; Depmeier, W.; Rahmoun, N. S.; Filatov, S. K.; Ugolkov, V. L. A New Borosilicate Feldspar, KBSi3O8: Synthesis, Crystal Structure and Thermal Behavior. *Zeitschrift fur Krist.* **2012**, *227* (7), 446–451.

(42) Kyono, A.; Kimata, M. Refinement of the Crystal Structure of a Synthetic Non-Stoichiometric Rb-Feldspar. *Mineral. Mag.* **2001**, *65* (4), 523–531.

(43) Flehmig, W. The Synthesis of Feldspars at Temperature between 0°-80° C, Their Ordering Behaviour and Twinning. *Contrib. to Mineral. Petrol.* **1977**, *65* (1), 1–9.

(44) Liu, C.; Komarneni, S.; Roy, R. Epitaxy in the Crystallization of Feldspar Gels and Glasses. *MRS Proc.* **1994**, *346*, 721.

(45) Buljan, I.; Kosanovic, C.; Kralj, D. A Novel Synthesis of Nano-Sized Mullite from

Aluminosilicate Precursors. *J. Alloys Compd.* **2011**, *509* (32), 8256–8261.

(46) Rodriguez, E. T.; Anovitz, L. M.; Clement, C. D.; Rondinone, A. J.; Cheshire, M. C. Facile Emulsion Mediated Synthesis of Phase-Pure Diopside Nanoparticles. *Sci. Rep.* **2018**, *8* (1), 6–12.

(47) Gresoiu, I.; Burghelea, V.; Popescu, M. I.; Predoana, L.; Zaharescu, M. The Influence of Crystalline Additives on the Properties of Raw Glazes. *Phys. Chem. Glas. Eur. J. Glas. Sci. Technol. Part B* **2007**, *48* (5), 336–339.

(48) Schairer, J. F.; Bowen, N. L. The System Na2O-Al2O3-SiO2. *Am. J. Sci.* **1956**, *254*, 129–195.

(49) Selvaraj, U.; Liu, C. L.; Komarneni, S.; Roy, R. Epitaxial Crystallization of Seeded Albite Glass. *J. Am. Ceram. Soc.* **1991**, *74* (6), 1378–1381.

(50) Liu, C.; Komarneni, S.; Roy, R. Crystallization of Anorthite-Seeded Albite Glass by Solid-State Epitaxy. *J. Am. Ceram. Soc.* **1992**, *75* (10), 2665–2670.

(51) Krzmanc, M. M.; Valant, M.; Suvorov, D. A Structural and Dielectric Characterization of NaxCa(1 − x)Al2−xSi(2+x)O8(x = 0 and 1) Ceramics. *J. Eur. Ceram. Soc.* **2005**, *25*, 2835–2838.

(52) Riello, P.; Canton, P.; Comelato, N.; Polizzi, S.; Verità, M.; Fagherazzi, G.; Hofmeister, H.; Hopfe, S. Nucleation and Crystallization Behavior of Glass-Ceramic Materials in the Li2O-Al2O3-SiO2 System of Interest for Their Transparency Properties. *J. Non. Cryst. Solids* **2001**, *288* (1–3), 127–139.

(53) Khabas, T. A.; Klimova, V. V.; Starosvetskiy, S. I.; Vasilyeva, A. P.; Zvigintsev, M. A. Crystal Phase Formation in Colored Leucite-Reinforced Glass-Ceramics for Dental Restorations. *Inorg. Mater. Appl. Res.* **2017**, *8* (1), 186–193.

(54) De Vicente-Mingarro, I.; Callejas, P.; Rincón, J. . M. Materiales Vitrocerámicos : El Proceso Vitrocerámico. **1993**, *32* (3), 157–167.

(55) Zanotto, E. D. A Bright Future for Glass-Ceramics. *Am. Ceram. Soc. Bull.* **2011**, *89* (8), 609–612.

(56) Hölland, W.; Beall, G. *Glass–ceramic Technology*; 2012.

(57) Boulon, G. Luminescence in Glassy and Glass Ceramic Materials. *Mater. Chem. Phys.* **1987**, *16* (3–4), 301–347.

(58) Ehrt, D. Photoluminescence in Glasses and Glass Ceramics. *IOP Conf. Ser. Mater. Sci. Eng.* **2009**, *2*.

(59) Nikl, M.; Mares, J. A.; Mihokova, E.; Nitsch, K.; Solovieva, N.; Babin, V.; Krasnikov, A.; Zazubovich, S.; Martini, M.; Vedda, A.; et al. Radio- and Thermoluminescence and Energy Transfer Processes in Ce3+(Tb3+)-Doped Phosphate Scintillating Glasses. *Radiat. Meas.* **2001**, *33* (5), 593–596.

(60) Dymshits, O.; Shepilov, M.; Zhilin, A. Transparent Glass-Ceramics for Optical Applications. *MRS Bull.* **2017**, *42* (3), 200–205.

(61) Rojas-Hernandez, R. E.; Rubio-Marcos, F.; Serrano, A.; Campo, A. Del; Fernandez, J. F. Precise Tuning of the Nanostructured Surface Leading to the Luminescence Enhancement in SrAl2 O4 Based Core/Shell Structure. *Sci. Rep.* **2017**, *7* (1), 1–9.

(62) Ronda, C. R.; Jüstel, T.; Nikol, H. Rare Earth Phosphors: Fundamentals and Applications. *J. Alloys Compd.* **1998**, *275–277*, 669–676.

(63) Chiriu, D.; Stagi, L.; Carbonaro, C. M.; Ricci, P. C. Strength and Weakness of Rare Earths Based Phosphors: Strategies to Replace Critical Raw Materials. *Phys. Status Solidi Curr. Top. Solid State Phys.* **2016**, *13* (10–12), 989–997.

(64) Hurst, C. China's Rare Earth Elements Industry: What Can the West Learn? *Inst. Anal. Glob. Secur.* **2010**, No. March, 43.

(65) Boonsin, R.; Chadeyron, G.; Roblin, J. P.; Boyer, D.; Mahiou, R. Development of Rare-Earth-Free Phosphors for Eco-Energy Lighting Based LEDs. *J. Mater. Chem. C* **2015**, *3* (37), 9580–9587.

(66) Lin, H.; Hu, T.; Cheng, Y.; Chen, M.; Wang, Y. Glass Ceramic Phosphors: Towards Long-Lifetime High-Power White Light-Emitting-Diode Applications–A Review. *Laser Photonics Rev.* **2018**, *12* (6).

(67) Barbin, V Pagel, M Blanc, P Ohnenstetter, D. *Cathodoluminescence in Geosciences*; 2000.

(68) Garcia-Guinea, J.; Townsend, P. D.; Sanchez-Munoz, L.; Rojo, J. M. Ultraviolet-Blue Ionic Luminescence of Alkali Feldspars from Bulk and Interfaces. *Phys. Chem. Miner.* **1999**, *26* (8), 658–667.

(69) Kayama, M.; Nakano, S.; Nishido, H. Characteristics of Emission Centers in Alkali Feldspar: A New Approach by Using Cathodoluminescence Spectral Deconvolution. *Am. Mineral.* **2010**, *95* (11–12), 1783–1795.

(70) Krbetschek, M. R.; Götze, J.; Irmer, G.; Rieser, U.; Trautmann, T. The Red Luminescence Emission of Feldspar and Its Wavelength Dependence on K, Na, Ca - Composition. *Mineral. Petrol.* **2002**, *76* (3–4), 167–177.

(71) Garcia-Guinea, J.; Rendell, H.; Sanchez-Muñoz, L. Luminescence Spectra of Alkali Feldspars: Some Relationships between Structural Features and Luminescence Emission. *Radiation Protection Dosimetry*. 1996, pp 395–398.

(72) Slaats, P. G. G.; Dirksen, G. J.; Blasse, G. Luminescence of Some Activators in Synthetic Potassium Feldspar Crystals. *Mater. Chem. Phys.* **1991**, *30* (1), 19–23.

(73) Contreras, J. E.; Rodríguez, E. A. Nanostructured Insulators – A Review of Nanotechnology Concepts for Outdoor Ceramic Insulators. *Ceram. Int.* **2017**, *43* (12), 8545–8550.

(74) Liebault, J.; Vallayer, J.; Goeuriot, D.; Treheux, D.; Thevenot, F. How the Trapping of Charges Can Explain the Dielectric Breakdown Performance of Alumina Ceramics. *J. Eur. Ceram. Soc.* **2001**, *21* (3), 389–397.

(75) Touzin, M.; Goeuriot, D.; Guerret-piécourt, C.; Juvé, D.; Fitting, H. Alumina Based Ceramics for High-Voltage Insulation. *J. Eur. Ceram. Soc.* **2010**, *30* (4), 805–817.

(76) Krzmanc, M. M.; Valant, M.; Suvorov, D. A Structural and Dielectric Characterization of Na x Ca 1 − x Al 2 − x Si 2 + x O 8 (x = 0 and 1) Ceramics. **2005**, *25*, 2835–2838.

(77) Adnan, R.; Chan, Y. C.; Islam, F. Structure–property Relationship in High-Tension Ceramic Insulator Fired at High Temperature. *Mater. Sci. Eng. B* **2004**, *106* (2), 132–140.

(78) Relva C.Buchanan. Ceramic Materials for Electronics. **2004**, *Third edit*, 525–526.

(79) Yoshimura, M.; Bowen, H. K. Electrical Breakdown Strength of Alumina at High

Temperatures. *J. Am. Ceram. Soc.* **1981**, *64* (7), 404–410.

(80) O'Dwyer, J. J. *The Theory of Dielectric Breakdown in Solids*; 1964.

(81) Eyring, H. Dielectric Breakdown of Solids. *J. Chem. Educ.* **195AD**, *29* (2), 108.

(82) Khan, Z. H.; Zanganeh, K.; Salvador, C. Experimental Study of Dielectric Break-down of Refractory Board Materials for Application in High-Temperature Sieving Electrostatic Precipitator. *Proc. Jt. Electrost. Conf.* **2012**, 1–9.

(83) O'Dwyer, J. J. The Theory of Avalanche Breakdown in Solid Dielectrics. *J. Phys. Chem. Solids* **1967**, *28* (7), 1137–1144.

(84) Hu, H.; Li, H.; Dai, L.; Shan, S.; Zhu, C. Electrical Conductivity of Alkali Feldspar Solid Solutions at High Temperatures and High Pressures. *Phys. Chem. Miner.* **2013**, *40* (1), 51–62.

(85) Haiying, H.; Heping, L.; Dai, L.; Shan, S.; Zhu, C. Electrical Conductivity of Albite at High Temperatures and High Pressures. *Am. Mineral.* **2011**, *96* (11–12), 1821–1827.

(86) Rosenholtz, J. L.; Smith, D. T. The Dielectric Constant of Mineral Powders. *Am. Mineral.* **1936**, *21* (2), 115–120.

(87) Rasteiro, M. G.; Gassman, T.; Santos, R.; Antunes, E. Crystalline Phase Characterization of Glass-Ceramic Glazes. *Ceram. Int.* **2007**, *33* (3), 345–354.

(88) Ghosh, S.; Pal, K. S.; Dandapat, N.; Ghosh, J.; Datta, S. Glass-Ceramic Glazes for Future Generation Floor Tiles. *J. Eur. Ceram. Soc.* **2013**, *33* (5), 935–942.

(89) Yekta, B. E.; Alizadeh, P.; Rezazadeh, L. Synthesis of Glass-Ceramic Glazes in the ZnO-Al2O3-SiO2-ZrO2 System. *J. Eur. Ceram. Soc.* **2007**, *27* (5), 2311–2315.

(90) Gómez-Tena, M. P.; Gilabert, J.; Toledo, J.; Ibáñez, M. J.; Muñoz, A. Determination of the Wear Resistance of Traditional Ceramic Tile Glazes Using a Pin-on-Disk Tribometer. *Int. J. Surf. Sci. Eng.* **2011**, *5* (4), 272–285.

(91) Carbajal, L.; Rubio-Marcos, F.; Bengochea, M. a.; Fernandez, J. F. Properties Related Phase Evolution in Porcelain Ceramics. *J. Eur. Ceram. Soc.* **2007**, *27* (13–15), 4065–4069.

(92) Pina-Zapardiel, R.; Esteban-Cubillo, A.; Bartolomé, J. F.; Pecharromán, C.; Moya, J. S. High Wear Resistance White Ceramic Glaze Containing Needle like Zircon Single Crystals by the Addition of Sepiolite N-ZrO2. *J. Eur. Ceram. Soc.* **2013**, *33* (15–16), 3379–3385.

(93) Yekta, B. E.; Alizadeh, P.; Rezazadeh, L. Floor Tile Glass-Ceramic Glaze for Improvement of Glaze Surface Properties. *J. Eur. Ceram. Soc.* **2006**, *26* (16), 3809–3812.

(94) Marangoni, M.; Nait-Ali, B.; Smith, D. S.; Binhussain, M.; Colombo, P.; Bernardo, E. White Sintered Glass-Ceramic Tiles with Improved Thermal Insulation Properties for Building Applications. *J. Eur. Ceram. Soc.* **2017**, *37* (3), 1117–1125.

(95) Medvedovski, E. Wear-Resistant Engineering Ceramics. *Wear* **2001**, *249* (9), 821–828.

(96) Doğan, C. P.; Hawk, J. a. Role of Composition and Microstructure in the Abrasive Wear of High-Alumina Ceramics. *Wear* **1999**, *225–229*, 1050–1058.

(97) Latella, B. A.; O'Connor, B. H. Effect of Porosity on the Erosive Wear of Liquid-Phase-Sintered Alumina Ceramics. *J. Am. Ceram. Soc.* **1999**, *82* (8), 2145–2149.

(98) Zhao, J.; Xie, D. Effect of Nanoparticles on Wear Resistance and Surface Hardness of a Dental Glass-Ionomer Cement. *J. Compos. Mater.* **2009**, *43* (23), 2739–2752.

(99) Journal, I. Influence of Nano-Particle on the Wear Behaviour of Thin Film Coatings A Review Influence of Nano-Particle on the Wear Behaviour of Thin Film Coatings. **2018**, *13* (April), 4053–4058.

(100) Heo, S.; Kim, S.; Kim, U.; Pee, J.; Han, Y.; Kim, S.; Lee, S.; Kim, H.; Oh, Y. Tribological Behavior of Whiteware with Different Transparent Glazes. *J. Korean Ceram. Soc.* **2015**, *52* (3), 186–191.

(101) Zhao, M.; Pan, W.; Wan, C.; Qu, Z.; Li, Z.; Yang, J. Defect Engineering in Development of Low Thermal Conductivity Materials: A Review. *J. Eur. Ceram. Soc.* **2017**, *37* (1), 1–13.

(102) Kingery, W. D.; Mcquarrie, M. C. Thermal Conductivity: I, Concepts of Measurement and Factors Affecting Thermal Conductivity of Ceramic Materials. *J. Am. Ceram. Soc.* **1954**, *37* (2), 67–72.

(103) Linvill, M. L.; Vandersande, J. W.; Pohl, R. O. Thermal Conductivity of Feldspars. *Bull.*

Minéralogie **1984**, *107* (3–4), 521–527.

(104) Treviño-Cardona, B.; Gómez-de-la-Fuente, I.; Colás, R. Method Used to Measure the Thermal Diffusivity of Ceramic Materials. *J. Am. Ceram. Soc.* **2004**, *87* (5), 973–976.

(105) Ferrari, C.; Libbra, A.; Muscio, A.; Siligardi, C. Design of Ceramic Tiles with High Solar Reflectance through the Development of a Functional Engobe. *Ceram. Int.* **2013**, *39* (8), 9583–9590.

(106) Chung, M. H.; Park, J. C.; Ko, M. J. Effect of the Solar Radiative Properties of Existing Building Roof Materials on the Energy Use in Humid Continental Climates. *Energy Build.* **2015**, *102*, 172–180.

(107) Shahmohamadi, P.; Che-Ani, A. I.; Etessam, I.; Maulud, K. N. A.; Tawil, N. M. Healthy Environment: The Need to Mitigate Urban Heat Island Effects on Human Health. *Procedia Eng.* **2011**, *20*, 61–70.

(108) Santamouris, M. On the Energy Impact of Urban Heat Island and Global Warming on Buildings. *Energy Build.* **2014**, *82*, 100–113.

(109) Sarrat, C.; Lemonsu, A.; Masson, V.; Guedalia, D. Impact of Urban Heat Island on Regional Atmospheric Pollution. *Atmos. Environ.* **2006**, *40* (10), 1743–1758.

(110) La isla de calor (2ª parte de la serie "Cubiertas vegetales") http://urbanismoytransporte.com/la-isla-de-calor-2a-parte-de-la-serie-cubiertas-vegetales/.

(111) Santamouris, M. Cooling the Cities - A Review of Reflective and Green Roof Mitigation Technologies to Fight Heat Island and Improve Comfort in Urban Environments. *Sol. Energy* **2014**, *103*, 682–703.

(112) Elton, N. J.; Legrix, A. Wavelength Dependence of Kubelka-Munk Scattering Spectra for Studies of TiO2 Microstructure and Aggregation in Paints. *J. Coatings Technol. Res.* **2014**, *11* (4), 555–566.

(113) Karlessi, T.; Santamouris, M.; Apostolakis, K.; Synnefa, A.; Livada, I. Development and Testing of Thermochromic Coatings for Buildings and Urban Structures. *Sol. Energy* **2009**, *83* (4), 538–551.

(114) Kinoshita, S.; Yoshida, A. Investigating Performance Prediction and Optimization of

Spectral Solar Reflectance of Cool Painted Layers. *Energy Build.* **2016**, *114*, 214–220.

(115) Levinson, R.; Berdahl, P.; Asefaw Berhe, A.; Akbari, H. Effects of Soiling and Cleaning on the Reflectance and Solar Heat Gain of a Light-Colored Roofing Membrane. *Atmos. Environ.* **2005**, *39* (40), 7807–7824.

(116) Álvarez-Docio, C. M.; Reinosa, J. J.; del Campo, A.; Fernández, J. F. 2D Particles Forming a Nanostructured Shell: A Step Forward Cool NIR Reflectivity for CoAl2O4pigments. *Dye. Pigment.* **2017**, *137*, 1–11.

(117) Sarasamma Vishnu, V.; Lakshmipathi Reddy, M. Near-Infrared Reflecting Inorganic Pigments Based on Molybdenum and Praseodymium Doped Yttrium Cerate: Synthesis, Characterization and Optical Properties. *Sol. Energy Mater. Sol. Cells* **2011**, *95* (9), 2685–2692.

(118) Levinson, R.; Berdahl, P.; Akbari, H.; Miller, W.; Joedicke, I.; Reilly, J.; Suzuki, Y.; Vondran, M. Methods of Creating Solar-Reflective Nonwhite Surfaces and Their Application to Residential Roofing Materials. *Sol. Energy Mater. Sol. Cells* **2007**, *91* (4), 304–314.

(119) Pisello, A. L.; Cotana, F.; Nicolini, A.; Brinchi, L. Development of Clay Tile Coatings for Steep-Sloped Cool Roofs. *Energies* **2013**, *6* (8), 3637–3653.

(120) Zhu, M.; Ji, R.; Li, Z.; Wang, H.; Liu, L. L.; Zhang, Z. Preparation of Glass Ceramic Foams for Thermal Insulation Applications from Coal Fly Ash and Waste Glass. *Constr. Build. Mater.* **2016**, *112* (June), 398–405.

(121) Orts, M. J.; Escardino, A.; Amorós, J. L.; Negre, F. Microstructural Changes during the Firing of Stoneware Floor Tiles. *Appl. Clay Sci.* **1993**, *8* (2–3), 193–205.

(122) García, E.; De Pablos, A.; Bengoechea, M. A.; Guaita, L.; Osendi, M. I.; Miranzo, P. Thermal Conductivity Studies on Ceramic Floor Tiles. *Ceram. Int.* **2011**, *37* (1), 369–375.

(123) Torres, P.; Manjate, R. S.; Quaresma, S.; Fernandes, H. R.; Ferreira, J. M. F. Development of Ceramic Floor Tile Compositions Based on Quartzite and Granite Sludges. *J. Eur. Ceram. Soc.* **2007**, *27* (16), 4649–4655.

(124) Montero, M. A.; Jordán, M. M.; Almendro-Candel, M. B.; Sanfeliu, T.; Hernández-Crespo, M. S. The Use of a Calcium Carbonate Residue from the Stone Industry in Manufacturing

of Ceramic Tile Bodies. *Appl. Clay Sci.* **2009**, *43* (2), 186–189.

(125) Luz, A. P.; Ribeiro, S. Use of Glass Waste as a Raw Material in Porcelain Stoneware Tile Mixtures. *Ceram. Int.* **2007**, *33* (5), 761–765.

(126) Nassetti, G. Technological and Productive Innovations in the Ceramic Industry with Particular Reference to Ceramic Floor and Wall Tiles. *Mater. Sci. Eng. A* **1989**, *109* (C), 417–425.

(127) Bribiesca, S.; Equihua, R.; Villaseñor, L. Photoacoustic Thermal Characterization of Electrical Porcelains: Effect of Alumina Additions on Thermal Diffusivity and Elastic Constants. *J. Eur. Ceram. Soc.* **1999**, *19* (11), 1979–1985.

(128) Michot, A.; Smith, D. S.; Degot, S.; Gault, C. Thermal Conductivity and Specific Heat of Kaolinite: Evolution with Thermal Treatment. *J. Eur. Ceram. Soc.* **2008**, *28* (14), 2639–2644.

(129) Skauge, A.; Fuller, N.; Hepler, L. G. Specific Heats of Clay Minerals: Sodium and Calcium Kaolinites, Sodium and Calcium Montmorillonites, Illite, and Attapulgite. *Thermochim. Acta* **1983**, *61* (1–2), 139–145.

(130) García Ten, J.; Orts, M. J.; Saburit, A.; Silva, G. Thermal Conductivity of Traditional Ceramics. Part I: Influence of Bulk Density and Firing Temperature. *Ceram. Int.* **2010**, *36* (6), 1951–1959.

(131) Feng, X.; Huang, X.; Wang, X. Thermal Conductivity and Secondary Porosity of Single Anatase TiO2 Nanowire. *Nanotechnology* **2012**, *23* (18).

(132) Jiménez-Pérez, J. L.; Gutiérrez Fuentes, R.; Sánchez-Sosa, R.; Zapata Torres, M. G.; Correa-Pacheco, Z. N.; Sánchez Ramírez, J. F. Thermal Diffusivity Study of Nanoparticles and Nanorods of Titanium Dioxide (TiO<inf>2</Inf>) and Titanium Dioxide Coated with Cadmium Sulfide (TiO<inf>2</Inf>CdS). *Mater. Sci. Semicond. Process.* **2015**, *37*, 62–67.

(133) Meyer, L.; Grishko, V.; Jayaram, S.; Cherney, E.; Duley, W. W. Thermal Characteristics of Silicone Rubber Filled with ATH and Silica under Laser Heating. *Annu. Rep. Conf. Electr. Insul. Dielectr. Phenom.* **2002**, No. February, 848–852.

(134) Shi, Z.; Fu, R.; Agathopoulos, S.; Gu, X.; Zhao, W. Thermal Conductivity and Fire Resistance of Epoxy Molding Compounds Filled with Si3N4and Al(OH)3. *Mater. Des.*

2012, *34*, 820–824.

(135) Barbin, V. *(Eds .) Cathodoluminescence in Geosciences*.

(136) Bersani, D.; Aliatis, I.; Tribaudino, M.; Mantovani, L.; Benisek, A.; Carpenter, M. A.; Gatta, G. D.; Lottici, P. P. Plagioclase Composition by Raman Spectroscopy. *J. Raman Spectrosc.* **2018**, *49* (4), 684–698.

(137) Filonenko, O. V; Kuts, V. S.; Terebinska, M. I.; Lobanov, V. V. Quantum Chemical Calculation of 29Si NMR Spectrum of Silicone Dioxide Fullerene-like Molecules. *Chem. Phys. Technol. Surf.* **2015**, *6* (2), 263–268.

(138) MacKenzie, K. J. D.; Mark, E. S. *Multinuclear Solid-State NMR of Inorganic Materials*; 2002.

(139) Barrachina, E.; Esquinas, M.; Llop, J.; Notari, M. D.; Carda, J. B. Development of a Glass-Ceramic Glaze Formulated from Industrial Residues to Improve the Mechanical Properties of the Porcelain Stoneware Tiles. *Mater. Lett.* **2018**, *220*, 226–228.

(140) Enríquez, E.; Fuertes, V.; Cabrera, M. J.; Seores, J.; Muñoz, D.; Fernández, J. F. New Strategy to Mitigate Urban Heat Island Effect: Energy Saving by Combining High Albedo and Low Thermal Diffusivity in Glass Ceramic Materials. *Sol. Energy* **2017**, *149*, 114–124.

Anexo I. Patente

Marcador de seguridad a medida mediante espectroscopia Raman

MINISTERIO
DE INDUSTRIA, ENERGÍA
Y TURISMO

Oficina Española
de Patentes y Marcas

Acknowledgement of receipt

We hereby acknowledge receipt of your request for grant of a European patent as follows:

Submission number	300304032	
Application number	EP19382045.3	
File No. to be used for priority declarations	EP19382045	
Date of receipt	22 January 2019	
Your reference	P15084EP00	
Applicant	FÁBRICA NACIONAL DE MONEDA Y TIMBRE - REAL CASA DE LA MONEDA	
Country	ES	
Title		
Documents submitted	package-data.xml	ep-request.xml
	application-body.xml	ep-request.pdf (5 p.)
	SPECNONEPO.pdf\AAF_P15084EP00_Texto para presentar.pdf (97 p.)	f1002-1.pdf (2 p.)
Submitted by	CN=Juan Arias Sanz 7240	
Method of submission	Online	
Date and time receipt generated	22 January 2019, 17:43:55 (CET)	
Official Digest of Submission	00:D1:1E:04:BD:88:BA:C9:0A:C0:7B:1A:A0:EC:18:F1:FD:9B:C6:33	

/Madrid, Oficina Receptora/

Form 1002 - 1: Public inventor(s)

Designation of inventor

User reference: P15084EP00
Application No:

Public

	Inventor	
	Name:	MOURE ARROYO, Mr. Alberto
	Company:	CONSEJO SUPERIOR DE INVESTIGACIONES CIENTÍFICAS
	Department:	Instituto de Cerámica y Vidrio, ICV-CSIC
	Address:	Kelsen, 5
		E-28049 Madrid
		Spain
	The applicant has acquired the right to the European patent:	As employer
	Inventor	
	Name:	FERNÁNDEZ LOZANO, Mr. José Francisco
	Company:	CONSEJO SUPERIOR DE INVESTIGACIONES CIENTÍFICAS
	Department:	Instituto de Cerámica y Vidrio, ICV-CSIC
	Address:	Kelsen, 5
		E-28049 Madrid
		Spain
	The applicant has acquired the right to the European patent:	As employer
	Inventor	
	Name:	FUERTES DE LA LLAVE, Mr. Víctor
	Company:	CONSEJO SUPERIOR DE INVESTIGACIONES CIENTÍFICAS
	Department:	Instituto de Cerámica y Vidrio, ICV-CSIC
	Address:	Kelsen, 5
		E-28049 Madrid
		Spain
	The applicant has acquired the right to the European patent:	As employer
	Inventor	
	Name:	ENRÍQUEZ PÉREZ, Ms. Esther
	Company:	CONSEJO SUPERIOR DE INVESTIGACIONES CIENTÍFICAS
	Department:	Instituto de Cerámica y Vidrio, ICV-CSIC
	Address:	Kelsen, 5
		E-28049 Madrid
		Spain
	The applicant has acquired the right to the European patent:	As employer

User reference: P15084EP00
Application No:

	Inventor	
	Name:	GARCÍA JUEZ, Mr. Vicente
	Company:	FÁBRICA NACIONAL DE MONEDA Y TIMBRE - REAL CASA DE LA MONEDA
	Address:	Jorge Juan, 106 E-28009 Madrid Spain
	The applicant has acquired the right to the European patent:	As employer

Signature(s)

Place:	**Madrid**
Date:	**22 January 2019**
Signed by:	**Juan Arias Sanz 7240**
Association:	**ABG Intellectual Property Law, S.L.**
Representative name:	**ARIAS SANZ, Juan**
Capacity:	**(Representative)**

Europäisches Patentamt
European Patent Office
Office européen des brevets

Request for grant of a European patent

For official use only		
1 Application number:	MKEY	
2 Date of receipt (Rule 35(2) EPC):	DREC	
3 Date of receipt at EPO (Rule 35(4) EPC):	RENA	
4 Date of filing:		

5 Grant of European patent, and examination of the application under Article 94, are hereby requested. ☒

5.1 The applicant waives his right to be asked whether he wishes to proceed further with the application (Rule 70(2)) ☐

Procedural language: en

Filing Language: es

6 Applicant's or representative's reference: P15084EP00

Filing Office: ES

Applicant 1

7-1 Name: FÁBRICA NACIONAL DE MONEDA Y TIMBRE - REAL CASA DE LA MONEDA

8-1 Address: C/ Jorge Juan, 106
E-28009 Madrid
Spain

10-1 State of residence or of principal place of business: Spain

Applicant 2

7-2 Name: CONSEJO SUPERIOR DE INVESTIGACIONES CIENTÍFICAS

8-2 Address: Serrano, 142
E-28006 Madrid
Spain

10-1 State of residence or of principal place of business: Spain

14.1 The/Each applicant hereby declares that he is an entity or a natural person under Rule 6(4) EPC. ☐

Representative 1

15-1	Name:	ABG Intellectual Property Law, S.L.
	Association No.:	234
16-1	Address of place of business:	Avenida de Burgos ,16D Edificio Euromor E-28036 Madrid Spain
17-1	Telephone:	+34 91 417 13 00
17-1	Fax:	+34 91 417 13 01
17-1	E-mail:	informacion@abg-ip.com

Inventor(s)

23 Designation of inventor attached ☒

24 **Title of invention**

25 **Declaration of priority (Rule 52) and search results under Rule 141(1)**

A declaration of priority is hereby made for the following applications

25.2 The EPO is requested to retrieve a certified copy of the following previous application(s) (priority document(s)) via the WIPO Digital Access Service (DAS) using the indicated access code(s):

Request	Application number :	Access Code

25.3 This application is a complete translation of the previous application ☐

25.4 It is not intended to file a (further) declaration of priority ☒

26 **Reference to a previously filed application**

27 **Divisional application** ☐

28 **Article 61(1)(b) application** ☐

29 **Claims**

Number of claims: 15

29.1 ☒ as attached

29.2 ☐ as in the previously filed application (see Section 26.2)

29.3 ☐ The claims will be filed later

30 Figures

It is proposed that the abstract be published together with figure No. [ ]

31 Designation of contracting states

All the contracting states party to the EPC at the time of filing of the European patent application are deemed to be designated (see Article 79(1)).

32 Different applicants for different contracting states

33 Extension/Validation

This application is deemed to be a request to extend the effects of the European patent application and the European patent granted in respect of it to all non-contracting states to the EPC with which extension or validation agreements are in force on the date on which the application is filed. However, the request is deemed withdrawn if the extension fee or the validation fee, whichever is applicable, is not paid within the prescribed time limit.

33.1 It is intended to pay the extension fee(s) for the following state(s): [ ]

33.2 It is intended to pay the validation fee(s) for the following state(s): [ ]

34 Biological material

38 Nucleotide and amino acid sequences

38.1 The description contains a sequence listing in accordance with Rule 30(1) EPC. [ ]

38.2 The sequence listing is filed in electronic form [ ]

38.4 The sequence listing is attached in PDF format [ ]

Further indications

39 Additional copies of the documents cited in the European search report are requested

Number of additional sets of copies: [ ]

40 Refund of the search fee under to Article 9 of the Rules relating to Fees is requested [ ]

Application or publication number of earlier search report: [ ]

42 Payment

Method of payment: Debit from deposit account

The European Patent Office is hereby authorised, to debit from the deposit account with the EPO any fees and costs indicated on the fees section below.

Currency: EUR

Deposit account number:	28120063
Account holder:	ABG Intellectual Property Law, S.L.

43 Refunds

Any refunds should be made to EPO deposit account:	28120063
Account holder:	ABG Intellectual Property Law, S.L.

Fees	Factor applied	Fee schedule	Amount to be paid
001 Filing fee - EP direct - online	1	120.00	120.00
002 Fee for a European search - Applications filed on/after 01.07.2005	1	1 300.00	1 300.00
015 Claims fee - For the 16th to the 50th claim	0	235.00	0.00
015e Claims fee - For the 51st and each subsequent claim	0	585.00	0.00
501 Additional filing fee for the 36th and each subsequent page	62	15.00	930.00
Total:		**EUR**	**2 350.00**

44-A Forms		Details:	System file name:
A-1	Request		as ep-request.pdf
A-2	1. Designation of inventor	1. Inventor	as f1002-1.pdf

44-B Technical documents		Original file name:	System file name:
B-1	Specification in admissible non-EPO language	AAF_P15084EP00_Texto para presentar.pdf 15 claims 16 figure(s)	SPECNONEPO.pdf

44-C Other documents	Original file name:	System file name:

45	General authorisation:	

46 Signature(s)

Place: **Madrid**

Date: **22 January 2019**

Signed by:	**Juan Arias Sanz 7240**
Association:	**ABG Intellectual Property Law, S.L.**
Representative name:	**ARIAS SANZ, Juan**
Capacity:	**(Representative)**

Factura No.:	201900400	Fecha Factura:	23 de enero de 2019

Condiciones de pago.	30	**Fecha Vencimiento.**	22 de febrero de 2019
Nuestra Ref.	P15084EP00	**Su Ref.**	MRA (Marcador Raman Avanzado)
Cliente No.	3303	**N° de pedido.**	**45223398**
TL:	JA	**Posición.**	30 BURGOS

Dirección de Facturación:

FÁBRICA NACIONAL DE MONEDA Y TIMBRE - REAL CASA DE LA MONEDA
C/ Jorge Juan, 106
28009-Madrid

CIF.: Q2826004J

Dirección de Correspondencia:

FÁBRICA NACIONAL DE MONEDA Y TIMBRE-REAL CASA DE LA MONEDA
Jorge Juan, 106
E-28009 Madrid

Att.: Dpto. Jurídico
Mario Garriga

Asunto: **Solicitud de patente Europea nº EP19382045.3 con título "MARCADORES RAMAN" a nombre de FÁBRICA NACIONAL DE MONEDA Y TIMBRE - REAL CASA DE LA MONEDA y CONSEJO SUPERIOR DE INVESTIGACIONES CIENTÍFICAS**

Honorarios Profesionales Técnicos

Elaboración de borradores de solicitud hasta emisión de borrador final (97 págs) incluyendo adaptar figuras y revisión de documentos iniciales.	1.950,00
Total Honorarios Técnicos:	**EUR 1.950,00**

Honorarios Profesionales Administrativos

Presentación de la solicitud de patente europea.	375,00
Total Honorarios Administrativos:	**EUR 375,00**

Tasas Oficiales (No aplica IVA)

Presentación (120,00), búsqueda (1300,00) y páginas en exceso de 35 (930,00 (62 pgs x 15€/página))	1.175,00
Total Tasas Oficiales:	**EUR 1.175,00**

NOTA: Esta factura corresponde al 50% del total

TOTAL	3.500,00
BASE IMPONIBLE	2.325,00
IVA 21,00 %	488,25
TOTAL	**EUR 3.988,25**

ABG Intellectual Property Law, S.L.
Avda. de Burgos 16D
Edificio EUROMOR
E-28036 Madrid
Spain

E-mail: informacion@abg-ip.com
Tel.: +34 91 417 1300
CIF. : B83769737
VAT. : ES B83769737

Por favor indique siempre nuestro número de factura.

Forma de pago:
Banco: La Caixa
Número de cuenta.: 2100-4128-80-2200078658
IBAN : ES40 2100 4128 8022 0007 8658
BIC (SWIFT): CAIXESBB

Reg. Mercantil de Madrid, Tomo 19.273, Libro 0, Folio 112, Sección 8, Hoja M-337602 – Inscripción 1ª - CIF B83769737

Anexo II.

Currículum obtenido durante el período de Tesis Doctoral

PUBLICACIONES O DOCUMENTOS CIENTÍFICO-TÉCNICOS

Artículos incluidos en la tesis doctoral

1. E. Enríquez, V. Fuertes, M.J. Cabrera, J. Seores, D. Muñoz, J.F. Fernández, New strategy to mitigate urban heat island effect: Energy saving by combining high albedo and low thermal diffusivity in glass ceramic materials, Sol. Energy. 149 (2017) 114–124.

2. V. Fuertes, M.J. Cabrera, J. Seores, D. Muñoz, J.F. Fernández, E. Enríquez, Hierarchical micro-nanostructured albite-based glass-ceramic for high dielectric strength insulators, J. Eur. Ceram. Soc. 38 (2018) 2759–2766.

3. V. Fuertes, M.J. Cabrera, J. Seores, D. Muñoz, J.F. Fernández, E. Enríquez, Microstructural study of dielectric breakdown in glass-ceramics insulators, J. Eur. Ceram. Soc. 39 (2019) 376–383.

4. V. Fuertes de la Llave, A. del Campo, J.F. Fernández, E. Enríquez, Structural insights of hierarchically engineered feldspars by confocal Raman microscopy, J. Raman Spectrosc. 50 (2019) 741–754.

5. E. Enríquez, V. Fuertes, M.J. Cabrera, J. Seores, D. Muñoz, B. Galiana, et al., Study of the crystallization in fast sintered Na-rich plagioclase glass-ceramic, Ceram. Int. 45, (2019)

8899-8907.

6. V. Fuertes, M.J. Cabrera, J. Seores, D. Muñoz, J.F. Fernández, E. Enríquez, Enhanced Wear Resistance of engineered Glass-ceramic by nanostructured self-lubrication, Mater. Des. 168 (2019), 107623.

7. V. Fuertes, J. F. Fernández, E. Enríquez, Enhanced Luminescence in Rare-earth free Fast Sintering Glass-ceramic, Optica, 6 (2019) 668-679.

8. V.Fuertes, J. F. Fernández, E. Enríquez Tunable UV/blue Luminescence in Rare-earth Free Glass-ceramic Phosphor, J. Eur. Ceram. Soc. 39 (2019), 3221-3228.

9. E. Enríquez, V. Fuertes, M.J. Cabrera, Jaime Seores, D. Muñoz, J. F. Fernández, Absence of surface flaking in hierarchical glass-ceramic coating: high impact resistant ceramic tiles, J. Eur. Ceram. Soc. (bajo revisión).

Otros artículos realizados durante la tesis doctoral

10. V. Fuertes, A. Mariscal, R. Serna, F.J. Mompeán, M. García-Hernández, J.F. Fernández, et al., Multifunctional ZnO/Fe-O and graphene oxide nanocomposites: Enhancement of optical and magnetic properties, J. Eur. Ceram. Soc. 37 (2017).

11. E. Enríquez, V. Fuertes, M.J. Cabrera, J. Seores, D. Muñoz, W. More, et al., Model to evaluate the thermal comfort factor: Dynamic measurement of heat flow in building materials, J. Build. Eng. 20 (2018) 344–352.

Patente solicitada

Autores: A. Moure, J. F. Fernández, V. Fuertes, E. Enríquez, V. García-Juez
Título: Marcadores Raman
Titularidad: 50% Consejo Superior Investigaciones Científicas y 50% Fábrica Nacional de la Moneda y Timbre-Real Casa de la Moneda
Nº registro: EP19382045.3 22-Enero-2019

CONTRIBUCIONES A CONGRESOS

1. V.Fuertes; E.Enríquez; J.F. Fernández. "Synthesis and characterization of ZnO/GO/NPs FeO(OH) composites ".
   Electroceramics XV, Limoges (Francia), 2016.
2. V.Fuertes; E.Enríquez; J.F. Fernández. "Síntesis y caracterización dieléctrica de una nueva familia de materiales vitrocerámicos micro-nanoestructurados ".
   V Jornadas de jóvenes investigadores en ICV, Madrid (España), 2016.
3. V.Fuertes; E.Enríquez; J.F. Fernández. "Synthesis and characterization of ZnO/GO/NPs FeO(OH) composites ".
   International Workshop on Graphene/Ceramic Composites (WGCC), Cuenca (España), 2016.
4. V.Fuertes; E.Enríquez; J.F. Fernández "Desarrollo de una nueva familia de materiales vitrocerámicos micro-nanoestructurados: caracterización de propiedades y búsqueda de aplicaciones".
   Jornadas de Doctorandos en Físicas y Astrofísica UCM 2016/2017, Madrid (España), 2017
5. V.Fuertes; E.Enríquez; A. del Campo, J.F. Fernández. "Structural characterization of nanostructured glass ceramic materials ".
   Workshop: Understanding materials structure and performance by Raman Confocal Microscopy, Madrid (España), 2017.
6. V.Fuertes; E.Enríquez; J.F. Fernández. "Dielectric behaviour in albite and anorthite micro-nanostructured".
   ICE 2017, 8th International Conference on Electroceramics, Nagoya (Japón), 2017.
7. V.Fuertes; E.Enríquez; J.F. Fernández. "Albita vitrocerámica micro-nanoestructurada: Síntesis y caracterización microestructural"
   VI Jornadas de jóvenes investigadores en ICV, Madrid (España), 2017.
8. V.Fuertes; E.Enríquez; J.F. Fernández. "Micro-nanostructured glass-ceramic phosphor: enhanced luminescence behaviour"
   VII Jornadas de jóvenes investigadores en ICV, Madrid (España), 2018.